UNIVERSITÄT DUISBURG ESSEN

Open-Minded

Tailoring Cobalt-based Spinels for the Investigation of Composition- and Mesostructure-Activity Relationships in Oxidation Catalysis

Dissertation

Zur Erlangung des akademischen Grades eines

Doktors der Naturwissenschaften

– Dr. rer. nat. –

vorgelegt von

Anna Rabe

Fakultät für Chemie
der
Universität Duisburg-Essen

November 2023

DOI: 10.17185/duepublico/81857
URN: urn:nbn:de:hbz:465-20240419-095451-2

Diese Arbeit wurde in der Zeit von Oktober 2018 bis November 2023 an der Fakultät für Chemie der

Universität Duisburg-Essen

in der Arbeitsgruppe von

Prof. Dr. Malte Behrens

angefertigt.

Tag der Abgabe: 27.11.2023

Tag der Disputation: 12.04.2024

Gutachter:	Prof. Dr. Malte Behrens
	Prof. Dr. Kristina Tschulik
	Prof. Dr. Stephan Schulz
Vorsitzender:	Prof. Dr. Alexander Probst

Acknowledgement

First and most importantly I want to thank Prof. Dr. Malte Behrens for giving me the opportunity to work on this thesis in his group. Thank you for all the fruitful discussions, ideas, giving me a lot of freedom doing my research, and the opportunity for participating in so many conferences and workshops.

Secondly, I want to thank Prof. Dr. Kristina Tschulik for being the second examiner of this work and for the successful cooperations within the CRC/TRR 247.

I thank Prof. Dr. Stephan Schulz for being the third examiner and also for the discussions and feedback within the CRC and in the joint seminars during my time in Essen.

Dr. Klaus Friedel I thank for being a supportive supervisor during my first steps within this field of research. Thank you for supervising me, providing ideas, feedback, and for also letting me work freely.

I am thanking Dr. Maik Dreyer for being a great colleague and friend throughout the years and still. I thank you for the great discussions, advice, but also for distractions from the sometimes stressful life of a PhD student.

Nicolas Cosanne I want to thank for being a great Bachelor student, “Hiwi”, and now cooperation partner.

All members of the Behrens group, especially Dr. Benjamin Mockenhaupt, Dr. Jil Gieser, Dr. Sharif Najafishirtari, Dr. Fatih Özcan, Dr. Stephanie Becker, Dr. Justus Heese, and Dr. Manuel Heimann, I want to thank you for helping out, fun lunch breaks, conferences, and fruitful discussions throughout the years.

Next to the Behrens group I also want to thank the Schulz group, with whom we shared not only the floor during my time in Essen, but many fun barbecues or beer and pizza evenings.

I also want the thank my current group, AG Wende, for taking me in warmheartedly last year.

Next to all the coauthors, whom I am very grateful to, but who are mentioned at the beginning of the specific chapters of this thesis, I want to acknowledge all the people who contributed to my work, even though some of their names might not appear in the list of coauthors. Thank you to Dr. Kateryna Loza for measuring SEM, Dietrich Tönnis for PXRD measurements, Robin Meya for AAS und CHNS analysis, Dr. Markus Heidelmann for TEM, and Dr. Ulrich Hagemann for measuring XPS. A special thanks goes to Dr. Eko Budiyanto, who not only was my close collaborator in the project C1, but supported my work a lot by advising and providing measurements.

To the coordinators of the CRC 247, Dr. Franziska Günther, Dr. Carina Marek, and Susanne Moser I pronounce my gratitude for organizing events and support in general. I also want to thank all of my PhD colleagues from UnOCat for the fun summer schools, retreat, and conferences.

I want to thank my family, especially my parents for being patient, and for always supporting me in every possible way.

Naturally I thank all of my friends who were and are by my side along all of these years. Thank you for the fun nights out, talks, trips and vacations, and else.

Last but not least I want to thank my partner Leo, who has patiently dealt with my ups and downs throughout the years. Thank you for supporting me and providing distractions when I needed them the most.

Abstract

Heterogeneous oxidation catalysis in the liquid phase amongst other things is pivotal for the production of base chemicals, energy storage, and energy conversion. In comparison to the often used and well investigated catalytic gas phase reactions, which usually have to be conducted at rather harsh conditions, not enough is known about the active sites and reaction mechanisms of liquid phase catalysis, making the design of cheaper, more active, and more stable catalysts difficult. As a consequence, the systematic investigation of composition- and mesostructure-activity relationships is of very high importance, since it enables a more rational design of efficient heterogeneous catalysts. The mesostructure of a catalyst can be defined by numerous features, e.g., morphology, porosity, crystallinity, exposed surface facets, defects, or possible inhomogeneities on the micro or nano scale. Therefore, the main focus of this thesis lies upon the development of robust synthesis methods for liquid-phase catalysts, the systematic tuning of composition and mesostructure of the same, and their catalytic testing. Herein, cobalt-based spinels have been chosen as prototypic case study for (mixed) metal oxide catalysts.

To investigate the impact of composition the crystalline precursor decomposition approach was applied to synthesize a substitution series containing Co_3O_4, $MgCo_2O_4$, Co_2FeO_4, Co_2AlO_4, and $CoFe_2O_4$, with all catalysts exhibiting a porous platelet morphology and a predominant 111 surface termination. To also compare the impact of different surface terminations isotropic Co_3O_4 and $CoFe_2O_4$ were prepared. Catalytic testing in chemical water oxidation using ceric ammonium nitrate (CAN test), electrochemical oxygen evolution reaction (OER) and H_2O_2 decomposition was conducted. For the water oxidation reactions, Co^{3+} was found to play the major role for high activity. For H_2O_2 decomposition on the other hand, Co^{2+} is most important. Overall, in all reactions Co_3O_4 exhibited the highest activity. At constant Co^{3+} to other metal cation ratios redox active cations incorporated in the structure were beneficial for catalytic activity compared to the spinels containing redox inactive cations, therewith underlining the important role of redox pairs. The predominant 111 surface termination was only favorable for the Co^{3+} containing Co_3O_4, for $CoFe_2O_4$ no trend was observed.

Next to composition and surface termination, the precise tuning of other mesostructural features such as pore size is desirable. Therefore the crystalline precursor decomposition approach was combined with microemulsion-assisted co-precipitation (MACP). Through

limiting the particle growth within micelles and variation of the constant pH during synthesis, the pore size was systematically effected and the as-prepared layered double hydroxides (LDHs) and corresponding spinels are suited for the systematic investigation of confinement effects during OER. A threshold pore size at which the overpotential increased significantly was identified. Electrochemical impedance spectroscopy (EIS) hinted towards a change in OER mechanism, connected to the oxygen release step. It is proposed, that in the smaller pores, the critical radius for oxygen bubble formation is not met, so no oxygen bubbles are blocking the pores, resulting in the observed lower overpotential for samples with smaller pore sizes.

A detailed study on the structure of Co_2FeO_4 prepared by the crystalline precursor decomposition approach was conducted to better understand the formation of the oxide and porous mesostructure from the precursor. Due to a miscibility gap in the phase diagram at this composition, phase separation occurs during the decomposition step of the precursor. This results in porous crystalline nano-flakes, which exhibit spatial composition fluctuations of cobalt and iron rich domains with a size of around 5 nm. A surprisingly small lattice parameter for the iron rich phase was explained by density functional theory results with a higher compressibility of this phase and the high number of interfaces due to the phase separation on the nano scale. Investigation of the magnetic properties revealed an exchange bias effect, due to the strong coupling of the adjacent antiferromagnetic cobalt rich and ferrimagnetic iron rich regions within the platelets. This finding underlines the versatility of the crystalline precursor decomposition approach for not only the systematic and reproducible tuning of composition and mesostructure for catalytic applications, but also for synthesizing spinels with unusual crystallographic and magnetic properties.

Kurzzusammenfassung

Heterogen katalysierte Oxidationsreaktionen sind unter anderem von entscheidender Bedeutung für die Herstellung von Grundchemikalien, Energiespeicherung und Energieumwandlung. Im Vergleich mit der häufig verwendeten und gut untersuchten Gasphasenkatalyse, die oft bei anspruchsvollen Reaktionsbedingungen durchgeführt werden muss, ist nicht viel bekannt über die aktiven Zentren und Reaktionsmechanismen von Flüssigphasenkatalysatoren. Dies erschwert insbesondere die Entwicklung billigerer, aktiverer und stabilerer Katalysatoren. Daher ist die systematische Untersuchung von Zusammensetzungs- und Mesostrukturaktivitätsbeziehungen von großer Bedeutung, da sie ein rationelleres Design effizienterer heterogener Katalysatoren ermöglicht. Die Mesostruktur eines Katalysators kann durch viele Charakteristika beschrieben werden, zum Beispiel Morphologie, Porosität, Kristallinität, Oberflächenterminierungen, Defekte oder Inhomogenitäten auf der Mikro- oder Nanoskala. Auf Grund dessen liegt der Schwerpunkt dieser Arbeit auf der Entwicklung robuster Synthesemethoden für Flüssigphasenkatalysatoren, der systematischen Variation von Zusammensetzung und Mesostruktur, sowie der katalytischen Testung. Als prototypische Fallstudie wurden kobaltbasierte Mischmetaloxidkatalysatoren ausgewählt.

Um den Einfluss unterschiedlicher Zusammensetzungen auf die katalytische Aktivität zu untersuchen wurde mit Hilfe des *crystalline precursor decomposition approach* eine Substitutionsreihe bestehend aus Co_3O_4, $MgCo_2O_4$, Co_2FeO_4, Co_2AlO_4 und $CoFe_2O_4$ hergestellt. Alle Katalysatoren besitzen eine poröse Plättchemorphologie und eine vorherrschende 111-Oberflächenterminierung. Um auch den Einfluss unterschiedlicher Oberflächenterminierungen zu untersuchen, wurden isotropes Co_3O_4 und $CoFe_2O_4$ hergestellt. Zur Untersuchung der katalytischen Aktivität wurde die chemische Wasseroxidation mit Hilfe von Cer(IV)-ammoniumnitrat (CAN-Test), die elektrochemische Sauerstoffentwicklungsreaktion (OER) und die H_2O_2 Zersetzung durchgeführt. Für die Wasseroxidationsreaktionen spielte Co^{3+} die entscheidende Rolle für eine vergleichsweise hohe Aktivität, für die H_2O_2 Zersetzung auf der anderen Seite war Co^{2+} am wichtigsten. Bei allen Reaktionen zeigte Co_3O_4 die höchste Aktivität. Zusätzlich wirkten sich bei einem konstanten Anteil von Co^{3+} in der Spinellstruktur redoxaktive Kationen positiv auf die katalytische Aktivität aus, was die Relevanz von Redoxpaaren unterstreicht. Die

vorherrschende 111-Oberflächenterminierung war im Fall vom Co^{3+} enthaltendem Co_3O_4 vorteilhaft, für $CoFe_2O_4$ war kein Trend zu beobachten.

Neben Zusammensetzung und Oberflächenterminierung ist die Möglichkeit zur gezielten Variation anderer mesostruktureller Merkmale wie zum Beispiel die Porengröße wünschenswert. Daher wurde der *crystalline precursor decomposition approach* mit der mikroemulsionsbasierten Cofällung (*microemulsion-assisted co-precipitation,* (MACP)), kombiniert. Durch die Begrenzung des Partikelwachstums innerhalb der Mizellen und die Variation des konstanten pH Wertes während der Synthese wurde die Porengröße systematisch beeinflusst und die so hergestellten *layered double hydroxides* (LDHs) und entsprechenden Spinelle eignen sich so für die systematische Untersuchung von sog. *confinements effects* während der OER. Hierbei wurde eine Schwellenwert für die Porengröße identifiziert, oberhalb dessen es zu einen signifikantem Anstieg des Überpotentials kommt. Ergebnisse der elektrochemischen Impedanzspektroskopie (EIS) deuteten auf eine Änderung des OER Mechanismus hin, die mit dem Schritt der Sauerstofffreisetzung verbunden ist. Es wird angenommen, dass in den kleineren Poren der kritische Radius für die Bildung von Sauerstoffblasen nicht erreicht werden kann, sodass keine Sauerstoffblasen die Poren blockieren, was in diesem Fall wiederum zu einem geringen Überpotential führt.

Um die Oxidbildung aus dem *precursor* und die poröse Mesostruktur besser zu verstehen, wurde eine detaillierte Untersuchung der Struktur des durch den *crystalline precursor decomposition approach* hergestellten Co_2FeO_4 durchgeführt. Aufgrund einer Mischungslücke im Phasendiagramm bei dieser Zusammensetzung kommt es während des Zersetzungsschrittes des *precursors* zu einer Phasenseparation. Dies führt zu porösen und kristallinen *nano flakes*, die räumliche Schwankungen im Kobalt- und Eisengehalt mit einer Domänengröße von etwa 5 nm aufweisen. Ein überraschend kleiner Gitterparameter der eisenreichen Phase wurde durch Ergebnisse der Dichtefunktionaltheorie mit einer höheren Kompressibilität dieser Phase und der hohen Anzahl von Grenzflächen aufgrund der nanoskaligen Phasentrennung erklärt. Die Untersuchung der magnetischen Eigenschaften ergab einen *exchange bias effect* aufgrund der starken Kopplung der benachbarten antiferromagnetischen kobaltreichen und ferrimagnetischen eisenreichen Bereiche innerhalb der Plättchen. Dieser Befund unterstreicht die Vielseitigkeit des *crystalline precursor decomposition approach*. Nicht nur ist die systematische und reproduzierbare Variation der Zusammensetzung und Mesostruktur für katalytische Anwendungen möglich, sondern auch die Synthese von Spinellen mit ungewöhnlichen kristallographischen und magnetischen Eigenschaften.

Abbreviations

AAS	atomic absorption spectroscopy
AFM	antiferromagnetic
BET	Brunauer-Emmett-Teller
BJH	Barrett-Joyner-Hallenda
CV	cyclic voltammogram
DFT+*U*	density functional theory with a Hubbard *U* term
DLS	dynamic light scattering
DRT	distribution of relaxation times
DTG	differential thermogravimetry
ECSA	electrochemically active surface area
EDX	energy dispersive X-ray spectroscopy
EIS	electrochemical impedance spectroscopy
EXAFS	extended X-ray absorption fine structure
FC	field cooled
FFT	fast fourier transform
FiM	ferrimagnetic
f.u.	formula unit
GC	glassy carbon
GOF	goodness of fit
HER	hydrogen evolution reaction
HR	high resolution
ICP-OES	inductively coupled plasma optical emission spectrometry
ICSD	inorganic crystal structure database
IF	interface
IR	infrared
LDH	layered double hydroxide
LDOS	local density of states
LS	low spin
LSV	linear sweep voltammetry
MACP	microemulsion-assisted co-precipitation
NHE	normal hydrogen electrode

NLDFT	non-local density functional theory
OCP	open circuit potential
OER	oxygen evolution reaction
ORR	oxygen reduction reaction
PAW	projector augmented wave
PBEsol	Perdew-Burke-Enzerhof for solids
PDOS	projected density of states
PSD	pore size distribution
PXRD	powder X-ray diffraction
RDE	rotating disk electrode
RHE	reversible hydrogen electrode
RRDE	rotating ring disk electrode
SAED	selected area surface diffraction
SECCM	scanning electrochemical cell microscopy
SEM	scanning electron microscopy
SI	supporting information
STEM	scanning transmission electron microscopy
SXRD	surface X-ray diffraction
TEM	transmission electron microscopy
TGA	thermogravimetric analysis
UV/VIS	ultraviolet/visible
VASP	Vienna ab initio simulation package
VOC	volatile organic compound
VSM	vibrating sample magnetometer
WAXS	wide angle X-ray scattering
XAS	X-ray absorption spectroscopy
XPS	X-ray photoelectron spectroscopy
XRD	X-ray diffraction
XRF	X-ray fluorescence
ZFC	zero field cooled

Table of Contents

1. Introduction and Motivation

Catalysis is one of the most important technologies in our modern day lives. Nearly all industrial productions of chemicals depend on catalytic reactions, most of them heterogeneous.[1] As nowadays fossil fuels are a more and more fading resource, even more effective catalytic processes are needed to further satisfy the demand of the ever-growing world population. Next to the chemical supply chain, a special focus lies upon the energy sector, which also is still heavily dependent on coal, oil, and gas. Therefore, the production of green hydrogen is increasingly seen as a solution to the global energy crisis and an important step towards a net-zero carbon emission economy to limit climate change.[2]

A lot of the heterogeneous catalyzed oxidation reactions in industry are gas phase reactions. Frequently applied is the functionalization, often oxidation, of hydrocarbons and alcohols.[3] Famous examples are the synthesis of formaldehyde from methanol over iron molybdate or the oxidation of propene.[4] Even though gas phase reactions are regularly used, they have the extreme downside of a high energy demand due to high temperatures and low selectivity, e.g., the total oxidation to CO_2 and H_2O is often inevitable. If total oxidation does not occur, often a complex mixture of products is obtained, calling for extensive separation processes.[5] Hence, a new focus falls upon liquid phase reactions, which are conducted at lower temperatures, therefore have a significantly lower energy demand and selectivity problems can often be addressed much more easily. Industrially manifested is for one the propylene epoxidation using H_2O_2 in water and methanol, which does not yield any by-products except water.[6] A special field in catalysis is electrocatalysis, which is the other exception for application of catalysis in the liquid phase. It is an important bridge between the world of catalysis with the energy supply sector with applications such as water electrolyzers and fuel cells but is hardly used within the chemical value chain.[7]

Compared to metal catalysis in the gas phase, very little is known about the active sites and reaction mechanisms at solid-liquid interfaces.[8] It would be desirable to gain knowledge about the above-mentioned variables for actual working catalysts, which are often very different to the much investigated ideal single crystal surfaces. This insight will enable the development of synthesis procedures and rational, knowledge-based design strategies for well-performing oxidation catalysts applicable in the liquid phase.[9] Next to lowering the energy demand and increase the selectivity by going to the liquid phase, it would be preferable to replace expensive precious metal catalysts, to make industrial application profitable. Promising candidates for well-performing liquid phase oxidation catalysts and

water splitting catalysts are cobalt iron containing layered double hydroxides (LDHs) and spinels. Cobalt and iron are earth abundant and therefore cheap. Furthermore, the crystal structures exhibit a huge flexibility for isomorphous cation substitution, resulting in extremely tunable properties.[10]

This thesis was prepared in the scope of the Collaborative Research Center 247, which has the overall task to decipher the role of composition and the so-called real structure of mixed metal oxides during oxidation catalysis in the liquid phase. The real structure includes numerous mesostructural features, e.g., morphology, porosity, crystallinity, exposed surface facets, defects, and possible inhomogeneities on the micro or nano scale.

The main goals of this work are the establishment of robust synthesis procedures for phase pure layered double hydroxides and spinels, the characterization of the precursors and as-prepared catalysts, and testing of the catalytic activity in liquid phase oxidation reactions. The syntheses should be reproducible and allow scalability, to provide other research groups with a reliable materials base for the investigation of the impact of composition and mesostructure on the activity in various oxidation reactions and allow for further *in situ* or *operando* studies. By applying direct co-precipitation of spinels or the crystalline precursor decomposition approach, which was already employed by Friedel et al. for cobalt ferrite from a layered double hydroxide precursor,[11] key parameters of the mesostructure are controlled. The individual contributions and interplay of the different features are investigated. It is aimed for an understanding of the impact of synthesis parameters far beyond the phenomenological approach, which is still often used. All of this enables the gaining of knowledge about composition and (real) structure-reactivity relationships.

The first pillar of this work is the investigation of composition-activity relationships for cobalt-based spinel oxides. A systematic substitution of redox active and redox inactive cations in the spinel structure, with otherwise as much as possible fixed mesostructure, allows to investigate the role of redox pairs during electrochemical oxygen evolution reaction (OER), chemical water splitting using Ce^{4+} as oxidizing agent, and H_2O_2 decomposition. The second pillar is the study of the impact of different mesostructures with otherwise fixed composition, meaning mesostructure-activity relationships. In the first part of this chapter, the impact of morphology and predominant surface termination is addressed for the aforementioned oxidation reactions. Furthermore, microemulsion-assisted co-precipitation of LDHs is established and the impact of the constant pH during precipitation on the OER activity of the LDHs and corresponding spinels is analyzed. The third pillar focuses on the advanced examination of the mesostructure of iron cobaltites. It underlines the pivotal importance of

complementary characterization methods to unravel unusual mesostructural features and resulting electronic and magnetic properties.

2. State of the Art

As already discussed in the introductory part of this thesis, oxides and (layered double) hydroxides of transition metals play a major role in heterogeneous catalysis. Herein, the two very promising candidates layered double hydroxides and spinels are introduced in more detail. In addition, more insight is given on advanced synthesis methods, namely the co-precipitation in general and the connection to the crystalline precursor decomposition approach. The last part of this chapter spotlights electrocatalysis as it is the common catalytic reaction throughout this research.
In each of the forthcoming chapters an own detailed introduction to the specific research question is going to be given, hence repetition cannot be ruled out.

2.1 Layered Double Hydroxides

Layered double hydroxides are clay-like materials with the general formula $[M^{2+}_{1-x}M^{3+}_{x}(OH)_2]^{x+}[A^{n-}_{\frac{x}{n}}]^{x-} \cdot mH_2O$, which descend from the eponymous compound hydrotalcite with the composition $Mg_6Al_2(OH)_{16}CO_3 \cdot 4H_2O$.[12] The layered structure is composed of brucite-like layers with cations octahedrally coordinated by hydroxide anions. Within the layers the octahedrons are connected by common edges. In the genuine brucite structure exclusively bivalent cations are incorporated.[13] Inside the LDH structure, a certain amount of bivalent cations in the sheets is isomorphously substituted by trivalent cations, leading to an excess positive charge. The resulting charge imbalance is compensated through intercalation of anions between the brucite-like sheets. The layers are thus held together by electrostatic interactions and through hydrogen bonding of additionally incorporated water.[14] The exact position and fluctuating interactions of the occupants in the anionic interlayers are hard to investigate, therefore Figure 2.1.1 displays the LDH structure schematically, without assignment of exact positions for the exemplary chosen carbonate anions and water. For the formation of phase pure LDHs the value for x has to stay within a certain range, which is usually reported to be in the range of $0.2 < x > 0.33$.[15] A multitude of trivalent cations qualify to substitute the bivalent cations within the layers, the most important requirement

being similar ionic radii. Table 2.1.1 shows a selection of cations suitable for LDH synthesis and their respective ionic radii.

Table 2.1.1: Selection of bivalent and trivalent cations suitable for the synthesis of LDHs and their respective ionic radii in octahedral coordination.[16]

M^{2+}	Radius [nm]	M^{3+}	Radius [nm]
Fe	0.061	**Al**	0.054
Co	0.065	**Co**	0.055
Ni	0.069	**Fe**	0.055
Mg	0.072	**Mn**	0.058
Cu	0.073	**Ga**	0.062
Zn	0.074	**Rh**	0.067
Mn	0.083	**Ru**	0.068

Next to the flexibility in cations, which can be incorporated, a plethora of anions can be built into the interlayer structure. The intercalation of carbonate is very common, but also for example nitrate, chloride, sulfate, and a whole range of organic anions can be incorporated.[17] One of the biggest advantages of LDHs is the even distribution of the different cations within the brucite-like sheets. Even though, reports of experimental and theoretical investigations of the long- and short-range order in the layers are somewhat inconclusive, studies could clearly show that for example in Mg_nFe LDHs (n = 2,3,4) the trivalent iron cations never occupy neighboring sites if possible.[18] This even distribution can unlock unknown properties and advantages for several applications in which cation distribution is of profound importance.

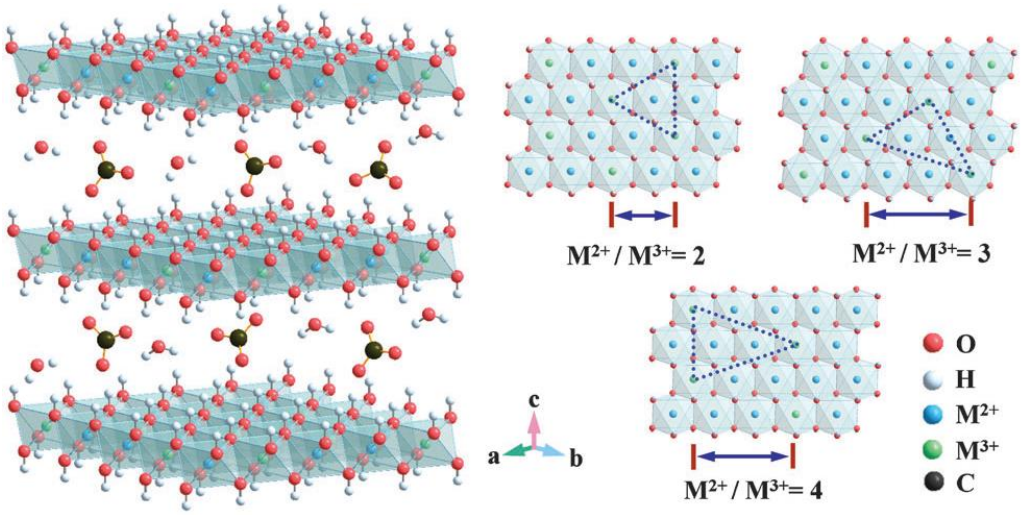

Figure 2.1.1: Layered structure of LDH (left) and exemplary cation distribution within the layers (right).[19]

The well distributed cations within the layers, the tunable physicochemical properties, and the flexibility of the structure lead to a high scientific interest and numerous applications of LDHs and their derivatives. Utilizations are e.g., as ion exchangers,[20] adsorption materials for small molecules such as CO_2 and NO_x,[21] sensing of volatile organic compounds (VOCs),[22] adsorption of aqueous pollutants,[23] in drug delivery,[24] as additives in functional polymer materials,[25] and many more. Moreover, a special focus falls upon their use in different catalytic applications. The as-prepared LDHs as such already perform well as electrocatalysts or photocatalysts.[26] Furthermore, intercalation, delamination, or deposition alters the properties of the as-prepared layered structures, advancing the performance and fields of catalytic application.[27]

Another advantage of LDHs is their comparably easy and affordable synthesis. To achieve the formation of LDHs with various properties, specially designed for their application purpose, different synthesis approaches are used. Typical synthesis techniques are co-precipitation,[28] the urea decomposition approach,[29] hydrothermal (post-)treatment,[30] and sol-gel synthesis.[31] If particle dimensions smaller than the usual near sub-micron platelet size are desired there are two mainly used options. On the one hand, already synthesized particles can be exfoliated e.g., by sonication or solution intercalation of surfactants,[32] or on the other hand particle growth can be limited directly during synthesis through employment of surfactants or even defined emulsions.[33]

However, next to the enormous flexibility of the structure and the multitude of applications derived from that, LDHs have a disadvantage. They are in most cases not very temperature stable and are therefore not suited to be used in e.g., thermal catalysis at elevated temperatures. Nevertheless, they are feasible precursors for metal catalysts or mixed transition metal catalysts. During thermal treatment of LDHs, in general a 3-step decomposition takes place, involving the dehydration, dehydroxylation and, in the case of carbonates as anions, decarboxylation.[34] Depending on the composition of the LDH different oxides are formed upon calcination. Very common is the formation of a rock salt type oxide and a spinel type oxide. However, if the LDH contains oxidizable bivalent cations and the right ratio of bivalent to trivalent cations is met, phase pure spinel can be obtained.[16] This possibility is the core of the synthesis approach applied in this thesis, the crystalline precursor decomposition approach. In the next part of this chapter spinel type oxides are going to be introduced, followed by a more detailed introduction to co-precipitation and the crystalline precursor decomposition approach.

2.2 Spinel

The spinel structure $(A^{2+})_t(B^{3+}{}_2)_oO_4$ is named after the mineral spinel $MgAl_2O_4$. Usually these materials are oxides, but other chalcogens can serve as anions as well. The crystal structure is built of cubic close-packed O^{2-}anions in which one half of the octahedral sites (*o*) is occupied by B^{3+} cations and one eighth of the tetrahedral sites (*t*) is occupied by A^{2+}cations. This results in the coordination of one O^{2-} anion by one A and three B cations. Figure 2.2.1 shows the unit cell of the cubic spinel consisting of 56 atoms, with 32 cubic close-packed oxygen anions, leading to a general formula of $A_8B_{16}O_{32.}$ Next to the typical bivalent and trivalent cation containing spinel, the so-called (2,3) spinel, spinels can also consist of other combinations of cations resulting in an overall number of 8 positive charges, e.g. (4,2) or (6,1) spinels.[35]

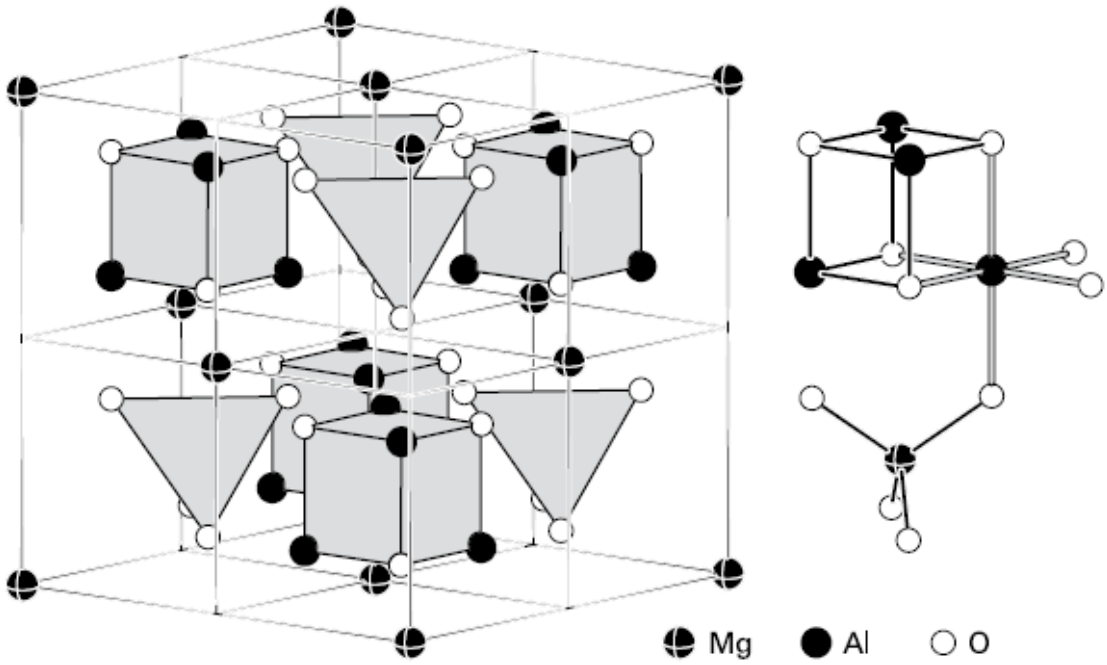

Figure 2.2.1: Unit cell of the spinel structure. [35b]

The exemplary shown $MgAl_2O_4$ in Figure 2.2.1 depicts the normal spinel structure with above-described cation occupation. Next to this, inverse spinels $(A^{2+}{}_{1-x}B^{3+}{}_x)_t(A^{2+}{}_xB^{3+}{}_{2-x})_oO_4$ exist, *x* being the degree of inversion. For a normal spinel $x = 0$. If $x = 1$, an inverse spinel structure is present. In this structure the bivalent A cations occupy octahedral sites and trivalent cations are equally distributed in octahedral and tetrahedral sites. All other degrees of

inversion between the two extrema are possible as well.[36] The degree of inversion is depending on many parameters, often mentioned are the cation radii, ionic charge, ligand field stabilization energies, temperature, and even the mere particle size.[35b, 37] Theoretical methods can calculate the degree of inversion for a given system and it can be experimentally determined by several characterization methods, e.g., X-ray absorption spectroscopy, nuclear magnetic resonance spectroscopy, or, for iron containing samples, Mössbauer spectroscopy.[38] The degree of inversion has a particular influence on the magnetic, electronic and optical properties of the spinel, leading to many possible applications such as supercapacitors,[39] battery materials,[40] drug delivery,[41] photocatalytic reactions,[42] as well as electrocatalysis and thermal catalysis.[43]

Another reason for their use is their relatively easy synthesis and they only/mostly contain earth abundant transition or main group metals. Often used synthesis techniques are direct co-precipitation,[44] sol-gel synthesis,[45] hydro- and solvothermal synthesis,[46] nanocasting,[47] and solid-state synthesis.[48] Next to the previously mentioned direct co-precipitation, spinels can be derived from co-precipitated precursor materials through thermal treatment, the so-called crystalline precursor decomposition approach. This approach and its advantages will be briefly discussed in the following paragraph.

2.2.1 Crystalline Precursor Decomposition Approach

As already discussed in the two chapters above, LDHs and spinels are not only used in similar applications, but LDHs can be used as precursors for the synthesis of well-defined spinels, applying the crystalline precursor decomposition approach. In the first step, a crystalline precursor, often a hydroxide or hydroxy carbonate like LDHs is (co-)precipitated, aged, washed, and dried. Subsequently, this precursor is thermally transformed into an oxide, serving as the as-prepared catalyst (Figure 2.2.2).

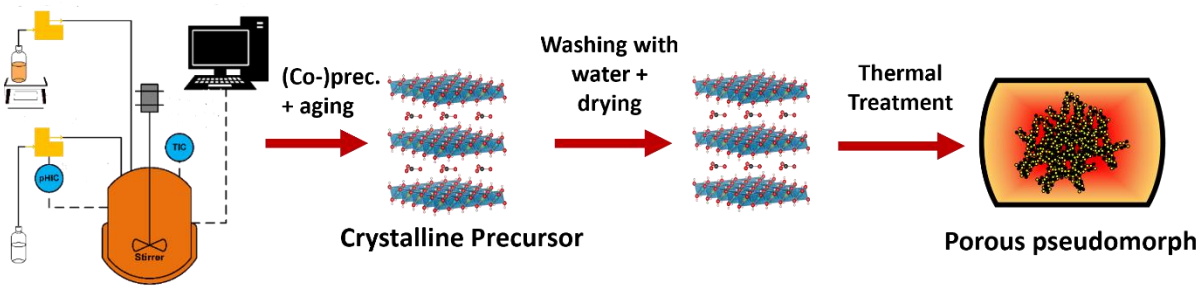

Figure 2.2.2: Schematic representation of a typical computer-controlled (co-)precipitation. The crystalline precursor is (co-)precipitated, washed with water, dried, and subsequently thermally transformed into a porous pseudomorph of the precursor.

Co-precipitation in general is a powerful approach for the synthesis of high surface area materials as it is usually done under mild conditions, therefore preventing sintering of particles or pores. It is affected by a multitude of parameters, yet allowing the tuning of a lot of materials properties like crystallinity, phase composition, etc. An overview is shown in Figure 2.2.3.[49]

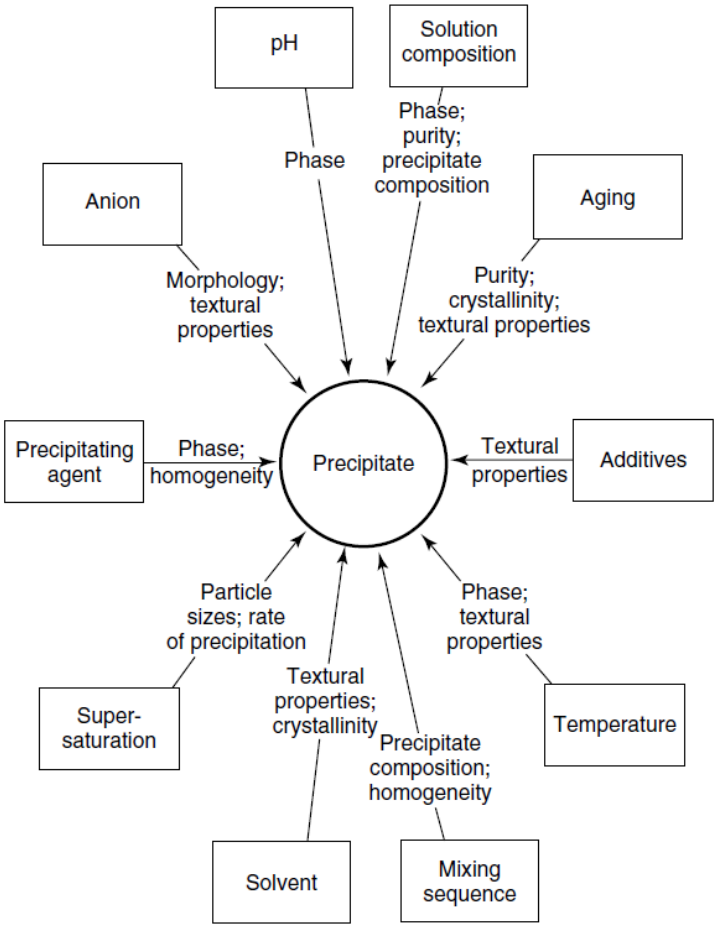

Figure 2.2.3: Parameters influencing materials properties during co-precipitation.[49]

One great advantage of the crystalline precursor decomposition approach is the accessibility of unusual mesostructures. When spinels are synthesized via direct (co-)precipitation of metal salts, usually isotropic particles are obtained due to the minimization of the surface energy, which is automatically fulfilled if no stabilizers are added. The precipitated (layered double) hydroxide precursors on the other hand form rather large platelets with high aspect ratios without the addition of surfactants, because of their layered crystal structure. Upon thermal treatment, the morphology is retained, giving access to rather untypical morphologies, so-called pseudomorphs.[11]

Depending on the applied crystalline precursor, another huge advantage comes into play. In the case of $Co(OH)_2$ as a precursor, the thermal transformation to Co_3O_4 occurs in a topotactic manner from the (001) plane of the precursor to the (111) plane in the spinel, due to the very similar lattice spacing.[50] This results in cobalt oxides with a platelet morphology and a predominant (111) surface termination, making them feasible model catalysts for the investigation of the activity of one specific surface termination. Friedel et al. have shown that this approach is transferable to cobalt ferrite as well.[11]

The crystalline precursor decomposition approach therefore gives rise to well-defined but unusual morphologies for spinel type oxides in high quantities due to easy reproducibility if computer-controlled co-precipitation is applied. The formation of these particles is accomplished without the addition of organic surfactants, which may influence the catalytic properties of the material.

As electrocatalysis is a large and promising area of application for both LDHs and spinels, the fundamental theoretical background is discussed in the following chapter.

2.3 Electrocatalysis

As already described in the motivation of this thesis, finding alternative solutions for fuel, at best free of carbon emissions, is an important task for researchers these days. An extremely promising and already in use fossil fuel alternative is hydrogen produced from electrochemical water splitting.[51] Next to the storage of energy, the produced hydrogen can be used as feedstock for high value-added chemicals.[52]

This process can for example be conducted in electrolyzers powered by renewable energy sources, with the hydrogen evolution reaction (HER) taking place at the cathode and the oxygen evolution reaction (OER) taking place at the anode.

Equations 1-3 show the anodic and cathodic half reactions in alkaline medium as well as the overall occurring reaction.

$$\text{Anode: } 4OH^- \rightarrow 2H_2O + O_2 + 4e^- \quad \text{Eq. 1}$$

$$\text{Cathode: } 4H_2O + 4e^- \rightarrow 2H_2 + 4OH^- \quad \text{Eq. 2}$$

$$\text{Overall: } 2H_2O \rightarrow 2H_2 + O_2 \quad \text{Eq. 3}$$

In equilibrium a potential E_0 of 1.23 V is needed for the overall water splitting reaction.[53] Nevertheless, the actual applied potential E to reach a certain current density is always higher than the equilibrium potential. The difference is defined as the so-called overpotential η (Eq. 4).

$$\eta = E - E_0 \quad \text{Eq. 4}$$

The HER exhibits a way smaller cathodic overpotential η_c compared to the anodic overpotential for OER η_a. This is due to the significantly more sluggish kinetics of the OER, as it is a four-electron process and therefore limiting the HER. Consequently, to make hydrogen evolution via electrocatalytic water splitting more feasible, the OER process must be optimized, meaning lowering the overpotential.

The overpotential is caused by several contributions, for example electrolyte resistance, electronic resistances of the electrodes, concentration losses or mass transfer limitations, and reaction kinetics.[54] Next to optimizing the cell design and therewith lowering the overpotential, reaction kinetics play a pivotal role in electrocatalysis.

When assuming electron transfer to be rate determining, the Butler-Volmer equation (Eq. 5) describes the relation between the current density i and the overpotential at an electrode.

$$i = i_0 \left(exp \frac{(1-\alpha)nF\eta}{RT} - exp \frac{-\alpha nF\eta}{RT} \right) \quad \text{Eq. 5}$$

i_0 is the exchange current density, α the symmetry factor or transfer coefficient, n the number of electrons involved in the reaction, F the Faraday constant, R the universal gas constant, and T the temperature. The oxygen evolution reaction usually takes place at high anodic

overpotentials, so the oxidation can be assumed to be dominant, allowing for simplifications leading to the Tafel equation. (Eq. 6).[53a, 55]

$$\eta = const + b \log i \qquad \text{Eq. 6}$$

The Tafel slope b is common descriptor for charge transfer and with that the activity of an electrocatalyst. The smaller b the higher the rate of electron transfer, resulting in a higher efficiency of the catalyst.[56] Several commonly investigated parameters to compare the performance of electrocatalysts exist. The most often used is the above described overpotential at 10 mA cm^{-2} and the Tafel slope. Additionally, the electrochemically active surface area (ECSA) is frequently determined. For this purpose, several approaches exist such as estimating the ECSA from the double-layer capacitance from cyclovoltammetry, or from electrochemical impedance spectroscopy (EIS).[57] For evaluation of the stability either cycling studies can be performed, meaning recording at least several hundreds or thousands of cyclovoltammograms while monitoring the benchmarking overpotential at 10 mA cm^{-2}. Also, chronoamperometric, and chronopotentiometric studies are applied.[56, 57c] More insight into oxidation and reduction processes can be gained from cyclovoltammography and for the investigation of mechanistic details, for example the rate limiting step, electrochemical impedance spectroscopy is used.[58] All the above-described performance descriptors of catalysts can be easily determined by using a typical three electrode setup with a reference electrode, a counter electrode, and a working electrode, which often consists of glassy carbon modified with the corresponding electrocatalyst.

To minimize the most frequently used performance parameter, the overpotential η, countless studies on setup idealization and materials have been conducted. Precious metal oxides such as IrO_2 and RuO_2 are good OER catalysts, but extremely rare and therefore expensive.[59] In addition they suffer from limited stability under highly oxidizing potentials.[60] Mixed transition metal oxides have proven to be promising candidates since they are earth abundant and therefore cheap. They are mostly not stable in acidic conditions, so alkaline conditions are applied.

Next to comparing the experimentally derived activities of innumerable catalysts, theoretical calculations are helpful to predict and tune the performance of electrocatalysts. A proposed and often used mechanism of the OER is the following adsorption-based four step mechanism (Equations 7-10).

$$H_2O + \quad ^* \rightarrow HO^* + H^+ + e^- \qquad \text{Eq. 7}$$

$$HO^* \rightarrow O^* + e^- + H^+ \qquad \text{Eq. 8}$$

$$O^* + H_2O \rightarrow HOO^* + e^- + H^+ \qquad \text{Eq. 9}$$

$$HOO^* \rightarrow \quad ^* + O_{2(g)} + e^- + H^+ \qquad \text{Eq. 10}$$

Based on this mechanism Rossmeisl and coworkers derived a volcano curve for common materials used in the OER shown in Figure 2.3.1.[61] It is based on the Sabatier principle, which states that an optimal performing catalyst exhibits intermediate bonding energies for reactants, meaning that the surface of a good catalyst neither binds intermediates too strong nor too weak. If the intermediate binds too weakly to the electrode surface, the reaction will not take place because no activation is occurring, if it is bound too strongly, all surface sites will be blocked.[62]

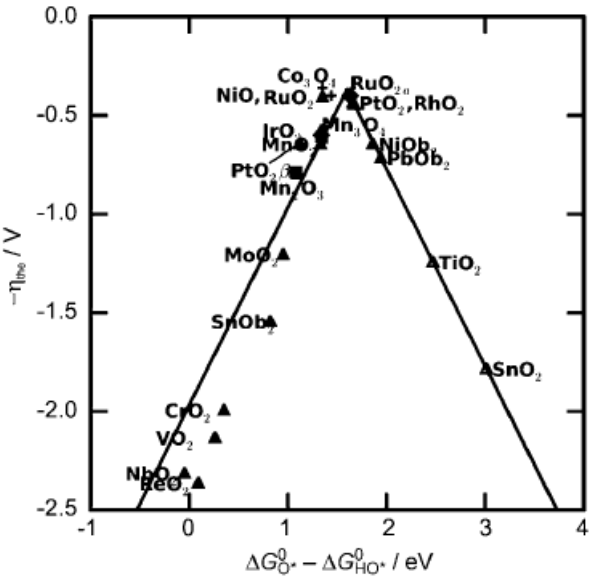

Figure 2.3.1: Activity trend towards oxygen evolution for several oxides. The negative theoretical overpotential is plotted against the standard free energy of $\Delta G^0_{O^*} - \Delta G^0_{HO^*}$.[61]

This leads to the fact that the activity is by a large extent determined by the binding energy of the intermediates. In Figure 2.3.1 the descriptor used is the standard free energy of $\Delta G^0_{O^*} - \Delta G^0_{HO^*}$. Even though this form of volcano plot does not include any kinetic barriers, the agreement of theoretical and experimentally derived overpotentials is very good, therefore enables the identification of trends, and allows quantitative theoretical predictions of catalyst activity based on the empirical Sabatier principle.[63] The volcano plot reveals overpotentials for cobalt and nickel oxides in the range of the best performing precious metal oxides, making

especially cobalt-based spinel oxides an interesting area of research towards better performing electrocatalysts, with many studies already conducted.[64]

The above-described theoretical and experimental performance descriptors are very useful to get a first idea of the relative activity of catalysts and the experimentally accessible parameters can be easily obtained from rotating disc electrode (RDE) or rotating ring disc electrodes (RRDE) measurements. Nevertheless, even though these measurement procedures are convenient to perform and are a feasible tool for catalyst evaluation, they can carry certain pitfalls with them, which should be avoided and/or considered during data evaluation. For example, the coffee ring effect from drop casting the catalyst can lead to non-uniform catalyst distribution,[65] bubble formation may block active sites,[66] or binder effects might influence the catalysts performance,[67] which all in all may hinder the investigation of the real intrinsic activity of a catalyst.

Nowadays, new, and more progressive methods come in to play, among them single entity electrochemistry, *in situ,* and *operando* methods. Since catalysts under working conditions usually drastically change in structure, the exact tracking of these changes during conditioning and actual catalysis is desirable and essential to be able to design more active and stable catalysts. For example, nano impact electrochemistry eliminates the uncertainty of the bulk electrodes, which are often used. The powder catalyst is dispersed in the electrolyte and meets an inert microelectrode through Brownian motion. Upon contact a current is detected.[68] Tschulik and coworkers were able to investigate the intrinsic activity of single 4 nm cobalt ferrite nanoparticles by using the nano impact technique.[69] If particles are bigger, another feasible method is scanning electrochemical cell microscopy (SECCM), enabling measurement of electrochemical activity on top of particles, on edges, terraces, etc., therefore providing precise information about structure-reactivity correlations within one particle.[70] For example, it was shown that for as-prepared hexagonal β-$Co(OH)_2$ platelets the edge facets show a significantly higher activity than the basal plane.[71]

With these methods the above-mentioned possible pitfalls of RDE measurements are circumvented.

To gain more insight into the actual active phase of electrocatalysts, *in situ* or *operando* studies are conducted. With the help of *operando* wide-angle X-ray scattering (WAXS) NiFe and CoFe layered double hydroxides were shown to transform to a so-called γ-phase at anodic potentials in alkaline electrolyte, exchanging the intercalated anions with K^+, leading to a contraction of the crystal lattice.[72] Bergmann et al. employed *operando* and surface-sensitive X-ray absorption spectroscopy (XAS) and surface voltammetry, showing that under applied

anodic potential Co^{2+} in Co(oxyhydr)oxides transforms into predominantly octahedrally coordinated, di-μ-oxo-bridged Co^{3+}.[73] Furthermore, using *operando* surface X-ray diffraction (SXRD) Magnussen and coworkers found an X-ray amorphous skin layer for Co_3O_4 catalysts, which was attributed to a $CoO_x(OH)_y$ phase with an increased cobalt oxidation state. In addition, a dependence of the thickness of the skin layer and the OER activity was observed.[74] Consequently, the combination of theoretical prediction, catalyst evaluation on classical RDE setups and in depth characterization with *in situ* and *operando* methods, also supported by theory, provides a feasible toolbox for the development of more active and stable OER catalysts.

3. The Roles of Composition and Mesostructure of Cobalt-based Spinel Catalysts in Oxygen Evolution Reactions

Anna Rabe,[a] Julia Büker,[b] Soma Salamon,[c] Adarsh Koul,[d] Ulrich Hagemann,[e,f] Joachim Landers,[c] Klaus Friedel Ortega,[g] Baoxiang Peng,[b] Martin Muhler,[b] Heiko Wende,[c] Wolfgang Schuhmann,[d] and Malte Behrens*[a,f,g]

[a] M. Sc. Anna Rabe, Prof. Dr. Malte Behrens
Faculty of Chemistry
University of Duisburg-Essen and Center for Nanointegration Duisburg-Essen (CENIDE)
Universitätsstr. 7, 45141 Essen, Germany
E-mail: mbehrens@ac.uni-kiel.de

[b] M. Sc. Julia Büker, Dr. Baoxiang Peng, Prof. Dr. Martin Muhler
Laboratory of Industrial Chemistry
Faculty of Chemistry and Biochemistry, Ruhr University Bochum
Universitätsstr. 150, 44780 Bochum, Germany

[c] Dr. Soma Salamon, Dr. Joachim Landers, Prof. Dr. Heiko Wende
Faculty of Physics and CENIDE
University of Duisburg-Essen
Lotharstraße 1, 45057 Duisburg, Germany

[d] M. Sc. Adarsh Koul, Prof. Dr. Wolfgang Schuhmann
Analytical Chemistry – Center for Electrochemical Sciences (CES)
Faculty of Chemistry and Biochemistry, Ruhr University Bochum
Universitätsstr. 150, 44780 Bochum, Germany

[e] Dr. Ulrich Hagemann
Interdisciplinary Center for Analytics on the Nanoscale (ICAN)
University of Duisburg-Essen
Carl-Benz-Straße 199, 47057 Duisburg, Germany

[f] Center for Nanointegration Duisburg-Essen (CENIDE)
Carl-Benz-Straße 199, 47057 Duisburg, Germany

[g] Dr. Klaus Friedel Ortega, Prof. Dr. Malte Behrens
Institute for Inorganic Chemistry
Christian-Albrechts-Universität zu Kiel
Max-Eyth-Str. 2, 24118 Kiel, Germany

This chapter is published as a paper in the journal *Chemistry – A European Journal*. (Copyright 2021- Wiley-VCH; link to publication: https://doi.org/10.1002/chem.202102400)

Keywords: co-precipitation • crystalline precursor decomposition approach • cobalt spinel • structure-reactivity relationship • oxygen evolution reaction

Entry for the Table of Contents:

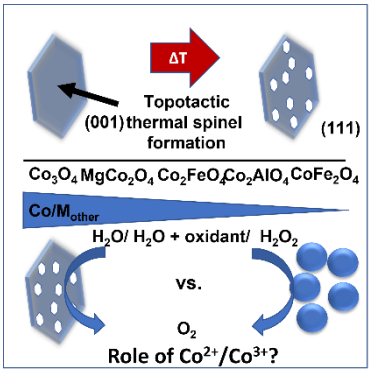

The particle anisotropy and cobalt content in spinel oxides is systematically varied and the impact on oxygen evolving reactions is investigated. For chemical and electrochemical water oxidation as well as H_2O_2 decomposition the reactivity changes with the cobalt to metal ratio and degree of anisotropy. Furthermore, the importance of the interplay of redox pairs and different active sites are highlighted.

Anna Rabe conceptualized the sample series, developed the synthesis procedures and synthesized the catalysts. Furthermore, she took care of coordination and evaluation of the characterization methods, except the methods mentioned in the following. Also, the measurement of the activity for chemical water oxidation was performed by her. The first draft of the manuscript was written by her.

Julia Büker performed the H_2O_2 decomposition reactions and Adarsh Koul did the electrochemical OER measurements. Soma Salamon and Joachim Landers were responsible for Mössbauer spectroscopy measurements and evaluation. Ulrich Hagemann did the XPS

measurements and evaluation. Klaus Friedel Ortega and Baoxiang Peng conceptualized and supervised parts of the work. Malte Behrens conceptualized the work and acquired funding, as did Martin Muhler, Heiko Wende, and Wolfgang Schuhmann. The manuscript was read and edited by all co-authors before submission.

3.1 Abstract

Using the crystalline precursor decomposition approach and direct co-precipitation the composition and mesostructure of cobalt-based spinels can be controlled. A systematic substitution of cobalt with redox-active iron and redox-inactive magnesium and aluminum in a cobalt spinel with anisotropic particle morphology with a preferred 111 surface termination is presented, resulting in a substitution series including Co_3O_4, $MgCo_2O_4$, Co_2FeO_4, Co_2AlO_4 and $CoFe_2O_4$. The role of redox pairs in the spinels is investigated in chemical water oxidation using ceric ammonium nitrate (CAN test), electrochemical oxygen evolution reaction (OER) and H_2O_2 decomposition. Studying the effect of dominant surface termination, isotropic Co_3O_4 and $CoFe_2O_4$ catalysts with more or less spherical particles are compared to their anisotropic analogs. For CAN-test and OER, Co^{3+} plays the major role for high activity. In H_2O_2 decomposition, Co^{2+} reveals itself to be of major importance. Redox active cations in the structure enhance the catalytic activity in all reactions. A benefit of a predominant 111 surface termination depends on the cobalt oxidation state in the as-prepared catalysts and the investigated reaction.

3.2 Introduction

Heterogeneous oxidation catalysis over mixed metal oxides depends critically on their composition and also properties like particle size, particle morphology, and porosity – here summarized as mesostructure – play an important role.[47, 75] Applied catalysts usually have complex multi-cation compositions that are specifically optimized for a given process.[76] However, systematic studies including different reactions over the same catalyst and comprehensive knowledge of real structure-reactivity correlation are scarce and have the potential to reveal general trends in heterogeneous catalysis of mixed oxides. Therefore, the herein presented work systematically investigates the impact of composition and mesostructure of cobalt-based spinel oxide catalysts on a variety of oxidation reactions.

Spinel oxides are an attractive playground for such studies as isomorphous substitution of transition as well as main group metal cations is possible while allowing single-phase materials. The normal spinel oxide structure has the generic formula $(A^{II}_t)(B^{III}_o)_2O_4$ consisting of cubic closed packed oxygen atoms with the B metal cations occupying half of the octahedral sites (index *o*) and the A atoms occupying one eighth of the tetrahedral sites (index

t).[77] Already countless investigations of their general properties have been conducted and applications as e.g. Li-ion battery materials,[78] super capacitors,[79] and electro catalysts[80] have been reported. Sojka *et al.* have recently reported an example for the potential of a comparative study of a spinel isomorphous substitution series for determining the roles of different cations in catalytic N_2O decomposition. They were able to identify Co^{3+} in octahedral sites as active site for this specific reaction.[43] The same group investigated the activity of different supported cobalt-based spinel catalysts in the electrochemical oxygen reduction reaction (ORR). For example, they found the ratio of exposed facets to be of importance for the activity of a manganese-cobalt spinel on various carbon supports.[81] In addition they showed the influence of composition and especially phase purity for the selectivity and activity of mixed iron cobalt spinels.[82] Using systematic cation substitution and tuning of the catalysts mesostructure with constant cation ratios, we herein exploit and extend this powerful approach to different oxygen evolving reactions.

Spinel oxides can be synthesized by various approaches, for example direct co-precipitation,[44] sol-gel method,[83] hydro- and solvothermal synthesis,[46] nanocasting,[47] or solid state reactions.[48]. Most of these synthesis methods result in mostly isotropic particles or contain organic residues, which complicate structure-reactivity investigations. We recently reported the synthesis of an anisotropic cobalt ferrite spinel using the crystalline precursor decomposition approach.[11] With this technique anisotropic phase pure mixed spinels without organic surfactants can be reproducibly synthesized. As crystalline precursors hydroxides as well as layered double hydroxides (LDH), both typically crystallizing in a platelet-like morphology, turned out to be the most convenient for several reasons.

Layered double hydroxides are so called hydrotalcite-like materials with the general formula $[M_{1-x}^{2+}M_x^{3+}(OH)_2]^{x+}[A_{x/n}]^{n-}\cdot xH_2O$. These compounds consist of brucite-like $M(OH)_2$ layers, with a fraction of bivalent cations substituted by trivalent cations. The resulting excessive charge is compensated by intercalation of anions between the layers leading to strong electrostatic interactions connecting the positively charged brucite layers with the anionic inter-layers. In addition, water molecules are intercalated in the layered structure and form hydrogen bonds.[14] These materials usually exhibit a well-defined hexagonal platelet morphology. A vast variety of cations M and anions A, in air usually carbonate, can be built into the structure and a homogeneous cation distribution is found.[84] The crystalline nature assures a high reproducibility of the as-prepared hydroxide precursors. A limiting factor for phase pure LDH formation is x, representing the ratio of bivalent to trivalent cations. x should not exceed 0.4, otherwise by-phase formation is observed.[16]

If a fraction of the incorporated cations can be oxidized upon thermal treatment the needed cation stoichiometry M^{2+}/M^{3+} of 1:2 for spinel formation can be achieved through partial oxidation of divalent to trivalent cations when decomposing the LDH precursor. Through mild calcination temperatures a topotactic transformation along the $(001)_{LDH}$I$(111)_{Spinel}$ planes without significant diffusion of the cations occurs.[50b] The resulting spinels are pseudo-morphs of the precursor hydroxides, retaining the unusual and unique hexagonal platelet morphology and defined cation distribution. In addition, the thermal treatment leads to decomposition of the intercalated carbonate and water creating pores within the platelet structure, maximizing the surface area of the formed calcination products. Because of the topotactic transformation a dominant 111 surface termination is formed, making spinels synthesized by this approach perfect candidates for investigating structure-reactivity correlations.[11, 50b]

With a systematic substitution series of bivalent and trivalent cations in the precursor structure with redox active and redox inactive metals the composition and the ratio of Co^{2+}/Co^{3+} is systematically varied. As a starting point the pure cobalt hydroxide is used and substituted with the redox active transition metal iron and redox inactive, meaning a fixed oxidation state, bivalent and trivalent main group elements magnesium and aluminum. The resulting anisotropic cobalt spinel substitution series is Co_3O_4, $MgCo_2O_4$, Co_2FeO_4, Co_2AlO_4 and $CoFe_2O_4$.

In addition to investigating the impact of composition, especially the interplay of redox pairs, the effect of morphology and its anisotropy is examined. Therefore, isotropic Co_3O_4 and $CoFe_2O_4$ is synthesized via a crystalline precursor and direct co-precipitation, respectively, for comparison. These isotropic particles are assumed to not have a predominant surface termination and therefore show differences in catalytic activity compared to their analogs with a predominant 111 surface termination.

Herein we extend our previous work on the crystalline precursor decomposition approach to new compositions and combine it with the above-mentioned isomorphous substitution study to learn about the role of the different cations and morphology in different oxygen evolving reactions. The investigated reactions are chemical water oxidation, using Ce^{4+} as an oxidizing agent (CAN: cerium ammonium nitrate). This reaction is mainly governed by the exposed surface of the catalysts and is established as a probe reaction for water oxidation on other catalysts.[85] Electrochemical oxygen evolution reaction (OER) in alkaline medium is performed, requiring additional charge transport through the catalyst layers by electric conductivity of the samples. Due to its sluggish kinetics, it is considered the bottleneck for

electrochemical hydrogen and oxygen production and therefore a crucial reaction to be investigated in the energy context.[86] As a comparatively facile oxygen evolving reaction, H_2O_2 decomposition is conducted as a third probe reaction. Decomposition of peroxide species represents a potential intermediate step for oxygen evolution from water and is of relevance for Fenton-like oxidation reactions.

3.3 Results and Discussion

A systematic substitution series of cobalt containing spinel catalysts was synthesized using the crystalline precursor decomposition approach. The precipitation reactions were performed under highly controlled conditions, leading to repetitious accuracy of the synthesized catalysts' properties. Further information on reproducibility can be found in the supporting information (Figure 3.6.1 -Figure 3.6.3). The as-prepared precursors were labeled according to their relative nominal metal cation composition and hydroxide type, the spinel catalysts were labeled by their nominal metal cation composition. To differentiate the isotropic Co_3O_4 and $CoFe_2O_4$ with spherical particles from their anisotropic analogs with platelet morphology, the prefix iso- is introduced.

3.3.1 Precursor Characterization

The five hydroxides and layered double hydroxides acting as crystalline precursors for the anisotropic substitution series were co-precipitated and thoroughly characterized. Synthesis protocols demonstrating the controlled synthesis conditions can be found in Figure 3.6.4 and full details on precipitation conditions are given in the experimental section. Figure 3.3.1 shows the PXRD patterns proving phase purity of the as-prepared precursors. For the $Fe^{2+}_{1/3}Co^{2+}_{1/3}Fe^{3+}_{1/3}$ LDH Mössbauer spectroscopy and X-ray photoelectron spectroscopy (XPS) were performed to analyze the metal cation oxidation states in detail. The results and discussion can be found in the supporting information (Figure 3.6.5). All precipitated materials exhibit a mostly hexagonal platelet morphology with varying aspect ratios depending on the composition (Figure 3.6.6). The cationic sub-lattices of these as-prepared crystalline precursors function as templates for the desired pseudo-morphic spinel catalysts.

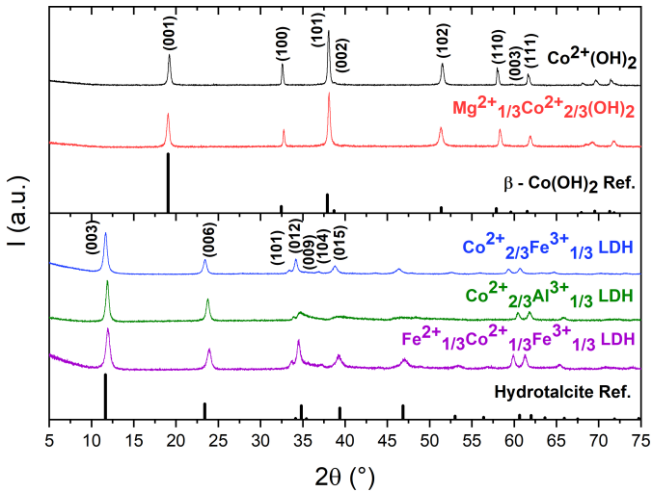

Figure 3.3.1: PXRD patterns of the as-prepared hydroxide (top), layered double hydroxide (bottom) precursors and the corresponding reference patterns of β-Co(OH)$_2$ (ICSD No. 88940) and Hydrotalcite (ICSD. No. 6296).

To investigate the behavior of the precursors upon thermal treatment, thermogravimetric analysis was performed. All precursors show the expected behavior upon thermal treatment as reported in literature. Figure 3.3.2 shows the derivative thermogravimetric (DTG) curves, ensuring complete precursor decomposition at 400 °C, which was chosen as calcination temperature for most samples. The relative mass loss curves are shown in Figure 3.6.7. For cobalt hydroxide and cobalt magnesium hydroxide the dominant weight loss step is assigned to dehydroxylation. The layered double hydroxides show a typical twostep decomposition consisting of dehydroxylation and decarboxylation.[34] For the cobalt spinel, magnesium cobaltite and iron cobaltite, an additional mass loss at 909°C, 826°C and 942°C respectively, is observed. This can be explained by the thermal reduction of Co(III) oxide to Co(II) oxide confirming the presence of trivalent Co(III) in these materials.[87] Co_2AlO_4 and $CoFe_2O_4$ do not show this additional thermal reduction step as the spinel structure with these compositions is stable up to higher temperatures investigated here.[88]

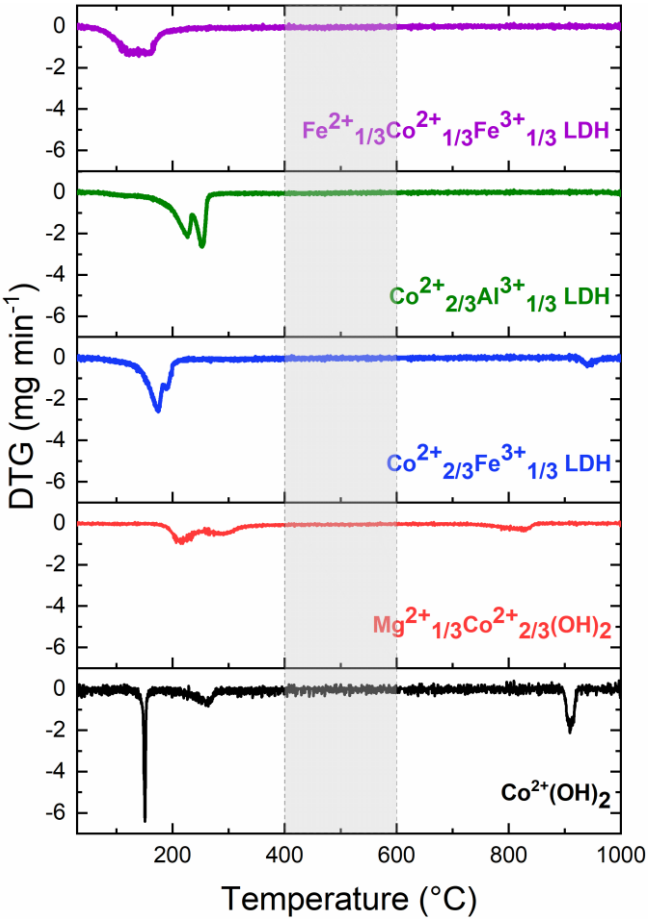

Figure 3.3.2: DTG curves resulting from the thermogravimetric analysis of the precursors. In the temperature range highlighted in grey no mass loss occurs and calcination temperatures were therefore chosen within this range.

Thermogravimetric analysis suggests a sufficient calcination temperature of 400 °C for all samples except $CoFe_2O_4$. For this composition, a small amount of a hematite by-phase was observed upon thermal treatment at 400 °C but vanished at 600 °C. A more detailed discussion and characterization of the respective samples can be found in the supporting information (Figure 3.6.8). To not only investigate the impact of composition but that of morphology isotropic Co_3O_4 and $CoFe_2O_4$ were synthesized. In case of Co_3O_4 a cobalt hydroxy carbonate was precipitated and thermally oxidized to a cobalt spinel. Isotropic $CoFe_2O_4$ was directly precipitated and thermally treated to trigger crystallization of potential X-ray amorphous by-phases. Further experimental details are available in the experimental section. Synthesis protocols, PXRD patterns, SEM micrographs and TGA results can be found in the supporting information (Figure 3.6.9 -Figure 3.6.12).

The as-prepared anisotropic and isotropic precursors were thoroughly characterized and subsequently oxidized to the desired spinel catalysts.

3.3.2 Catalyst Characterization

Upon calcination the targeted substituted cobalt spinel catalysts were formed. Figure 3.3.3 displays the PXRD patterns of the substitution series, confirming at first sight only single spinel phases present. In case of Co_2FeO_4 the phase diagram predicts a miscibility gap with phase segregation into a cobalt richer and an iron richer spinel phase.[88] The establishment of phase purity is not straightforward based alone on PXRD data of this nanostructured sample. This aspect is in the focus of our forthcoming work, and we assume segregation into two phases according to the phase diagram. Here in this contribution, we use a two-spinel phase model for the refinement of the X-ray data of this sample. Rietveld refinement further underlines the phase purity of the other samples and the absence of non-spinel phases in all samples. The determined lattice parameters (Table 3.3.1) agree with literature values. The domain sizes were extracted from Rietveld refinement as well. Due to the quite low calcination temperatures the absolute values of the domain sizes are low. The peak width of the diffractograms fit the determined values perfectly. The most defined diffraction patterns show the highest crystallinity and vice versa. Rietveld fit parameters are listed in Table 3.6.1.

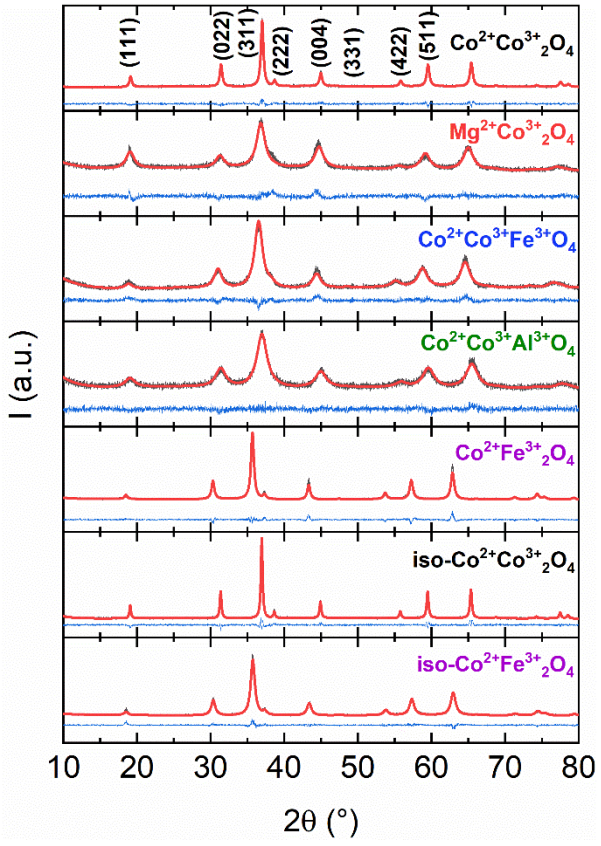

Figure 3.3.3: Rietveld refinements of the anisotropic cobalt spinel substitution series and isotropic Co_3O_4 and $CoFe_2O_4$. Measured data is shown in grey, the calculated pattern in red and the difference plot in blue. The main reflections of the cubic spinel phase were labelled.

The textural properties of the spinels were investigated with nitrogen physisorption experiments and BET theory. Surface areas of the catalysts are listed in Table 3.3.1 and vary significantly with composition. Nevertheless, all samples show the expected mesoporosity. Complete adsorption desorption isotherms and pore size distributions of the spinels and their precursors are shown in Figure 3.6.13 - Figure 3.6.14.

Table 3.3.1: Lattice parameters, domain sizes, surface areas, nominal and experimental cobalt to metal ratios of the anisotropic cobalt spinel substitution series and the isotropic Co_3O_4 and $CoFe_2O_4$.

Sample	Lit. Lattice parameter [Å]	Lattice parameter [Å] [a]	Domain Size [nm] [b]	Surface area $[m^2g^{-1}]$ [c]	Nominal Co/M	Exp. Co/M [d]
Co_3O_4	8.065[89]	8.078	15.0	30	-	-
$MgCo_2O_4$	8.107[90]	8.130	4.3	50	2	2.33±0.43
Co_2FeO_4	8.242[91]	8.130 8.171	5.8 4.6	90	2	1.80±0.04
Co_2AlO_4	8.087[92]	8.058	3.5	176	2	2.38±0.44
$CoFe_2O_4$	8.394[91]	8.376	12.8	28	0.5	0.46±0.01
iso-Co_3O_4	8.065	8.079	23.2	30	-	-
iso-$CoFe_2O_4$	8.394	8.366	8.8	40	0.5	0.50±0.01

[a] Derived from Rietveld refinement. All samples consist of a cubic spinel phase with the space group Fd3m. a=b=c. [b] The domain size was determined as the volume-weight mean column height from integral breadth. [c] Calculated with the BET method. [d] Based on XRF of the spinel catalysts. The error was determined by error propagation using the uncertainty specified by the instrument.

The SEM micrographs in Figure 3.3.5 give an overview of the preserved anisotropic morphology for the substitution series dictated by the (layered double) hydroxide precursors, which is contrasted by the isotropic Co_3O_4 and $CoFe_2O_4$ particles. Even though the degree of anisotropy, in other word aspect ratio, differs within the anisotropic samples, all catalysts of this substitution series clearly exhibit a hexagonal platelet-like morphology. Due to the decomposition of the anions in the layered precursor structure, holey platelets are formed, increasing the surface area of the catalysts. A comparison of the precursor surface areas and the spinels is shown in Figure 3.6.15. Only the anisotropic $CoFe_2O_4$ sample shows a decrease in surface area compared to its precursor. This is explained by the higher calcination temperature required to remove the hematite by-phase leading to sintering of the pores. In Figure 3.6.16 TEM images of the particles are shown confirming the porous and platelet morphology of the substitution series. As mentioned in the introduction, the transformation from the anisotropic precursor to the cubic spinel was previously found to occur topotactically, leading to a predominant 111 termination on the lateral surface of the platelets. This was shown for $CoFe_2O_4$ and Co_3O_4 synthesized by a similar technique by us and

others.[11, 50b] In Figure 3.3.4 the electron diffraction pattern of a single Co_2FeO_4 flake from this work is shown, underlining this statement also for this composition. The diffraction pattern resembles one that would be expected for a single crystal with a viewing direction along [111]. Together with the knowledge of the platelet-like particle morphology and its orientation perpendicular to the electron beam, a predominant 111 termination can be concluded. The TEM images of the isotropic spinels give rise of a few small platelet-like structures for the Co_3O_4 sample, most likely due to $Co(OH)_2$ by-phase formation during the precipitation of the precursor. Nevertheless, the isotropy of this sample is far more pronounced than for its anisotropic counterpart derived from a hydroxide structure. The selected area electron diffraction pattern clearly shows the transition towards a ring pattern indicating a more statistical distribution of the crystallite's orientations. Based on their more spherical shape, the isotropic spinels are thus expected to exhibit a less predominant surface termination, which is less affected by their preparation history compared to the anisotropic materials derived from the crystalline precursor decomposition approach. Furthermore, first principles calculations and inverse Wulff constructions of Co_3O_4 nanoparticles emphasize a surface termination with several low indexed facets like 100, 110, 112 and 111.[93] The TEM images of all sample are shown in Figure 3.6.16. Due to the intergrown nature of the materials, it was not possible to obtain electron diffraction on individual platelets in all cases. As a consequence, spotty diffraction patterns with different tendencies towards diffraction rings were obtained and the evidence for the preferred 111 termination of the platelets was not as clearly established as for Co_2FeO_4 (Figure 3.3.4) or in previous literature reports for Co_3O_4 and $CoFe_2O_4$.[11, 50b] However, based on the indications discussed in the SI, we assume the preferred 111 termination for all our samples relative to the iso-catalysts and will discuss the catalytic properties in the light of this assumption. Particle size distributions of all catalysts were estimated based on the electron microscopy data which is shown in Figure 3.6.17 and were found to be monomodal, but scatter between 61±13 nm (Co_2AlO_4) and 1147±309 nm (Co_3O_4) for the anisotropic and between 18±6 nm ($CoFe_2O_4$) and 29±8 nm (Co_3O_4) for the isotropic spinel particles.

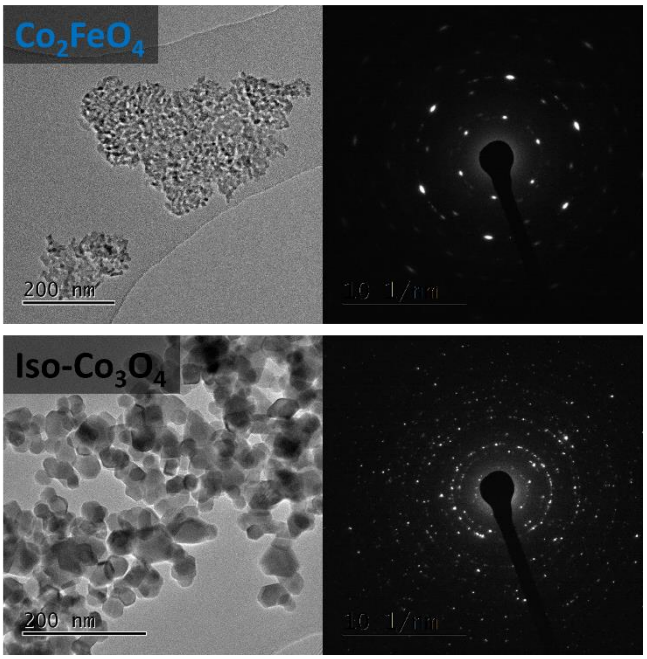

Figure 3.3.4: SAED and TEM micrographs of iso-Co_3O_4 and Co_2FeO_4 showing the ordered orientation of the spinel crystallites within one platelet in the former and the disordered orientation in the latter sample. The zone axis is [111] relative to the spinel structure suggesting together with the platelet orientation perpendicular to the viewing direction a predominant 111 termination of the lateral surfaces of the platelets.

In conclusion, the anisotropic cobalt spinel substitution series as well as the isotropic cobalt spinel and cobalt ferrite were thoroughly characterized. They consist only of spinel phases and exhibit the expected morphology differences between anisotropic and isotropic samples. The specific surface areas were analyzed and found to cover a wide range from 28 to 176 m^2/g. These values will be used to normalize the kinetic results to allow an accurate comparison of the catalytic testing, which is presented in the following paragraphs.

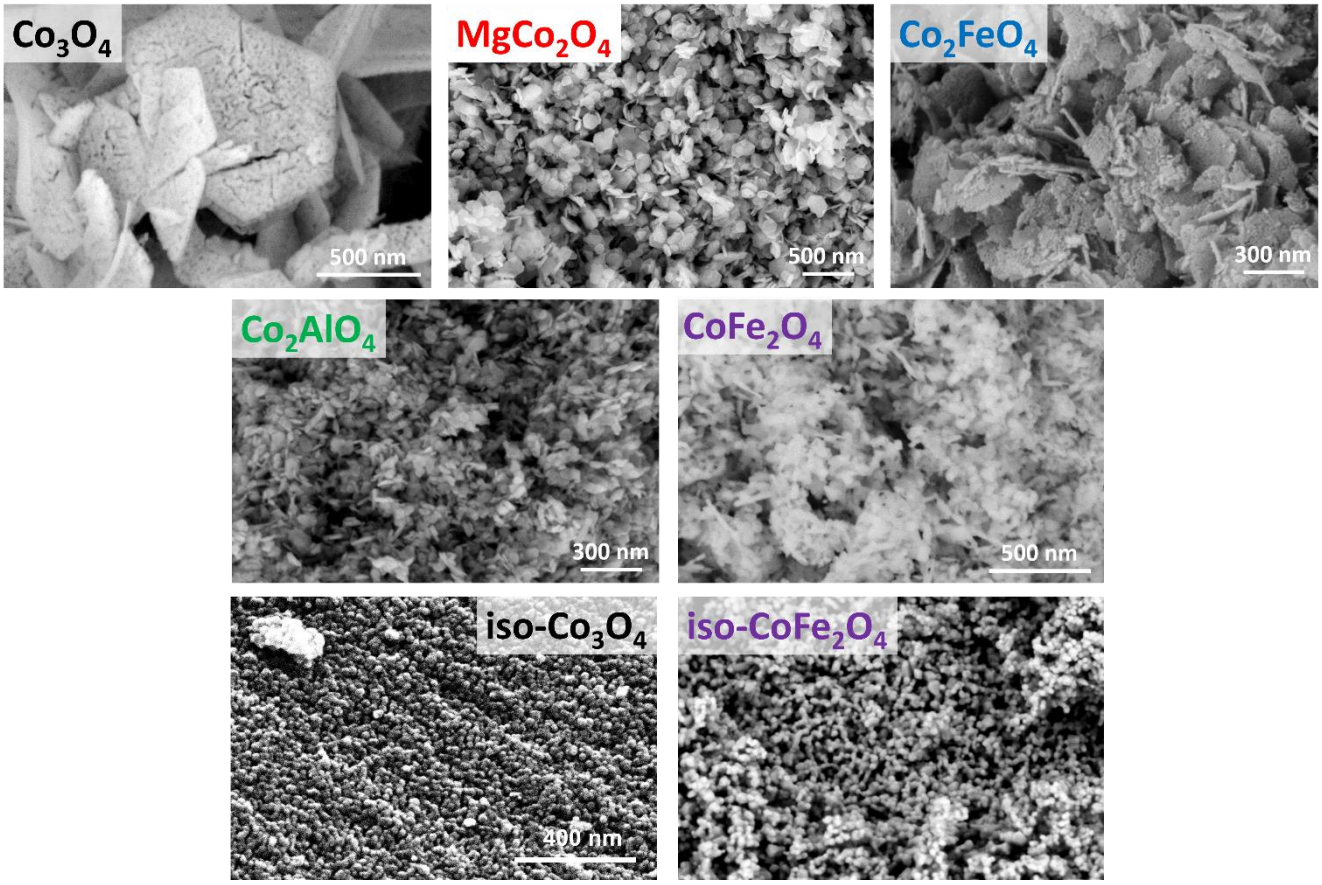

Figure 3.3.5: SEM images of the as-prepared spinel substitution series.

3.3.3 Catalysis

The prepared substituted cobalt spinel series as well as the isotropic cobalt spinel and cobalt ferrite were tested for their performance in chemical water oxidation using Ce^{4+} as an oxidizing agent (CAN test), electrochemical oxygen evolution reaction (OER) under alkaline conditions and H_2O_2 decomposition. Here, we discuss the activity trends in the three probe reactions in the context of the spinel composition, with a focus on the total cobalt content and the relative amount of Co^{3+}, and the comparison between the anisotropic and isotropic Co_3O_4 and $CoFe_2O_4$ samples.

Figure 3.3.6 shows the initial rates of the substitution series and the isotropic samples for the CAN test after normalization by BET surface area, and the total oxygen evolution over 2 h for Co_2AlO_4 as an example in the insert. The total oxygen evolution for the other samples is shown in Figure 3.6.18. The CAN test has been used as a probe reaction for OER with the important difference that the purely chemical driving force by the oxidation potential of the dissolved Ce^{4+} is exposed uniformly to the immersed catalyst's surface and the activity is thus

less affected by transport phenomena, binder additives, electrical contact problems or electrochemical ensemble effects compared to electrochemical testing.[85a]

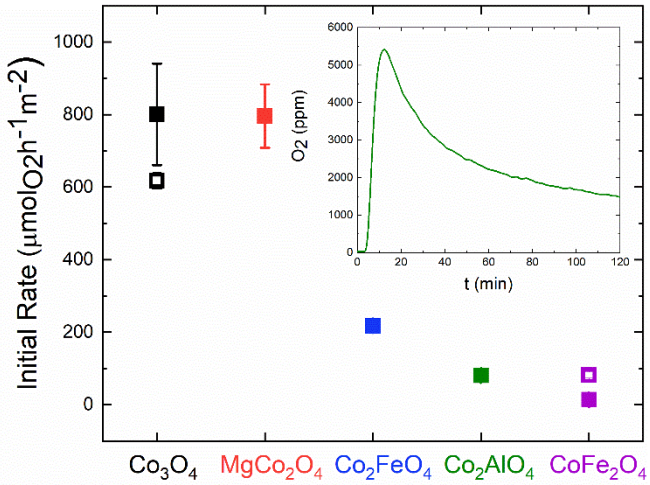

Figure 3.3.6: Initial rates for the CAN test of the anisotropic cobalt spinel substitution series (closed symbols) and the isotropic samples (open symbols). Error bars result from twofold measurements. For anisotropic Co_2FeO_2, Co_2AlO_4, $CoFe_2O_4$ and the isotropic spinels the error bars do not exceed the symbol sizes. The inset shows the oxygen evolution per time unit over 2 h for Co_2AlO_4 as an example.

Co_3O_4 and $MgCo_2O_4$ both have a nominal 2:1 ratio of Co^{3+}: M^{2+} (M = Co, Mg) and exhibit the same and the highest activity suggesting that the role of Co^{2+} is only minor and can be played as well by the redox-inert Mg^{2+}. Upon substitution of half of the Co^{3+} cations in Co_3O_4 with Fe^{3+} or Al^{3+}, a significant decrease in activity is observed, highlighting again the critical catalytic role of this cation. In addition, Co_2AlO_4 containing the non-redox active cation Al^{3+} shows a smaller initial rate than its iron containing analog Co_2FeO_4. This observation is in line with the reports that iron, in contrast to aluminum, can act as a promoter for oxygen evolution in cobalt or nickel-based materials.[94] This finding supports the importance of the interplay in the electronic structure of oxidation catalysts, in short, the redox pairs involved in the catalytic cycle.[95] However, also a phase separation into an iron rich and cobalt rich spinel as discussed earlier (see Table 3.3.1), has to be taken into account, which could give rise to an activity intermediate between Co_3O_4 and $CoFe_2O_4$. Cobalt ferrite shows the lowest activity in the series, underlining again the importance of Co^{3+} for the CAN-induced chemical oxygen evolution reaction.

As exposed surface facets and catalytic performance are related, a difference in activity is anticipated and observed for the samples with same composition and different morphology. The predominantly 111 terminated Co_3O_4 performs better than its isotropic analog, suggesting

that Co^{3+} might be especially effective if residing in this facet. However, the isotropic $CoFe_2O_4$ shows an enhanced catalytic activity compared to the 111 terminated cobalt ferrite, it even shows a comparable initial rate to the Co^{3+} containing Co_2AlO_4. Hence preferred orientation does not seem to play a significant positive role if no trivalent cobalt is present.

Electrochemical oxygen evolution was conducted for the whole anisotropic series and the isotropic analogs after drop casting the powder on glassy carbon electrodes. Recent investigations showed the transformation of cobalt-based catalysts during OER. Independent of the initial oxidation state of cobalt, a $CoO_x(OH)_y$ is reversibly formed as active phase at applied anodic potentials required for the OER.[73] Nevertheless, the activity correlates with other cations incorporated in the structure due to different stabilization abilities of surface species of the formed oxyhydroxides.[96] The current density as a function of the applied potential normalized by the geometric area of the electrode are shown in Figure 3.6.19 and the corresponding potentials at 10 mA cm^{-2} are shown in Figure 3.3.7. They exhibit the same distinct dependence on the composition as found for the CAN test.

Furthermore, the isotropic cobalt oxide shows a slightly higher overpotential for the OER than its anisotropic equivalent. On the contrary, the isotropic cobalt ferrite showed an extreme increase in overpotential, not even reaching 10 mA cm^{-2} at the highest applied potential. In case of Co_3O_4 the preferred orientation does not play a significant role, while for the Co^{3+}-free cobalt ferrite it indeed does.

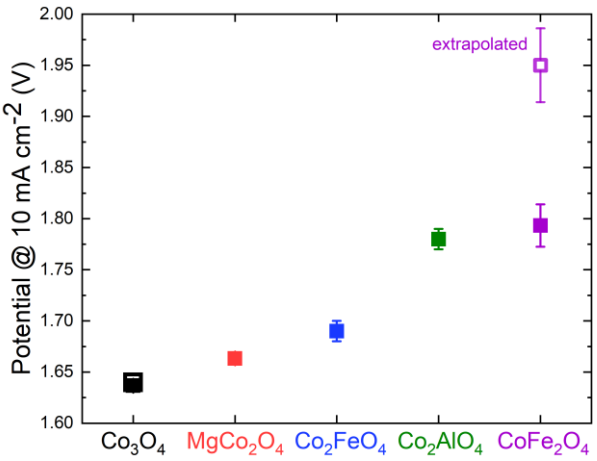

Figure 3.3.7: Measured potential at 10 mA cm^{-2} normalized by the geometric area of the electrode for the anisotropic substitution series (closed symbol) and the isotropic samples (open symbols). 10 mA cm^{-2} was chosen as point for comparison based on the suggestion by McCrory et al.[57c] The data point for isotropic cobalt ferrite was extrapolated, as it did not reach 10 mA cm^{-2} in the applied potential range. Error bars result from three independent measurements.

To address the topic of normalization in electrochemical investigations with rotating disk electrodes the current densities were further normalized by the BET surface area of the catalysts (Figure 3.6.19). In general, the trend is preserved with one exception. The high surface area of the Co_2AlO_4 leads to a decrease in the performance upon BET area normalization, causing an apparent higher catalytic activity of the anisotropic cobalt ferrite. The double layer capacitances C_{dl} of the catalysts were determined as well as it scales with the electrochemically active surface area (ECSA).[97] Details of the procedure for C_{dl} determination are given in the experimental section. Figure 3.6.21 shows an exemplary procedure of the determination for the anisotropic Co_3O_4 catalyst. The potential at 10 mA cm^{-2} as a function of C_{dl} is shown in Figure 3.6.20. As different compositions in spinels have an enormous impact on C_{dl}, a normalization by double layer capacitance is not feasible for the substitution series with different elements.[98] However, the comparison of samples with the same composition is reasonable and gives further insight in possible structure-reactivity relationships. The two cobalt spinels exhibit nearly the same overpotential, but a significantly different value for C_{dl}. The two cobalt ferrites on the other hand show nearly the same C_{dl} but very different activities. This underlines the importance of the mesostructure for this reaction, as differences or similarities in activity cannot simply be explained by variation of the ECSA.

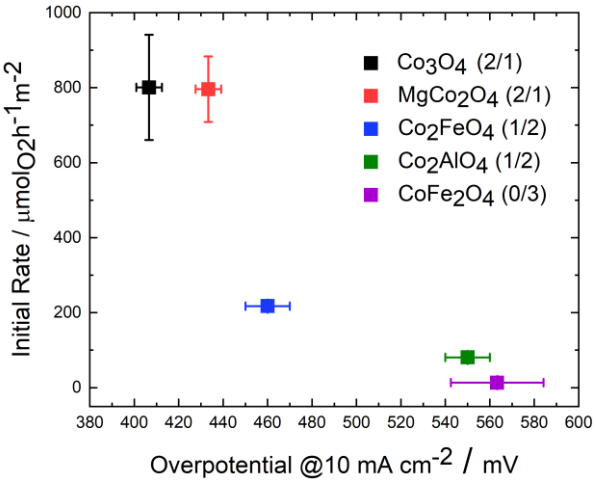

Figure 3.3.8: Initial rates for chemical water oxidation (CAN test) vs. the overpotential for electrochemical OER at 10 mA cm^{-2} for the cobalt spinel substitution series. The ratio Co^3/M_{others} is specified in brackets) Error bars for the overpotential are determined from three independent measurements.

Figure 3.3.8 shows the initial rates in the CAN test plotted against the overpotential at 10 mA cm^{-2} for the anisotropic substitution series. Here, a clear correlation of activity with Co^{3+} content (stated in brackets in the legend of Figure 3.3.8) of the spinels is observed for

both the CAN test and the electrochemical OER. Initial rates for chemical water oxidation decrease with decreasing Co^{3+} content and the overpotentials for the OER increase significantly with decreasing Co^{3+} content. Contrarily, the OER performance of differently prepared α-MnO_2 catalysts was found not to scale with the CAN trend in a similar comparison of catalysts with different microstructure and the same composition.[85a] For the OER, charge carrier mobility is of importance and electric conductivity is considered as a major beneficial property for oxide electro-catalysts. This property is not of superior relevance for the chemical oxygen evolution, as the reaction is taking place at the surface in the presence of a liquid oxidant and no electron transfer through the electrode and back contact must occur. The similar trend for CAN test and electrochemical OER suggests that the activity differences indeed can be traced back to variations in the intrinsic activities of the catalysts and their composition.

With H_2O_2 decomposition a reaction is investigated, for which Co^{2+} in octahedral sites is considered to be the active site.[99] Figure 3.3.9 shows the rates after 3 min for all samples. The oxygen evolution as a function of time is shown in Figure 3.6.18.

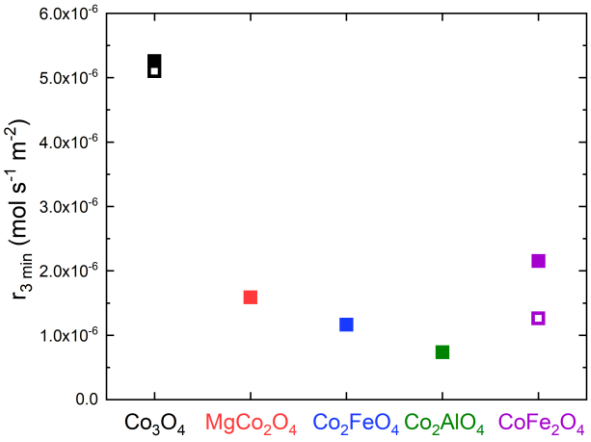

Figure 3.3.9: Rates after 3 min for H_2O_2 decomposition of the anisotropic cobalt spinel substitution series (closed symbols) and the isotropic samples (open symbols).

As observed for the two reactions presented before, Co_3O_4 was the best performing catalyst. The systematic substitution of the redox active cobalt cations with redox inactive magnesium or aluminium leads to a decrease in activity suggesting a trend with the total cobalt content of the mixed oxide. On the other hand, the relevance of Co^{2+} is undeniable when looking at the relative high activity of $CoFe_2O_4$. Considering that ferrite spinels are expected to show a cation ordering described as the inverse spinel structure with iron cations preferably

occupying the tetrahedrally coordinated sites according to $(Fe^{3+}_t)(Co^{2+}_o)(Fe^{3+}_o)O_4$, this catalyst contains the active octahedral Co^{2+} sites for the H_2O_2 decomposition. For the previous reactions, cobalt ferrite showed the lowest activity, therefore in turn indicating the significance of Co^{3+} for the chemical and electrochemical oxygen evolution.

Similar to the electrochemical OER, the anisotropic samples with a preferred 111 termination outperform their isotropic counterparts. On one side, this effect is very small for the Co^{2+} and Co^{3+} containing Co_3O_4, but the activity of the only Co^{2+} containing cobalt ferrite is boosted significantly with this preferred orientation. Figure 3.3.10 shows the normalized initial rates for chemical water oxidation, H_2O_2 decomposition and the overpotential at 10 mA cm^{-2} for electrochemical OER for the anisotropic spinel substitution series.

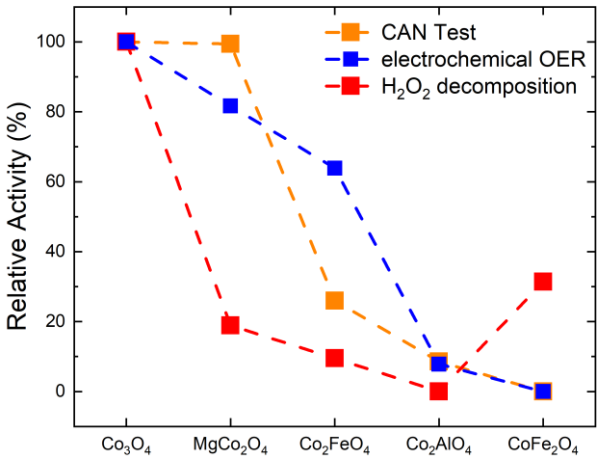

Figure 3.3.10: Normalized relative activity for the three investigated reactions. The most active catalyst was set to 100 % performance and the least active to 0 % to highlight the relative differences.

Despite the different nature of all oxygen evolution reactions studied here, the catalyst with the highest cobalt content, Co_3O_4, is always identified as the most active catalyst within the anisotropic substitution series highlighting the catalytic role of this element for oxygen evolution. When substituting other cations for cobalt, a loss in activity was observed for all compositions and reactions except for $MgCo_2O_4$ in the CAN test. This sample where Co^{2+} was substituted by Mg^{2+}, was the second-best catalyst underlining the catalytic role of the remaining Co^{3+} for the CAN test and the electrochemical OER with only a little activity loss. In case of the H_2O_2 decomposition, a substantial activity loss was observed when going from Co_3O_4 to $MgCo_2O_4$, which is consistent with a Co^{2+}-centered reaction as suggested in the literature.[99] Within the samples with two thirds of cobalt cations, there is a consistent and

almost linear decreasing trend when going from $MgCo_2O_4$ to Co_2FeO_4 and finally to Co_2AlO_4 suggesting that the positive effect of Co^{3+} is more important than the promoting effect of the redox-active iron cation. The latter effect was most prominent when comparing Co_2FeO_4 and Co_2AlO_4 in electrochemical OER and may be related to a better "hopping" conductivity when Fe-based redox pairs are present in the spinel structure. On a relative scale, the performance of the Co_2AlO_4 catalyst is consistently at the lower end for all three reactions, but the $CoFe_2O_4$ was the worst catalyst in the CAN test and the OER showing again that the promoting effect by iron cannot compensate the lower amount of cobalt and especially the absence of Co^{3+} in this material. However, in the H_2O_2 decomposition, $CoFe_2O_4$ shows the second highest activity behind Co_3O_4.

The investigation of the activity of different mesostructures showed a higher activity for the preferentially 111 terminated Co_3O_4 compared to the isotropic counterpart with no predominant surface termination. With no Co^{3+} in the spinel structure present as it is the case for cobalt ferrite, predominant surface termination does not have a systematic effect on the activity in the herein investigated reactions. Based on this observation, it can be speculated that the beneficial effect of Co^{3+} species is particularly strong if these species reside in a 111 spinel termination. With oxygen ligands, Co^{3+} is expected to be most stable in octahedral low spin configuration (normal spinel structure) rendering the B site termination a promising candidate for the catalytically active surface in spinels or for its precursor. In conclusion, these findings underline the complexity of heterogeneous catalysts and the importance of composition and mesostructure for a given reaction, especially surface termination, and they at the same time highlight the potential of comparative investigations on systematic sample series to tackle this complexity.

3.3.4 Conclusion

A thoroughly characterized sample series of cobalt-based spinel oxides was synthesized by co-precipitation employing the crystalline precursor decomposition approach. The as-prepared (layered double) hydroxide precursors as well as the desired spinel catalysts were shown to be phase pure and exhibited an anisotropic platelet morphology. The topotactic transformation of the precursors into the spinel catalysts enable a high control over the catalysts mesostructure, especially surface termination, cation distribution and porosity. The cationic composition of the mixed oxides was systematically varied by substitution of $Co^{2+/3+}$ by Mg^{2+}, Fe^{3+} and Al^{3+}.

Furthermore, the cobalt spinel and cobalt ferrite exhibiting an anisotropic platelet-like morphology were compared to isotropic Co_3O_4 and $CoFe_2O_4$ with more spherical particles. The oxygen evolving CAN test, the electrochemical OER and the decomposition of H_2O_2 were used as probe reaction to study the catalytic properties of the spinel samples.

For all reactions Co_3O_4 is identified as the most active catalyst within the anisotropic substitution series. All samples containing Co^{3+} show the same trend with substitution. For the two water oxidation reactions, even a semi-quantitative similarity was observed rendering the CAN test a robust probe reaction for OER for these catalysts. With decreasing amount of Co^{3+} the activity decreases as well. Furthermore, redox active cations such as iron enhance the catalytic performance when the same relative Co^{3+} content is considered. For the CAN test and the electrochemical OER Co^{3+} clearly plays a major role for the catalytic reactivity. In contrast Co^{2+} dominates for H_2O_2 decomposition, showing a higher relative activity for the only Co^{2+} containing cobalt ferrite. These results underline the general importance of cobalt and of Co^{3+} in particular for the water oxidation reactions and are in agreement with the current literature. The investigation of the activity of different mesostructures showed a higher activity for the 111 terminated Co_3O_4 compared to the isotropic counterpart with no predominant surface termination suggesting an important role of Co^{3+} species in this facet, most likely with the B site termination.

These proposals for structure reactivity relationships were enabled by controlled synthesis conditions, thorough characterization, and precise kinetic testing. Further investigations for validation are required and will include *operando* and *in situ* techniques to give additional insight into factors governing the dynamics and activity of the solid-liquid interface. The approach to develop inspiration for such work from composition- and mesostructured-activity correlations can be extended in the future to other heterogeneous oxidation reactions, looking into additional selectivity issues not common to oxygen evolution.

3.4 Experimental Section

3.4.1 Synthesis

All syntheses were conducted in an automatic lab reactor system (*OptiMax 1001, Mettler Toledo*). Co-precipitation of the hydroxide and layered double hydroxide precursors was achieved by simultaneously dosing a metal salt solution and a precipitation agent into the reactor, prefilled with 200 mL of distilled water. The pH was controlled by an InLab Semi-Micro-L pH electrode and kept at a fixed value by automatically dosing the precipitation agent. The temperature was kept constant during the whole synthesis procedure. All precipitates were washed by repeatedly dispersing in demineralized water and subsequent centrifugation until the conductivity of the supernatant was below 100 µm S.

Co_3O_4: For the $Co(OH)_2$ precursor 125 g of a 0.8 M $Co(NO_3)_2x6H_2O$ (≥ 98 %, Carl Roth) solution were dosed continuously over 1 h at pH 8.5 and 50 °C with 0.6 M NaOH (98.5%, VWR) as precipitation agent. Following precipitation, the material was aged for 1 h without pH control at 50 °C. During the reaction, the reactor was continuously purged with N_2 and stirred at 300 rpm. After cooling to room temperature, the precipitate was washed with water several times and dried at room temperature in vacuum. Subsequently the dried precursor was calcined at 400 °C (2 K min^{-1}) for 3 h in a muffle furnace (*Nabertherm LE 6/11/B150*).

$MgCo_2O_4$: 125 g of a metal salt solution containing 0.533 M $Co(NO_3)_2x6H_2O$ and 0.266 M $Mg(NO_3)_2x9H_2O$ (99 %, Fisher Scientific) were dosed in 1 h at pH 11.0 and 50 °C with a 1.0 M NaOH as precipitation agent. Following precipitation, the material was aged for 1 h without pH control at 50 °C. During the reaction, the reactor was continuously purged with N_2 and stirred at 300 rpm. After cooling to room temperature, the precipitated $Mg_{1/3}Co_{2/3}(OH)_2$ was washed with water several times and dried overnight at 80 °C in static air. Subsequently the dried precursor was calcined at 400 °C (2 K min^{-1}) for 3 h in a muffle furnace.

Co_2FeO_4: For precipitation of a $Co^{2+}Fe^{3+}$ LDH precursor 125 g of a metal salt solution containing 0.533 M $Co(NO_3)_2x6H_2O$ and 0.266 M $Fe(NO_3)_3x9H_2O$ (≥ 98 %, Sigma Aldrich) were dosed in 1 h at pH 8.5 and 50 °C with a precipitation agent containing 0.6 M NaOH and 0.09 M Na_2CO_3 (≥99.5%, Carl Roth). Following precipitation, the material was aged for 1 h without pH control at 50 °C. During the reaction, the reactor was continuously stirred at 300 rpm. After cooling to room temperature, the precipitated $Mg_{1/3}Co_{2/3}(OH)_2$ was washed

with water several times and dried overnight at 80 °C in static air. Subsequently the dried precursor was calcined at 400 °C (2 K min^{-1}) for 3 h in a muffle furnace.

Co_2AlO_4: For precipitation of a $Co^{2+}Al^{3+}$ LDH precursor 125 g of a metal salt solution containing 0.533 M $Co(NO_3)_2x9H_2O$ and 0.266 M $Al(NO_3)_3x6H_2O$ (≥98%, Carl Roth) were dosed in 1 h at pH 10.0 and 50 °C with a precipitation agent containing 1.0 M NaOH and 1.2 M Na_2CO_3. Following precipitation, the material was aged for 1 h without pH control at 50 °C. During the reaction, the reactor was continuously stirred at 300 rpm. After cooling to room temperature, the precipitated $Mg_{1/3}Co_{2/3}(OH)_2$ was washed with water several times and dried overnight at 80 °C in static air. Subsequently the dried precursor was calcined at 400 °C (2 K min^{-1}) for 3 h in a muffle furnace.

$CoFe_2O_4$: For precipitation of a $Co^{2+}Fe^{2+}Fe^{3+}$ LDH precursor 125 g of a metal salt solution containing 0.133 M $CoCl_2x6H_2O$ (99.9 %, Alfa Aesar), 0.133 M $FeCl_2x4H_2O$ (>99 % Acros Organics) and 0.133 M $FeCl_3x6H_2O$ (≥ 99 %, Carl Roth) were dosed in 1 h at pH 8.5 and 10 °C with precipitation agent containing 0.6 M NaOH and 0.09 M Na_2CO_3. Following precipitation, the material was aged for 24 h without pH control at 10 °C. During the reaction, the reactor was continuously purged with N_2 and stirred at 300 rpm. After cooling to room temperature, the precipitated $Co^{2+}Fe^{2+}Fe^{3+}$ LDH was washed with water several times and dried at room temperature in vacuum. Subsequently the dried LDH precursor was calcined at 600 °C (2 K min^{-1}) for 3 h in a muffle furnace.

Isotropic Co_3O_4: Isotropic Co_3O_4 was synthesized by thermal treatment of a precipitated hydroxy carbonate precursor. The automatic lab reactor system described above was prefilled with 200 mL of a 0.5 M $Co(NO_3)_2x6H_2O$ solution. The prefilled solution was stirred at 300 rpm, held at 25 °C and a pH of 9 was set with a 1 M Na_2CO_3 solution. After aging for one hour without pH control, the precipitate was washed and dried overnight in static air at 100 °C. The dried precursor was calcined at 500 °C (2 K min^{-1}) for 3 h in a muffle furnace.

Isotropic $CoFe_2O_4$: Isotropic $CoFe_2O_4$ was directly precipitated. Therefor a 125 g of a metal salt solution containing 0.233 M $Co(NO_3)_2x9H_2O$ and 0.566 M $Fe(NO_3)_3x6H_2O$ were dosed into the prefilled (200 mL distilled H_2O) reactor over the course of 1 h. A constant pH of 10 was kept with a 1.5 M NaOH solution and the temperature was held at 10 °C. Following precipitation, the material was aged for 1 h without pH control at 10 °C. During the reaction, the reactor was continuously purged with N_2 and stirred at 300 rpm. After cooling to room temperature, the precipitated $CoFe_2O_4$ was washed with water several times and dried at 80 °C

in static air. Subsequently the dried precipitate was calcined at 500 °C (2 K min^{-1}) for 3 h in a muffle furnace.

3.4.2 Characterization

Powder X-Ray Diffraction (PXRD) was performed with a Bruker D8 Advance diffractometer with a Cu X-ray source in Bragg-Brentano geometry, using a LynxEye XE-T detector. The samples were dispersed in ethanol on a PMMA sample holder and diffraction patterns were recorded in the angular range from 5 ° to 90 ° 2θ with a step size of 0.01 ° and a counting time of 1.5 s. During the measurement, the sample holder was slowly rotated. For showing phase purity, determination of lattice parameters of the as-prepared spinels Rietveld refinement was performed with the Bruker software TOPAS.

Scanning electron microscopy (SEM) was conducted with an Apreo S LoVac (Thermo Fisher Scientific). Prior to the measurements, the samples were sputtered with Pt/Au.

The ratio of the incorporated metal cations in the spinels catalysts was determined by X-ray fluorescence using a Bruker S8 TIGER Series (4 kW).

Thermogravimetric analysis (TGA) of the as-prepared precursors was carried out with a NETZSCH STA 449f F3 Jupiter (NETSCH GmbH, Germany). The mass loss was recorded as a function of the temperature with a linear heating rate of β= 5 K min^{-1} in a temperature range from 30 °C to 1000 °C and a gas stream of O_2 (21 mL min^{-1}) and Ar (79 mL min^{-1}).

BET surface areas were measured using N_2 physisorption at 77 K with a NOVA3000 (Quantachrome GmbH, Germany). Prior to the measurements, the samples were degassed at 80 °C in vacuum for 2 h. Pore volume and the pore size distribution were determined by applying the BJH method.

Mössbauer spectra were recorded on powder samples in standard transmission geometry, using a ^{57}Co radiation source mounted on a WissEl driving unit operating in constant acceleration mode. A liquid helium bath cryostat was utilized to attain low temperatures and high fields, containing a superconducting solenoid in split-pair geometry. A homogenous magnetic field of 5 T was applied at the sample position, with the field orientation parallel to the γ-ray propagation direction (in-axis).

Magnetic properties were analyzed with the vibrating sample magnetometer (VSM) option of a Quantum Design PPMS DynaCool. The field dependent properties were characterized via M(H) loops recorded at 4.3 K and 300 K at magnetic fields up to 9 T, while temperature dependent properties were recorded via M(T) sweeps between 5 K and 400 K using the zero field cooled – field cooled (ZFC-FC) regime at an applied field of 1 T.

TEM micrographs were recorded with a JEOL 2200FS with a probe-side Cs-corrector operated at 200 kV acceleration voltage**.** Selected area electron diffraction images were taken at a camera length of 30 cm.

XPS measurements were performed on a VersaProbe II micro-focus X-ray photoelectron spectrometer (UlvacPhi) using monochromatic Al-Kα light at 1486.6 eV photon energy. Charging effects were compensated using a dual-beam neutralizing approach using electrons and slow moving argon ions.

3.4.3 Catalysis

Chemical water oxidation was performed using Ce^{4+} as oxidizing agent. During the oxidation process of water to oxygen the single-electron oxidant Ce^{4+} is reduced to Ce^{3+} ($E^0(Ce^{3+}/Ce^{4+})$ = 1.72 V vs. NHE at pH=0).

$$4Ce^{4+} + 2H_2O \xrightarrow{spinel\ catalyst} 4H^+ + O_2 + 4Ce^{3+}$$

For determination of the initial rates for chemical water oxidation 100 mg of catalyst were dispersed in 45 mL water. The setup was purged with Ar (50 mL min^{-1}) to ensure an oxygen free environment. 5 mL of a $(NH_4)_2Ce(NO_3)_6$ solution (2.5 mol L^{-1}) were added to the dispersion and the evolving oxygen was detected by an oxygen analyzer (EC900, Systech Illinios) over 2 h. For each catalyst twofold measurements were performed.

The **electrochemical measurements**, namely the determination of the OER activity and the C_{dl} were carried out in a 3-electrode electrochemical cell using an AUTOLAB PGSTAT 204´´ potentiostat and a Metrohm rotator. The working electrode consisted of drop-casted catalyst ink on a glassy carbon (GC) disk, a double junction Ag/AgCl/3 M KCl/1 M KOH electrode was used as reference electrode, and a platinum mesh which was separated by a frit acted as the counter electrode. The catalyst ink was prepared by dispersing 1 mg of catalyst ink in 98 µL water, 98 µL ethanol and 4 µL Nafion (~5% (w/v)) which was used as binder. The GC

electrode was polished using 0.05 µm alumina paste until a mirror-like finish was achieved. 4.8 µL of the catalyst ink was drop-casted on the GC electrode to acquire a final loading of 210 µg/cm². Argon saturated 1 M KOH was used as the electrolyte. Prior to use, the electrolyte was purified by removing metal impurities using a chelating ion resin (Chelex 100, Bio-Rad). A small stream of argon was flushed continuously during the measurement over the electrolyte to maintain gas saturation. The electrochemical activity was measured using linear sweep voltammetry (LSV). The LSVs were recorded at a scan rate of 0.005 V/s at a rotation speed of 1600 rpm. Each catalyst was measured in triplicate. Each measurement included a galvanostatic impedance measurement at 0 A, which was later used to correct for the uncompensated solution resistance. The C_{DL} measurements were done by potentiodynamic cycling in the non-faradaic region of the voltammogram at different scan rates of 0.01, 0.05, 0.1, 0.15, 0.20 V/s. The anodic and cathodic currents were extracted, and the average was plotted against the respective scan rate. The slope of the linear regression was used to determine C_{DL}. All potentials were converted to RHE using the following equation.

$$E_{RHE} = E_{Ag/AgCl/KCl} + 0.207 + 0.059*pH \qquad Eq(1)$$

H_2O_2 decomposition was carried out in a peroxide decomposition set up (Gassmess-5). 10 mg catalyst were dispersed in 30 mL acetonitrile. The solution was kept at 30 °C and stirred at 600 rpm. 80 µL H_2O_2 (30 wt. %) were added and the gas volume measurement was started immediately. The decomposition reaction was run for 30 min.

3.5 Acknowledgements

This research was funded by the Deutsche Forschungsgemeinschaft (DFG, German Research Foundation) in the framework of the Collaborative Research Center / Transregio "Heterogeneous Oxidation Catalysis in the Liquid Phase" – 388390466 – TRR 247 (Project C1, A1, A2, B2 and S) and by the Mercator Research Center Ruhr (MERCUR, Pe-2018-0034). Furthermore, the authors would like to thank Dr. Kateryna Loza (SEM), Benjamin Mockenhaupt, Eko Budiyanto (BET), Robin Meya (AAS), Dr. Markus Heidelmann (TEM), Nicolas Cosanne (Synthesis) and Jurij Jakobi (XRF) for their assistance in the experimental work.

3.6 Supporting Information

As reproducibility is of pivotal importance in catalyst synthesis, this aspect is being highlighted for the magnesium cobalt hydroxide precursor and the resulting spinel catalyst. Figure 3.6.1 to Figure 3.6.3 display the synthesis protocols, PXRD patterns and BET analysis to prove batch to batch reproducibility.

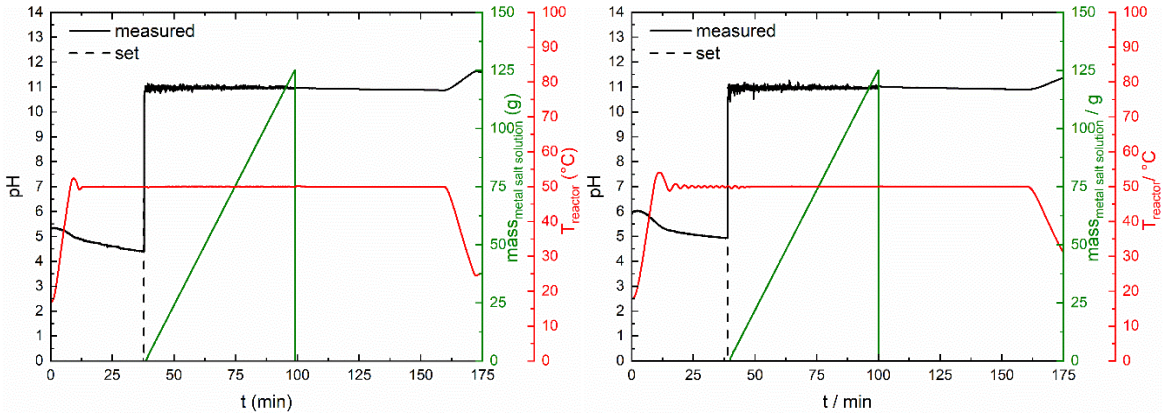

Figure 3.6.1: Synthesis protocols of two different batches $Mg^{2+}_{1/3}Co^{2+}_{2/3}(OH)_2$. pH, dosing speed and temperature are perfectly controlled, therefore ensuring reproducible catalyst properties.

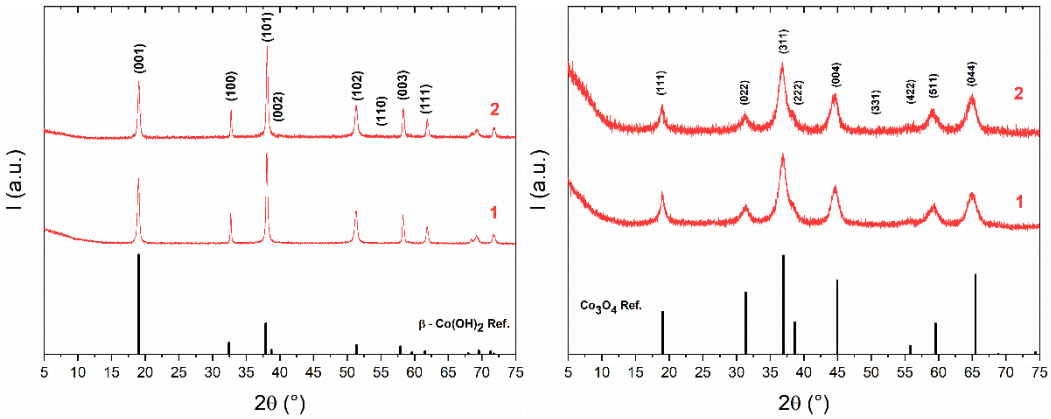

Figure 3.6.2: PXRD patterns of the as-prepared $Mg^{2+}_{1/3}Co^{2+}_{2/3}(OH)_2$precursors (left) and $MgCo_2O_4$ catalysts after calcination at 400 °C (right).

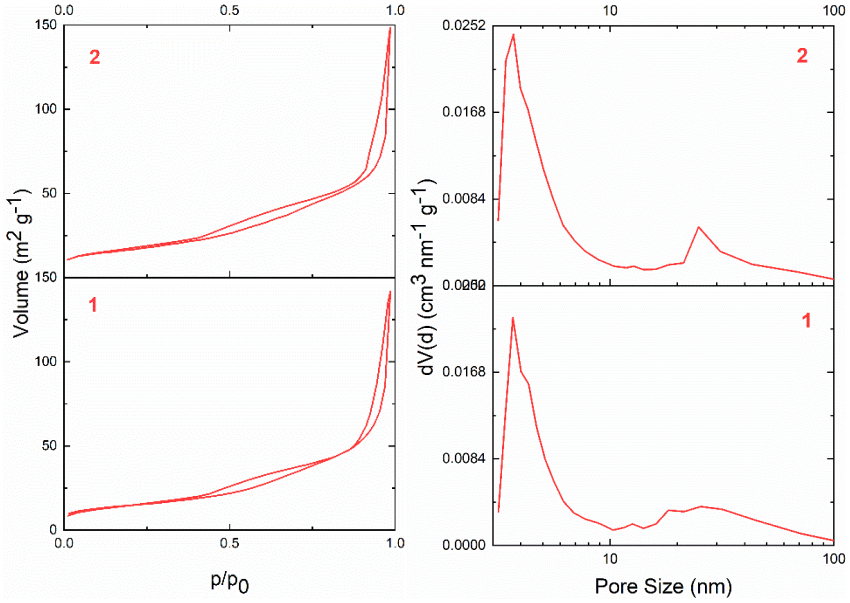

Figure 3.6.3: Adsorption desorption isotherms (left) and pore size distributions (right) of two different batches of $MgCo_2O_4$. The surface area was determined to 55 m^2g^{-1}± 6 m^2g^{-1}.

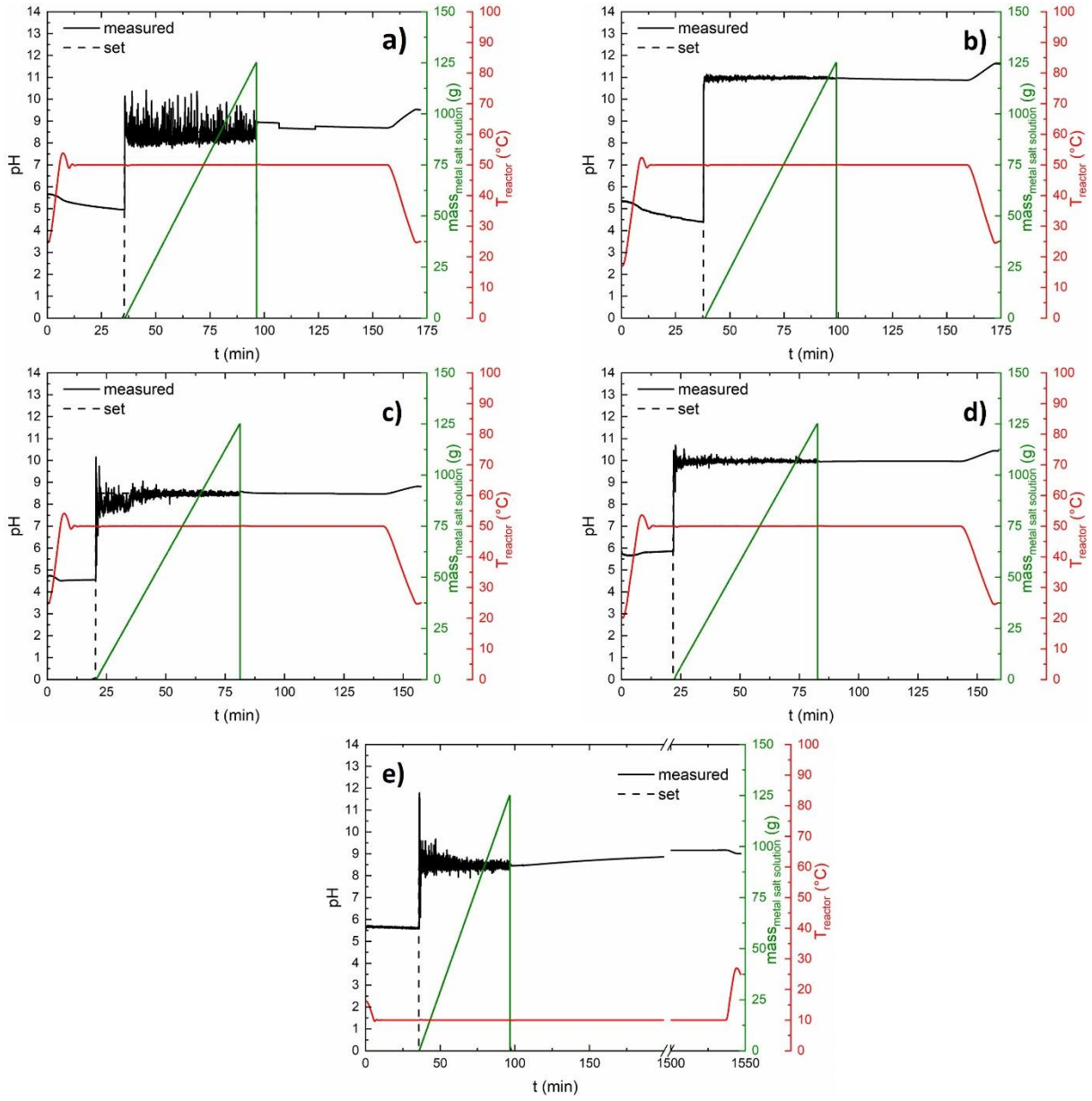

Figure 3.6.4: Synthesis protocols of the precursor precipitation and aging. a) $Co^{2+}(OH)_2$, b) $Mg^{2+}_{1/3}Co^{2+}_{2/3}(OH)_2$, c) $Co^{2+}_{2/3}Fe^{3+}_{1/3}$ LDH, d) $Co^{2+}_{2/3}Al^{3+}_{1/3}$ LDH, e) $Fe^{2+}_{1/3}Co^{2+}_{1/3}Fe^{3+}_{1/3}$ LDH.

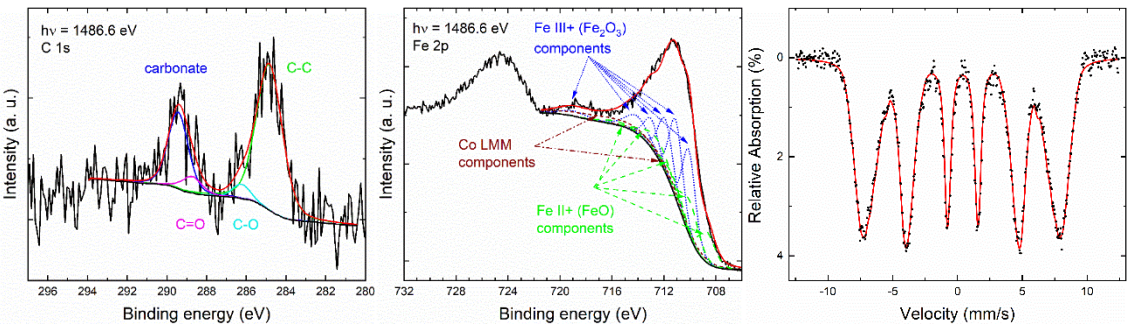

Figure 3.6.5: C 1s (left), Fe 2p, (middle) XP spectra and Mössbauer spectra (right) of the $Fe^{2+}_{1/3}Co^{2+}_{1/3}Fe^{3+}_{1/3}$ LDH precursor.

As Fe^{2+} is easily oxidized to Fe^{3+} in air, the actual existence of Fe^{2+} has to be proven. For this reason, XPS and Mössbauer spectroscopy were performed. XPS showed an amount of 33±10 % Fe^{2+} of the overall Fe content and a total Fe/Co ratio of 1.66±0.15, agreeing with the determined 1.65 ratio from AAS. Furthermore, XPS showed minor amounts of carbon, underlining the claim of "organic free" synthesis. The expected interlayer carbonate is clearly visible in the C 1s spectrum.

Mössbauer spectra were recorded at low temperature (4.3 K) and high magnetic field (5 T) parallel to the γ-ray propagation direction. For the $Fe^{2+}_{1/3}Co^{2+}_{1/3}Fe^{3+}_{1/3}$ LDH precursor material, the line intensity ratio A_{23} close to 2 reveals mainly antiferromagnetic behavior with random spin orientation, as it would be expected for LDH-based materials.[100] As a result, the evaluation of the experimental data points was achieved by means of an equidistant distribution of magnetic hyperfine fields, as no individual subspectra corresponding to different crystallographic sites could be discerned. With this method, we obtain a mean magnetic hyperfine field of ca. 46 T, with an isomer shift of 0.48 mm/s indicating that we are mainly dealing with Fe^{3+} contributions. This is presumably caused by the extended measurement time required for Mössbauer spectroscopy, and the associated oxidation of the originally present Fe^{2+} fraction, which was verified in XPS measurements. The sample preparation for XPS is comparatively fast and yet not the expected amount of 50 % of Fe^{2+} is found. However, the contribution of the measured Mössbauer spectrum is predominantly from one phase and the X-ray diffraction pattern did not show any sign of a secondary phase. In our recently published paper, a premature spinel by-phase was detected by XRD and Mössbauer spectroscopy.[11] The synthesis, washing and drying procedure in the present work was improved and prevented this premature oxidation and consequential by-phase formation. Even though oxidation occurs during sample preparation and measurement of the X-ray diffraction data, the phase purity is potentially explained by a green rust - mössbauerite related situation.[101] Fe^{2+} oxidizes to Fe^{3+}, but through deprotonation of the hydroxyl groups the resulting additional excess charge in the brucite-like layers is compensated and the structure is stable.

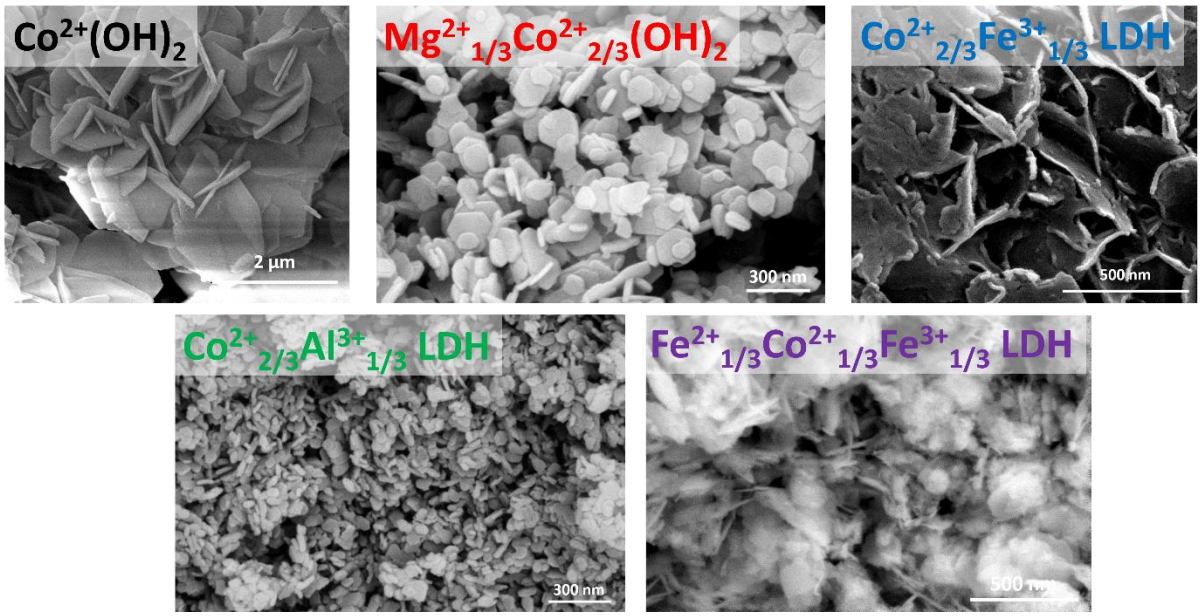

Figure 3.6.6: SEM micrographs of the as-prepared hydroxide and layered double hydroxide precursors.

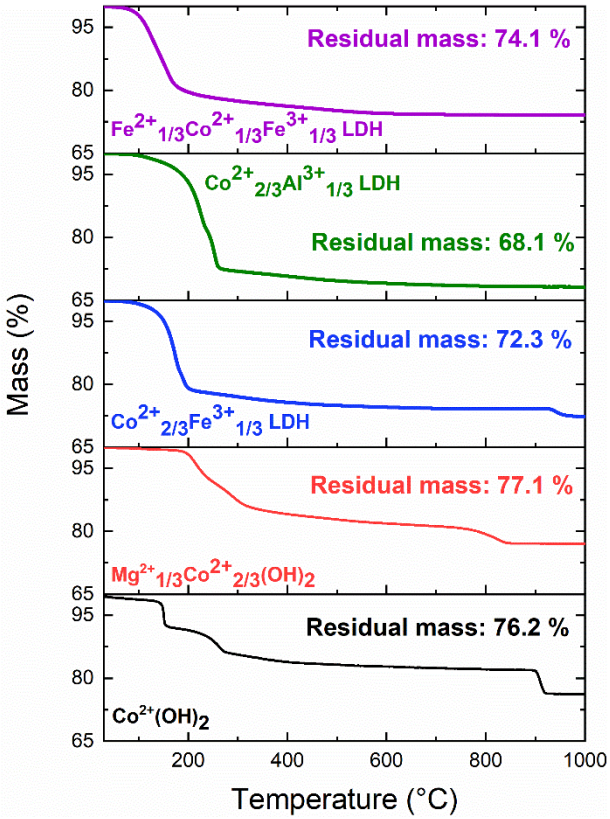

Figure 3.6.7: Relative mass loss as a function of temperature and residual mass for the as-prepared anisotropic precursors.

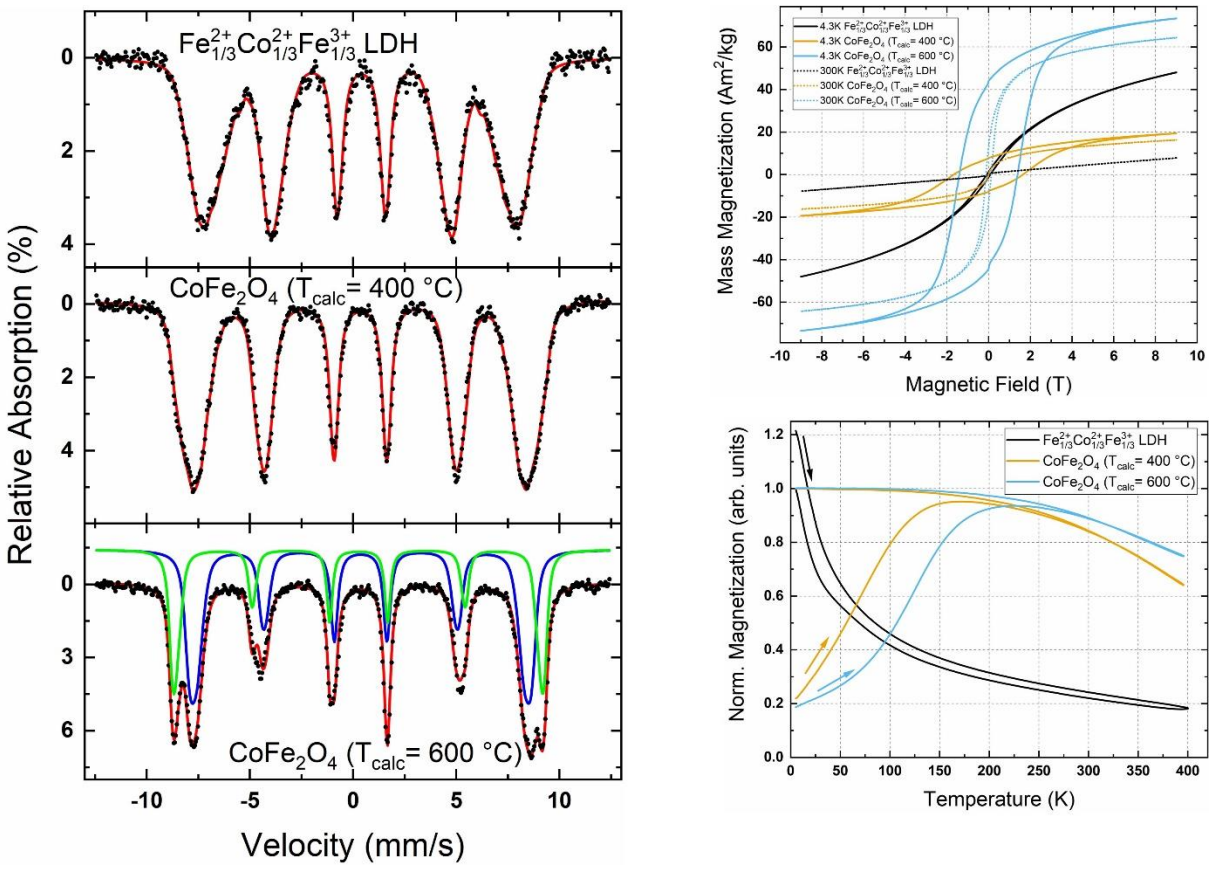

Figure 3.6.8: (a) Mössbauer spectra recorded at 4.3 K and 5 T, M(H) (b) and M(T) (c) measurements of as-prepared layered double hydroxide precursor and samples calcinated at 400°C and 600°C.

In order to obtain a more detailed view on potential structural changes between precursor, resulting product, and possible by-phases, Mössbauer spectra were also recorded for a sample calcined at 400 °C and 600 °C. The results for the $Fe^{2+}_{1/3}Co^{2+}_{1/3}Fe^{3+}_{1/3}$ LDH precursor material are discussed above.

Some changes can be observed for the sample heated to 400 °C, such as the increase of the magnetic hyperfine field to ca. 50 T, pointing towards a general phase change of the material, while the isomer shift is nearly unchanged. The magnetic hyperfine field distribution shows first signs of two spectral contributions, which, together with the reduction in A_{23} to ca. 1.8, representing beginning ferrimagnetic in-field alignment, indicates the starting formation of spinel material.

The most dramatic change takes place after heating to 600 °C, with the resulting spectrum revealing two clearly separated sextet subspectra. Such a spectral structure is typical for ferrimagnetic spinel systems, making it possible to calculate the degree of inversion from the relative spectral areas, as these are proportional to the number of Fe ions on the tetrahedral and octahedral sites. We obtain an inversion parameter of 0.76(3), with this material thus

being closer to the inverse (1) than the regular spinel (0), as one would expect for phase pure $CoFe_2O_4$.[102] The mean spin canting angle, derived from A_{23}, decreased to ca. 40°, which is still substantial, usually caused by the high magnetocrystalline anisotropy and canted surface spins. Latter could here be connected to the enhanced surface fraction and the strongly porous nature of the material.

As Mössbauer spectra displayed a considerable change in magnetic structure, the formation of spinel material from the LDH precursor was also investigated by magnetometry. The M(H) sweep of the LDH precursor sample displays a quasi-paramagnetic behavior at room temperature, while a slow rise in magnetization is seen at 4.3 K, indicative of the strongly canted state and resulting lack of full saturation. A very minute saturation effect is observable at very small fields at 300 K, which could represent a miniscule parasitic phase. After heating to 400 °C, the 9 T magnetization at 4.3 K has decreased from 48 Am^2/kg to ca. 19 Am^2/kg, while the sample now also shows a significant remanence and coercive field that were almost completely absent in the untreated sample. The most dramatic change takes place after heating to 600 °C, where we observe a very broad hysteresis curve at 4.3 K, with a high magnetization of ca. 73 Am^2/kg at 9 T. This value is only slightly below the literature value of 80 Am^2/kg[103] for pure, well-ordered $CoFe_2O_4$ nanoparticles, which can be explained by the still substantial degree of spin canting deduced from the 5 T Mössbauer spectrum for this sample. We can therefore assume that this slightly lowered magnetization is caused by unordered surface spins, and not by an impurity of the material at hand. Regarding the M(T) sweeps, we can of course observe the same changes in magnetization, but as the materials are not in saturation at the applied field of 1 T, we chose to normalize the curves to the end points of the FC branches. Thanks to this, we can directly compare the qualitative temperature dependent progression of each sample's magnetization. We can observe that the LDH precursor does not display any distinct features, with the magnetization continuously dropping towards higher temperatures after attaining the paramagnetic state. In contrast, both the 400 °C and the 600 °C heated sample display typical relaxation behavior known from magnetic nanoparticles, with the inflection points of ca. 86 K for the 400 °C and 130 K for the 600 °C sample clearly showing a rise in blocking temperatures.

In conclusion the magnetic investigations underline the phase purity of the sample calcined at 600 °C, indicating a possible minor by-phase or incomplete transformation for the sample calcined at 400 °C.

Isotropic Co_3O_4 and $CoFe_2O_4$ was synthesized to further investigate the impact of morphology on the catalytic activity. In Figure 3.6.9 to Figure 3.6.12 characterization data of the before mentioned can be found.

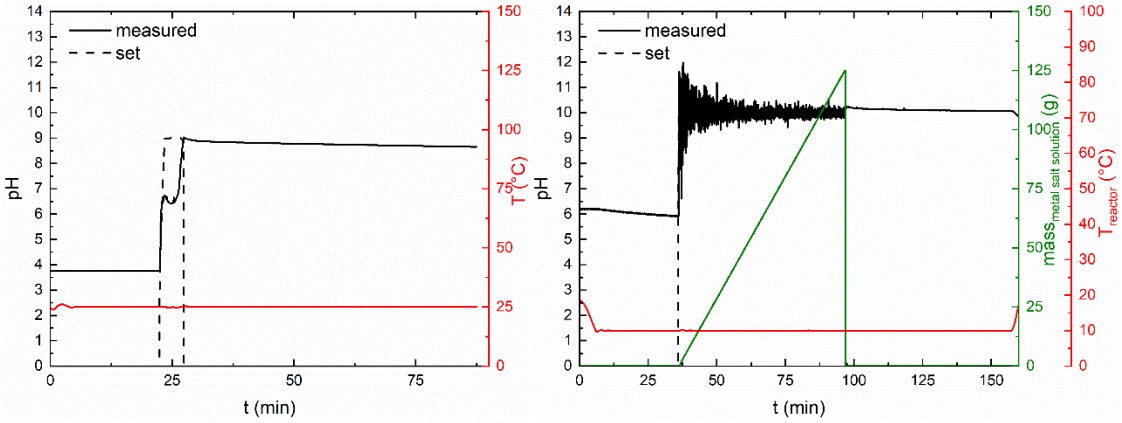

Figure 3.6.9: Synthesis protocols of iso-Co_3O_4 (left) and iso-$CoFe_2O_4$(right).

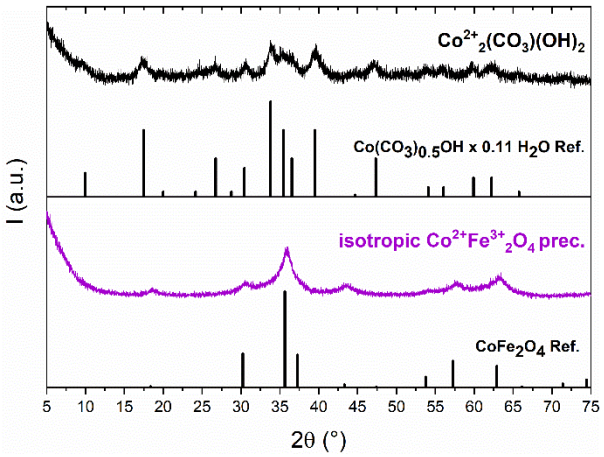

Figure 3.6.10: As-prepared precursor for isotropic Co_3O_4 and $CoFe_2O_4$.

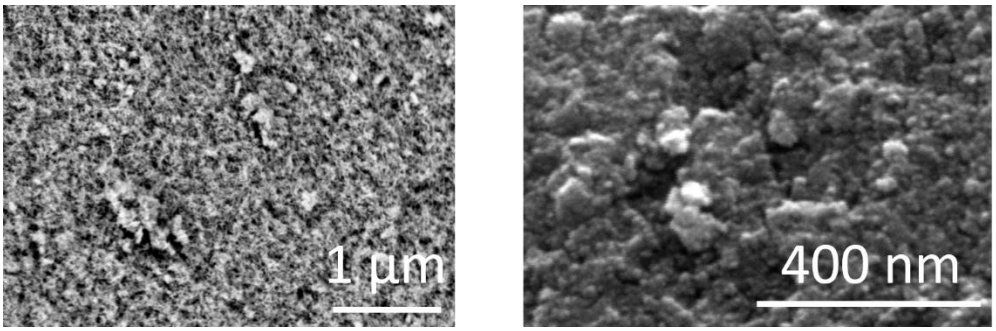

Figure 3.6.11: SEM micrographs of the as-prepared cobalt hydroxy carbonate precursor (left) and directly precipitated $CoFe_2O_4$.

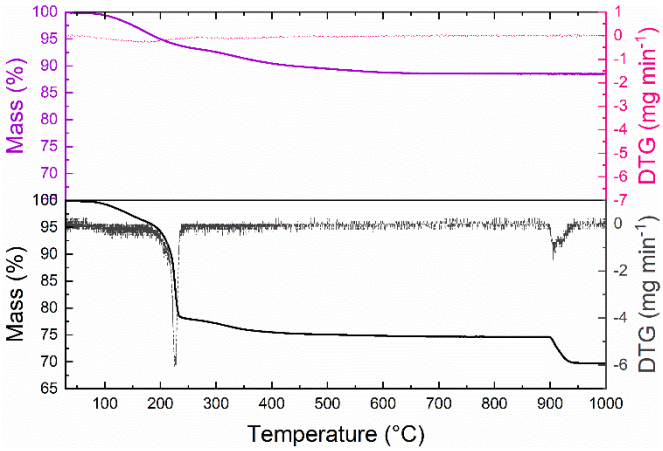

Figure 3.6.12: Thermogravimetric analysis of the precursors for isotropic Co_3O_4 (bottom) and $CoFe_2O_4$ (top).

Table 3.6.1: Rietveld refinement parameters for the anisotropic substitution series and isotropic cobalt spinel and cobalt ferrite.

Sample	R_{exp}	R_{wp}	R_p	R_{exp}'	R_{wp}'	R_p'
Co_3O_4	6.51	7.24	5.76	11.83	13.16	12.37
$MgCo_2O_4$	5.45	6.46	5.12	12.04	14.29	12.34
Co_2FeO_4	6.21	7.22	5.71	9.04	10.51	8.91
Co_2AlO_4	5.59	5.86	4.64	9.49	9.94	8.5
$CoFe_2O_4$	12.56	14.96	11.54	12.65	15.07	12.2
iso-Co_3O_4	6.1	7.17	5.68	10.22	12	10.86
iso-$CoFe_2O_4$	10.44	11.58	8.85	11.57	12.83	10.24

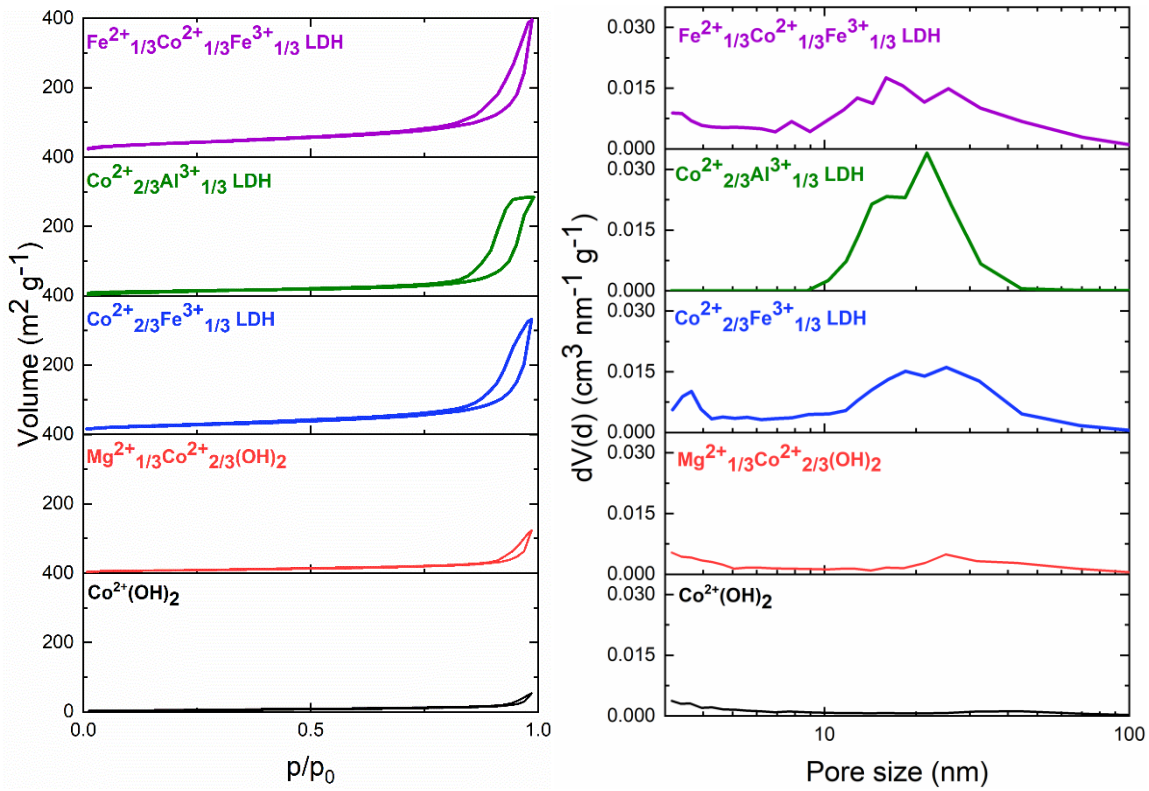

Figure 3.6.13: Adsorption desorption isotherms and pore size distributions of the as-prepared (layered double) hydroxide precursors of the anisotropic spinel substitution series.

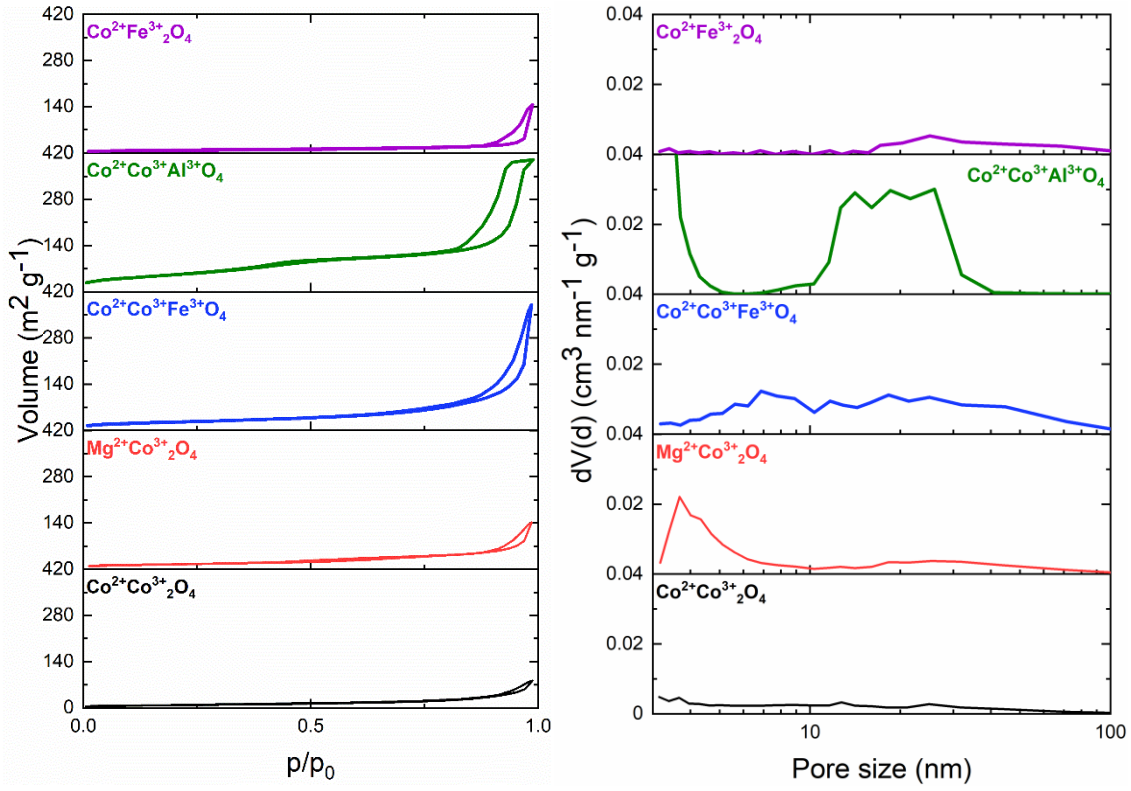

Figure 3.6.14: Adsorption desorption isotherms of the anisotropic spinel substitution series.

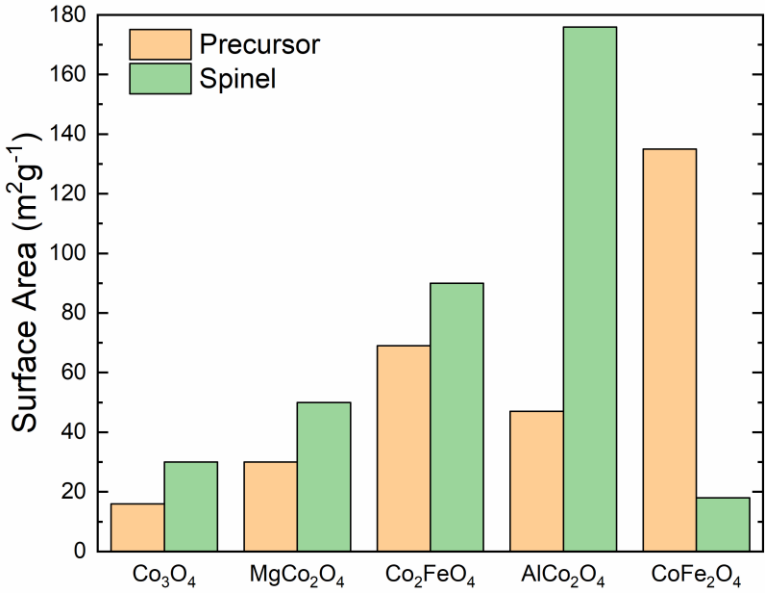

Figure 3.6.15: Comparison of surface areas of as-prepared precursors and calcined spinels. For the cobalt ferrite a decrease in surface area is observed because of the higher calcination temperature.

To analyze the preferred surface termination of the anisotropic samples and to show a more statistical facet distribution for the isotropic analogs, TEM measurements and electron diffraction were performed. Due to the intergrown nature of the anisotropic particles, it was not possible to achieve electron diffraction patterns of a single platelet in most cases. The aggregates make a surface termination determination nearly impossible. Nevertheless, a 111 surface termination is considered for all samples of the anisotropic substitution series. For Co_3O_4 several reports can be found in literature, confirming the topotactic spinel formation.[40, 50b] The related dehydroxylation of $Mg(OH)_2$ to MgO has been investigated as well.[104] For $CoFe_2O_4$ we recently showed the same transformation and for Co_2FeO_4 it was shown in the present work (See Figure 3.3.4 in the main text).[11] The 111 planes of the spinel and the 001 planes of the brucite type hydroxides exhibit a very similar d-spacing and therefore transformation occurs along them. This topotactic transformation leads to the preservation of the morphology. As all anisotropic spinels clearly exhibit the hexagonal platelet morphology of their (layered double) hydroxide precursor, this is additional prove for the suggested predominant surface termination.

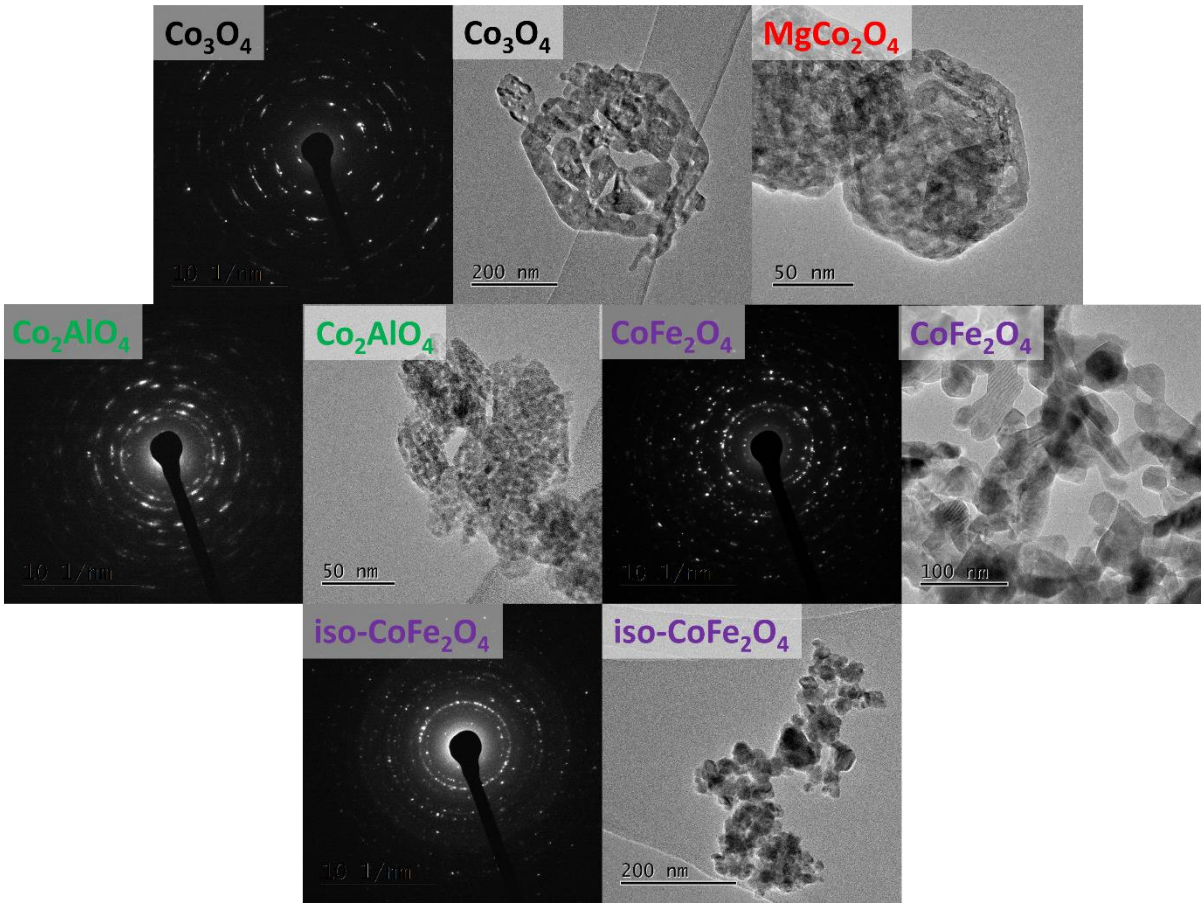

Figure 3.6.16: TEM images and electron diffraction of anisotropic Co_3O_4, $MgCo_2O_4$, Co_2AlO_4, $CoFe_2O_4$ and isotropic $CoFe_2O_4$.

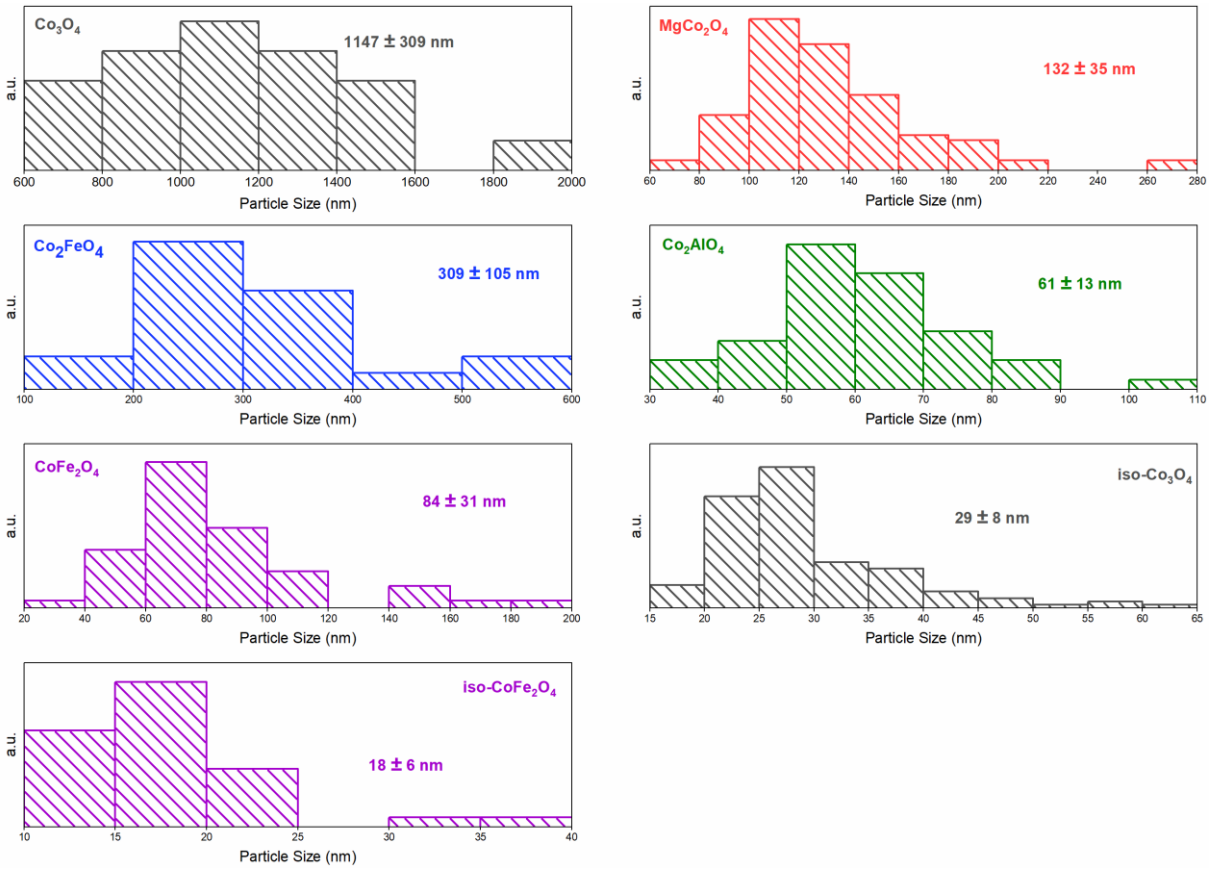

Figure 3.6.17: Particle size histograms of the anisotropic substitution series and the isotropic Co_3O_4 and $CoFe_2O_4$. Particles sizes for the anisotropic substitution series were obtained from SEM micrographs and for the isotropic spinels from TEM images.

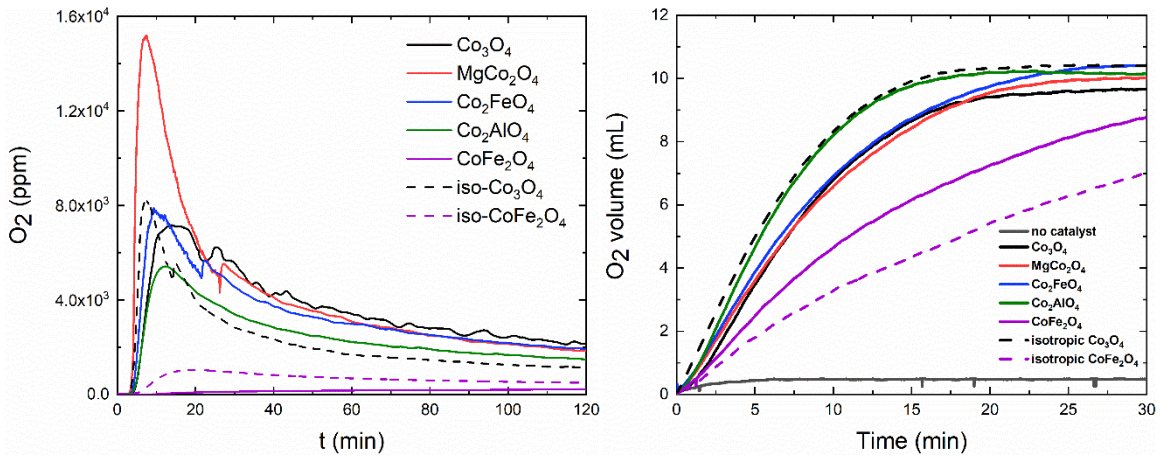

Figure 3.6.18: Oxygen evolution for all catalysts over 120 min for the CAN test (left) and oxygen evolution over 30 min for H_2O_2 decomposition (right).

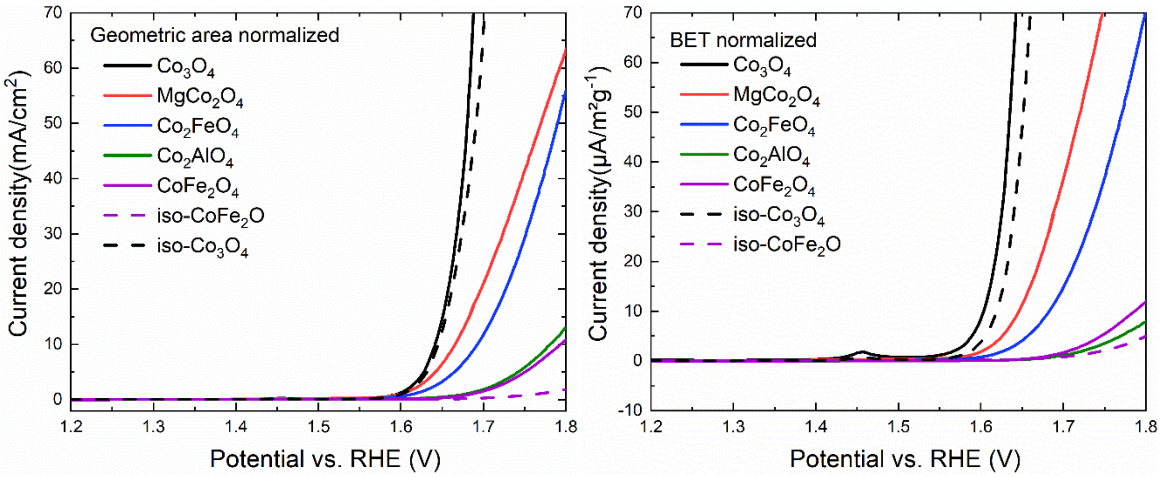

Figure 3.6.19: Current densities as a function of applied potential normalized in the geometric area of the electrode (left) and the BET surface area (right).

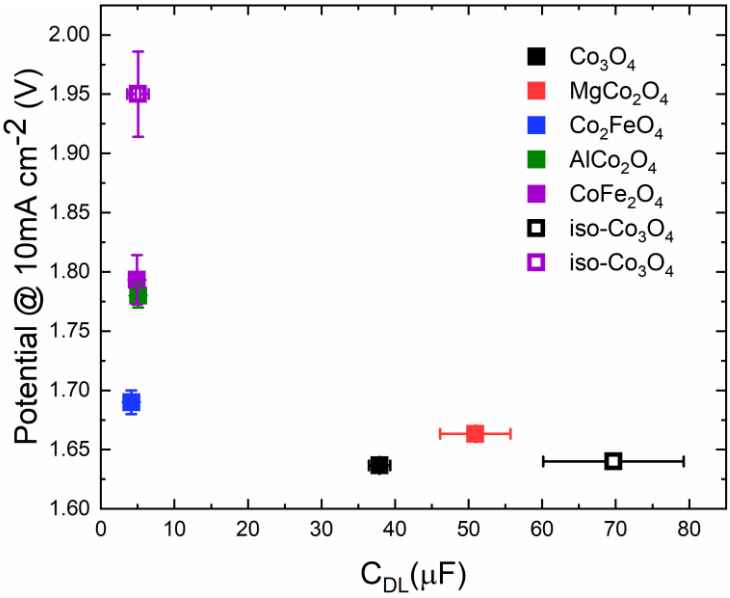

Figure 3.6.20: Double layer capacitance of all samples as a function of the potential at 10 mA cm^{-2}.

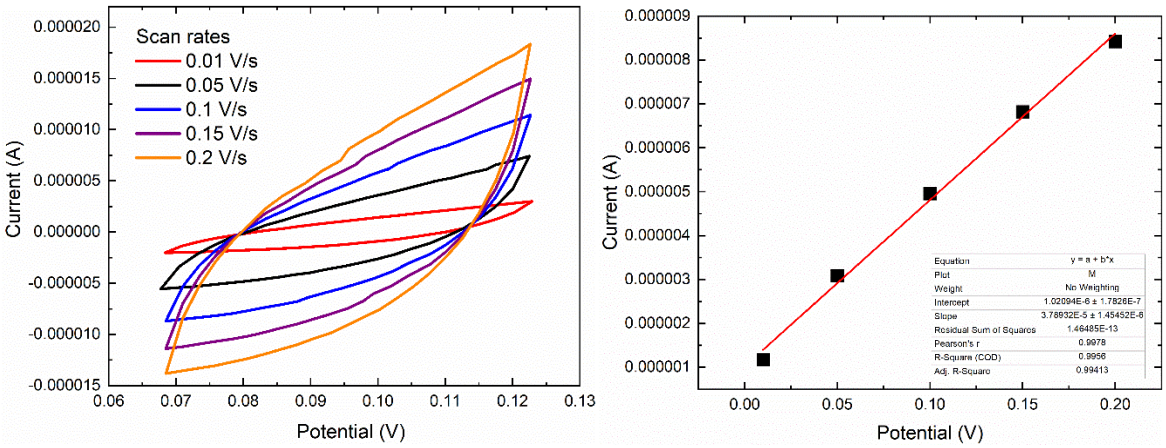

Figure 3.6.21: Cyclic voltammograms with different scan rates (left) and linear regression of the cathodic and anodic potentials.

4. Tailoring Pore Size and Catalytic Activity in Cobalt Iron Layered Double Hydroxides and Spinels by Microemulsion-assisted pH-controlled Co-precipitation

Anna Rabe,[a,c] Maximilian Jaugstetter,[b] Felix Hiege,[b] Nicolas Cosanne,[c] Klaus Friedel Ortega,[c] Julia Linnemann,[b] Kristina Tschulik,[b] Malte Behrens*[a,c,d]

[a] M. Sc. Anna Rabe, Prof. Dr. Malte Behrens
Faculty of Chemistry
University of Duisburg-Essen and Center for Nanointegration Duisburg-Essen (CENIDE)
Universitätsstr. 7, 45141 Essen, Germany
E-mail: mbehrens@ac.uni-kiel.de

[b] Dr. Maximilian Jaugstetter, M. Sc. Felix Hiege, Dr. Julia Linnemann, Prof. Dr. Kristina Tschulik
Faculty of Chemistry and Biochemistry
Analytical Chemistry II
Ruhr-University Bochum
44780 Bochum, Germany

[c] M. Sc. Nicolas Cosanne, Dr. Klaus Friedel Ortega, Prof. Dr. Malte Behrens
Institute for Inorganic Chemistry
Christian-Albrechts-Universität zu Kiel
Max-Eyth-Str. 2, 24118 Kiel, Germany

[d] Prof. Dr. Malte Behrens
Ertl Center for Electrochemistry and CatalysisInstitute for Inorganic Chemistry
Gwangju Institute of Science (GIST)
123 Cheomdan-gwagiro (Oryang-dong), Buk-gu, Gwangju 500-712, Korea

This chapter is published as a paper in the journal *ChemSusChem*. (Copyright 2023- Wiley-VCH; link to publication: https://doi.org/10.1002/cssc.202202015)

Keywords: cobalt iron spinel • co-precipitation • layered double hydroxides • structure-activity relationships • water splitting

Entry for the Table of Contents:

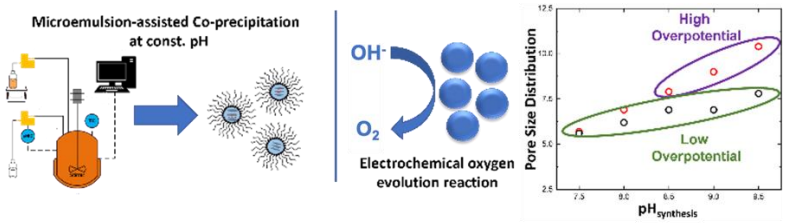

Through application of microemulsions during computer-controlled co-precipitation at constant pH nano-scaled cobalt iron layered double hydroxides and spinels with controllable pore size were synthesized. Pores smaller than a certain threshold size turned out to be beneficial for electrochemical oxygen evolution reaction.

Anna Rabe developed the synthesis technique including the post synthesis treatment and conceptualized the sample series. She synthesized most of the samples and evaluated sample characterization. She supervised and planned the work for Nicolas Cosanne, who supported with synthesis and characterization during his Bachelor thesis and as student assistant. The first draft of the manuscript was also written by her.

Electrochemical investigations and evaluation of impedance data was performed by Maximilian Jaugstetter, Felix Hiege, and Julia Linnemann. Maximilian Jaugstetter was also responsible for STEM of the micelles.

Malte Behrens, Klaus Friedel Ortega, and Kristina Tschulik were responsible for conceptualizing the project, supervising the work, and the funding acquisition. The manuscript was read and edited by all co-authors before submission.

4.1 Abstract

Cobalt iron containing layered double hydroxides (LDHs) and spinels are promising catalysts for the electrochemical oxygen evolution reaction (OER). Towards development of better performing catalysts, the precise tuning of mesostructural features such as pore size is desirable, but often hard to achieve. We herein established computer-controlled microemulsion-assisted co-precipitation (MACP) at constant pH and compared it to conventional co-precipitation. With MACP the particle growth is limited and through variation of the constant pH during synthesis the pore size of the as-prepared catalysts is controlled, generating materials for the systematic investigation of confinement effects during OER. At a threshold pore size, overpotential increased significantly. Electrochemical impedance spectroscopy (EIS) indicated a change in OER mechanism, involving the oxygen release step. It is assumed that in smaller pores the critical radius for gas bubble formation is not met and therefore a smaller charge-transfer resistance is observed for medium frequencies.

4.2 Introduction

Hydrogen is generated by electrocatalytic water splitting as a clean energy carrier.[2a, 105] The anodic half reaction, the oxygen evolution reaction (OER), exhibits sluggish kinetics and therefore represents the bottleneck of the overall reaction, which results in a high overpotential.[106] A vast number of publications on decreasing the OER overpotential have been published including both screening studies and mechanistical investigations on a broad variety of electrode materials. In alkaline medium, 3d transition metal-based catalysts are up-and-coming materials.[53a, 57c, 72, 107] Undoubtedly, it is desirable to find and further develop catalysts based on earth abundant and therefore cheaper materials with low overpotential and high stability. Layered double hydroxides (LDHs) as well as cobalt-based spinels have proven to be promising candidates for this endeavor.[47, 56, 108] We recently studied the systematic cobalt substitution in spinel catalysts, showing the impact of composition and surface facets for the OER.[109] The therein observed effect of exposed crystallographic facets, as well as many other literature reports, underline that the mesostructure of electrocatalysts, i.e., the particle size, shape and porosity, influences the performance significantly,[110] offering great potential for improved OER catalysts and calling for a systematic investigation and development of synthetic tools to control the mesostructure.

Mesostructure, in particular porosity, is known to play a major role in thermal catalysis, for example in reactions catalyzed by zeolites, metal organic frameworks, covalent organic frameworks, and metals as well as oxides on host structures.[111] Observed positive impact can be assigned to the change of adsorption energy, electronic effects or altered mass transport. Such effects could also play a role in electrocatalysis. For example, the control over catalyst pore size allows the investigation of electrocatalysis under spatial confinement in the pores. In this rapidly progressing field, so-called confinement effects shall alter and improve kinetics, mass transport, and ion specific selectivity of electrochemical reactions.[112] Based on detailed understanding of such effects and their interaction, confinement could be strategically employed to design superior electrocatalysts. In this respect, OER catalysts represent a key area of research due to both, the high technological relevance of electrochemical water splitting and the complexity of the electrochemical process comprising a multi-step reaction mechanism and transport phenomena related to gas evolution. Despite the recent progress made in the fabrication of nanostructured OER catalysts,[113] the synthesis of well-defined nano- or mesoporous systems remains challenging.

For this purpose, we further developed the catalyst synthesis by the crystalline precursor decomposition approach based on Co-containing LDH precursors forming pseudo-morphous spinels through thermal treatment.[109] LDHs are layered materials that usually exhibit a typical platelet morphology and a homogeneous cation distribution,[84] and are well-known OER catalysts,[18b] especially in form of nickel iron containing LDHs.[72, 114] Cobalt iron containing LDHs and derived (oxy)hydroxides exhibit a comparable activity in OER and are also highly suitable candidates for OER catalysts.[95a, 115] Through thermal decomposition, LDH precursors can be transformed into mixed metal oxides.[116] Given the LDH is at least partly built from oxidizable cations allowing a ratio of bivalent to trivalent cations of 1 to 2, spinels can topotactically form as a single oxide phase,[50b, 109] which also can be attractive OER catalysts.[109] To allow controlling the meso-structure of LDH and LDH-derived spinel OER catalysts, we present a synthesis method using water in oil microemulsions as nanoreactors in combination with computer-controlled constant-pH co-precipitation in this work. Surfactant-stabilized microemulsions[117] can form reverse micelles as a confined reaction space for co-precipitation to limit the particle growth. Such microemulsions have been used as a reaction medium for, e.g., metal nanoparticles,[118] metal salt aggregates,[119] core shell nanoparticles,[120] polymers,[121] hydroxides,[122] and oxides,[123] including LDHs.[33a, 124] While confinement of particle growth has been accomplished in these works, exact control to tune particle and pore size by specific synthesis parameters is often lacking, but highly

desirable for the investigation of mesostructure-reactivity relationships and confinement effects.

The herein presented work establishes the microemulsion-assisted co-precipitation (MACP) under highly controlled conditions, allowing a systematic variation of important synthesis parameters, especially the pH value of co-precipitation. The constant-pH nature of the co-precipitation is based on simultaneous dosing of the metal salt microemulsion and the precipitating agent microemulsion, allowing in principle a continuous process that can tackle the notorious up-scaling problem of syntheses involving microemulsions. A cobalt to iron ratio of 2 to 1 was chosen to achieve the formation of phase pure LDHs, which can be thermally transformed to spinels. The impact of the synthesis pH values during such MACP on the mesostructure of the as-prepared LDHs and the corresponding Co_2FeO_4 spinels has been investigated in detail and compared to conventional aqueous co-precipitation. A special focus falls upon the investigation of conceivable confinement effects during OER.

4.3 Results and Discussion

Two series of cobalt iron layered double hydroxides with the same cobalt to iron ratio of 2 to 1 were synthesized and thoroughly characterized. Computer-controlled synthesis conditions were applied for all reactions, ensuring reproducibility (Figure 4.6.1). The first series was prepared by conventional co-precipitation using only aqueous solutions without any further additives. Five samples were prepared by varying the constant pH during precipitation from pH 7.5 to pH 9.5 in steps of 0.5 and are labeled according to the corresponding precipitation pH c75 to c95 throughout this manuscript.

The second series was prepared by microemulsion-assisted co-precipitation (MACP), confining the reaction space within the reverse micelles of a microemulsion. A suited formulation was adapted from literature,[125] ensuring stable microemulsions containing water, metal salt solution or the alkaline precipitation agent as aqueous phase. Using these microemulsions five syntheses at constant pH values from pH 7.5 to pH 9.5 were performed as described above. The resulting samples are labeled m75 to m95. Further details on the synthesis procedures can be found in the experimental part and synthesis protocols for both synthesis approaches are shown in Figure 4.6.2 and Figure 4.6.3.

Through thermal decomposition and oxidation of a fraction of Co^{2+} to Co^{3+} the layered double hydroxides prepared by conventional co-precipitation and MACP were transformed into Co_2FeO_4 spinels and are marked with the suffix s accordingly.

4.3.1 Micelles

The mesostructure of the as-prepared MACP LDHs and the corresponding spinels reported in this work is based upon the confinement of the reaction space within reverse micelles, limiting the particle growth. To prove this confinement and to gain further insight about the size of the micelles, dynamic light scattering and TEM after plasma treatment were performed. More details can be found in the experimental section. Figure 4.3.1 shows STEM images of the template microemulsion, in other words the microemulsion containing only water, after drying and plasma treatment. Well defined spherical carbon walls with a cavity in the center are observed. A diameter of 13.1 ± 4.6 nm was found by TEM, which agrees within the margin of error with the result of 16 nm from dynamic light scattering.

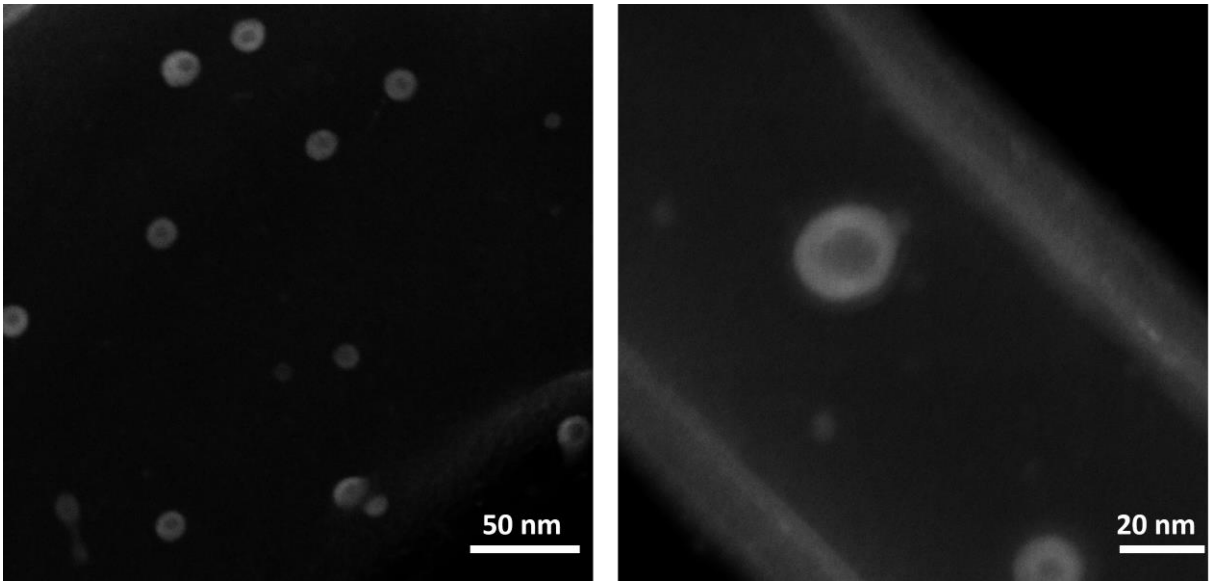

Figure 4.3.1: STEM images of the dried-out template micelles after plasma treatment.

Even though high-quality images with well-defined micelles were obtained for the template microemulsion, imaging of the microemulsions containing the metal salt solution and alkaline precipitation agent were more challenging. Due to higher ionic strength of the aqueous phase within these microemulsions, aggregation of the micelles upon deposition on the substrate

took place and no reliable size determination was possible. The resulting TEM images can be found in Figure 4.6.4. Next to size evaluation with TEM, dynamic light scattering was conducted. Micelle diameters from both methods are listed in Table 4.3.1 and clearly show small micelles sizes in the range of 20 nm, which are suitable to confine the reaction space during co-precipitation. To investigate a potential change in plain micelle size, pH-dependent measurements were performed. The results can be found in Figure 4.6.5 but showed no significant difference in the investigated pH range and margin of error. Particle growth during co-precipitation is assumed to mainly take place within the reverse micelles, accomplished by stirring and a coalescence-exchange mechanism.[126]

Table 4.3.1: : Micelle diameters derived from TEM and DLS in nm. DLS measurements were performed at 50 °C.

Aqueous phase within the micelles	$Diameter_{TEM}$ (nm)	$Diameter_{DLS}$ (nm)
Template	13.1 ± 4.6	16
Metal salt solution	-	25
Alkaline precipitation agent	-	17

4.3.2 Layered Double Hydroxides

Figure 4.3.2a shows the powder X-ray diffraction (PXRD) patterns of the as-prepared conventional and microemulsion-assisted samples at pH 8.5. Diffraction patterns of the complete series are shown in Figure 4.6.6 and no differences with precipitation pH within the groups are observed.

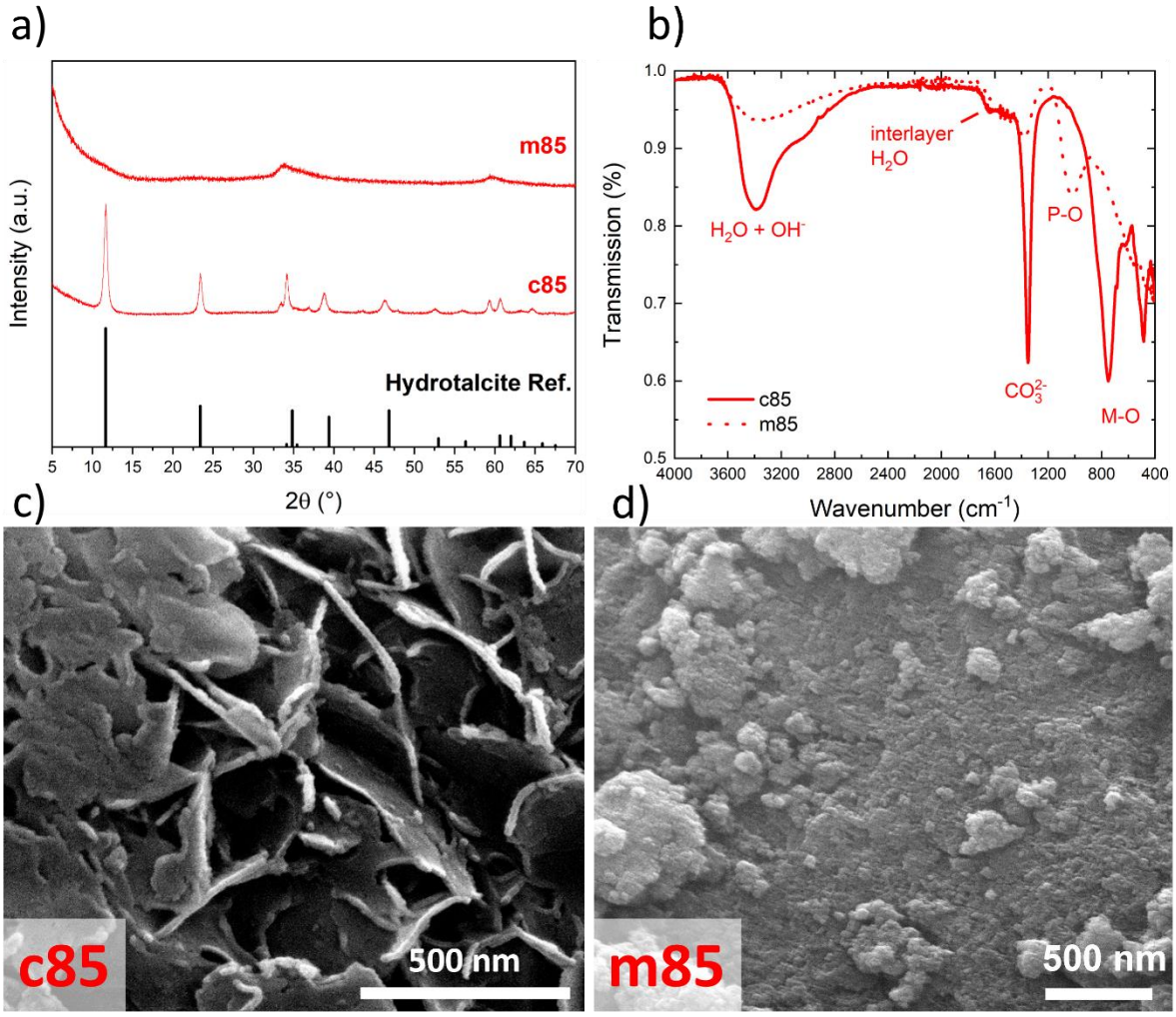

Figure 4.3.2: a) PXRD patterns of the conventionally prepared sample c85, the corresponding microemulsion-assisted sample m85 and the Hydrotalcite reference (ICSD. No. 6296[12]); b) IR spectra of c85 and m85; c) SEM micrograph of the conventionally prepared LDH c85; d) SEM micrograph of m85.

For the conventionally prepared samples a typical crystalline layered double hydroxide is obtained, and no crystalline by-phases are identified. The series from MACP on the other hand shows extremely broadened reflections. This can be caused by highly nano scaled particles, which consist of only a few brucite-like layers. Even though the main reflections of

the Hydrotalcite reference can barely be identified, theoretic calculations anticipated this behavior with decreasing slab size.[127] With just a few layers remaining, most of the reflections are not visible anymore and the formation of a nano scaled, almost X-ray amorphous layered double hydroxide phase is therefore assumed. Exemplary IR spectra for the samples prepared at pH 8.5 are shown in Figure 4.3.2b. IR spectra of the complete series and a reference spectrum of the surfactant Triton X-100 can be found in Figure 4.6.9 and Figure 4.6.10. Independent of the synthesis approach the spectra mainly exhibit the same features. The broad bands with a maximum at 3390 cm^{-1} is assigned to water and OH^-, interlayer water exhibits a band at around 1640 cm^{-1}.[128] At 1350 cm^{-1} the vibration of the interlayer carbonate is visible and the bands below 1000 cm^{-1} are assigned to M-O, M-O-M, O-M-O, and M-OH vibrations.[129] All bands of the conventional samples are significantly more pronounced than the bands of the MACP analogs, agreeing with the more crystalline nature of the former. For the MACP samples, the typical C-H stretching bands of the surfactant are absent indicating that the organic part has been effectively removed from the sample by washing and drying. An additional broad band at around 1015 cm^{-1} is observed. With the help of UV-Vis spectroscopy of m85 a minor phosphate contamination was identified (Table 4.6.1) and the band at 1015 cm^{-1} was therefore mainly assigned to the P-O vibration.[130] Additional minor carbonaceous residues cannot be completely excluded, given the slightly increased content of C and H. As the conventionally prepared LDHs do not exhibit this additional band, the phosphate is assumed to be brought in during synthesis using the microemulsion. The IR spectrum of the used pure Triton X-100 in Figure 4.6.10 shows the most prominent band at 1100 cm^{-1} with a broad shoulder in the wavenumber range of the additionally observed band in the MACP LDH spectra, making it a probable source for the phosphate. Partial intercalation of phosphates between the brucitic layers of the LDH was observed in literature,[131] which might explain the continuing presence of the phosphate after washing. Scanning electron microscopy micrographs of the corresponding samples in Figure 4.3.2c and d underline the findings from X-ray diffraction and IR spectroscopy. The conventional sample shows the expected anisotropic platelet morphology opposed by the aggregates of very small primary particles of m85 that appear rather isotropic at the resolution of the SEM. For all other precipitation pH, the SEM images are shown in Figure 4.6.7 and Figure 4.6.8. Conventional co-precipitation yielded anisotropic platelets in all cases. For the MACP LDHs, significantly smaller and more isotropic nanoparticles are formed and an elongation of the particles with increasing precipitation pH is observed. Elemental analysis proved a cobalt to iron ratio close to the desired ratio of 2 to 1 for all samples (Table 4.3.2).

Table 4.3.2: Fe to Co ratios and carbon plus hydrogen content for both sample series.

Prec. pH	Co/Fe ratio conv.	Co/Fe ratio MACP	C + H content (at%) conv.	C + H content (at%) MACP
7.5	2.10 ± 0.03	2.07 ± 0.06	7.4 ± 0.6	12.1 ± 0.6
8.0	2.12 ± 0.04	2.21 ± 0.08	7.2 ± 0.8	10.9 ± 0.6
8.5	2.16 ± 0.03	2.29 ± 0.17	7.1 ± 0.0	10.5 ± 0.9
9.0	2.27 ± 0.01	2.15 ± 0.05	7.4 ± 0.5	9.6 ± 0.3
9.5	2.29 ± 0.00	2.23 ± 0.05	7.2 ± 0.8	8.4 ± 1.2

Some samples exhibit a slightly larger ratio, which can be explained by the hygroscopic nature of the iron nitrate precursor, leading to weighing errors and too small amounts of iron in the metal salt solution. CHN analysis showed no nitrogen indicating the complete removal of the nitrate counter ions by the washing procedure. The sample series prepared by microemulsion-assisted co-precipitation shows a somewhat higher content of carbon and hydrogen implying incomplete removal of the surfactant. On the other hand, IR spectroscopy does not show any bands assigned to the surfactant, pointing towards minor amounts or a changed adsorption behavior due to the nano structuring of the MACP samples.

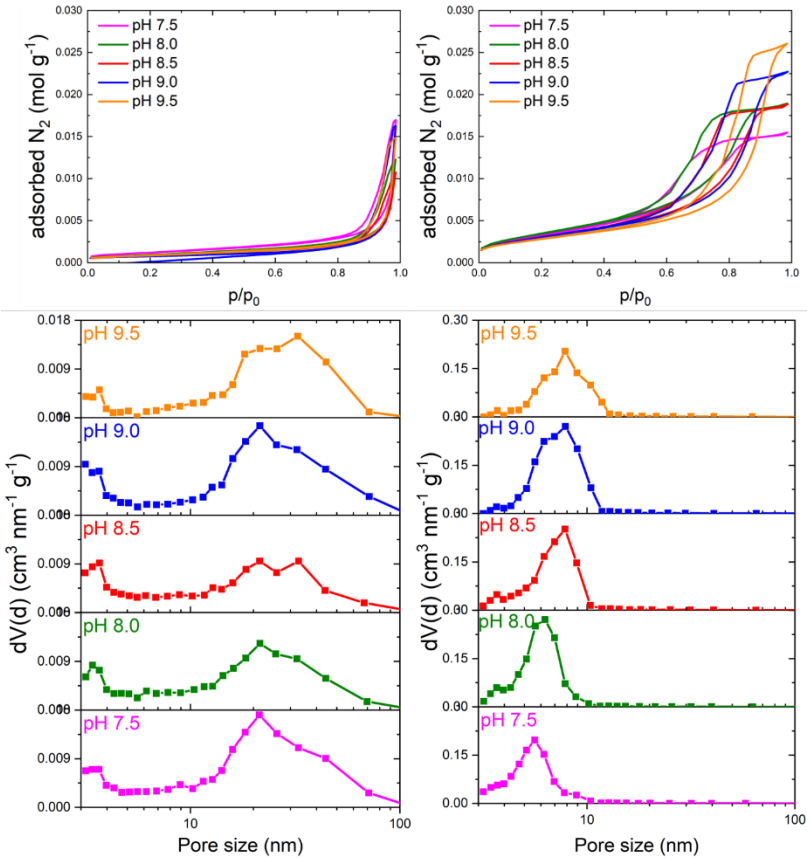

Figure 4.3.3: Top: N_2 adsorption/desorption isotherms of the conventionally prepared LDHs (left) and microemulsion-assisted LDHs (right). Bottom: Pore size distributions of the c (left) and m samples (right). Note the different y axis scaling.

The textural properties were analyzed by N_2 physisorption experiments and BET theory. Figure 4.3.3 depicts the adsorption desorption isotherms as well as the pore size distribution for both series. The micropore volume and total pore volume can be found in the supporting information (Table 4.6.2 and Table 4.6.3). As already seen in PXRD, IR, and SEM, enormous differences in terms of adsorption capacity and hysteresis shape are encountered. For the conventional samples no trend with precipitation pH in the type IV isotherms with an H3 hysteresis loop is observed. This behavior is typical for mesoporous solids with slit shaped pores and nonuniform size or shape, agreeing with the platelet morphology observed in SEM. On the contrary, the type IV isotherms of the series derived from MACP exhibit a clear trend with synthesis pH. The H2-like hysteresis as well as the pore size distribution increases with increasing pH.[132] Surface areas for the microemulsion-based LDHs are found to be up to 4 times higher than those of their conventionally prepared counterparts, congruent with the nano sized particles found by PXRD and microscopy. Nevertheless, surface areas do not show any trend with precipitation pH (Table 4.3.3). Instead, a trend of the pore size distribution maximum of the MACP samples as determined by the BJH method was observed. The pores

are substantially smaller than in the conventionally prepared LDHs and fall into a regime between 5.7 and 10.4 nm. In this size range, a steady increase with increasing co-precipitation pH is observed.

Figure 4.3.4b shows a clear and linear relationship between particle properties of the MACP LDHs, in this case the maximum of the pore size distribution, (open red symbols) and the synthesis parameter pH, by which the MACP LDH mesostructure can be controlled. The pH during synthesis influences the coalescence of the micelles in the microemulsion. Higher pH means a higher ionic strength and with that presumably more exchange due to increasing instability of the reverse micelles,[133] leading to stronger growth of the particles and apparently widening of the inter-particle voids. For the conventionally prepared LDHs (Figure 4.3.4a, closed red symbols) no such control was provided, consequently no trend of mesostructure with precipitation pH is observed.

Table 4.3.3: Surface areas and pore size distribution maximum of both sample series.

Prec. pH	Surface Area ($m^2 g^{-1}$) conv.	Surface Area ($m^2 g^{-1}$) MACP	Pore Size Distribution Max. (nm) conv.	Pore Size Distribution Max. (nm) MACP
7.5	97	281	21.3	5.7
8.0	75	295	21.5	6.9
8.5	69	255	32.8	7.9
9.0	57	255	21.4	9.0
9.5	69	233	32.5	10.4

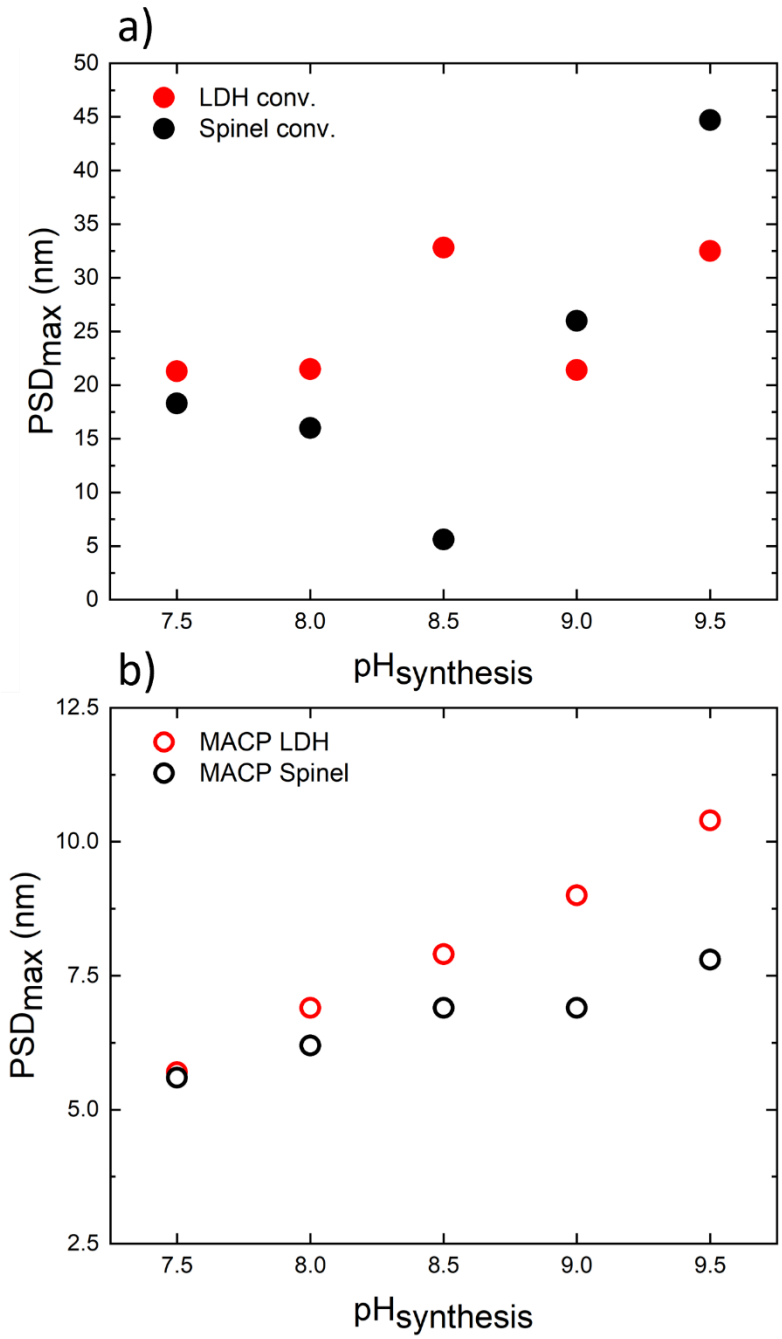

Figure 4.3.4: The maximum of the pore size distribution PSD_{max} of all LDHs and spinels for all $pH_{synthesis}$. a) LDHs and spinels from conventional co-precipitation, b) MACP LDHs and corresponding spinels. Note the different scaling of the y axis.

For thermal transformation of the LDHs into spinels, a suited calcination temperature had to be defined. Therefore, thermogravimetric analysis was performed and is shown exemplary in Figure 4.3.5. In all cases decomposition takes place in two steps, namely dehydroxylation and decarbonization and is completed below 400 °C, which was therefore chosen as calcination temperature.[34] Above 900 °C, the thermal reduction of Co^{III} oxidic species to $Co^{II}O$ can be observed. TGA for all samples is shown in Figure 4.6.11.

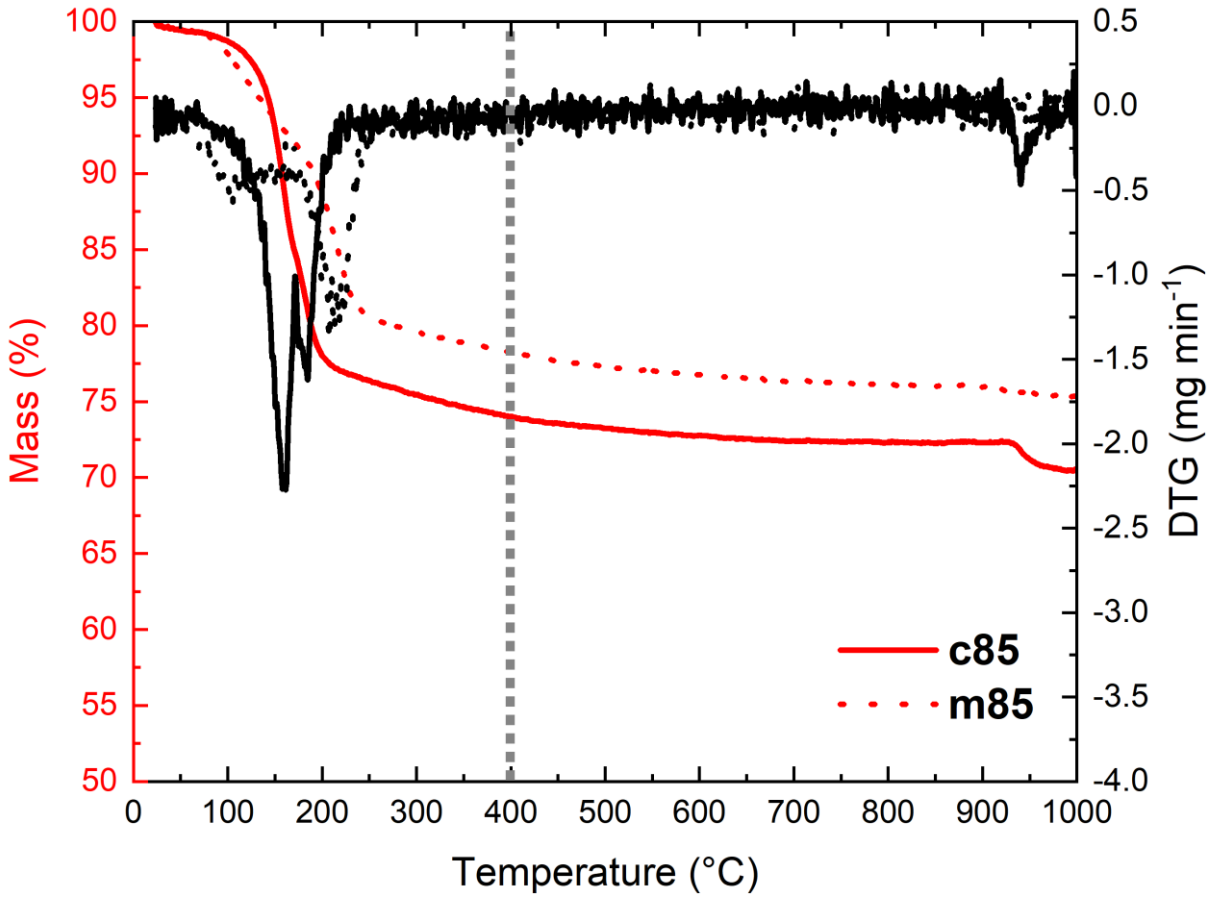

Figure 4.3.5: Thermogravimetric analysis of c85 and m85. The grey dotted line highlights the chosen calcination temperature of 400 °C.

4.3.3 Spinels

Figure 4.3.6 shows the PXRD patterns of the spinels derived from conventional co-precipitation and MACP exemplarily for a synthesis at pH 8.5 for the LDH precursor as well as the corresponding SEM micrographs. The diffraction patterns and SEM micrographs for the whole two series are depicted in Figure 4.6.12 - Figure 4.6.14.

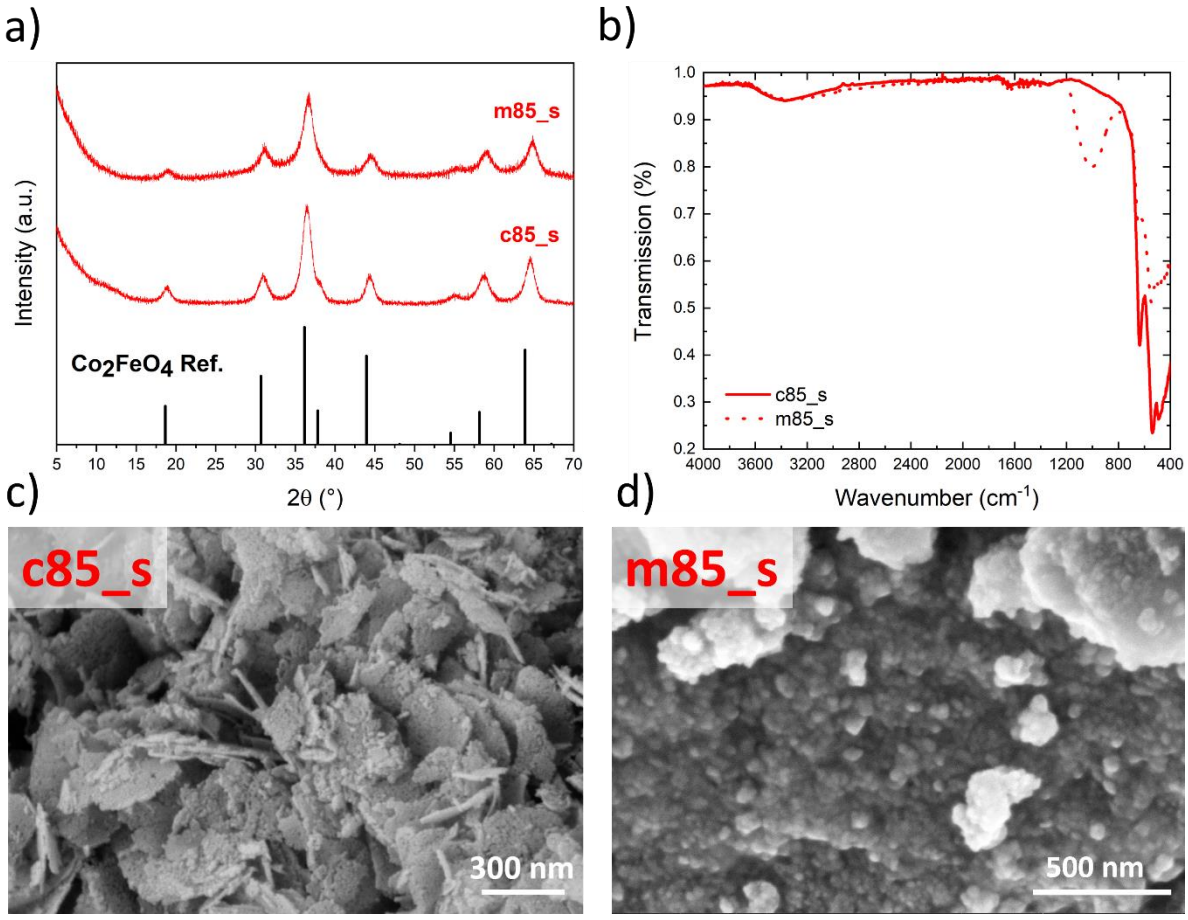

Figure 4.3.6: a) PXRD patterns of the calcined samples c85_s and m85_s; b) IR spectra of c85_s and m85_s; c) SEM micrograph of c85_s and d) m85_s.

The pronounced difference found for the as-prepared LDHs in the PXRD patterns is not visible anymore. The crystallinity of both samples is not very high, but the typical reflections of the spinel structure can be clearly observed, and no crystalline by-phases are visible. Previous work showed a nano-scale segregation of the oxides into two structurally very similar spinels, a cobalt richer and an iron richer spinel, as implied by the cobalt iron oxygen phase diagram,[88] which cannot be discriminated here due the broad XRD peaks. The small coherently scattering domains lead to the similar diffraction patterns.[109] The IR spectra of the

conventionally prepared spinels exhibit only the expected bands at 639 cm^{-1} and 538 cm^{-1}, which are assigned to M-O vibrations.[134] The spinels derived from LDHs prepared by MACP show a distinct band at around 1010 cm^{-1}, which again is assigned to phosphate introduced during synthesis of the LDH and is stable against thermal decomposition at the applied temperature.[135] As described before, the organic solvent and surfactant used for the synthesis are expected to be removed during washing and possible minor residues to be decomposed after thermal treatment at 400 °C for 3 h.[136] All IR spectra are shown in Figure 4.6.15. Electron microscopy showed the retainment of the platelet morphology for the samples derived from conventional co-precipitation. Additionally, a visible pore formation due to decomposition of the anions and emission of water in the precursor has been observed in our previous work by TEM for a spinel sample derived from a conventional LDH with the same composition and precipitation pH of 8.5, which can be seen by SEM as formation of holey platelets.[109] Moreover, the nano structuring of the spinels derived from MACP LDHs is retained.

For the LDHs prepared from MACP, a distinct trend between precipitation pH and pore size was found. Therefore, N_2 physisorption experiments were performed for the calcined samples to investigate the pore size distribution and surface area after transformation to the spinel phase (Figure 4.3.7). For the conventional spinels, pore size distribution evaluation using the BJH method yielded broad maxima for both interparticle and intraparticle pores, which are hard to differentiate. Due to the pore formation, the surface areas of the conventional spinels are higher than those of the corresponding LDHs in most cases. The maximum of the pore size distribution and the surface areas are listed in Table 4.3.4. For the samples from MACP, the nanosized particles seem to be preserved upon calcination based on the resolution of the SEM images. Pore formation is not visible due to the small particle size. The surface area after calcination for these samples is cut in half except for m75_s, which exhibits a smaller decrease in surface area. The decrease may seem contradicting, as the surface area increased for the conventional samples, but the small particle size of the as-prepared MACP LDH makes them more prone towards sintering. Interestingly, the general trend in pore size distribution maxima is retained upon calcination (see Figure 4.3.4), meaning that the MACP can be used not only for the mesostructure control of the LDHs, but the LDHs can also be used as templates for the controlled synthesis and creation of unusual morphologies and mesostructure of the resulting spinel materials, including control over pore size.

Summarizing the materials synthesis and characterization part, two sample series of LDHs and spinels were synthesized by conventional co-precipitation and MACP and characterized

thoroughly. In the case of the MACP series, highly nano-sized samples were formed, whose pore size scaled with the pH value of the synthesis. For the conventionally prepared samples, no such trend was found. In contrast to the mesostructure, the crystallinity of both spinel sample series was very similar. The linear dependance of the pore size maximum on the pH value of the synthesis was maintained upon spinel formation from the MACP LDH precursors, demonstrating the tunability of the mesostructure by this synthesis parameter.

Table 4.3.4: Surface areas and pore size distribution maximum of both spinel sample series.

Prec. pH	Surface Area ($m^2 g^{-1}$) conv.	Surface Area ($m^2 g^{-1}$) MACP	Pore Size Distribution Max. (nm) conv.	Pore Size Distribution Max. (nm) MACP
7.5	96	216	18.3	5.6
8.0	88	130	16.0	6.2
8.5	89	153	5.6	6.9
9.0	86	136	26.0	6.9
9.5	83	163	44.7	7.8

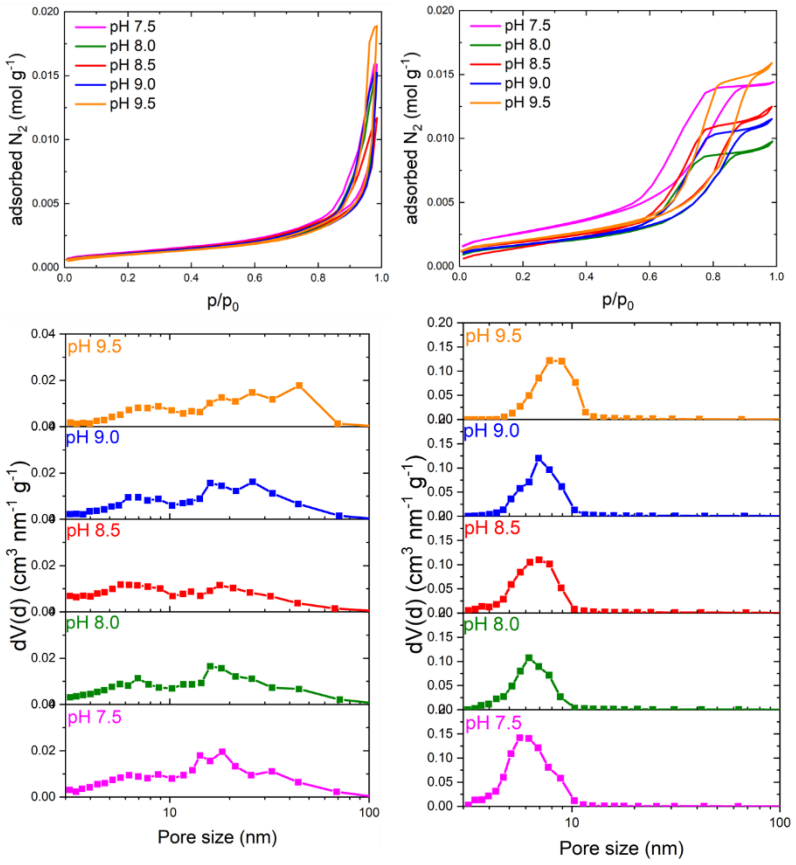

Figure 4.3.7: Top: N_2 adsorption/desorption isotherms of the conventionally prepared spinels (left) and microemulsion-assisted spinels (right). Bottom: Pore size distributions of the c (left) and m samples (right). Note the different y axis scaling.

4.3.4 Electrocatalytic Activity towards Oxygen Evolution

The above-described control of pore size makes the two sample series a suitable materials platform to study the effect of mesostructural confinement in electrocatalysis. Therefore, we, here, take advantage of the achieved set of LDH and spinel materials by assessing their catalytic activity towards OER under alkaline conditions.

Exemplary linear sweep voltammograms (LSVs) in aqueous 1 M KOH solution are displayed in Figure 4.3.8a for catalyst materials precipitated at pH 8.5 (complete series shown in Figure 4.6.16). Both sets of LDH samples exhibit low overpotentials as expected from literature.[26b] The two spinel series differ significantly with an increase in activity as a result of calcination for the MACP sample, but a very low activity of the conventionally prepared spinel samples. This performance difference of the spinels obtained at pH 8.5 was recently investigated in great detail and related to the favorable in-situ formation of Co^{3+}-rich domains in case of the MACP-derived catalyst.[137] Here, we focus on the performance trends with variation of the synthesis pH value of the three series of electrocatalytically active samples, i.e. the conventional and MACP-LDH materials and the MACP-LDH-derived spinels. The overpotentials at 10 mA cm^{-2} are shown as a function of the synthesis pH values in Figure 4.3.8b and the catalyst stabilities in chronopotentiometric tests for 2 h in Figure 4.3.8c (whole series and details in Figure 4.6.20 and Figure 4.6.21). The overpotentials exhibit no clear trends with the synthesis pH (see SI for detailed discussion), most of the materials exhibit similar overpotentials between 340 and 370 mV with lowest overpotentials for MACP spinels at high synthesis pH values. Yet, the plot exhibits a noteworthy peculiarity: three significantly higher overpotentials for MACP LDH samples synthesized at pH values ≥ 8.5. Figure 4.3.8d indicates the diminished electrocatalytic activity of these three MACP LDHs to correlate with maxima of the pore size distribution between 7.9 and 10.4 nm, while the other samples with respective pore sizes below 7.9 nm cluster in the range of lower overpotentials.

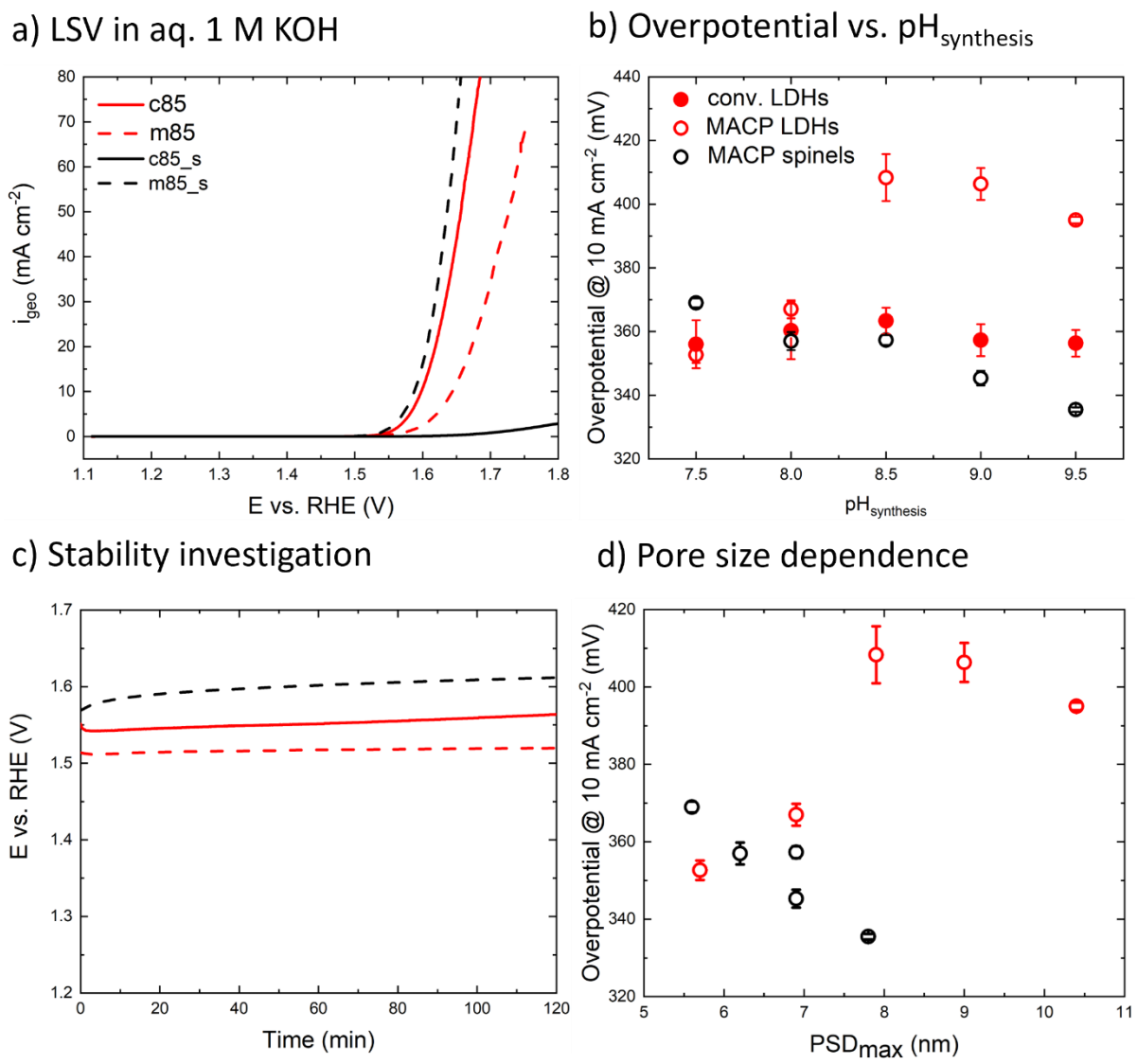

Figure 4.3.8: a) Linear sweep voltammograms in 1 M KOH, 1 mV s^{-1} @ 1600 rpm for the LDHs synthesized at pH 8.5 and their corresponding spinels. b) Overpotential at 10 mA cm^{-2} for all LDHs and MACP spinels. c) Chronopotentiometry in 1 M KOH for c85 (solid red line), m85 (dashed red line) and m85_s (dashed black line). d) Correlation of overpotential with PSD_{max} for the MACP LDHs (open red symbols) and MACP spinels (open black symbols).

To first explain the comparable electrocatalytic activity of the investigated LDH and spinel samples, the cyclic voltammograms (CVs) of the electrochemical pre-conditioning (Figure 4.3.9) are analyzed. Prior to the LSV measurements, these 50 CVs were always recorded in a potential range more negative than the OER onset and including the Co redox range, to obtain reproducible and reliable results, which was achieved as demonstrated by the sufficiently small error bars (*e.g.*, Figure 4.3.8b).

These pre-conditioning CVs (Figure 4.3.9) show major differences in current, peak positions and extents for different samples for the initial cycles but aligning CV shapes towards the 50th

cycle. The first CVs exhibit pronounced anodic conversion signals relating to the oxidative transformation to higher-oxidized cobalt oxide species.[138] This electrochemical conversion reaction is mostly irreversible as 5 to 8 times more charge is transferred during the anodic half-cycle compared to the cathodic part. In consequence, the surface or rather surface-near region changes in (mean) oxidation state during the initial cycles and may alter in phase and composition, as was already found for the MACP spinel prepared at pH 8.5 during OER by Haase et al.[137] For the 50th CV, the ratio of anodic and cathodic charge approaches 1, indicating that the respective electrochemically active material fraction can now be transformed reversibly. The similarity in electrochemical response at this stage implies that the surface properties are quite similar for all samples after pre-conditioning due to the cyclovoltammetrically induced changes, explaining the small range of observed OER-overpotentials.

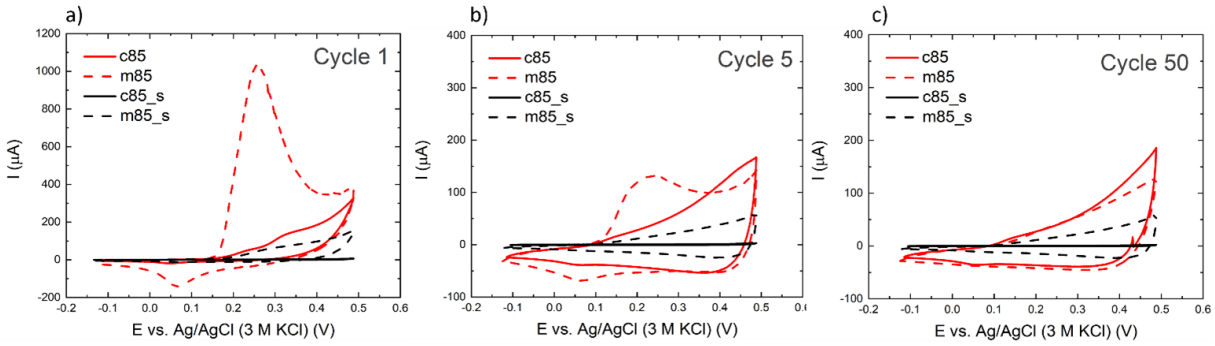

Figure 4.3.9: Pre-conditioning cyclovoltammograms of the samples synthesized at pH 8.5. a) First cycle, b) fifth cycle and c) 50th cycle. Note the difference in scaling of the y axis in a).

Figure 4.3.10a displays the ratio of anodic charge of the 50th CV in regard of the first anodic half-cycle for the microemulsion-templated materials. It is clearly seen that the charge relating to reversible transformation of the MACP-LDH-surface is small (12% – 15%) compared to the initial conversion charge corresponding also to irreversible conversion. This indicates large changes compared to the surface-near region of the MACP spinel samples where the reversible transformation charge makes up 36% to 89% of the first anodic CV half-cycle. Thereby, the two samples exhibiting the lowest overpotential (MACP spinels with $pH_{synthesis}$ = 9.0; 9.5) show a lower ratio of reversible charge to initial anodic charge than the other MACP spinel samples, indication for a possible stronger transformation of the as-synthesized state. Besides, the MACP spinels show also higher reversible anodic charge per BET-surface-area with increasing synthesis pH value (and correspondingly increasing pore size) as seen in

Figure 4.3.10c. Accordingly, the depth of the surface layer which can be anodically transformed and cathodically re-transformed is larger (for a specific scan rate).[139]

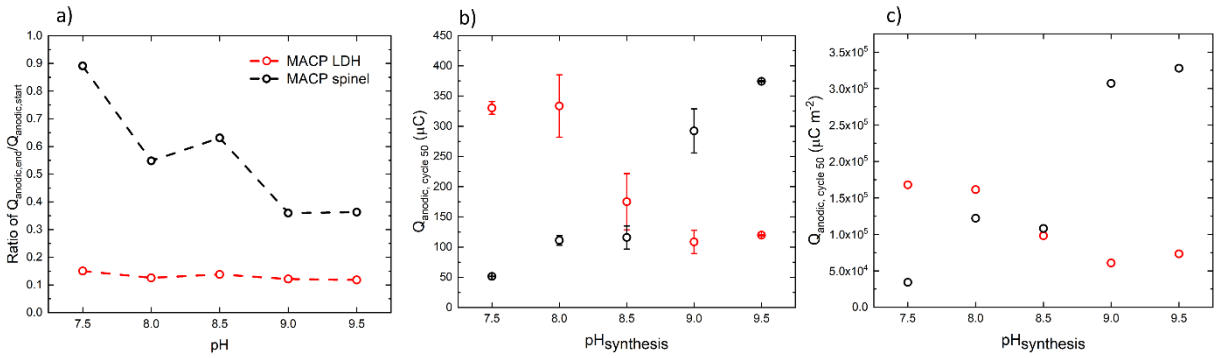

Figure 4.3.10: Ratio of Q_{anodic} at the end to Q_{anodic} at the start of the pre-conditioning (a), Q_{anodic} of the 50th in µC (b), and µC m^{-2} (c). The surface area was derived from N_2 physisorption measurements.

Conway and Liu[140] reported that OER kinetics are determined by the density of electrochemically oxidized Co sites at or near the surface which form intermediate states with adsorbed or rather discharged O and OH species. They respectively associated the potential-dependent pseudo-capacitance of cobalt spinel films as a measure of such (re-)chargeable surface-near regions. Recent findings describe the active surface of (initially) crystalline Co_3O_4 as a sub-nm thick shell which reversibly transforms into an X-ray amorphous $CoO_x(OH)_y$,[141] and show that lattice oxygen contributes to evolved O_2.[142] The consequently indicated 3-dimensionality of the surface-near oxide region involved in the OER was further confirmed by *operando*-XRD.[143] Haase et al. also found a higher amount of transformed surface for the MACP spinel (pH 8.5) compared to the inactive conventional spinel.[137] In this context, the increased depth of the anodically and cathodically active surface-near region observed for the more OER-active MACP spinels (Figure 4.3.10) may explain the lower overpotentials.

However, there is no clear trend observed for the MACP LDHs (Figure 4.3.10). Due to the different structure and with that less structural stability in regard to applied potential,[72] the LDHs show significantly higher amount of irreversible transformation during the initial cycling of the pre-conditioning. The changes of the active compared to the as-synthesized state are more significant and, thus, the materials properties and phases are less well-known. Furthermore, the pore morphology and size distribution may affect the material transformation and complicate interpretation due to ohmic drop within pores, altered mass transport conditions, as well as wetting properties.[144] However, considering the three MACP

LDH samples synthesized at pH ≥ 8.5 which exhibit significantly higher overpotentials, it seems likely that these effects cannot fully account for the diminished OER-activity due to the similar pre-conditioning behaviour of all LDH samples. As seen in Figure 4.3.10, the ratio of anodic charge of the 50th and first pre-conditioning CVs as well as the reversible anodic charge of the 50th CV differs only minorly within the series of MACP LDHs.

Therefore, electrochemical impedance spectroscopy (EIS) was employed to better understand the considerably higher overpotentials of the three MACP LDH samples synthesized at pH ≥ 8.5. Figure 4.3.11 compares the Tafel slopes and EIS results for the conventional and the MACP LDHs as well as the MACP spinel sample synthesized at pH 8.5. The analysis demonstrates that the higher overpotential of the MACP LDH is accompanied by a considerably increased charge transfer resistance (R_3 in Figure 4.3.11c) and a higher Tafel slope. Both suggest a change in the OER mechanism concerning the rate-determining step. The important role of the R_3 resistance is further emphasized by increased values for those three samples in the MACP LDH series exhibiting higher overpotentials ($pH_{Synthesis} \geq 8.5$, Figure 4.6.23b).

As reported previously,[145] EIS data of cobalt oxide/hydroxide surfaces where OER proceeds allows to distinguish several sub-processes of the electrocatalytic reaction. This is due to changing oxidation states of accessible cobalt sites when forming intermediates, which can be described as pseudo-capacitive (dis-)charging of the oxide/hydroxide film through Faradaic reactions with hydroxide and oxygen species. So, notably different time constants are present and, hence, allow to separate three charge transfer resistances parallel to double layer or pseudo-capacitors (inset, Figure 4.3.11b), because of the order-of-magnitude-different capacitance values. In the investigated frequency range (40 kHz – 2 Hz), the LDH samples exhibit a fourth signal for low frequencies which may be related to interlayer mass transport not described by semi-infinite diffusion.[146]

Accordingly, the equivalent circuit resistor R1 in parallel to the double layer capacitor C1 is assigned to the OH^- association step, which charges the pseudo-capacitor C2 with R2 representing the subsequent charge-transfer process of the reaction mechanism. To this end, R3 corresponds to the electrochemical step where oxygen is released. This assignment was further supported by recording EIS spectra in oxygen-purged and argon-purged KOH solution where the oxygen concentration in the electrolyte mostly affected the R3 resistance value (see SI for detailed discussion).

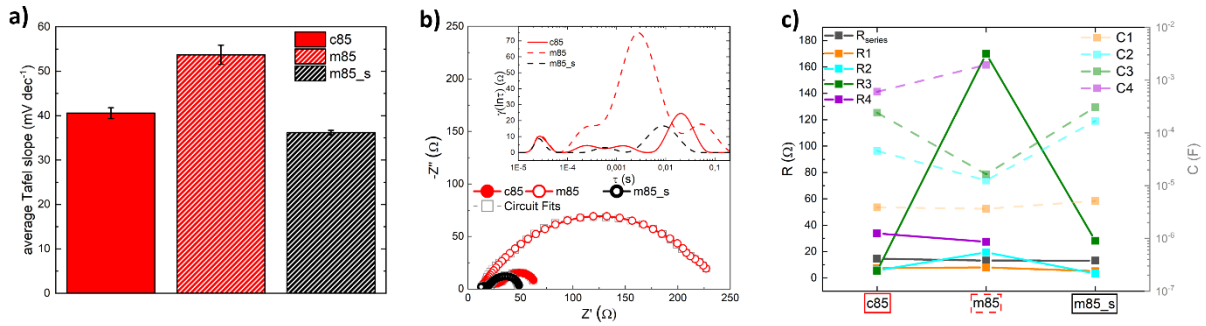

Figure 4.3.11: a) Tafel slopes from a 50 mV region where the charge transfer coefficient alpha is constant. b) Electrochemical impedance data in complex plane representation (Nyquist plot) and corresponding distribution functions of relaxation times γ(τ) (DRT, inset in b) for cyclovoltammetrically pre-conditioned LDHs and the MACP spinel synthesized at pH 8.5, obtained at 1.60 V vs. RHE and c) resistance and capacitance values determined from DRT analysis. The results for the complete conventional and MACP LDHs series as well the whole MACP spinel series can be found in Figure 4.6.23.

Relating the EIS investigation to the structural and morphological properties of the MACP LDH series, it is apparent that the increased resistances for the oxygen release step at $pH_{Synthesis} \geq 8.5$ are observed for bigger pore sizes with a threshold of 7.9 nm (Figure 4.3.8d) before the pre-conditioning. Thus, we hypothesize the formation of oxygen gas bubbles in these pores of the MACP LDHs to cause the diminished electrocatalytic activity, with the above-mentioned pore size being the lower limit for this phenomenon.

The evolution of gas bubbles inside the pores may not occur, if the pores are too small the critical radius for bubble formation cannot be met. For H_2 gas bubbles, the radius of curvature for nucleation was found to be around 5 nm on a Pt nanoelectrode, being in the expected order of magnitude.[147] The concentration profiles of dissolved oxygen in the pores depend on the diffusion characteristics transporting oxygen away from the electrode. For large enough pores, gas bubbles may form in the pores and block the connection to the bulk electrolyte. Thus, dissolved oxygen concentration will build-up in the pores leading to an increased charge transfer resistance for the oxygen release step. The mass transport of produced oxygen from the catalyst to the bulk electrolyte was also identified to limit the electrocatalytic activity for single cobalt spinel nanoparticles impacting an inert target electrode.[148]

In sum, the presented synthesis route for cobalt iron LDHs and spinels with tailored mesostructure allowed a detailed investigation of the effects on the electrocatalytic activity for oxygen evolution. The cyclovoltammetric pre-conditioning treatment, allowing for reproducibility and stable electrocatalytic performance, was found to cause material transformations in the near-surface regions. This leads to alignment of the electrocatalytic OER-activity whereas the amount of reversibly electrochemical transformable material

fraction varies. Thus, relatively comparable overpotentials and highest activities can be explained but another phenomenon must account for the significantly higher overpotentials observed for three samples of the MACP LDH series. Based on electrochemical impedance spectroscopy in conjunction with detailed mesostructure characterization, we suggest the formation of gas bubbles within larger pores as explanation.

4.3.5 Conclusion

Two series of cobalt iron layered double hydroxides and their corresponding Co_2FeO_4 spinels were synthesized and used to study the effect of mesostructure on OER performance. The first series was synthesized via conventional co-precipitation in aqueous medium, varying the pH during synthesis in 0.5 pH steps. The second series was derived from microemulsion-assisted co-precipitation, confining the reaction space within reverse micelles, with otherwise equal synthesis conditions. The systematic variation of the synthesis pH did not lead to significant differences in properties of the LDHs from conventional co-precipitation such as composition, crystallinity, surface area, pore size or their platelet morphology. The spinels formed upon thermal treatment also exhibited comparable characteristics. For the more isotropic and nano sized MACP LDHs on the other hand, a systematic increase of the comparably small pore size with increasing synthesis pH was observed, which was preserved after thermally forming the corresponding spinels. Based on this synthesis parameter-mesostructure relationship, it was possible to tailor the pore size of the as-synthesized LDHs and spinels likely due to the modified exchange between the reverse micelles in the reaction mixture with varying the precipitation pH.

The possibility of tuning the pore size of such materials qualified them for the investigation of confinement effects in the electrochemical oxygen evolution reaction. For both LDH series low overpotentials and satisfying stability were found as well as for the MACP spinel series. The conventionally prepared cobalt iron spinels on the other hand showed extremely diminished activity. The cause for this extreme difference in activity was thoroughly investigated for one example from the series elsewhere.[137] For the conventionally prepared samples, no trend of overpotential with mesostructural features was evident. However, the MACP LDHs and corresponding spinels showed a clear effect of the pore size on the overpotential. The MACP LDHs synthesized at pH $\geq$ 8.5 have pore sizes larger than 7.8 nm and with that the largest pore sizes of the MACP derived samples. At the same time, they

exhibit the highest overpotentials. All other samples from these two series exhibit smaller pore sizes and cluster in the range of lower overpotential.

Both observations, the surprisingly similar performance of all samples with smaller pores, and the diminished activity of those with lager pores can be explained by the electrochemical results. The performed pre-conditioning in the pre-OER region showed gradually changing CV shapes, which aligned towards the 50^{th} cycle, indicating similar surface properties despite the different starting states of the as-synthesized catalysts. Additionally, the highly active MACP spinels showed the highest portion of reversibly transforming catalyst material during cycling and can be associated with the largest extent of electrochemical changes during pre-conditioning. In light of literature reports on the in-situ formation of highly active near-surface states, this can explain the lowest overpotential observed for these samples by the highest number of active species.[141, 143] The striking high overpotential for the MACP LDHs synthesized at pH ≥ 8.5 was investigated by EIS, revealing an increased charge transfer resistance and a higher Tafel slope for these samples, hinting towards a change in OER mechanism concerning the rate determining step. For all samples with diminished activity, the R3 resistance, which we assume to correspond to the oxygen release step, was found to be increased. Interestingly, only samples with pore sizes larger than 7.8 nm (before pre-conditioning) show the increased resistance R3, suggesting that gas bubble formation within these larger pores is possible, which leads to the observed increased overpotentials. The gas bubbles hinder the transport of oxygen into the bulk electrolyte and with that reduce the activity of the catalyst. If pores are smaller than the observed threshold, however, gas bubbles may not form because the critical radius for bubble formation is not met.

4.4 Experimental Section

4.4.1 Synthesis

All syntheses of layered double hydroxides were carried out in an automatic lab reactor system (*OptiMax 1001, Mettler Toledo*). The aqueous conventional, i.e. without microemulsion, co-precipitation was adapted from a recently published paper by our group.[109] 125 mL metal salt solution containing 0.266 mol L^{-1} $Fe(NO_3)_3 \cdot 9H_2O$ (≥ 98%, Sigma Aldrich), 0.533 mol L^{-1} $Co(NO_3)_2 \cdot 6H_2O$ (≥ 98%, Carl Roth), and the precipitation agent consisting of 0.6 mol L^{-1} NaOH (98.5%, VWR) and 0.09 mol L^{-1} Na_2CO_3 (≥99.5%, Carl Roth) were simultaneously dosed into the reactor prefilled with 200 mL of distilled water over 1 h. The metal salt solution was dosed continuously through gravimetric control. The constant pH (pH 7.5 to .5, 0.5 pH unit steps) was controlled by an InLab Semi-Micro-L pH electrode and kept at a fixed value by automatically dosing the precipitation agent. pH 7.5 was chosen as the lowest co-precipitation pH to ensure complete precipitation of Fe^{3+}, which requires at least slightly alkaline conditions. The temperature was held at 50 °C. Afterwards, the precipitate was aged for 1 h at 50 °C without further pH control. Thereupon the reactor was cooled to room temperature, the dispersion was washed repeatedly with distilled water until the conductivity of the supernatant was below 100 µm S and subsequently dried for at least 12 h at 80 °C in static air.

The microemulsion-assisted co-precipitation was done like the procedure described above. The aqueous phases, more precisely the prefilled water template, the metal salt solution and the precipitation agent were each integrated into a water-in-oil microemulsion. 50 mL of a 0.133 mol L^{-1} $Fe(NO_3)_3 \cdot 9H_2O$ and 0.266 mol L^{-1} $Co(NO_3)_2 \cdot 6H_2O$ solution were used as the metal salt solution, the alkaline precipitation agent contained 0.15 mol L^{-1} NaOH and 0.0225 mol L^{-1} Na_2CO_3. For preparation of the microemulsions Triton X-100 (≥ 99%, Carl Roth), 1-hexanol (≥ 98%, Carl Roth), cyclohexane (p.a., Fisher Scientific) and the corresponding aqueous phase were mixed and stirred until a clear solution formed, indicating stable microemulsions. The composition of the microemulsion resulting in 8.7% aqueous phase by volume was adapted from literature.[125] Afterwards co-precipitation and aging were carried out as described above. To remove the surfactant the dispersion was washed with acetone for five times and with ethanol for ten times. Subsequently, the precipitate was dried for at least 12 h at 80 °C in static air.

The cobalt iron spinels were obtained by calcination at 400 °C (2 K min^{-1}) for 3 h in a muffle furnace (*Nabertherm LE 6/11/B150*).

4.4.2 Characterization

Powder X-Ray Diffraction (PXRD) was performed with a Bruker D8 Advance diffractometer with a Cu X-ray source in Bragg-Brentano geometry, using a LynxEye XE-T detector. The samples were dispersed in ethanol on a PMMA sample holder and diffraction patterns were recorded in the angular range from 5 ° to 90 ° 2θ with a step size of 0.01 ° and a counting time of 1.5 s. During the measurement, the sample holder was slowly rotated.

Scanning electron microscopy (SEM) was conducted with an Apreo S LoVac (Thermo Fisher Scientific). Prior to the measurements, the samples were sputtered with Pt/Au.

Scanning transmission electron microscopy (STEM) measurements of the dried-out micelles were conducted on a JEOL JEM-2800 electron microscope. Used electron source is a Schottky electron gun, working at 200 kV acceleration voltage. The system exhibits a point-to-point resolution of 0.14 nm. Microemulsions were directly drop cast on a lacey carbon Cu grid from PLANO and treated with a mild plasma for STEM measurements. Plasma treatment of the prepared TEM grids was conducted on a Model 1070 nanoclean system at a power of 25 W in a 25:75 Oxygen-Argon mixture at a pressure of 30 mbar for 15 s.

UV-Vis spectroscopy was performed with a Varian Cary 300 UV-Vis.

The ratio of the incorporated metal cations was determined by atomic absorption spectroscopy (Thermo Electron Corporation, M-Series) of the as-prepared precursors. The carbon and hydrogen contents were determined by CHNS analysis. For each sample twofold measurements were performed.

Thermogravimetric analysis (TGA) of the as-prepared precursors was carried out with a NETZSCH STA 449f F3 Jupiter (NETSCH GmbH, Germany). The mass loss was recorded as a function of temperature with a linear heating rate of $\beta = 5$ K min^{-1} in a temperature range from 30 °C to 1000 °C and a gas stream of O_2 (21 mL min^{-1}) and Ar (79 mL min^{-1}).

BET surface areas were measured using N_2 physisorption at 77 K with a NOVA3000 (Quantachrome GmbH, Germany). Prior to the measurements, the samples were degassed at 80 °C in vacuum for 2 h. Total pore volume and the pore size distribution were determined by

applying the BJH method, which was applied to the desorption branch of the isotherm. Because the BJH analysis may underestimate the contribution of narrow mesopores, alternative evaluation using the NLDFT (non-local density functional theory) method was also used and found to qualitatively confirm the observed trends with variation in the absolute pore diameters around the value determined by BJH depending on the model used. We therefore regard the observed trend as reliable and base our discussion on the BJH method. The micropore volume was determined with the method by Horvath and Kawazoe.[149]

IR spectra were recorded with a *Bruker Platinum ATR Diamond* spectrometer with a spectral range of 400 cm^{-1}-4000 cm^{-1} with a step size of 0.1 cm^{-1}.

Dynamic light scattering was performed with a *Zetasizer Nano ZS (Malvern Instruments Ltd.)*. For each microemulsion threefold consecutive measurements were performed at a scattering angle of 173° with a He-Ne laser with a wavelength of 633 nm. The stated results are the mean output values for three consecutive measurements of the same sample, which have been rounded to a full nanometer value.

4.4.3 Catalytic Testing

Electrocatalytic activity measurements were performed with a three-electrode setup in 1 M KOH. A counter electrode, an Ag/AgCl/3M KCl reference electrode and a glassy carbon electrode loaded with the catalyst was used as the working electrode. The setup was connected to a PalmSens4 potentiostat. For preparation of the ink 2.5 mg catalyst, 250 µL H_2O and 250 µL Ethanol were mixed and sonicated for 15 min. The glassy carbon electrode with a geometric area of 0.0707 cm^2 was polished, loaded with 1.4 µL of ink, and dried for 1 h. In the beginning of the measurement OCP determination for 60 s was performed, followed by an initial cycling from OCP to 1.5 V vs. RHE with 100 mV s^{-1} for 50 cycles. After that electrochemical impedance spectroscopy at OCP was performed. Cyclic voltammetry was done from 1.1 V to 1.8 V with 5 mV s^{-1} at 1600 rpm. For determination of the activity linear sweep voltammograms in the range of 1.1 V to 1.8 V vs. RHE with 1 mV s^{-1} were performed. The measured current density i was normalized to the geometric area of the glassy carbon electrode via

$$i_{geo}(mAcm^{-2}) = {(I(\mu A)/1000)}/{0.0707cm^2}$$

Electrochemical Impedance spectra were obtained at 1.60 V *vs.* RHE in the frequency range from 200 kHz to 1 Hz using a sine wave amplitude of 10 mV. The data were recorded after the LSV for OER investigation at 1 mV/s after an equilibration time of 60 s. Data checking and processing was performed using RelaxIS 3 (rhd instruments), applying a linear Kramers-Kronig test and a Z-HIT algorithm (40 kHz to 2 Hz range). Determination of the distribution of relaxation times (DRT)[150] was based on radial basis functions (RBF) with a discretization factor of 10^{-4} and terms proportional to the second derivative of RBF included as extra penalty in the sum of squares minimization. OriginPro 2019 (OriginLab) was used to fit DRT functions $\gamma(\ln\tau)$, determining resistance and capacitance values. Further, equivalent circuit fitting was performed with circuit models comprising two to four parallel RC elements (see Figure 4.6.22b) using suitable weighting modes.[145]

Chronopotentiometry was performed with a three-electrode setup in 1 mol L^{-1} KOH. A platinum counter electrode, an Ag/AgCl/3M KCl reference electrode and a glassy carbon electrode loaded with the catalyst was used as the working electrode. For preparation of the ink 2.5 mg catalyst, 249 µL H_2O, 249 µL Ethanol and 2 µL Nafion were mixed and sonicated for 15 min. The glassy carbon electrode with a geometric area of 0.0707 cm^2 was polished, loaded with 1.4 µL of ink, and dried for 1 h. A current density of 10 mA cm^{-2} was applied for 2 h and the corresponding potential recorded. The electrode was rotated with 4000 rpm during the measurements.

4.5 Acknowledgement

This research was funded by the Deutsche Forschungsgemeinschaft (DFG, German Research Foundation) in the framework of the Collaborative Research Center / Transregio "Heterogeneous Oxidation Catalysis in the Liquid Phase" – 388390466 – TRR 247 (Project C01, A02, and A09), the Mercator Research Center Ruhr (MERCUR, Pe-2018-0034), and the internal support of the University Duisburg-Essen for early stage researchers („Förderung des exzellenten wissenschaftlichen Nachwuchses"). Furthermore, the authors would like to thank Dr. Kateryna Loza (SEM), Benjamin Mockenhaupt (BET), and Robin Meya (AAS and UV-Vis spectroscopy) for their assistance in the experimental work.

4.6 Supporting Information

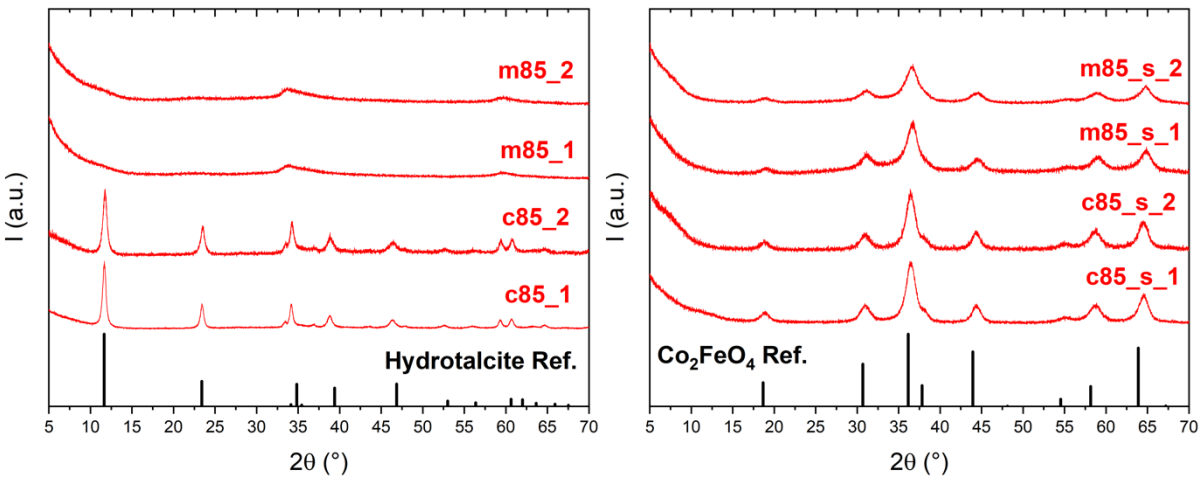

Figure 4.6.1: XRD patterns from two different batches of conventionally prepared and MACP LDH (left) and the corresponding spinels (right).

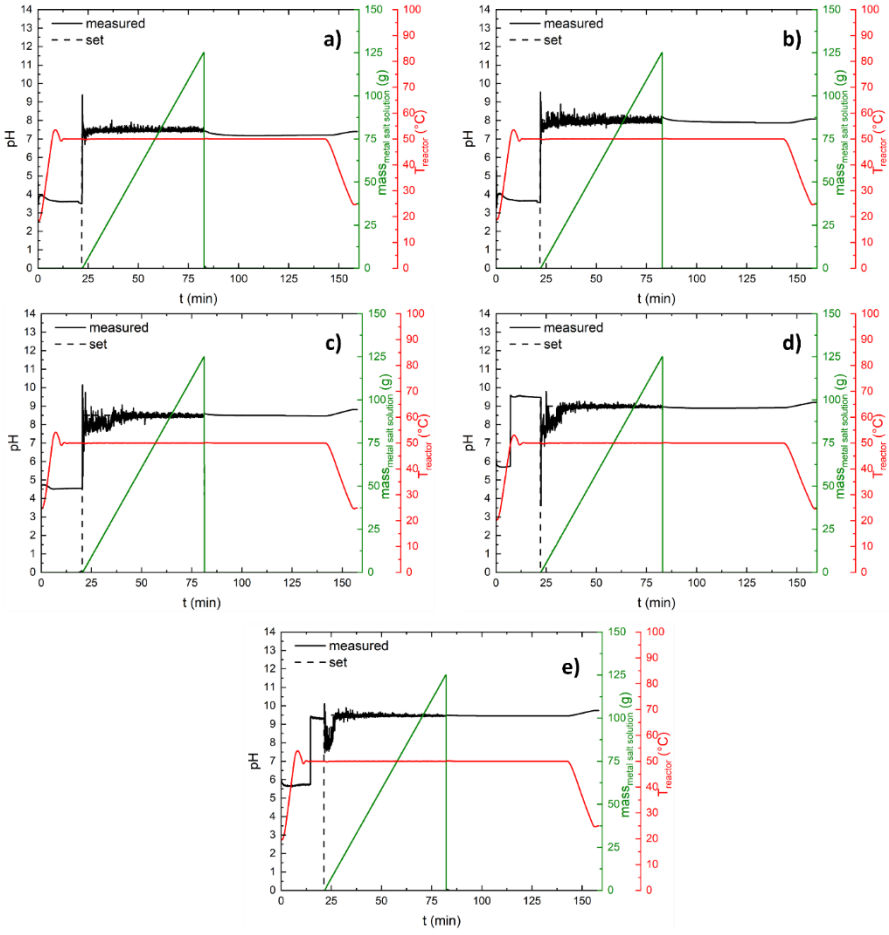

Figure 4.6.2: Synthesis protocols of all conventional synthesis from pH 7.5 (a) to pH 9.5 (e).

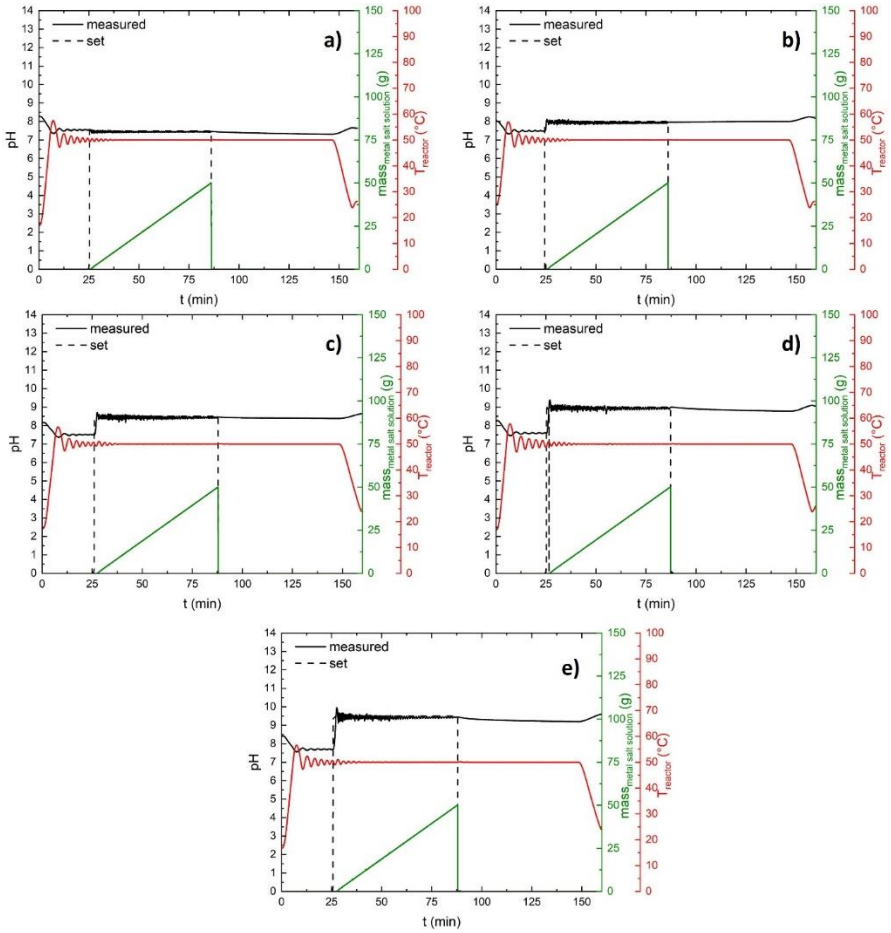

Figure 4.6.3: Synthesis protocols of all microemulsion-based synthesis from pH 7.5 (a) to pH 9.5 (e).

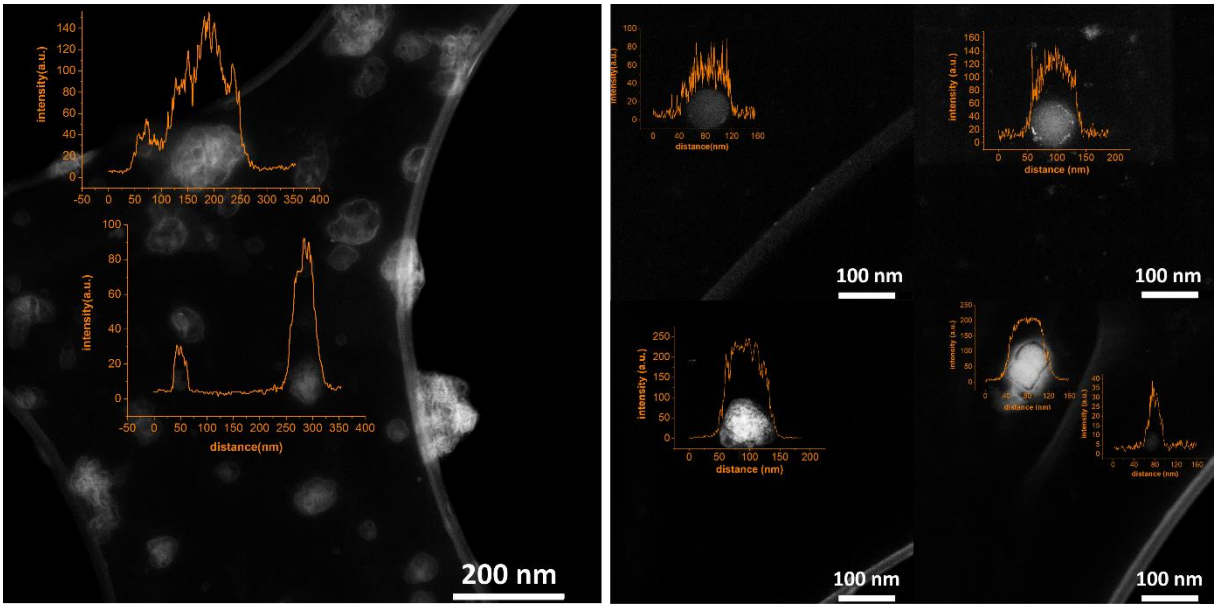

Figure 4.6.4: TEM images and line scans of the microemulsion containing the alkaline precipitation agent (left) and of the metal salt solution containing microemulsion (right).

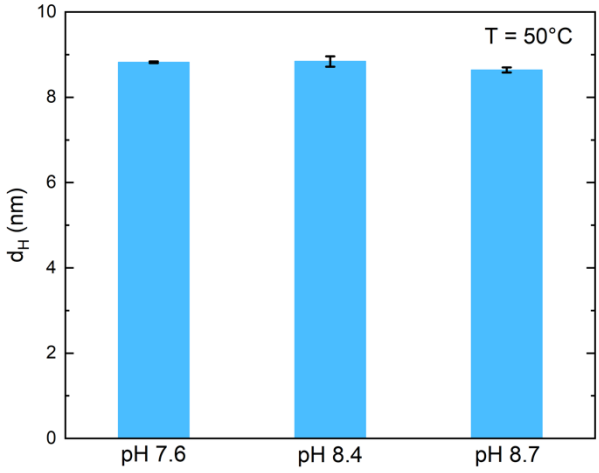

Figure 4.6.5: Hydrodynamic diameter d_h of the micelles at different pH values and 50 °C.

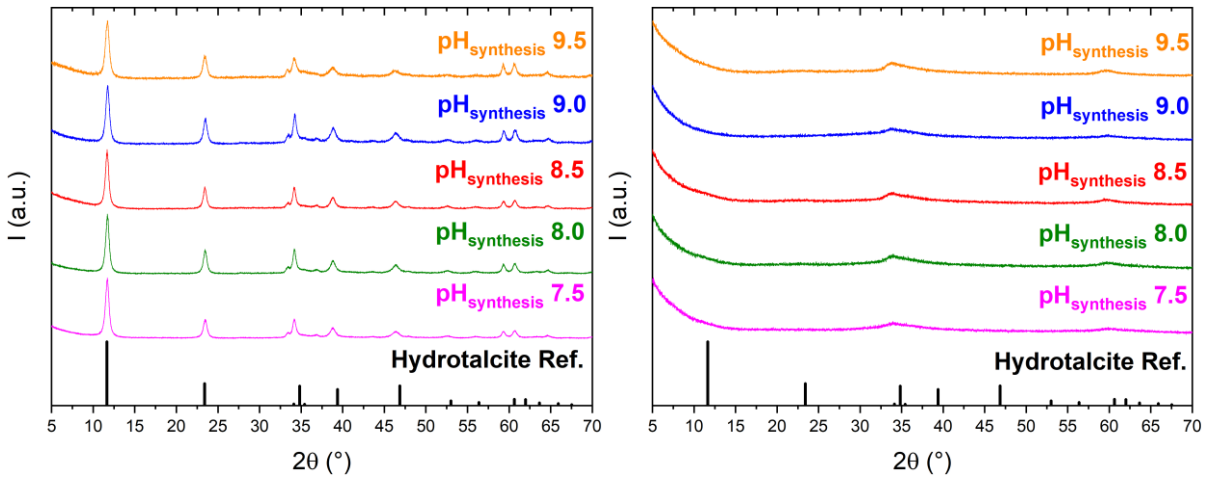

Figure 4.6.6: XRD patterns for the complete conventional (left) and microemulsion-assisted (right) LDH series.

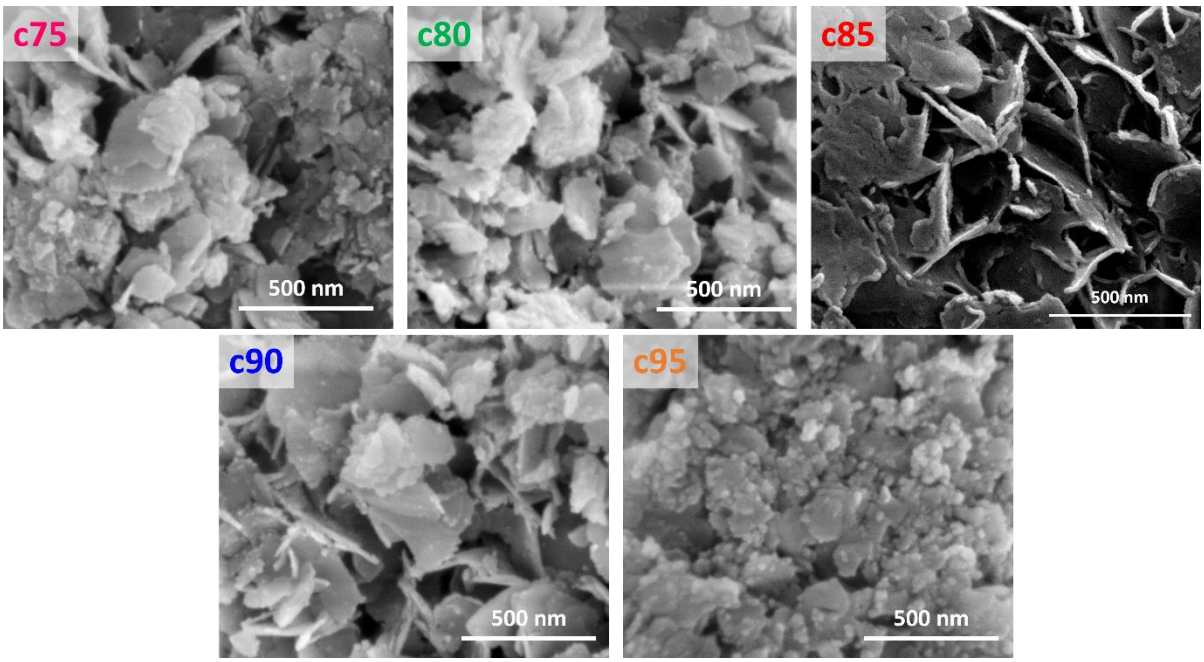

Figure 4.6.7: SEM micrographs of the conventionally prepared pH variation series (LDHs).

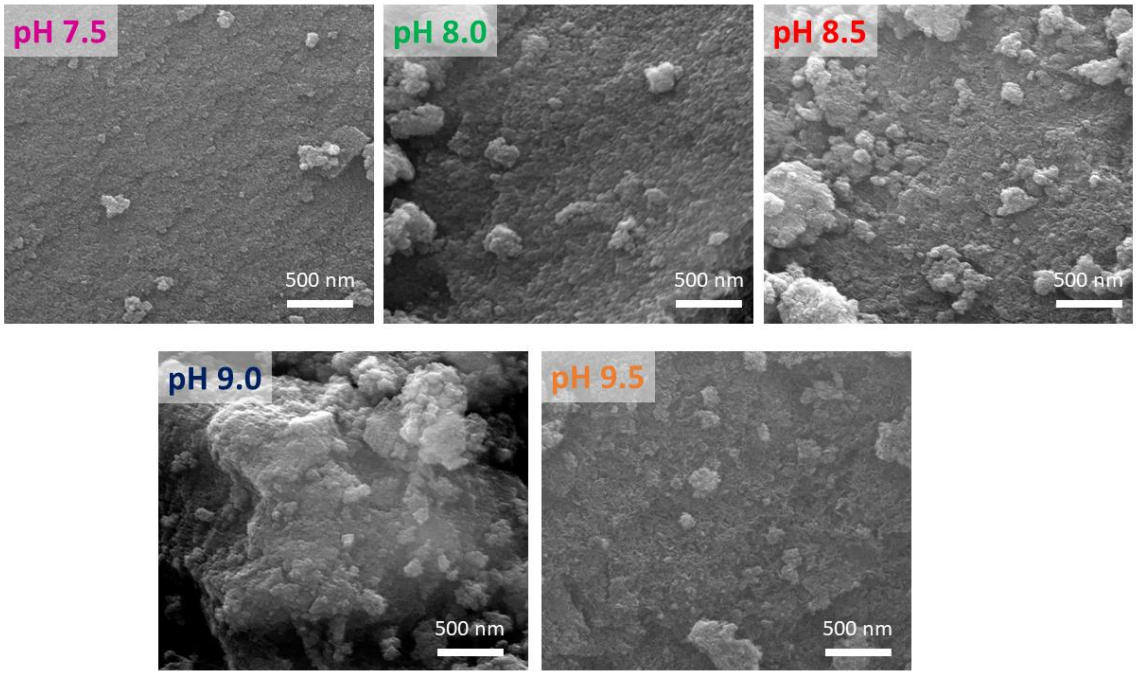

Figure 4.6.8: SEM micrographs of the microemulsion-assisted pH variation series (LDHs).

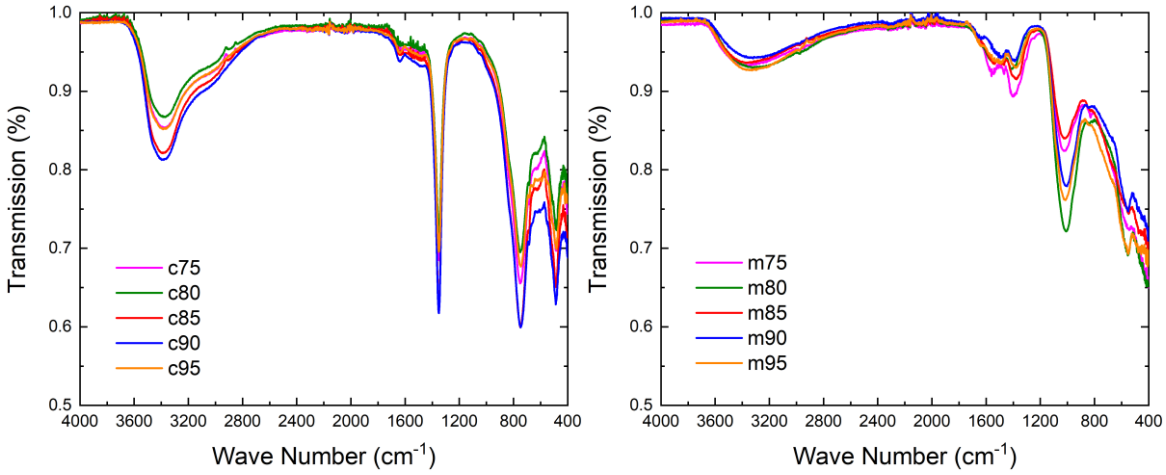

Figure 4.6.9: IR spectra of the conventionally prepared LDH (left) and LDHs prepared by microemulsion-assisted co-precipitation (right).

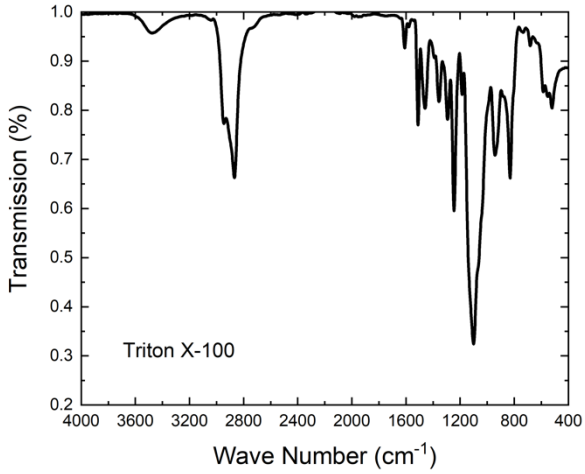

Figure 4.6.10: IR reference spectrum of the commercial Triton X-100.

Table 4.6.1: Results of CHNS analysis and UV-Vis spectroscopy in weight percent wt% for m85.

Species	Wt%
C	4.21 ± 0.45
H	2.1 ± 0.03
N	0
S	0
PO^{3-}_4	16.65 ± 0.49

Table 4.6.2: Micropore volume of all sample series.

$pH_{synthesis}$	Conv. LDH (cm^3g^{-1})	MACP LDH (cm^3g^{-1})	Conv. Spinel (cm^3g^{-1})	MACP spinel (cm^3g^{-1})
7.5	0.039	0.101	0.038	0.166
8.0	0.030	0.109	0.035	0.053
8.5	0.037	0.095	0.025	0.062
9.0	0.025	0.095	0.034	0.055
9.5	0.027	0.089	0.033	0.065

Table 4.6.3: Total pore volume of all sample series.

$pH_{synthesis}$	Conv. LDH (cm^3g^{-1})	MACP LDH (cm^3g^{-1})	Conv. Spinel (cm^3g^{-1})	MACP spinel (cm^3g^{-1})
7.5	0.583	0.575	0.554	1.130
8.0	0.409	0.716	0.529	0.371
8.5	0.509	0.708	0.403	0.489
9.0	0.594	0.861	0.533	0.436
9.5	0.513	0.966	0.664	0.599

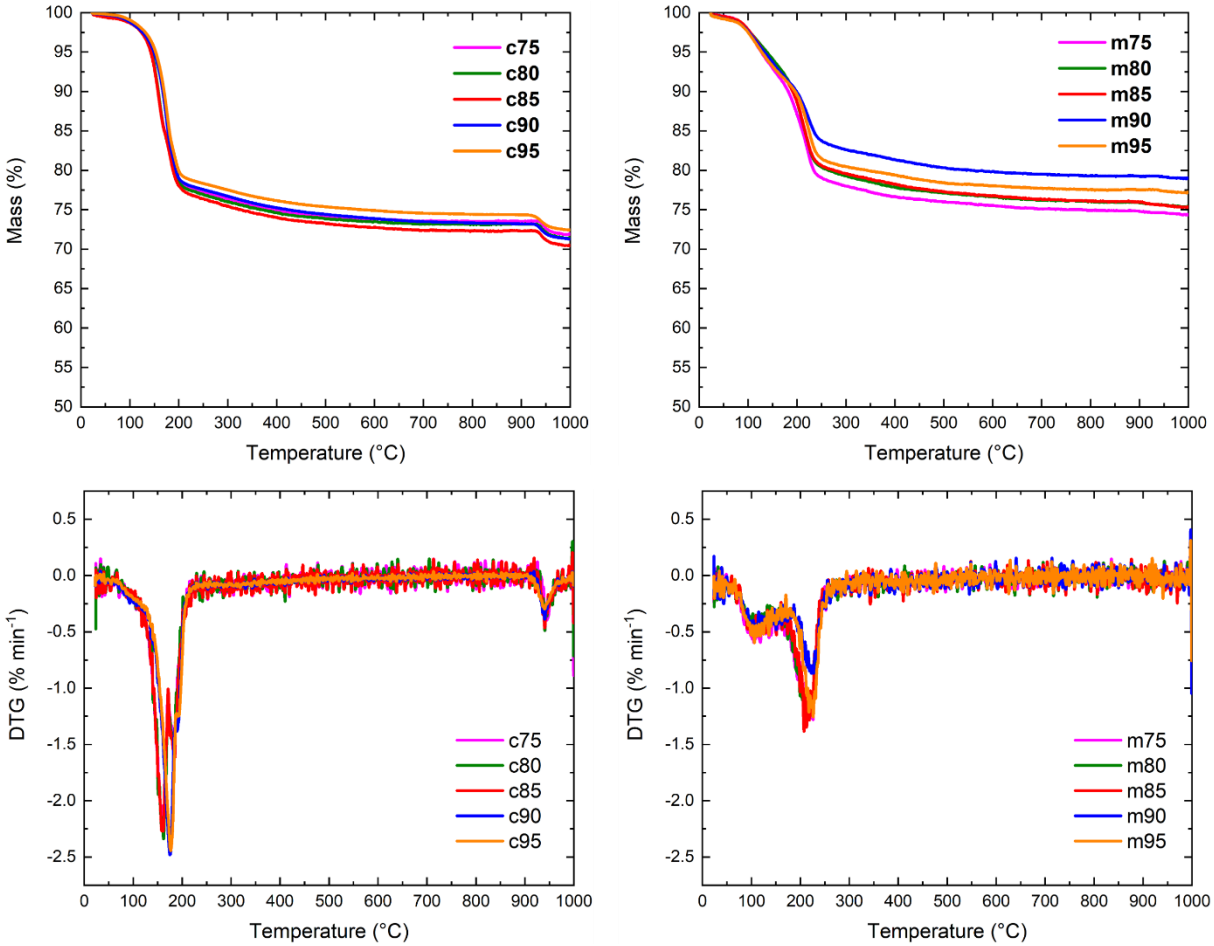

Figure 4.6.11: Mass loss as a function of temperature for both synthesis series (upper row) and corresponding DTG curves (lower row).

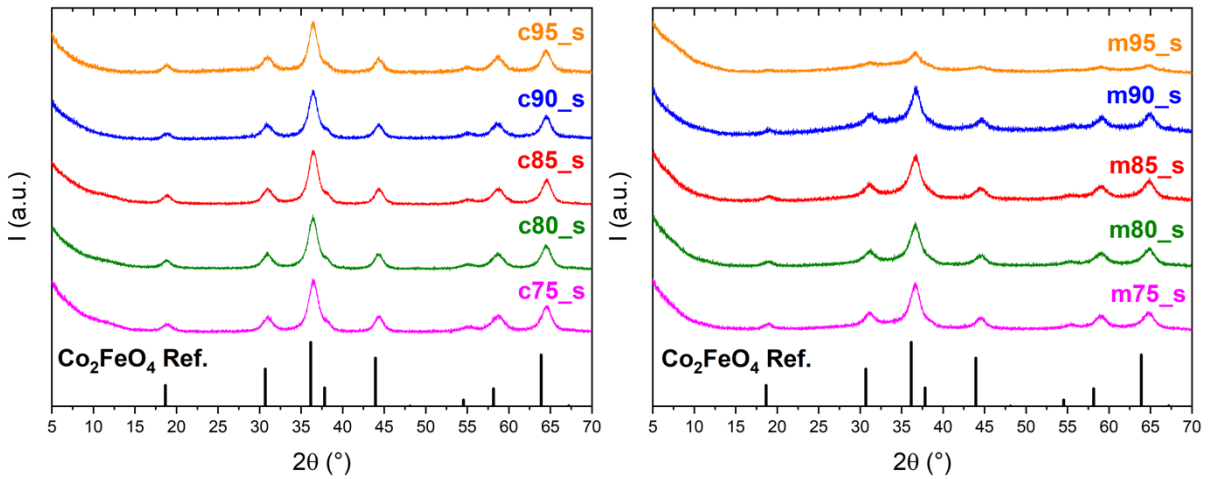

Figure 4.6.12: XRD patterns for the complete calcined conventional (left) and microemulsion-assisted (right) series.

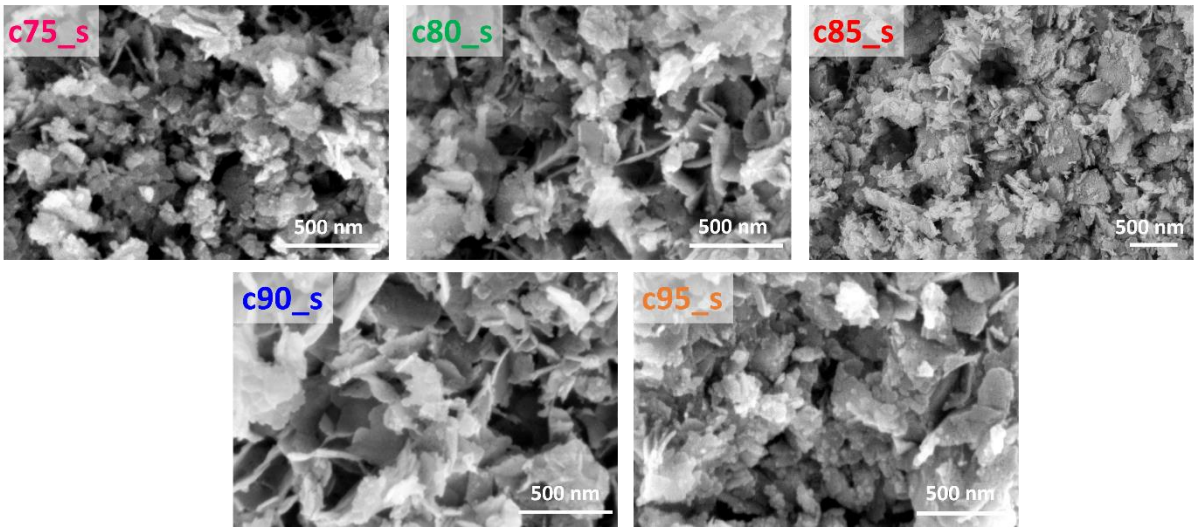

Figure 4.6.13: SEM micrographs for the spinels derived from the conventional pH variation series.

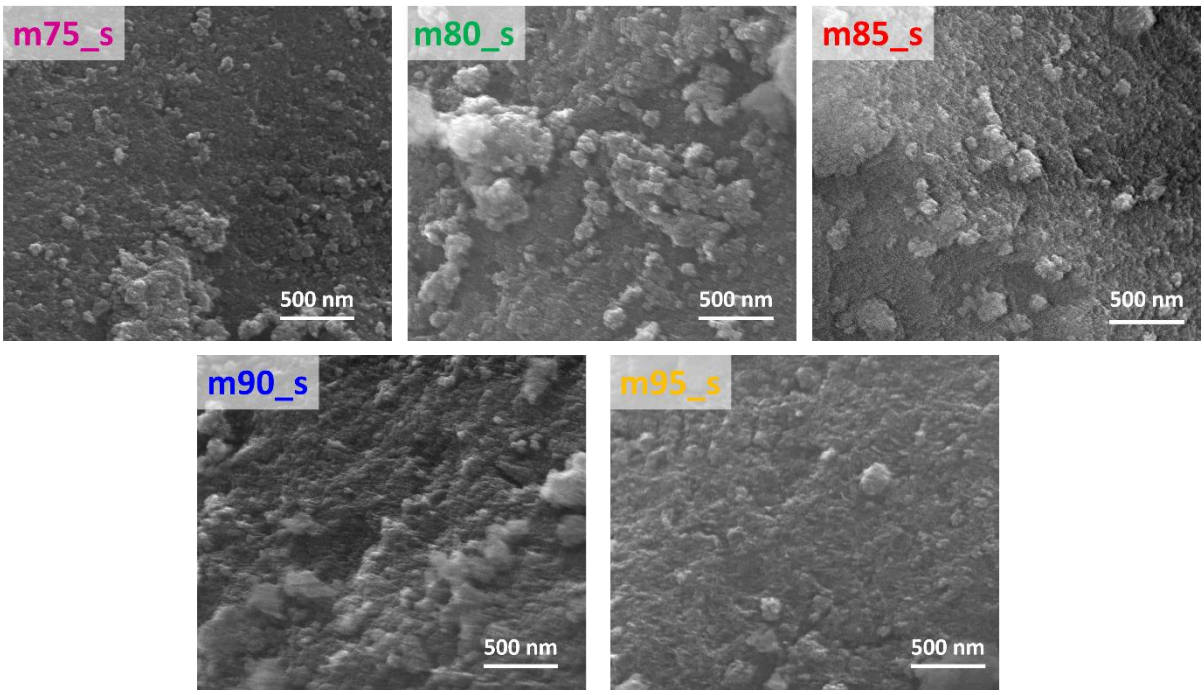

Figure 4.6.14: SEM images of the MACP spinels derived from LDH prepared by microemulsion-assisted co-precipitation.

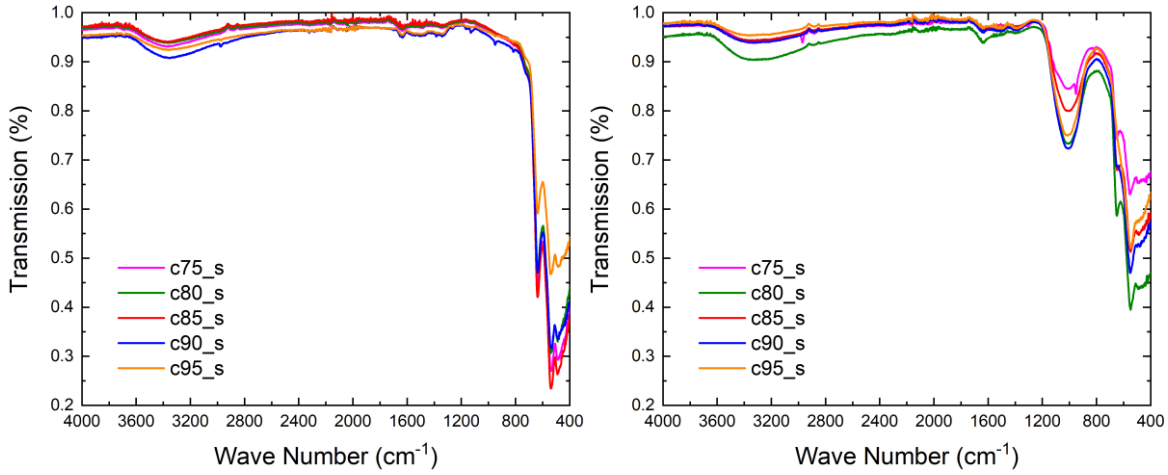

Figure 4.6.15: IR spectra of the conventionally prepared spinels (left) and spinels prepared by microemulsion-assisted co-precipitation (right).

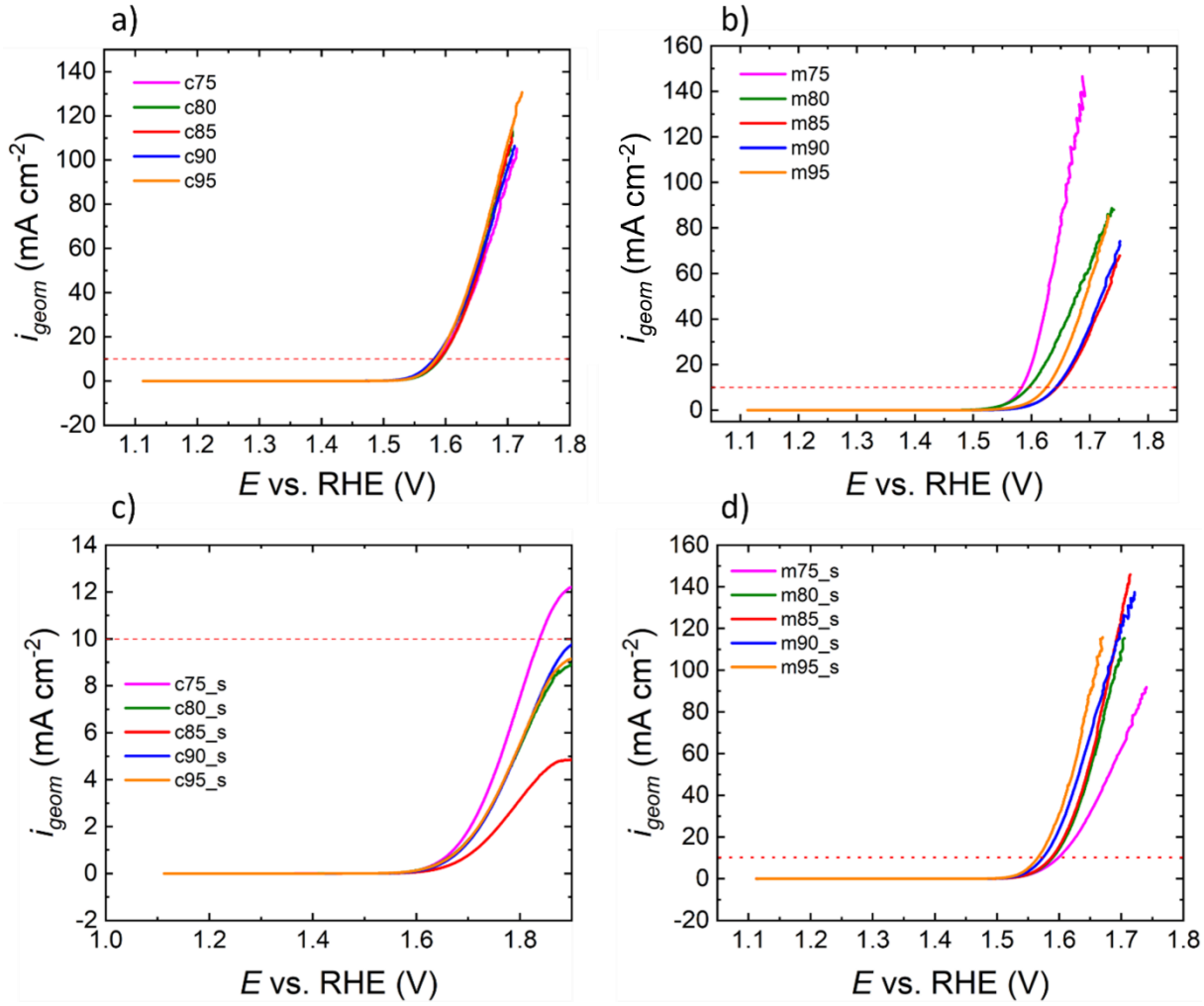

Figure 4.6.16: Exemplary linear sweep voltammograms of the conventional LDHs (a), MACP LDHS, (b), conventional spinels (c), and MACP spinels (d).

For the conventional LDHs, no clear trend with precipitation pH or microstructure is found, yet all samples exhibit a comparable overpotential at 10 mA cm^{-2} (Figure 4.3.8b, closed red symbols). This is in line with the similar mesostructural properties of the conventional LDHs and confirms the minor role of the synthesis pH within the range studied here for conventional co-precipitation. For the MACP samples on the other hand (Figure 4.3.8b, open red symbols), the lowest synthesis pH leads to the LDH with the lowest overpotential within this series. Upon calcination the conventional samples show a distinct increase in overpotential. This has been observed previously for cobalt-containing LDHs.[151] As depicted in Figure 4.3.8a, the increase was so severe that the overpotential at 10 mA cm^{-2} could not be determined. A large but measurable overpotential of around 460 mV was determined for the sample c85_s on another setup and with binder. The results are shown in Figure Figure 4.6.17 and agree with the results found in [109]. Minor differences are explained by differences in binder concentration, catalyst loading, and measurement procedure.

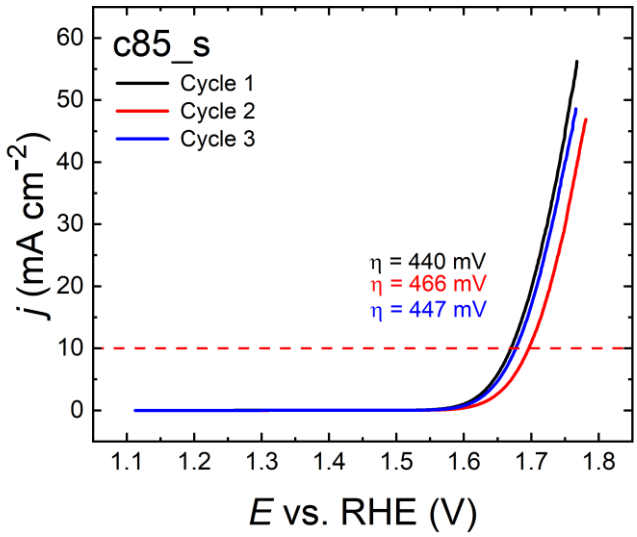

Figure 4.6.17: Linear sweep voltammograms of c85_s with binder.

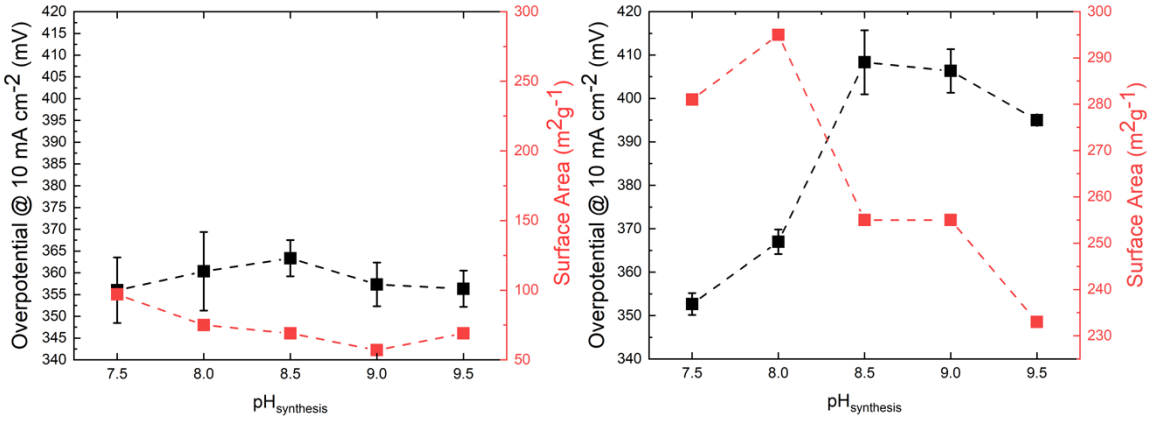

Figure 4.6.18: Overpotential and BET surface area as function of pH during synthesis for the conventionally prepared LDHs (left) and the MACP LDHs (right).

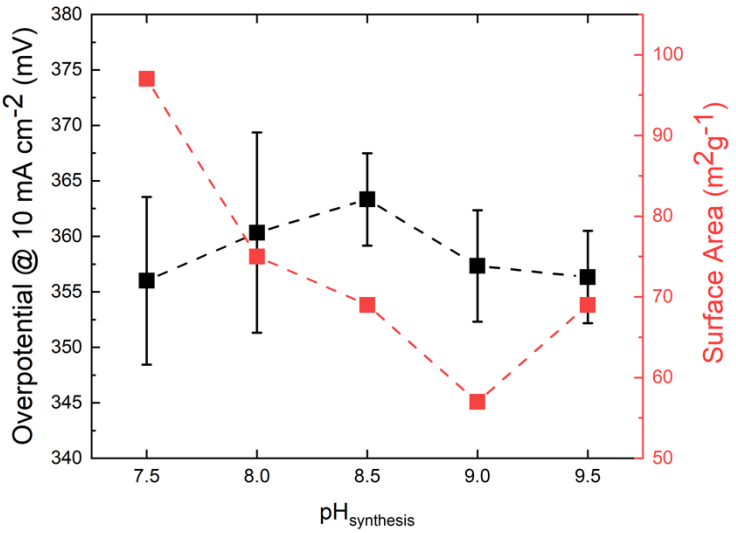

Figure 4.6.19: Overpotential and BET surface area as function of pH during synthesis for the MACP spinels.

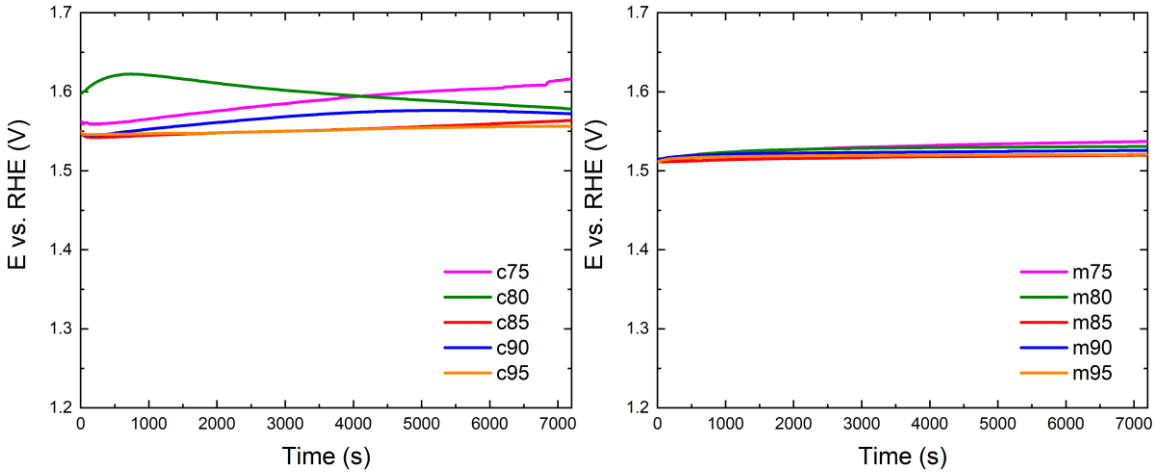

Figure 4.6.20: Chronopotentiometry in 1 M KOH and 4000 rpm for the conventional (left) and MACP series (right).

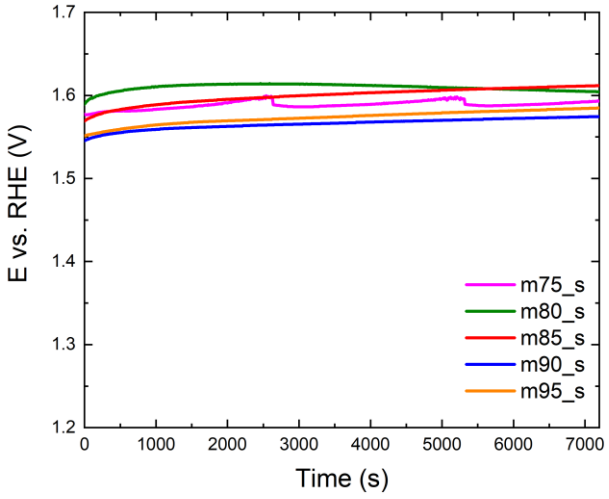

Figure 4.6.21: Chronopotentiometry in 1 M KOH and 4000 rpm for the MACP spinel series.

Chronopotentiometry at 10 mA cm^{-2} was performed for 2 h obtaining the data shown in Figure 4.6.20 and Figure 4.6.21. Both LDH series showed a satisfying stability in regard to the stability criteria defined by McCrory et al.[57c] The conventionally prepared samples slightly deactivate in the beginning but increase their activity over time. For the sample prepared at pH 8.0 this even results in a lower overpotential after 2 h than in the beginning. The MACP LDHs all show a slight increase in overpotential at the beginning and a steady behavior afterwards. The MACP spinel series also shows satisfying stability. Differences in the starting potential for the three series compared to the activity measurements are explained by using a binder to ensure the sticking of the catalyst to the glassy carbon during measurements and the absence of pre-treatment before chronopotentiometry.

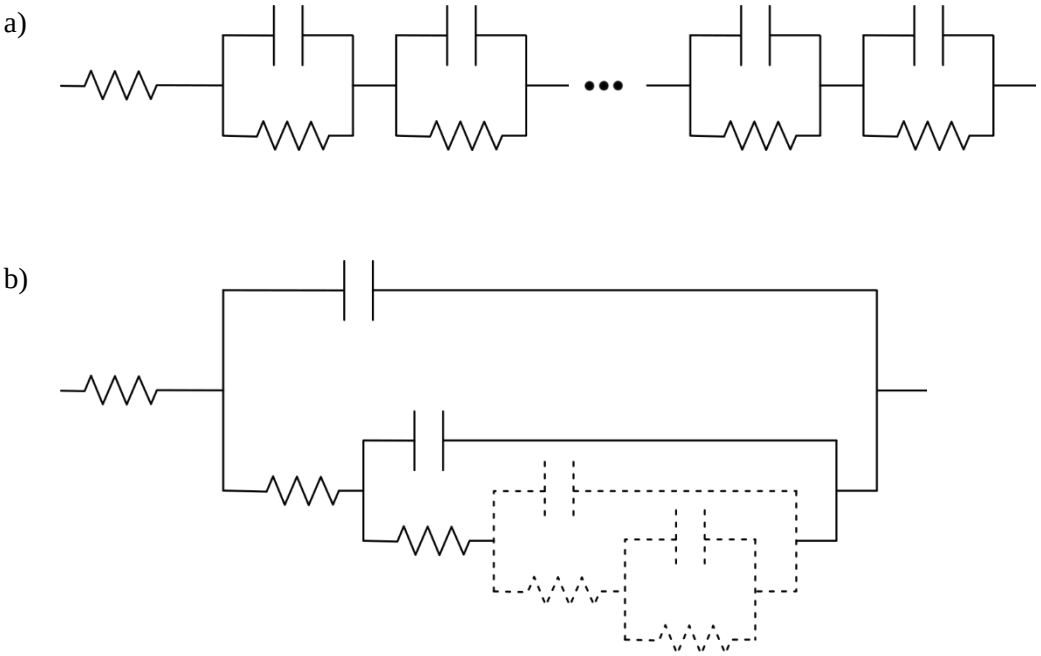

Figure 4.6.22: Equivalent circuit models used for impedance analysis with a) ohmic resistance with an infinite series of parallel RC elements for deconvoluting the distribution of relaxation times,[150] and b) nested circuit with two to four parallel RC elements.[58b]

As exemplified in Figure 4.3.11b, satisfying circuit fits can be obtained using the equivalent circuit(s) shown in Figure 4.6.22. However, the resulting values corresponding to the semicircle(s) related to the mid/low frequency range depend sensitively on the chosen starting parameters due to the strong overlap of semicircles or information is concealed if one (distorted) semicircle for this frequency range is considered. Thus, shown resistance and capacitance values are based on the DRT analysis.

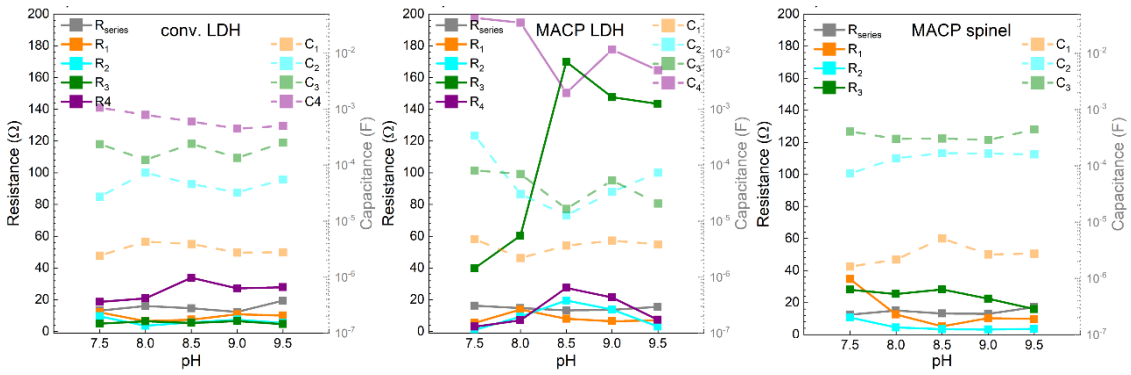

Figure 4.6.23: Resistance and capacitance values determined from DRT analysis for all (left) conventional LDHs, (middle) MACP LDHs, and (right) MACP spinels.

Differences in intrinsic activity can be explained by variations in reaction mechanisms. To investigate such phenomena, Tafel analysis and electrochemical impedance spectroscopy (EIS) are suitable approaches.

Tafel slopes were analyzed to evaluate the change of activation by higher applied overpotential, with deviations in Tafel slopes indicating differences regarding the OER mechanism, e.g., rate determining step, relations to other steps, or symmetry factor. The analysis showed a limited potential range of ca. 50 mV, where a linear dependence of the logarithm of the current density and the overpotential is observed and the charge transfer coefficient was nearly constant. The potential range characterized by Tafel behavior is generally constrained by mass transport limitation in the direction of higher overpotentials and, for very low overpotentials, as the back reaction is no longer negligible. However, the narrow Tafel region under the applied experimental conditions is a strong indication that the Tafel slope varies with potential in the surrounding potential ranges.

Tafel slopes change with potential when the partial surface coverage of adsorbed intermediates is potential-dependent. For multistep reactions such as the OER, this means potential ranges with almost constant Tafel slope are possible if (1) partial coverage remains very low, e.g., because intermediates are formed in the rate-determining step and consumed by the following considerably faster step, (2) partial coverage approaches unity as it cannot increase significantly with potential anymore and a step following formation of the considered intermediate is rate-determining and, thus, slower, or (3) a combination of two potential-dependent (sequential) intermediate coverages leads to a nearly potential-independent overall Tafel slope. For Co_3O_4 electrodes, a linear Tafel relation was found in a potential range of about 90 mV in between regions of changing Tafel slope.[152] The linear region corresponded to a range of nearly constant capacitance resulting from two overlapping potential-dependent pseudocapacitances which were assigned to the changing cobalt oxidation state and formation of discharged O and OH intermediates.

The DRT-peak corresponding to the R_3C_3 element – which is substantially more pronounced for the MACP LDH samples showing significantly diminished electrocatalytic activity (pH = 8.5, 9.0, 9.5) – is assumed to be related to the sub-process of the oxygen evolution reaction mechanism where oxygen is released. To investigate on the hypothesis of the oxygen release in this step, impedance spectra were recorded, first, with an oxygen-purged (for 2 h) and, subsequently, with an argon-purged (for 2 h) aqueous 1 M KOH electrolyte solution under OER-conditions by exchanging the electrolyte after the electrochemical pre-conditioning of

the catalyst material by cyclic voltammetry. As sample catalyst the conventionally at a synthesis pH value of 8.5 prepared LDH was chosen due to its similar crystal structure but different meso-morphology and due to the comparable general characteristics of the impedance spectra with four distinguishable peaks in the DRT plot. Because of the larger, more open pore morphology (PSD_{max} > 20 nm with wide pore size distribution and H3 hysteresis loop), the exchange of pore electrolyte components with bulk electrolyte components is enhanced and, thus, the conditions close to the catalyst/electrolyte interface can be affected more easily by bulk electrolyte treatments. However, the under OER-conditions already evolving oxygen is expected to affect the oxygen concentration, especially in front of the electrode, and, thus, diminishing the effect of the purging.

The results are represented in Figure 4.6.24 where it is seen that the resistances corresponding to the three DRT-peaks in the time constant range from 10^{-5} s to 10^{-2} s all decrease when a deoxygenated electrolyte solution is used. While R_1 and R_2 decline about 1 Ω (from 18 Ω to 17 Ω and 13 Ω to 12 Ω), R_3 is reduced by 6 Ω. The process related to R_3 is affected most by the reduced oxygen concentration in the electrolyte, indicating that R_3 is related to the oxygen release step where O_2 is formed and leaving the catalyst surface and that there are interdependencies with the other steps. The R_4C_4 peak becomes more pronounced for the Ar-purged electrolyte and is assumingly related to a mass transport process considering its time constant.

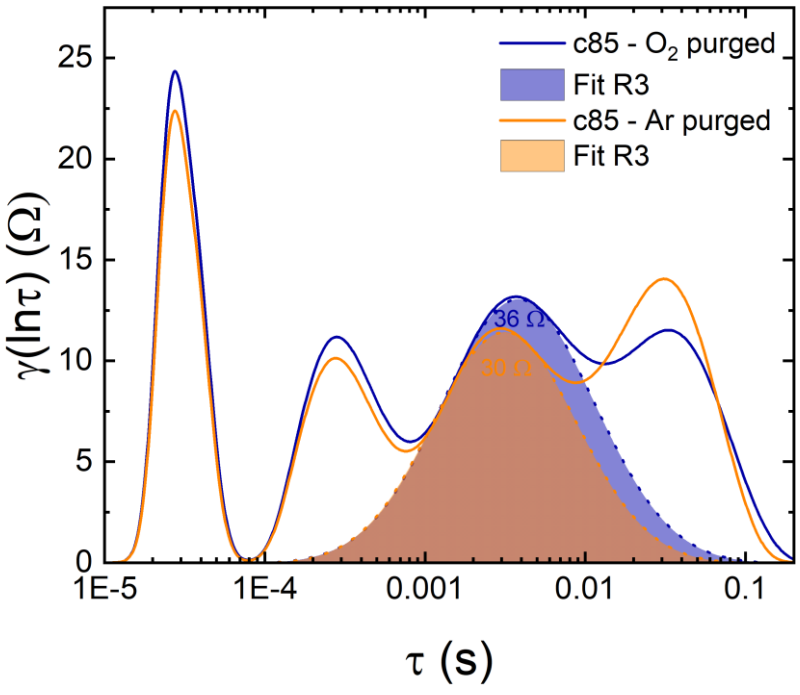

Figure 4.6.24: Distribution functions of relaxation times γ(τ) for c85 with O_2 and Ar purging.

5. Metastable Crystalline Cobalt Iron Oxide Nano-flakes with Antiferromagnetic/Ferrimagnetic Composition Mosaicity

Anna Rabe,[a,b] Franz-Philipp Schmidt,[c] Shohreh Rafiezadeh,[a] Soma Salamon,[a] Joachim Landers,[a] Mirco Eckhardt,[d] Christoph Pratsch,[e] Benedikt Beckmann,[f] Oliver Gutfleisch,[f] Mirijam Zobel,[g] Rossitza Pentcheva,[a] Heiko Wende,[a] Thomas Lunkenbein,[c] Malte Behrens[b,h]

---

[a] Anna Rabe, Shohreh Rafiezadeh, Soma Salamon, Joachim Landers, Rossitza Pentcheva, Heiko Wende
Faculty of Physics
University of Duisburg-Essen and Center for Nanointegration Duisburg-Essen (CENIDE)
Lotharstr. 1, 47057, Germany

[b] Anna Rabe, Malte Behrens
Faculty of Chemistry
University Duisburg-Essen
Universitätsstr. 7, 45141 Essen, Germany

[c] Franz-Philipp Schmidt, Thomas Lunkenbein
Department of Inorganic Chemistry
Fritz Haber Institute of the Max Planck Society
14195 Berlin, Germany

[d] Mirco Eckhardt
Department of Chemistry
University of Bayreuth
Universitätsstr. 30, 95440 Bayreuth, Germany

[e] Christoph Pratsch
Department of X-ray Microscopy
Helmholtz-Zentrum Berlin für Materialien und Energie GmbH
Albert-Einstein-Str. 15, 12489 Berlin, Germany

[f] Benedikt Beckmann, Oliver Gutfleisch
Institute of Materials Science
Technische Universität Darmstadt, 64287 Darmstadt, Germany

[g] Mirijam Zobel
Institute of Crystallography
RWTH Aachen University, 52066 Aachen, Germany

[h] Malte Behrens
Institute of Inorganic Chemistry
Kiel University
May-Eyth-Str. 2, 24118 Kiel, Germany

This chapter is a manuscript planned for publication.

Anna Rabe developed and performed the synthesis technique and conceptualized the sample series. Overall, she coordinated and conducted parts of the sample characterization, evaluation, and wrote the first draft of the manuscript.
Franz-Philipp Schmidt performed the HR-TEM measurements, evaluation was done by him and Christoph Pratsch. Shohreh Rafiezadeh and Rossitza Pentcheva provided the DFT+*U* calculations. Soma Salamon, Joachim Landers, Heiko Wende, Benedikt Beckmann, and Oliver Gutfleisch are responsible for Mössbauer spectroscopy and magnetometry. Mirco Eckhardt and Mirijam Zobel conducted PDF measurements and evaluation. Malte Behrens and Thomas Lunkenbein conceptualized the project.

5.1 Abstract

By thermal decomposition of a crystalline hydroxycarbonate precursor with a Co:Fe ratio of 2:1, crystals with alternating ferrimagnetic and antiferromagnetic nano-domains were synthesized using a facile synthetic approach that combined bottom-up co-precipitation of the precursor with a top-down nano-structuring during spinel formation. Due to the miscibility gap of the spinel phase diagram at this composition, a self-assembled and topotactic segregation into $CoFe_2O_4$-like and Co_3O_4-like domains takes place at 400 °C, giving rise to porous crystalline nano-flakes with spatial compositional fluctuations on a scale of approximately 5 nm. Experimental methods and density functional theory showed that the metastable nature of this interface-rich material is manifested in the unexpectedly low lattice parameter of the iron-rich domains, which can be explained by the compressive strain executed on this phase via multiple epitactic interfaces. Investigations of the magnetic properties revealed an exchange bias effect, due to this unique microstructure, which is typically known for thin films or core/shell nanoparticles. Treatment at temperatures higher than 450 °C causes this microstructure to break down, the strain to relax, and finally leads to properties expected for the thermodynamic stable phases according to the phase diagram.

5.2 Introduction

Spinel type oxides, especially those containing iron and/or cobalt, are multi-functional and low-cost materials in a broad variety of applications and their production via multiple routes in addition to their compositional flexibility allows fine tuning of the desired properties.[153] However, in powder materials, one usually investigates and tunes the properties of uniform single phase spinels, while composition gradients in thin films[88, 154] have shown great potential to enhance the accessible range of properties. Here we present a novel and cost-effective synthetic approach to spinel powders consisting of crystalline nanoparticles with mosaic composition fluctuations, which exhibit extraordinary structural and magnetic properties.

The spinel structure is generally expressed as $(A^{II}_t)(B^{III}_o)_2O_4$, where the divalent A cations occupy one eighth of the tetrahedral sites (*t)* and the trivalent B cations occupy half of the octahedral sites (*o)* in a face-centered cubic structure of oxygen atoms.[77] This structure is denoted as the normal spinel type. Inverse spinels are described by the formula

$(B^{III}_t)(A^{II},B^{III}_o)_2O_4$, in which the divalent A cations are in octahedral sites and the trivalent B cations are evenly distributed in tetrahedral and octahedral sites. Which spinel structure type is formed depends on the size of the cations, their ligand field stabilization and/or Madelung energy.[36] Often an intermediate state is observed, which can be described as partially inverse by $(A^{II}_{1-x}B^{III}_x)_t(A^{II}_xB^{III}_{2-x})_oO_4$ with a degree of inversion x.[35b, 155] A prototypical example is the antiferromagnetic (AFM) Co_3O_4, which crystallizes in the normal spinel structure. The substitution of two Co cations by Fe leads to the inverse spinel $CoFe_2O_4$, which is ferrimagnetic (FiM). The compound Co_2FeO_4 with a composition halfway between Co_3O_4 and $CoFe_2O_4$ is metastable at temperatures below 600 °C. In this regime the pseudo-binary $CoFe_2O_4$ – Co_3O_4 phase diagram shows a large miscibility gap (Figure 5.2.1).[156]
This miscibility gap causes the segregation of Co_2FeO_4 into an iron-rich, mostly inverse, FiM $CoFe_2O_4$-like phase and a cobalt-rich, mostly normal, AFM Co_3O_4-like phase by spinodal decomposition.[91] The position of Co_2FeO_4 inside the miscibility gap can thus be used for engineering FiM-AFM interfaces. Such FiM-AFM interfaces can give rise to an interesting magnetic phenomenon, the so-called exchange bias effect, which was first observed by Meiklejohn and Bean in core-shell system consisting of a metallic cobalt core and an oxidized CoO shell.[157] The exchange bias shifts the center of the hysteresis loop of a ferro- or ferrimagnet along the axis of the magnetic field. This effect is a consequence of the exchange coupling at the interface between the ferrimagnetic or ferromagnetic and antiferromagnetic domains.[158] Moreover, it is essential in technologies such as magnetic sensors or magnetic-storage applications.[159]

Naturally, the interface between the FiM and AFM component is pivotal for exchange bias to occur, so increasing the interfacial area between AFM and FiM components in a material is desirable. Usually, two crystallographically distinct phases are neighboring each other, with one phase exhibiting AFM and the other exhibiting FiM properties, modifying the magnetic exchange interactions across the shared interface. Typical examples are core shell particles or thin films.[160] On the other hand, it should be possible to increase the FiM-AFM interface area at the nanoscale, while using the AFM and FiM phases crystallizing in the same general structure type, the spinel lattice. Such atypical exchange bias between two isostructural phases has to the best of our knowledge so far mainly been observed in natural minerals.[161]
We herein present a synthetic strategy to enhance the specific FiM-AFM contact within crystalline spinel oxide flakes at the nanoscale and demonstrate its relevance for exchange bias. We employed a low-temperature approach based on the recently described topotactic decomposition of a layered double hydroxide (LDH) precursor to obtain a nano-sized and

anisotropic platelet-shaped spinel with a Co:Fe ratio of 2:1.[109] As the LDH precursor does not show any miscibility issue in this composition range, compositions within the miscibility gap of the resulting spinel are readily accessible.[109] The easily scalable thermal decomposition of the LDH precursor at only 400 °C yielded porous crystalline and metastable spinel nanoflakes, in which alternating FiM- and AFM mosaic domains are separated by epitactic solid-solid interfaces. As diffusion of atoms has been kinetically trapped at such low temperature, nanoscale domains form from the uniform precursor. This way, we are able to engineer the exchange bias effect usually only observed in thin films or core shell nanoparticles into a simple powder material, foregoing the requirement of complex synthesis or deposition procedures. The self-assembly of the magnetic domains within one individual crystal and the thermal evolution of this unique microstructure was investigated by X-ray diffraction (XRD), pair distribution functional (PDF) analysis, scanning electron microscopy (SEM), high resolution (scanning) transmission electron microscopy (HR-(S)TEM), combined STEM-energy dispersive X-ray spectroscopy (STEM-EDX), Mössbauer spectroscopy, and magnetometry. To gain insight into the underlying properties, density functional theory calculations are performed with an on-site Hubbard term (DFT+*U*).

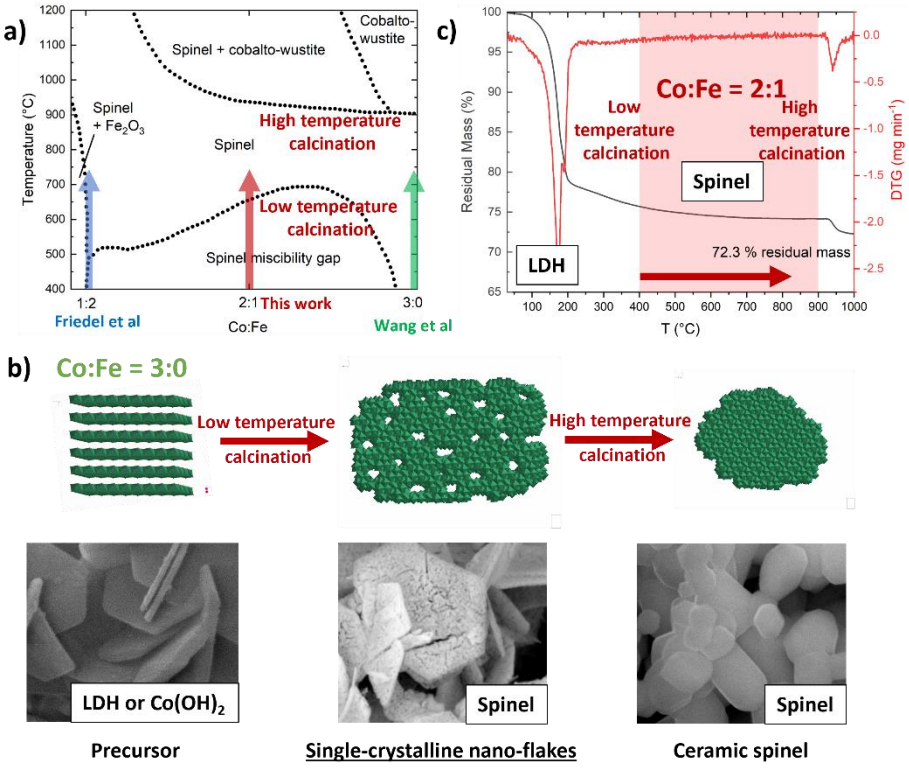

Figure 5.2.1: (a) Schematic representation of the Fe-Co-O phase diagram, adapted from [162]. The positions of $CoFe_2O_2$, Co_2FeO_4, and Co_3O_4 in the phase diagram were added.[11, 50b] (b) The crystalline precursor decomposition approach leading to single-crystalline nano-flakes and (c) thermogravimetric analysis for identifying feasible temperature ranges for spinel formation.

5.3 Results and Discussion

Metastable Co:Fe = 2:1 spinel-type oxides have been prepared by the thermal decomposition of crystalline precursors as described previously for Co:Fe = 1:2 yielding $CoFe_2O_4$ (from a $(Co^{II}_{0.33}Fe^{III}_{0.33}Fe^{III}_{0.33})(OH)_2(CO_3)_{0.17} \times mH_2O$ LDH-precursor, blue arrow in Figure 5.2.1a) and Co:Fe = 3:0 yielding Co_3O_4, (from a $Co^{II}_2(OH)_2$ hydroxide precursor, green arrow in Figure 5.2.1a).[109] For this work, a phase-pure LDH precursor of the general sum formula $(Co^{II}_{0.67}Fe^{III}_{0.33})(OH)_2(CO_3)_{0.17} \times mH_2O$ (Figure 5.6.1(a)) has also been synthesized with a composition falling into the miscibility gap of the spinel phase diagram (red arrow in Figure 5.2.1a). The precursor exhibits the typical intergrown platelet morphology of co-precipitated LDH materials with a platelet size of around 0.5 µm (Figure 5.6.1(b)).[109]

Next, this LDH precursor has been thermally decomposed in air to yield the desired Co_2FeO_4 spinel. Upon calcination in the presence of oxygen, half of the Co^{2+} cations are oxidized to Co^{3+} to adjust the trivalent to bivalent cation ratio needed for the formation of a spinel without need for extended cation diffusion. Figure 5.6.1(c) shows the thermogravimetric (TG) analysis of the precursor in synthetic air from which the complete precursor decomposition and the thermal re-reduction of the formed trivalent cobalt at high temperature can be derived. The LDH decomposition starts at temperatures around 200 °C, which is in line with literature.[34] After calcination at 400 °C the mass loss remains stable up to 922 °C, where the thermal reduction of Co^{3+} cations in the spinel and the conversion into cobalto-wustite takes place, which is in good agreement with the phase diagram (Figure 5.2.1). Therefore, temperatures from 400 °C to 900 °C were selected as suitable calcination temperatures in order to comparatively assess the stability and the magnetic properties of the synthesized spinel products.

Thermal decomposition of the LDH precursor was conducted in this temperature range in 50 °C steps for 3 h, while samples calcined at 400 °C, 800 °C, and 900 °C have been selected as representatives of samples in the miscibility gap (400 °C), at the border of the miscibility gap (800 °C), and in the stable single-phase regime (900 °C). The SEM images of these three calcination products are shown in Figure 5.3.1a-c. After calcination at 400 °C, porous pseudomorphs of the LDH precursor platelets are obtained as expected from the topotactic decomposition (Figure 5.3.1a). After calcination at 800 °C, sintering effects cause the depletion of pores and loss of the anisotropic morphology (Figure 5.3.1b). This effect is even more pronounced after calcination at 900 °C (Figure 5.3.1c). For the latter sample, a longer

dwell time of 17 h was needed for a complete “ceramic” homogenization yielding a phase pure Co_2FeO_4 sample after passing through the miscibility gap as determined by XRD (see below).[91]

Rietveld refined powder XRD patterns (Figure 5.3.1d-f) and PDF analysis (Figure 5.3.1g-i) of the calcination series show that the samples calcined at 800 °C and 900 °C are highly crystalline (Figure 5.3.1e-f). A phase mixture is observed for the sample calcined at 800 °C (Figure 5.3.1e) despite the fact that the calcination temperature was above the miscibility gap indicated in the phase diagram.[88] This shows that the sample has not reached thermodynamic equilibrium and still represents the instability of Co_2FeO_4 at low temperature. The cubic lattice parameter *a* derived from Rietveld refinement agrees with the phase separation into an iron-richer spinel (*a*=8.3208 Å) and a cobalt-richer spinel (*a*=8.1683 Å). A single Co_2FeO_4 phase was obtained only after prolonged annealing at 900 °C (Figure 5.3.1f). After calcination at 900 °C for 17 h no splitting in the reflections can be observed and the refined lattice parameter (*a*=8.2427 Å) agrees with that for phase pure Co_2FeO_4 reported in the literature, indicating that the thermodynamically stable state has been reached.[91] To further investigate the short- and intermediate- range order of the samples in greater detail, PDF measurements were performed. For the sample calcined at 800 °C (Figure 5.3.1g), a biphasic model with two spinels led to a satisfying fit and for the 900 °C sample a one-spinel model was used for satisfying results (Figure 5.3.1i), corroborating the results from Rietveld refined XRD data. In addition, the PDF analysis indicates a similar trend in the lattice parameter as provided by the XRD analysis (Table 5.3.1).

The 400 °C sample shows lower crystallinity in the PXRD data than the 800 °C sample. Rietveld refinement indicated two segregated spinel phases with significantly different lattice parameters. Interestingly, the lattice parameter for the iron enriched phase is significantly smaller than expected, which will be discussed below. In the PDF, a biphasic model resulted in an improved fit compared to one phase only, while the crystallite sizes were refined to about 7 nm for both phases. For the 800 °C sample these domain sizes have increased to 13 to 14 nm.

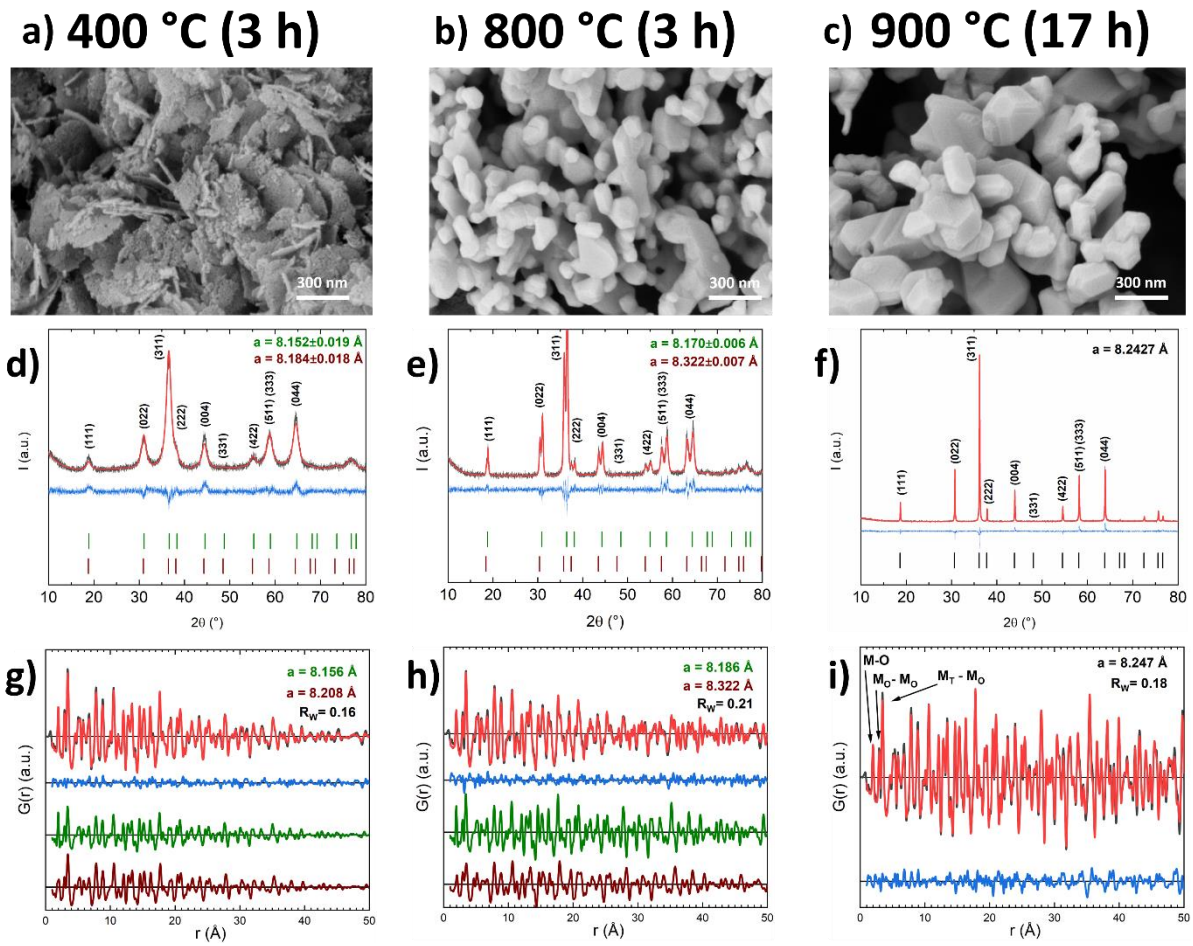

Figure 5.3.1: SEM micrographs (a-c), X-ray diffraction patterns (d-f) and PDF analysis (g-i) of the samples after thermal treatment at three different calcination temperatures. PXRD refinements (red) of experimental data (black) with difference curve (blue, in offset) are additionally indexed with Bragg reflections of the cobalt rich phase (green) and iron rich phase (brown) for 400 and 800 °C samples, and with Co_2FeO_4 for 900 °C. PDF refinements are shown with experimental PDF (black) and fit (red), as well as in offset the difference (blue), cobalt rich phase (green) and iron rich phase (brown).

To unravel the spatial distribution of phases and the composition of these novel materials, STEM-EDX measurements were conducted. Figure 5.3.2 shows STEM images and the corresponding EDX maps with spectra obtained for the indicated regions of the images (rectangles labelled by 1 and 2). For the sample calcined at 800 °C, the segregation into cobalt rich (yellow) and iron rich (blue) domains at sizes of several tens of nanometers is clearly evident and in agreement with a state "in the miscibility gap" already confirmed by XRD and PDF results. After prolonged thermal treatment at 900 °C, the phase segregation has vanished and the nominal atomic ratio of 2 to 1 is uniformly obtained (see inset in Figure 5.3.2c). For the 400 °C spinel however, a multitude of nano domains of sizes around only 5 nm are observed in the EDX map showing the lateral distribution of Co and Fe within the nano-flake (Figure 5.3.2a). This dimension is well in line with the PDF domain sizes of about 7 nm.

These domains are either enriched in cobalt or in iron, as shown in the middle and lower row of Figure 5.3.2. Thus, the STEM-EDX results confirm the co-existence of two different phases as concluded from the XRD and PDF data. According to the difference in lattice parameters and as evident from the EDX map, these two phases contain different amounts of Co and Fe and share interfaces with each other. However, due to the perfect intermixing of the cations in the precursor and the limited diffusion at the relatively low calcination temperature, the spinel is segregated only on the level of very small nano-domains.

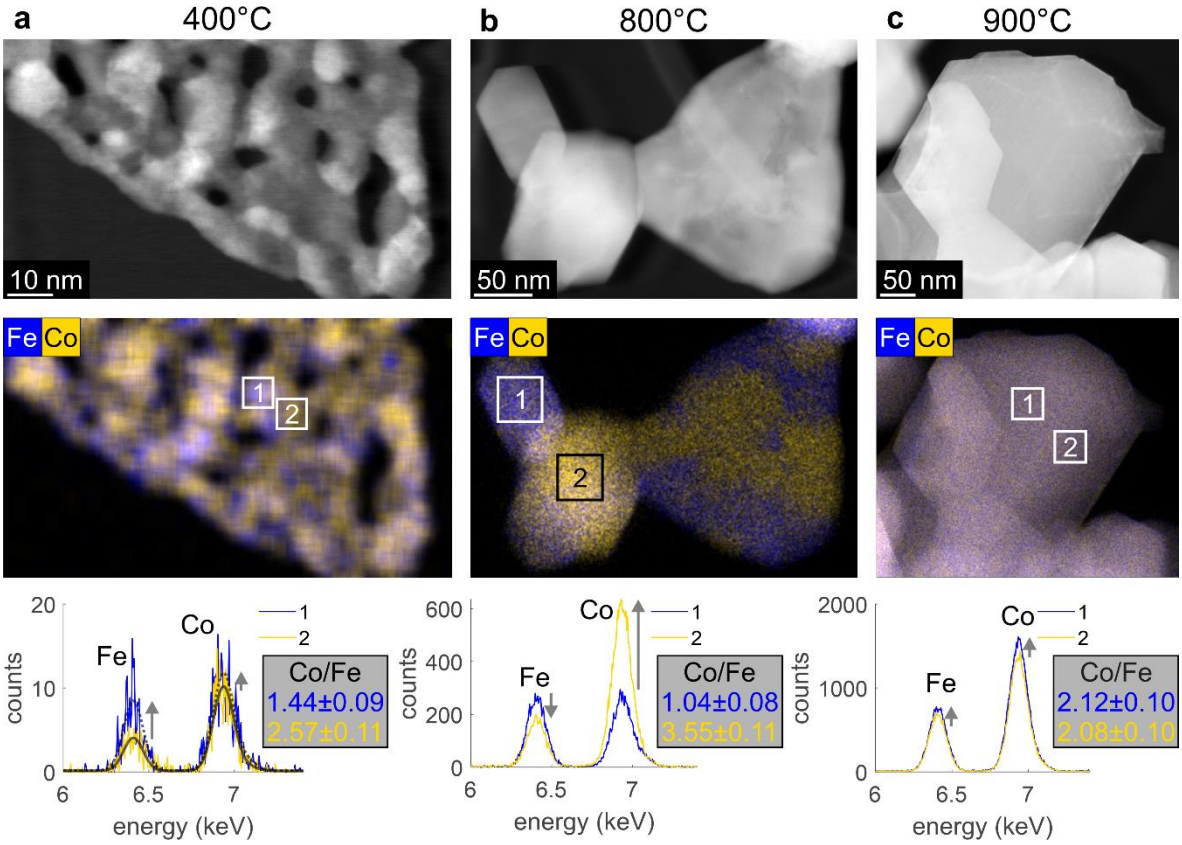

Figure 5.3.2: STEM images of all three samples (upper row), EDX maps with Fe represented in blue and cobalt represented in yellow (middle row) and the cobalt to iron atomic ratio derived from EDX spectra extracted from the two different areas 1 and 2 (lower row).

As mentioned above, the transformation from LDH precursors to spinels under mild conditions usually occurs topotactically, leading to single crystalline porous spinel platelets with their [111] direction oriented parallel to the stacking *c*-axis of the LDH (see Figure 5.2.1).[11] To study the crystallographic ordering and orientation in the 400 °C sample, consisting of two spinel phases with different cobalt to iron ratios, HR-TEM imaging on single platelets such as shown in Figure 5.3.3 was performed. The HR-TEM micrograph in Figure 5.3.3a shows atomic resolution and indicates a high and unperturbed crystalline

ordering in the whole nano-flake, which is interrupted, but not changed in orientation by the pores (see also Figure 5.6.2 in the Supporting Information). Consequently, even though there are two phases present, the Fast Fourier Transform (FFT) of the HR-TEM image in Figure 5.3.3b resembles that of a single-crystalline platelet as previously observed for the phase-pure spinels Co_3O_4 and $CoFe_2O_4$ synthesized by this approach.[11, 109] This is remarkable, as it implies that all nano-domains share the same crystallographic orientation (with [111] being the zone axis direction) and that a multitude of epitactic phase boundaries is present within each platelet, due to the very small size of the nano domains. Nevertheless, due to the different compositions of the nano domains, a description as a single crystal would not be correct. This is underlined by the detailed investigation of the FFT pattern, which showed a minimal splitting of the 4-2-2 reflections as a result of the difference in spinel lattice parameter in the two domain types (highlighted by the red and blue circle in the inset of Figure 5.3.3b). Therefore we propose a "single crystalline like" nature, with an intermediate state between single crystal and mesocrystal, as the latter is defined as arranged from individual nanoparticles and usually exhibits spatial separation between the domains,[163] which is not the case here. Inverse Fast Fourier transformation (iFFT) of the two contributions of the 4-2-2 reflection, unraveled the local distribution of the different domains. The iFFT images are superimposed with the HR-TEM image as red and blue components in Figure 5.3.3a. Most of these were found well-separated from each other, having comparable domain sizes as found for the iron and cobalt rich areas by EDX mapping. Two representative domains were selected to determine the interatomic distances in real space (Figure 5.3.3d), from which the lattice parameters for both domains were calculated from the HR-TEM image (8.0686 Å and 8.1323 Å) and summarized in Table 5.3.1.

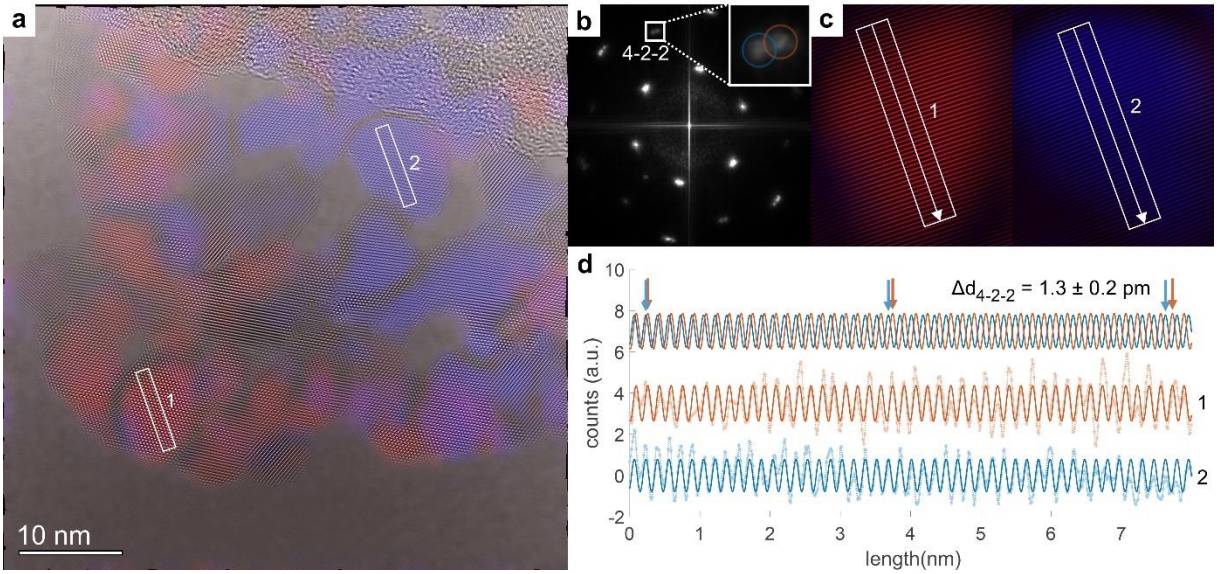

Figure 5.3.3: HR-TEM images with superimposed iFFT image of the 400 °C sample(a), FFT pattern (b), zoomed in areas 1 and 2 (c), and determination of the lattice parameter in real space (d).

Table 5.3.1 summarizes and compares the lattice parameters, and crystallite sizes derived from XRD, PDF and HR-TEM analysis. Even though all methods result in slightly different absolute values, the overall trend for all samples is the same. For the sample obtained at 400 °C with its peculiar microstructure the relative difference found between the lower and higher value is very similar independent of the method used (XRD: 0.4%, PDF: 0.6%, TEM: 0.8%). Given this consistency, the sample obtained at 400 °C can be described as holey single-crystalline-like nano-flakes with unique crystal properties between that of a single and mesocrystal.

Interestingly, all analytical techniques indicate that the lattice parameter of the iron rich phase for the sample calcined at 400 °C is significantly too small, compared to expectations from the spinodal decomposition.[88] Figure 5.3.4a shows the evolution of the lattice parameter found by Rietveld refinement with calcination temperature. The weighted average of the observed lattice parameters of the cobalt rich and the iron rich phases should result in the literature value for Co_2FeO_4[91] (dotted black line in Figure 5.3.4a), here being represented by the value for the sample calcined at 900 °C. This is only the case for calcination temperatures above 550 °C. Below, the lattice parameter of the Fe-rich phase is surprisingly small, which we attribute to the unique above-described meta-stable state of the samples. Variations in bulk composition between the samples, an incomplete LDH transformation or another side phase being present could be ruled out as an explanation as discussed in detail in the SI.

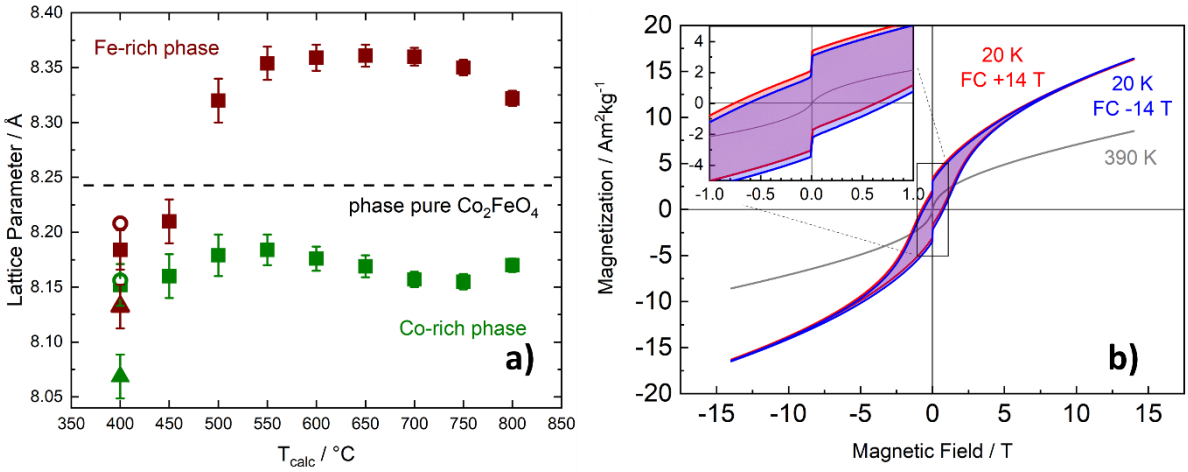

Figure 5.3.4: a) Lattice parameter of the cobalt (green)- and iron (brown) rich phases for the whole calcination series were determined by Rietveld refinement and are represented by squares. The lattice parameter for the 400 °C sample was also obtained from PDF data (open circles) and HR-TEM (triangles). b) Magnetic hysteresis loops of the sample calcined at 400 °C, measured subsequent to field cooling (FM) from 390 K at 14 T (red) and -14 T (blue).

Table 5.3.1: Lattice parameter and crystallite sizes derived from XRD, PDF and HR-TEM. The error for the lattice parameter from XRD were taken from Rietveld refinement (performed with the TOPAS software). Error for the lattice parameters from TEM result from the confidence interval of the fit. Domain size was determined as the volume-weight mean column height from integral breath.

T_{calc}	Phase	Lattice parameter XRD [Å]	Lattice parameter PDF [Å]	Lattice parameter HR-TEM [Å]	Crystallite size Lvol-IB[1] [nm]	Crystallite size PDF [nm]
400 °C	Co-rich	8.152±0.019	8.156	8.0686±0.02	5	7
	Fe-rich	8.184±0.018	8.208	8.1323±0.02	4	7
800 °C	Co-rich	8.170±0.006	8.186		16	14
	Fe-rich	8.322±0.007	8.322		18	13
900 °C	Co_2FeO_4	8.2427±0.0007	8.247		bulk-like (>50)	bulk-like

To investigate the origin of the decreased lattice parameter of the iron rich phase in the 400 °C sample and to gain deeper insight in the experimentally observed phase separation in Co- and Fe rich regions, density functional theory (DFT) calculations were performed with

the VASP code and the PBEsol exchange correlation functional[164] within the generalized-gradient approximation and an additional on-site Hubbard U = 3 eV term on both Co and Fe 3*d* states. For the calculations, we considered the bulk phases of Co_2FeO_4, the end members Co_3O_4 and $CoFe_2O_4$, as well as interfaces between the end members Co_3O_4 and $CoFe_2O_4$ with different crystallographic orientation. To model as close as possible the (111)-oriented platelets with Co and Fe rich regions, observed in the HR-TEM images, we have considered a heterostructure of (111)-oriented $CoFe_2O_4$ and Co_3O_4 with a lateral interface along the hexagonal *a*-direction ($\overline{1}\overline{1}2$). Other heterostructures with interfaces along the (111)-direction or oriented along (001) are discussed in the SI. The structural optimization of the $Co_3O_4/CoFe_2O_4$ heterostructure resulted in a decreased volume of 556.63 $Å^3$ in the Fe-rich part ($CoFe_2O_4$), which corresponds to a cubic lattice constant of 8.22 Å compared to the bulk volume of 577.13 $Å^3$ (a = 8.33 Å). The trend of the calculated values is similar to the experimental values found for the sample calcined at 400 °C (Table 5.3.1). The Co-rich part of the heterostructure, Co_3O_4, has a volume of 533.033 $Å^3$ (a= 8.11 Å) in agreement with the measurements (Table 5.3.1), which is enhanced compared to the Co_3O_4 bulk volume of 513.026 $Å^3$ (a = 8.01 Å). For comparison, the calculated lattice constant of bulk Co_2FeO_4 is 8.19 Å. Furthermore, the $Co_3O_4/CoFe_2O_4$(111) heterostructure is found to be energetically more stable by -0.15 eV/f.u. than the nominal stoichiometry Co_2FeO_4, which indicates that the spinodal decomposition into two phases is favored. The decreased lattice parameter of $CoFe_2O_4$ can be explained by the substantially smaller bulk modulus of $CoFe_2O_4$ (187.7 GPa) compared to Co_3O_4 (232.9 GPa) and Co_2FeO_4 (238 GPa), indicating a stronger compressibility of the $CoFe_2O_4$ spinel, which represents the iron rich domains, in the Co_3O_4-$CoFe_2O_4$ spinodal decomposition. The compression of the Fe-richer domains is realized due to the presence of many small alternating nano-domains, separated by epitactic interfaces. This unique state is thermally destroyed at higher calcination temperatures allowing enhanced atom mobility, i.e. around 450 to 500 °C in this case.

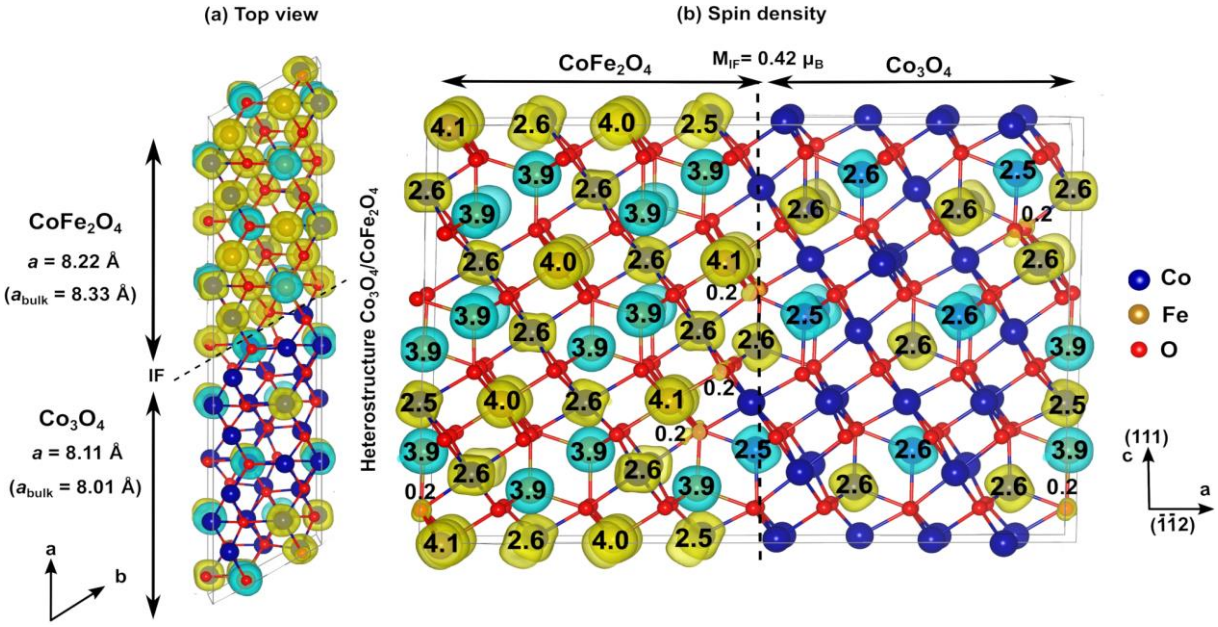

Figure 5.3.5: (a) Top and (b) side view of the structure and spin density of (111)-oriented heterostructure of $CoFe_2O_4$ and Co_3O_4 with an interface, along the a direction. Yellow and cyan colors represent the majority and minority spin density, respectively. M_{IF} presents the total magnetic moment of interface layer at the heterostructure in μ_B. a and a_{bulk} denote the lattice parameter of the $CoFe_2O_4$ and Co_3O_4 part of the heterostructure and the related bulk lattice constants, respectively.

In addition to these structural consequences, the unique morphology in the low-calcined samples is in particular interesting as the local compositional variations give rise to a multitude of interfaces between two phases with distinct magnetic properties. To further investigate the correlation of structural and magnetic properties, Mössbauer spectroscopy and magnetometry as well as DFT+*U* calculations of the magnetic properties in the bulk and at the interface were performed. The side view of the $Co_3O_4/CoFe_2O_4(111)$ heterostructures together with the spin density and magnetic moments obtained from DFT+*U*, shown in Figure 5.3.5a and b, indicates subtle changes of the magnetic moments in the vicinity of the interface: a slight enhancement of the magnetic moment of Fe^{3+} at the octahedral sites to 4.1 μ_B (bulk value: 4.0 μ_B) and a slight reduction of the magnetic moment of Co^{2+} at the tetrahedral sites to 2.5 μ_B close to the interface, the remaining Co^{2+} ions having a bulk-like magnetic moment of 2.6 μ_B. Additionally, we observe a noticeable spin-polarization of 0.2 μ_B at oxygen sites close to the interface. The layer- and element-resolved density of states, presented in Figure 5.6.4d in the SI gives further insight into the band alignment and electronic reconstruction at the interface. A noticeable exchange splitting in the majority and minority channel is obtained in the interface (IF) Co_3O_4 layer resulting in 0.42 μ_B net magnetization. Similarly, also the magnetization is enhanced also in the interface region of the $CoFe_2O_4$ part. These subtle

changes at the interface between the antiferromagnet (Co_3O_4) and the ferrimagnet ($CoFe_2O_4$) are likely the origin of the exchange bias, observed in magnetometry experiments.

Mössbauer spectroscopy was performed to analyze the cation distribution on different crystallographic positions, showing distinct variations for different annealing temperatures, as illustrated in the SI. The presence of Fe^{3+} in iron rich and cobalt rich surroundings is indicated by the appearance of a third subspectrum when comparing the single-phase material (900 °C) to the one obtained at mild calcination temperatures. At the same time, one observes marked increase in magnetic frustration, which could be assigned to a pinning of magnetic moments of the FiM iron rich regions, due to coupling to adjacent AFM Co_3O_4 like domains.

For the 400 °C sample, extensive field- and temperature-dependent magnetization measurements were performed. Results of the general magnetic characterization are illustrated in greater detail in the SI, Figure 5.6.13. All analytical techniques indicate the importance of interface effects between Co- and Fe-rich regions and support their AFM and FiM behavior accordingly. Thus, field cooling experiments were conducted to investigate possible coupling effects. To make sure to pass the Néel temperature of the cobalt rich phase during cooling, the sample was heated to 390 K and subsequently cooled to 20 K at 14 T and -14 T respectively before recording M(H) curves (see Figure 5.3.4b).[156b] The exact measurement protocol can be found in the method section. Next to a small amount of a magnetically soft phase, most interestingly the recorded M(H) curve exhibits a shift of 70 mT, which represents an exchange bias effect. Such an effect is usually only found within thin films, core-shell nanoparticles or natural minerals, and has so far not been observed in powders of particles with the above-described platelet morphology, prepared by the applied facile wet chemical and mild approach. The increase of magnetization at the interface between the nanodomains predicted by theory is assumed to be the reason for this phenomenon (see Figure 5.3.5 and further discussion in the SI). The observed exchange bias can therefore be assigned to the metastable state of the strongly intermixed AFM and FiM regions and possibly to the unusual compression of the crystal structure of the Fe-rich phase.

5.4 Conclusion

Within this work, a samples series was synthesized by applying the crystalline precursor decomposition approach to a LDH precursor with a Co:Fe ratio of 2:1 at temperatures in the range of 400 °C to 900 °C. The Co:Fe ratio lies within the miscibility gap of the spinel phase diagram, leading to samples with a differing degree of phase segregation. Using this approach led to the formation of a unique sample morphology at the mildest calcination temperature of 400 °C. Porous single-crystalline-like nano-flakes with spatial compositional fluctuations on the nano scale (ca. 5 nm) were obtained and thoroughly examined by state-of-the-art characterization methods. XRD, PDF, and HR-TEM analysis revealed a contraction of the lattice parameter of the Fe-rich phase as a result of this peculiar metastable microstructure, which can be explained by the DFT+*U* results with the higher compressibility of the Fe-rich phase and the presence of multiple interfaces. In addition, investigation of the magnetic properties showed an exchange bias effect, which we ascribe to strong coupling of adjacent AFM cobalt rich and FiM iron rich regions within the platelets, as also indicated by Mössbauer spectroscopy data. Such magnetic properties form the basis for different applications and are usually only observed in materials with designed interfaces, not self-assembled in powders. We believe that this facile synthetic approach can be transferred to other oxides and holds potential for unlocking new magnetic properties via self-assembled nanostructures.

5.5 Methods

Synthesis of the three investigated samples was done employing the crystalline precursor decomposition approach, reported earlier.[109] The layered double hydroxide precursor was precipitated in an automatic lab reactor system (*OptiMax, Mettler Toledo*) under constant pH and temperature. 125 mL of a metal salt solution containing 0.566 M $Co(NO_3)_2x6H_2O$ und 0.233 M $Fe(NO_3)_3x9H_2O$ was gravimetrically dosed into a single walled glass reactor, prefilled with 200 mL desalinated water, over the course of one hour. A 0.9 M NaOH and 0.06 M Na_2CO_3 basic solution serving as precipitation agent was dosed automatically into the reactor, constantly keeping a pH of 8.5 and the temperature at 50 °C during the precipitation

period. The pH was controlled by a Semi-Micro L pH electrode. After precipitation the precipitate was aged for 1 h at 50 °C without further pH control. After cooling down to room temperature, the precipitate was separated from the mother liquor by centrifugation and washed with desalinated water until the conductivity of the washing water fell under 100 µS. The washed powder was dried in static air at 80 °C for at least 12 h.

The as-prepared layered double hydroxide precursor was subjected to thermal treatments in a muffle furnace (*Nabertherm LE 6/11/B150*). With a heating ramp of 2 K min^{-1} thermal treatment was conducted at 400 °C to 900 °C in 50 °C steps, holding times being 3 h up to 850 °C and 17 h for the 900 °C.

X-ray diffraction patterns of the samples were recorded on a Bruker D8 Advance with a Cu X-ray source in Bragg-Brentano geometry, using a LYNXEYE XE-T detector. The samples were dispersed in ethanol on a PMMA sample holder and measurements were performed in the range from 5 ° to 90 ° 2θ with a step size of 0.01 ° and a counting time of 1.5 s. Rietveld refinements for phase analysis, determination of lattice parameters and crystallite size the TOPAS software was used.

Thermogravimetric analysis of the precursor was carried out on a Netzsch STA449F3A-1226-M thermobalance. The precursor was heated with a rate of β= 2 K min^{-1} in air up to 1000 °C and the mass loss was recorded.

Elemental analysis was performed via inductively coupled plasma – optical spectrometry (ICP_OES, Vista RL; Varian), the O content was determined with the carrier gas hot extraxtion method (THC 600, LECO).

Scanning electron microscopy (SEM) was conducted with an Apreo S LoVac (Thermo Fisher Scientific). Prior to the measurements, the samples were sputtered with Pt/Au.

Surface area determination for the LDH precursor and samples calcined at 400 °C and 800 °C were carried out in a NOVA 300 (Quantachrome GmbH). 100 mg of each sample were degassed and dried for 2 h at 80 °C in vacuum prior to the measurement. Complete sorption isotherms were obtained at liquid nitrogen temperature.

The surface area of the sample calcined at 900 °C was determined with Kr in a Belsorp-mini setup (MicrotracBEL Corp.) after pretreatment in a vacuum at 150 °C for 24 h.

Powder X-ray diffraction (XRD) for PDF analysis was carried out at room temperature with a STOE STADI P Mythen2 4K diffractometer (Ge(111) monochromator; Ag $K\alpha_1$ radiation, λ =

0.5594 Å) using four Dectris MYTHEN2 R 1K detectors in Debye–Scherrer geometry. Samples were measured in 0.5 mm diameter glass capillaries purchased from Hilgenberg (special purpose glass number 10) for 20 h. The Q-range was 20.4 $Å^{-1}$. For more information on this dedicated diffractometer for pair distribution function analysis, see [165]. PDF processing was carried out with xPDFsuite[166] using a Qmax of 19.5 $Å^{-1}$, and the refinement was done in PDFgui.[167] Parameters refined were the scale, cell parameters, crystalline domain sizes, correlated atomic motion and atomic displacement parameters. PDF were fit in the range of 1 – 50 Å for the 400 and 800 °C samples, and over 1 – 100 Å for the 900 °C sample.

Scanning transmission electron microscopy in combination with energy-dispersive X-ray spectroscopy (STEM-EDX) was performed on a Thermo Fisher Talos F200X. The microscope was equipped with a high brightness field emission gun (X-FEG) and 4 SDD EDX detectors, giving together a detection area of 0.9 sr. The electron beam energy was 200 keV and the beam current ranged from 100 to 450 pA. The point resolution of the microscope was 1.6 Å. A multiple frame approach was applied to reduce electron beam induced artifacts on the sample. Therefore, the electron beam was scanned across the region of interest several times (up to 210 frames), with short acquisition times ranging from 50 to 100 µs per pixel, and the signal was integrated later. To compensate for sample drift during EDS acquisition, Velox drift correction was applied by cross-correlation after each frame. For EDX quantification, an empirical background model together with Brown-Powell cross sections have been used, as implemented in Velox software. High-resolution transmission electron micrographs (HR-TEM) have been recorded in double-corrected Jeol JEM-ARM200F equipped with a cold field emission gun, operated at 200 keV. TEM images were acquired with a OneView camera by 4kx4k pixels. To minimize for lateral drift, a set of 20 images was recorded with short acquisition times and summed later. To correct for drift and reduce noise, the following post-processing routine was developed and applied.

For the post processing we developed an algorithm that suppresses noise in the data by averaging over structures that are similar. In this regard it is similar to Non-Local Means[168] and block matching[169] algorithms but instead of the usual way of finding patches for the averaging a combination of global pattern matching via normalized cross correlation and k-mean clustering is used. This allows for using the information contained in all acquired frames to suppress noise in each individual frame.

Mössbauer spectra were recorded in standard transmission geometry, using a ^{57}Co(Rh) radiation source mounted on a constant-acceleration driving unit (WissEl GmbH). Low temperatures and high magnetic fields were achieved with the help of two liquid helium bath cryostats (Thor Cryogenics, Oxford Instruments) containing superconducting split-pair field coils. Data evaluation was carried out with the "Pi" program package, with all spectra being referenced to α-Fe at room temperature.

Magnetic characterization of the whole calcination series was carried out with the vibrating sample magnetometer (VSM) option of a Quantum Design PPMS DynaCool, with field dependent M(H) loops being recorded up to maximum fields of ±9 T and temperatures down to 4.3 K. To check for the potential presence of exchange bias effects, the following procedure was utilized: The samples were heated up to 600 K for a duration of approximately 10 min, followed by cooling under selected applied magnetic fields down to the respective measurement temperatures.

For the 400 °C sample, the exchange bias was investigated with the VSM option of a Quantum Design PPMS with M(H) loops subsequent to field cooling in -14 T and +14 T.

The density functional theory (DFT) calculations were performed using Vienna ab initio simulation package (VASP code),[170] employing the projector augmented wave (PAW) method.[171] For the exchange-correlation functional the generalized-gradient approximation in the parametrization of Perdew-Burke-Enzerhof for solids (PBEsol) was used. Static correlation effects are taken into account by applying an on-site Coulomb repulsion parameter U=3 eV on the Co and Fe 3d states within the rotationally invariant formulation of Dudarev et al.[172] In this study we modeled the bulk compounds $CoFe_2O_4$, Co_3O_4 and Co_2FeO_4 with different cation and spin arrangements, as well as $Co_3O_4/CoFe_2O_4$ heterostructures with (001) and (111) orientation and for the latter case interfaces along the (111) and ($\overline{1}\overline{1}$2) direction, containing 56, 84 and 168 atoms in the unit cell, respectively, as shown in the SI Figure 5.6.5.

We used a plane-wave cut-off energy of 500 eV and a Gamma-centered k-point mesh of 10 × 10 × 5 for the (111)-oriented bulk of $CoFe_2O_4$, Co_2FeO_4 and Co_3O_4 ,2 × 10 × 5 and 10 x 10 x 2 for the (111) heterostructure along ($\overline{1}\overline{1}$2) and (111), and 10 x 10 x 4 for the (001) heterostructure. Both volume and internal parameters were optimized with the residual forces smaller than 0.01 eV/Å.

5.6 Supporting Information

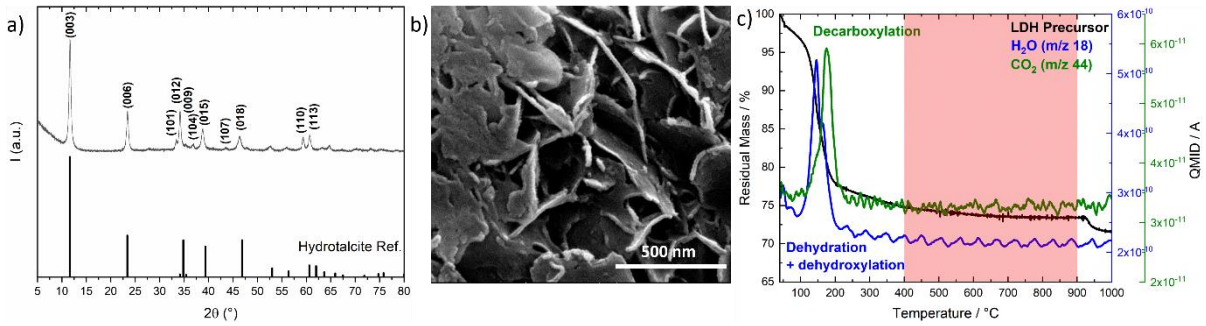

Figure 5.6.1: Characterization data of the $(Co^{2+}_{0.67}Fe^{3+}_{0.33})(OH)_2(CO_3)_{0.17} \times mH_2O$ precursor: a) XRD pattern of the as-synthesized LDH precursor, b) SEM micrograph of the as-synthesized precursor, c) and thermogravimetric analysis.

Table 5.6.1: Rietveld refinement parameter for the whole calcination series.

T_{calc} (°C)	R_{exp}	R_{wp}	R_p	R_{exp}'	R_{wp}'	R_p'	GOF
400	5.46	6.66	5.25	7.46	9.09	7.51	1.22
450	10.58	11.01	8.57	9.79	10.20	8.65	1.04
500	10.40	10.81	8.42	9.59	9.97	8.43	1.04
550	10.57	10.96	8.49	9.75	10.11	8.56	1.04
600	10.50	11.23	8.80	9.83	10.52	8.96	1.07
650	10.99	11.48	8.93	9.98	10.42	8.98	1.04
700	11.13	12.08	9.38	9.69	10.52	8.95	1.09
750	10.64	11.82	9.20	9.59	10.65	9.15	1.11
800	9.82	12.14	9.46	9.40	11.62	9.92	1.24
900	7.68	12.32	9.70	10.25	16.44	14.07	1.60

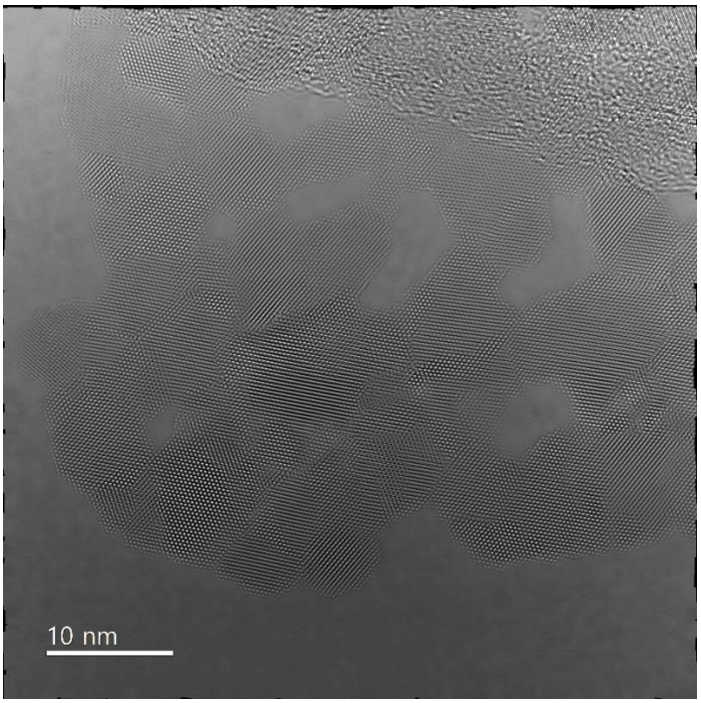

Figure 5.6.2: HR-TEM micrograph of a single nano flake calcined at 400 °C.

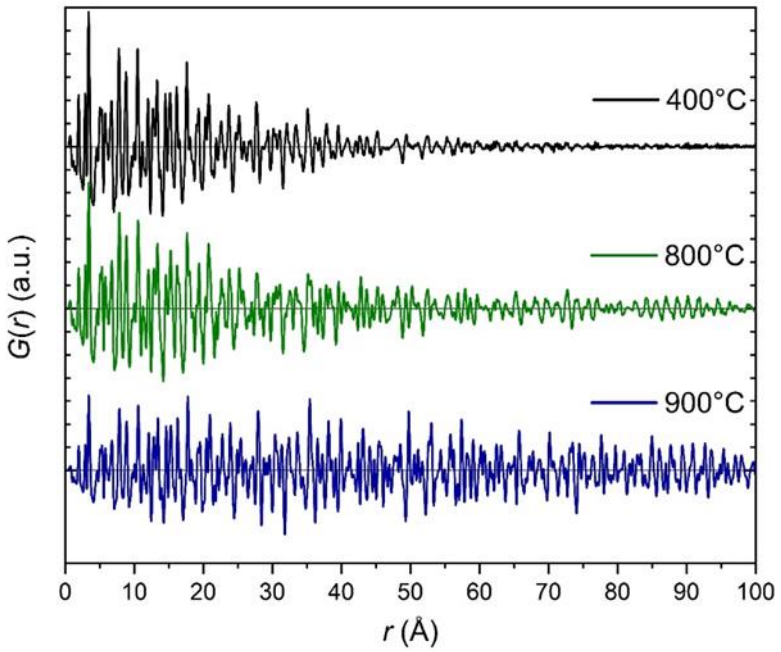

Figure 5.6.3: Experimental PDF data of Co/Fe LDH calcined at 400, 800 and 900 °C displayed up to 100 Å to show the differing crystallinity of the samples.

Table 5.6.2: Results of PDF refinements: refined parameters.

Sample	400 °C	400 °C		800 °C		900 °C
applied phases	Co_2FeO_4	Co_3O_4	$CoFe_2O_4$	Co_3O_4	$CoFe_2O_4$	Co_2FeO_4
ISCD number	98551	9362	109044	9362	109044	98551
a (Å) (start)	8.242	8.065	8.394	8.065	8.394	8.242
a (Å)	8.178	8.156(0)	8.208(5)	8.186(1)	8.322(2)	8.247(4)
crystallite size (Å)	60	69	65	139	128	"bulk" [a]
$U_{iso,TL}$ **(Å^2)**	0.013	0.010	0.013	0.009	0.014	0.011
$U_{iso,TL2}$ **(Å^2)**	-	0.010	-	0.011	-	-
$U_{iso,OL}$ **(Å^2)**	0.010	0.007	0.014	0.010	0.027	0.009
$U_{iso,O}$ **(Å^2)**	0.026	0.015	0.033	0.027	0.045	0.031
phase ratio	-	41 %	59 %	50 %	50 %	-
Fit range (Å)	1 – 50	1 - 50	1 - 50	1 - 100	1 - 100	1 - 100
R_w	0.20	0.16		0.21		0.18

Discussion of the decreased lattice parameter:

One might argue that the unexpectedly small lattice parameter is caused by a variation in bulk composition, an incomplete transformation of the LDH precursor, or another side phase being present after thermal treatment at 400 °C. To address these possible discrepancies, elemental analyses for all three representative samples were performed, the results are shown in Table 5.6.3.

Table 5.6.3: Atomic percentage of cobalt, iron, and oxygen and the respective ratios for the three calcination temperatures.

T_{calc}	Co %at	Fe %at	O %at	Co:Fe:O
400 °C	27.2	13.4	59.4	2.03:1:4.43
800 °C	29.5	14.5	56.0	2.04:1:3.86
900 °C	28.9	14.2	56.9	2.03:1:4.01

Next to the already confirmed ratio of Co:Fe of 2:1 from EDX measurements, the results only show minor deviations from the theoretical ratio for Co:Fe:O of 2:1:4. The ratio of Co:Fe in all cases again is very close to the desired value of 2:1, ruling out the argument of a variation in bulk composition, and with that eliminating the possibility of an iron deficiency in the sample lowering the overall lattice parameter. An incomplete transformation of the precursor LDH can be ruled out by thermogravimetric analysis and X-ray diffraction, which showed no significant mass loss after 400 °C (1.3%wt between 400 °C and 800 °C) and no crystalline by-phases in the diffraction pattern, respectively. However, small deviations in the overall amount of oxygen are observed in elemental analysis. The 400 °C sample exhibits the highest amount of oxygen, namely 2.3 at% more than the anticipated 57.1 at% nominal oxygen content. Again, an amorphous by-phase could be ruled out with the help of lattice parameter calculation using Vegard's law. The 2.3 at% oxygen is assumed to be incorporated in an iron containing by-phase. Even if from this it is generously presumed that 3%at iron is missing in the iron rich phase, the resulting lattice parameter is still significantly too small. After ruling out the above-mentioned possibilities, the increased amount of oxygen hints towards a spinel with excess oxygen $Co_2FeO_{4+\delta}$. It is known from literature that super stoichiometric spinels can exhibit decreased lattice parameters.[173] Nevertheless, the decrease in lattice parameter for the iron rich phase in the 400 °C sample is so pronounced that it is concluded that additional effects have to be considered in this case.

DFT:

To gain insight in the experimentally observed phase separation of Co_2FeO_4 in Co- and Fe rich regions and to investigate the origin of the decreased lattice parameter of the iron rich phase, density functional theory (DFT) calculations were performed with the VASP code and PBEsol exchange correlation functional[164] within the generalized-gradient approximation and an additional on-site Hubbard U = 3 eV term on both Co and Fe 3*d* states. We considered the bulk phases of Co_2FeO_4, the end members Co_3O_4 and $CoFe_2O_4$, as well as interfaces between the end members Co_3O_4 and $CoFe_2O_4$. In particular, we have considered interfaces with (111) and (001) surface orientation. For the (111)-orientation both interfaces along the c- and the a-axis were modelled, the latter being closest to the experimental observation of (111)-oriented platelets with mosaic pattern of Co- and Fe-rich regions. In the normal spinel Co_3O_4, low spin (LS) Co^{3+} cations with a quenched magnetic moment (see the spin density in

Figure 5.6.4) occupy the octahedral sites, whereas Co^{2+} cations with a magnetic moment of 2.6 μ_B fill the tetrahedral sites. The latter order antiferromagnetically, rendering Co_3O_4 an antiferromagnetic semiconductor. The calculated bulk lattice constant of 8.01 Å is 0.6-0.8% smaller than the experimentally reported value of 8.06-8.08 Å[174] and in agreement with previous theoretical values of 8.04 Å (PBEsol+*U*, *U* = 4.4 eV).[175]

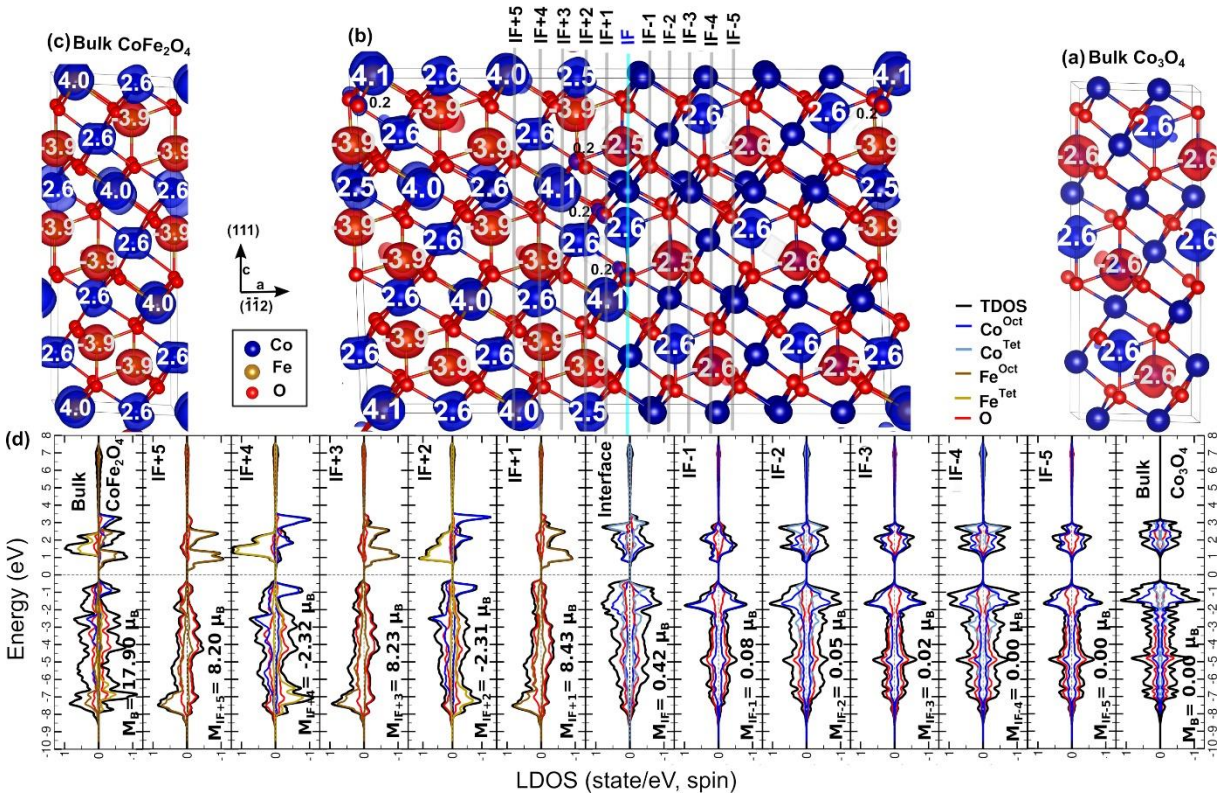

Figure 5.6.4: Structure and spin density of (111)-oriented (a) bulk Co_3O_4, (b) heterostructure of $CoFe_2O_4$ and Co_3O_4 with an interface, perpendicular to the a direction and (c) bulk $CoFe_2O_4$. Blue and red colors represent the majority and minority spin density, respectively.(d) Layer and element-resolved density of states of the $Co_3O_4/CoFe_2O_4$(111) heterostructure and also bulk of Co_3O_4 (right) and $CoFe_2O_4$ (left). M_{IF-n} presents the total magnetic moment of each layer at heterostructure in μ_B. The color code for the partial LDOS contribution of different ions is indicated in the upper right of LDOS.

On the other hand, in the fully inverse $CoFe_2O_4$ spinel, Co^{2+} cations with a magnetic moment of 2.6 μ_B occupy the octahedral sites, whereas the Fe^{3+} cations fill both tetrahedral and octahedral sites with magnetic moments of -3.9 μ_B and 4.0 μ_B, respectively. The latter two couple antiferromagnetically; the parallelly aligned Co^{2+} moments lead to the ferrimagnetic behavior of $CoFe_2O_4$. The calculated lattice constant of 8.33 Å is close to the experimental values (8.37-8.39 Å).[176] Moreover, the bulk modulus of $CoFe_2O_4$ is considerably smaller (187.7 GPa) than the one of Co_3O_4 (232.9 GPa), indicating a stronger compressibility.

For Co_2FeO_4 with the inverse spinel structure, Co cations are distributed at the tetrahedral and octahedral sites with a magnetic moment of 2.5 μ_B (Co^{2+}) and 0.0 μ_B (Co^{3+}), respectively. Fe^{3+} cations are located at octahedral sites with magnetic moments of 4.1 μ_B. The calculated lattice constant of 8.19 Å is 0.6% less than the experimental value of 8.24 Å.[174b, 177] (see also present XRD and PDF measurements presented in Table 5.3.1). Previous results using PBE+*U* (U_{Co}= 2 eV, U_{Fe}= 3 eV) [178] render a higher value of 8.27 Å As presented in Table 5.6.4, the calculated bulk modulus of 238 GPa for Co_2FeO_4 is higher than the value of 187.7 GPa for $CoFe_2O_4$ (experimental value: 185 GPa)[179] and 232.9 GPa for Co_3O_4 (experimental value 249±1 GPa).[180] Additionally, we also calculated the bulk modulus, lattice constant of other possible configurations, e.g. considering low spin states for Fe and Co and normal as well as inverse phases. The energy difference to the most stable phase (ΔE) and the heat of formation (ΔH) are presented in Table 5.6.4.

Table 5.6.4: Calculated lattice constants and bulk modulus for $CoFe_2O_4$, Co_3O_4 and Co_2FeO_4 for both normal and inverse spinel structures and considering Fe and Co ions for both low and high spin states with PBEsol+U ($U_{Co,Fe}$ = 3 eV). ΔE is the energy difference of each phase from the most stable one. ΔH is the heat of formation.

Structure	**Lattice constant (Å)**	**Bulk modulus (B_0) GPa**	**ΔE (eV/f.u)**	**ΔH (eV)**
inverse – $CoFe_2O_4$	**8.33** (Exp: 8.37-8.39)[176]	**187.7** (Exp: 185)[179]	**0.0**	**-11.43**
normal – $CoFe_2O_4$	**8.37**	**183.8**	**0.25**	**-11.18**
inverse – $CoFe_2O_4$ –Fe: low spin	**8.21**	**363.0**	**2.74**	**-8.70**
inverse – $CoFe_2O_4$ – Fe & Co: low spin	**7.97**	**247.8**	**3.21**	**8.23**
normal – $CoFe_2O_4$ – Fe: low spin	**8.10**	**248.0**	**1.58**	**-9.85**
normal – $CoFe_2O_4$ – Fe & Co: low spin	**8.14**	**561.7**	**2.62**	**-8.82**
normal – Co_3O_4	**8.01** (Exp: 8.06-8.08)[174]	**232.8** (Exp: 249±1)[180]	**0.0**	**-9.78**
inverse – Co_2FeO_4	**8.19** (Exp: 8.24)[137, 174b]	**238.8**	**0.0**	**-10.32**
inverse – Co_2FeO_4 – Fe: low spin	**8.06**	**252.5**	**0.55**	**-9.77**
normal - Co_2FeO_4	**8.10**	**278.8**	**0.45**	**-9.87**
normal – Co_2FeO_4 – Fe: low spin	**8.04**	**549.7**	**0.86**	**-9.45**

According to the HR-TEM images, the platelets are oriented along the (111)-direction with Co and Fe rich regions in a mosaic pattern. To model as close as possible to the experimental observation we have considered explicitly heterostructures of (111) oriented $CoFe_2O_4$ and Co_3O_4 with a lateral interface along the hexagonal *a*-direction (Figure 5.6.4). The DFT+*U* results for further heterostructures with (001) and (111) oriented interfaces are shown inFigure 5.6.5.

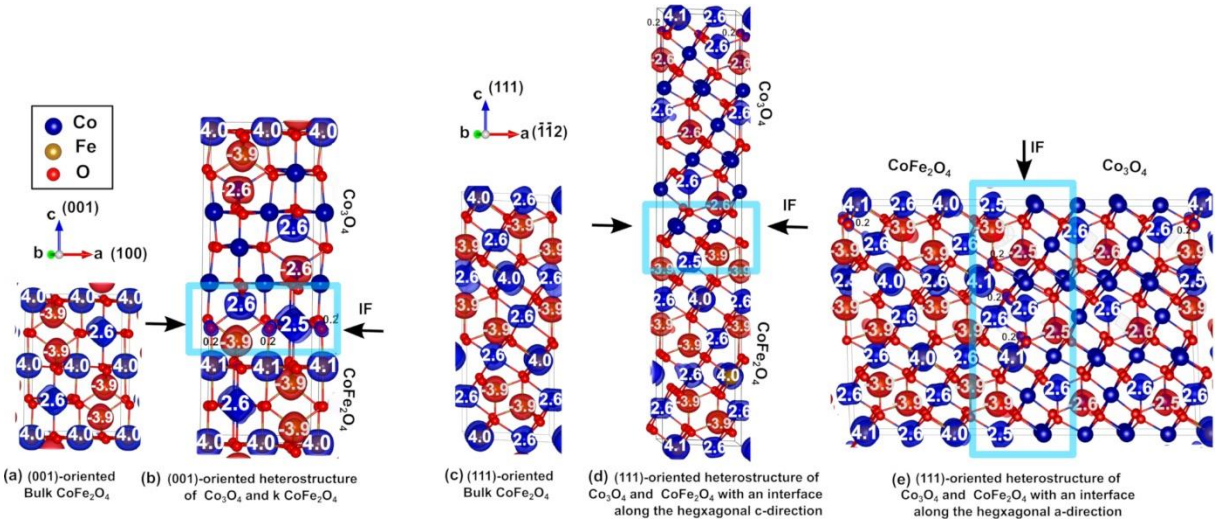

Figure 5.6.5: Side view of the structure and spin density of bulk phases and heterostructures with different orientations: (a) (001) and (c) (111) oriented bulk of $CoFe_2O_4$ (b) (001) and (d) (111)- oriented heterostructure of $CoFe_2O_4$ and Co_3O_4 with an interface along the (d) (111) (e) ($\bar{1}\bar{1}2$) direction.

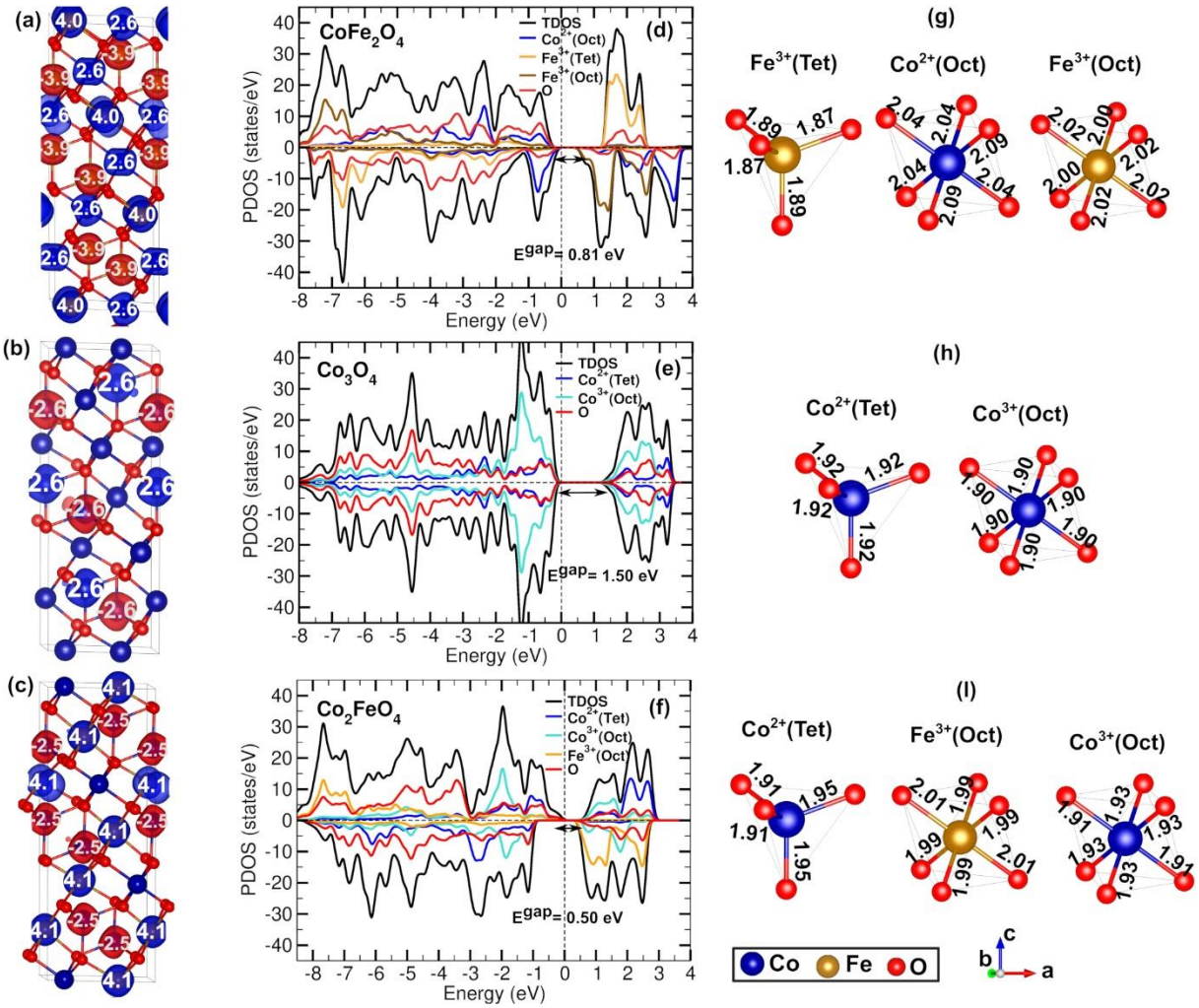

Figure 5.6.6: The spin density of bulk (a) $CoFe_2O_4$, (b) Co_3O_4, and (c) Co_2FeO_4 with their corresponding projected density of states (d,e,f,). The respective Fe-O and Co-O bond length at the tetrahedral (Tet) and octahedral (Oct) sites are presented in g-l.

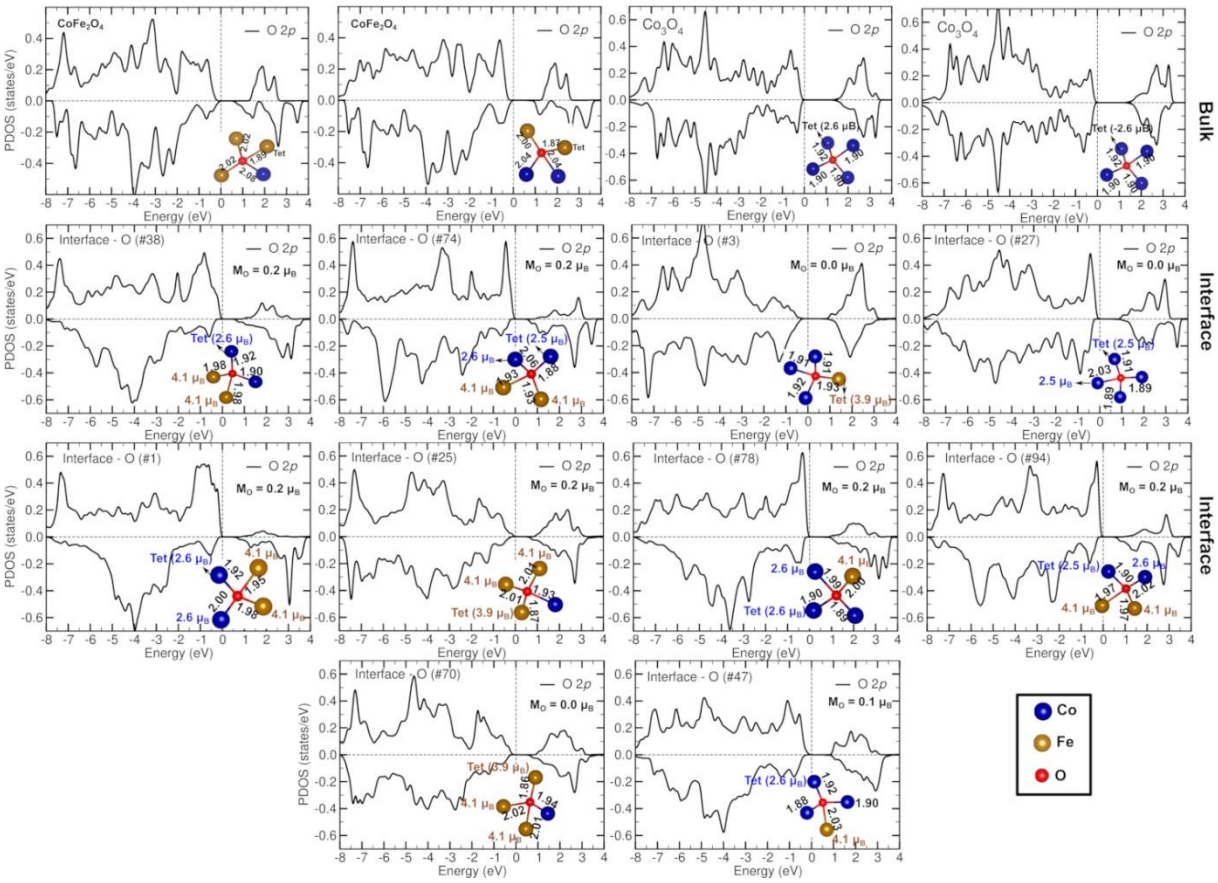

Figure 5.6.7: Projected density of states (PDOS) of oxygen 2p states in the bulk end members (first row) and the at the interface of the $Co_3O_4/CoFe_2O_4(111)$ heterostructure. The positions of the oxygen ions are numbered according to Figure 5.6.8. Tetrahedrally coordinated cations are denoted by Tet, the remaining are cations are positioned at the octahedral sites. All reported bond length (black) are in Å. M_o represents the magnetic moment of oxygen at the interface.

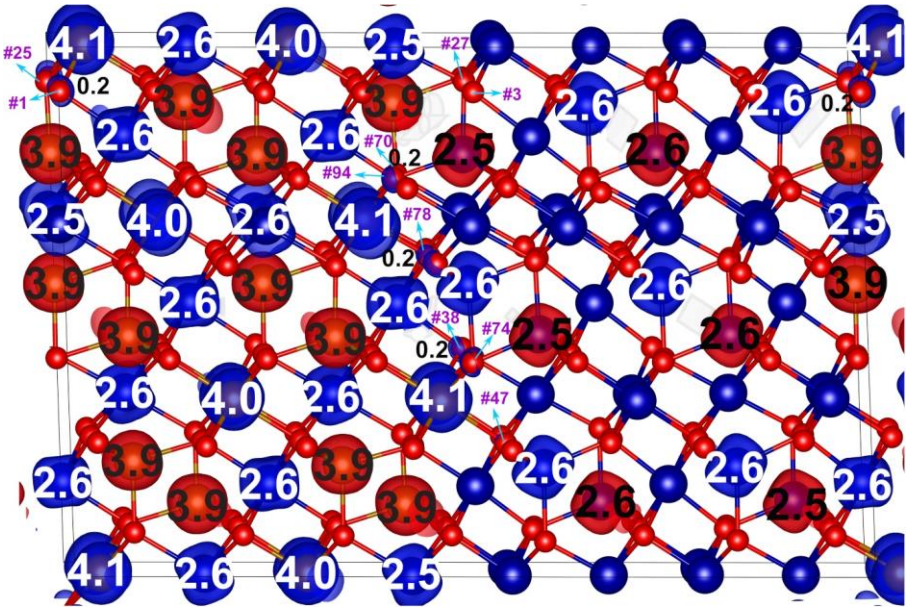

Figure 5.6.8: Side view and spin density of $Co_3O_4/CoFe_2O_4(111)$ heterostructure with an interface along the (112) direction. #n indicates the oxygens number at the interface of Co_3O_4 and $CoFe_2O_4$.

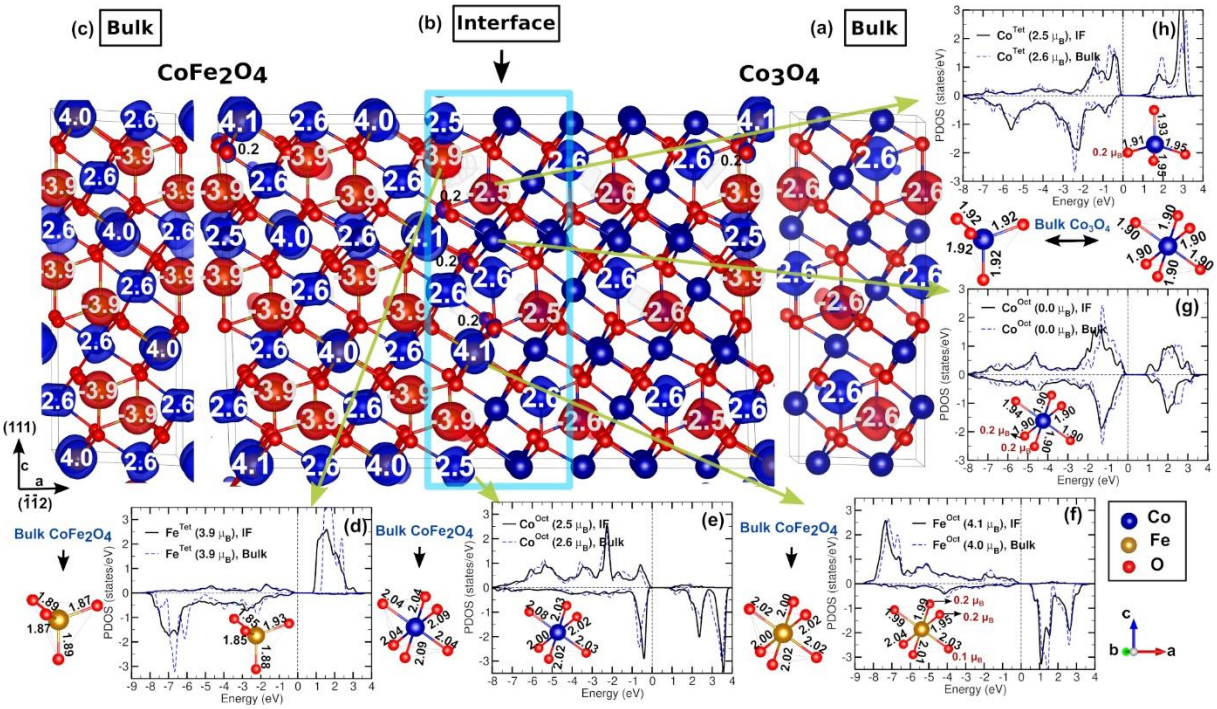

Figure 5.6.9: Structure and spin density of (111)-oriented (a) bulk $CoFe_2O_4$, (b) heterostructure of $CoFe_2O_4$ and Co_3O_4 with an interface, perpendicular to the a direction and (c) bulk Co_3O_4. Blue and red colors represent the majority and minority spin density, respectively. Additionally, the projected density of states (PDOS) of cations at the interface: (d) Co^{tet}, (e) Co^{oct}, (f) Fe^{tet}, (g) Co^{oct}, and (h) Fe^{oct} (black solid lines) is compared to the respective PDOS in the end member (dashed lines). The insets show the local environment and the Co-O and Fe-O bond length in Å for cations at the interface and the respective bulk end members.

The structural optimization of the $Co_3O_4/CoFe_2O_4$ heterostructure resulted in a decreased volume of 556.63 $Å^3$, which corresponds to a cubic lattice constant 8.22 Å in the Fe-rich part ($CoFe_2O_4$) of the heterostructure (experiment: 8.171 Å (XRD) and 8.208 Å (PDF)), compared to the bulk volume of 577.13 $Å^3$ (a = 8.33 Å). The Co-rich part of the heterostructure, Co_3O_4, has a volume of 533.033 $Å^3$ (a= 8.11 Å) in agreement with measurements (8.129 Å (XRD) and 8.156 Å (PDF)) which shows a slight increase compared to the Co_3O_4 bulk volume of 513.026 $Å^3$ (a = 8.01 Å) in agreement with the experimental observations. The $Co_3O_4/CoFe_2O_4$(111) heterostructure is found to be 0.15 eV/f.u. more favorable than the initial stoichiometry Co_2FeO_4 which indicates that the separation in the two phases is more favorable than the formation of Co_2FeO_4 in agreement with experiments.

A side view of the $Co_3O_4/CoFe_2O_4$(111) heterostructures together with the spin density is shown in Figure 5.6.4 along with the spin densities of the bulk phases (Figure 5.6.4a and c). While no drastic changes are observed at the cation sites, the magnetic moment of Fe^{3+} at the

octahedral sites close to the interface is slightly enhanced to 4.1 μ_B (bulk value: 4.0 μ_B). The magnetic moment of Co^{2+} at the tetrahedral sites close to the interface in the $CoFe_2O_4$ part is reduced to 2.5 μ_B, the remaining Co^{2+} ions having a magnetic moment of 2.6 μ_B, similar to bulk. Additionally, we observe a noticeable spin-polarization of 0.2 μ_B at oxygen sites close to the interface.

The layer and element-resolved density of states, presented in Figure 5.6.4d gives further insight into the band alignment and electronic reconstruction at the interface. In particular, the band gaps towards the center of each phase resemble the ones of the bulk phases (0.81 eV in $CoFe_2O_4$ and 1.5 eV in Co_3O_4, see Figure 5.6.6 for comparison), but are modified close to the interface, e.g. the one of Co_3O_4 is reduced. Remarkably, a significant exchange splitting in the majority and minority channel is obtained in the interface (IF) Co_3O_4 layer resulting in 0.42 μ_B net magnetization, in contrast to the zero net magnetization of the antiferromagnetic bulk Co_3O_4. The effect fades away from the interface and converges to bulk behavior towards the center of the Co_3O_4 region. A slight enhancement of the total magnetization is also obtained in the interface (IF+1) $CoFe_2O_4$ layer (8.43 μ_B) compared to the IF+3 (8.23 μ_B). The interface-induced magnetization may be responsible for the experimentally observed exchange bias. For further analysis, the projected density of states (PDOS) of Co and Fe cations at the interface as well as the corresponding Fe-O and Co-O bond lengths are plotted and compared to the ones in bulk Co_3O_4 and $CoFe_2O_4$ for both tetrahedral and octahedral sites in Figure 5.6.9d-h. In general, subtle changes occur and a slight downward shift of bands at the interface w.r.t. the bulk PDOS of Co_3O_4 and $CoFe_2O_4$. Overall, the Co^{Tet}-O bond lengths at the interface tend to be longer than in the respective bulk environments, the opposite trend is observed for the octahedral sites and Fe^{Tet}-O bond lengths. In particular shorter Fe^{Oct}-O bond lengths of 1.95 and 1.99 Å compared to the bulk (2.0 and 2.02 Å) emerge at the interface to oxygen ions with magnetic moments of 0.2 μ_B. Such an effect is not observed for the Co^{Oct}-O (Fe-rich part), the oxygen ions remain nonmagnetic in this case. The Co^{Oct}-O bond lengths (Co-rich) do not show remarkable changes compared to the bulk. These subtle changes at the interface between the antiferromagnet (Co_3O_4) and the ferrimagnet ($CoFe_2O_4$) are likely the origin of the observed exchange bias – an effect that was previously observed for other mostly polar oxide interfaces, e.g. CoO/Co_3O_4 [160d] and $Fe_2O_3/FeTiO_3$.[161c, 181]

Mössbauer Spectroscopy:

The sample calcined at 900 °C, is composed of two clearly separated subspectra as shown by the associated Mössbauer spectrum (Figure 5.6.10), representing Fe atoms on tetrahedrally coordinated A-sites (blue) and octahedrally coordinated B-sites (green) of the spinel lattice. We observe overall sharp spectral lines, reproduced via narrow hyperfine field distributions corresponding to a low variation of local surroundings of the Fe atoms, strongly suggesting a single-phase state of the sample after calcination in agreement to XRD data. The spectrum displays low intensity of lines 2 and 5 due to a very low degree of spin canting, which can be converted to spin canting angles of ca. 21(1) ° and 0(9) ° for the B- and A-site, respectively.[182] A comparison of the subspectral intensities indicates an occupation of 21(2) % of Fe^{3+} ions on tetrahedral lattice positions, and thereby a preferential B-site placement.[156b]

After calcination at 800 °C, the Mössbauer spectrum is accompanied by a slight increase in spin-canting, the spectral component of higher nuclear Zeeman splitting now consists of two subspectra (purple color in Figure 5.6.10) with slightly different hyperfine magnetic fields. This effect is more pronounced by comparing spectra of samples annealed at intermediate temperatures in the range of 450-750 °C shown in Figure 5.6.11. Presumably, this is caused by the presence of two distinct phases, where Fe atoms are placed on A-sites in either an Fe-rich ($CoFe_2O_4$-like) or Co-rich (Co_3O_4-like) environment, resulting in a minor variation of the hyperfine magnetic field.[183] However, it should be noted that findings by Takahashi et al indicated that at low temperatures the A sublattice magnetization may be dominant in cobalt rich spinels, in which case the violet subspectrum could correspond to B-site Fe^{3+} in an cobalt rich surrounding, alternatively.[156b]

For the 400 °C sample, the degree of spin canting is significantly increased which leads to a partial overlap of the three subspectra and thus individual contributions are difficult to resolve. Enhanced spin canting is indicative for magnetic pinning, which is here likely caused by the high specific interface area (domain sizes of only ca. 5 nm) of the strongly intermixed regions of differing composition. The spin canting increases rather abruptly for lower calcination temperatures, which is explained by the stronger interface coupling of both phases. The Co-rich phase tends to order antiferromagnetically for $x_{Co} \lessapprox 3$, also preventing the full orientation of the adjacent ferrimagnetic Fe-rich ($CoFe_2O_4$-like) phase, which is usually easily aligned at moderate magnetic fields of 10 T.

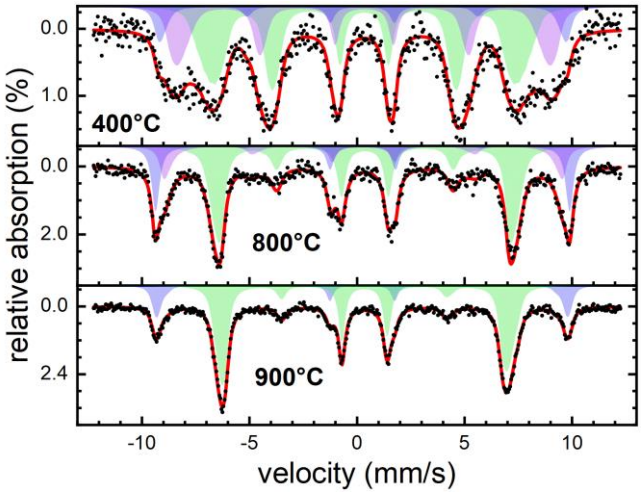

Figure 5.6.10: Mössbauer spectra recorded at 4.3K and an applied field of 10 T parallel to the γ-ray propagation direction on the representantive samples calcinated at 400 °C, 800 °C and 900 °C. Experimental data (black dots) is shown together with a theoretical data fit (red line) composed of several superimposed subspectra, representing Fe atoms residing on B- (green) and A-sites of the spinel lattice, with latter being assigned to contributions from Fe^{3+} ions in Fe-rich (blue) and Co-rich (violet) environments.

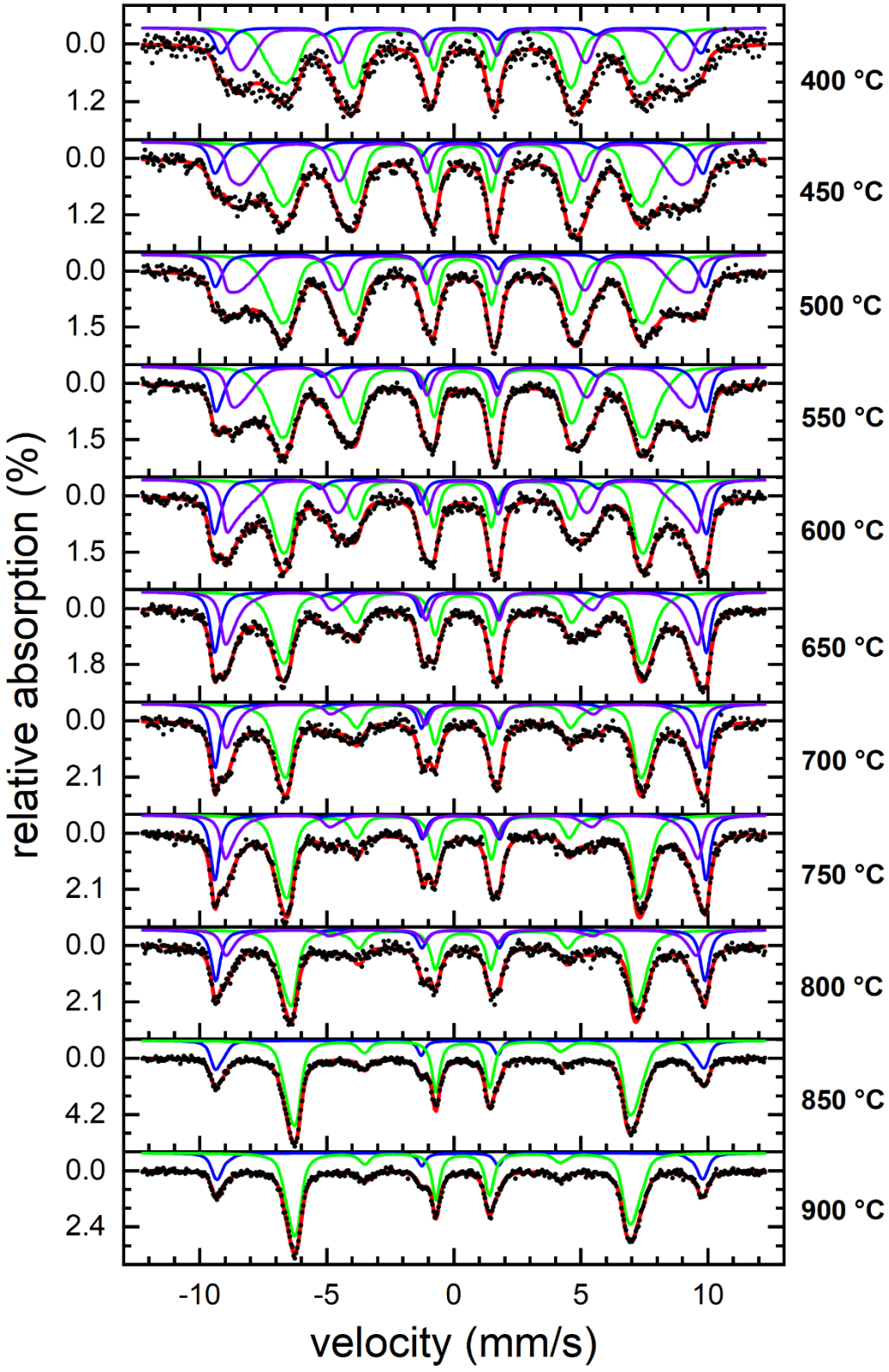

Figure 5.6.11: Mössbauer spectra measured for the complete calcination series in an external magnetic field of 10 T.

Figure 5.6.11 shows the 10 T Mössbauer spectra for the complete calcination series. The spectra of the samples calcined at or below 800 °C show a splitting of the A site contribution

into two contributions. It is assumed that the contribution with the lower isomer shift and higher hyper fine field (blue) can be assigned to the iron rich phase and the second contribution (purple) to a phase with a lower iron content.

Additionally, information about the individual phases is now accessible, e.g., the degree of canting. If for example the intensity ratio A_{23} is evaluated, a significantly higher magnetic frustration for the iron depleted phase compared to the iron rich phase is identified. This was anticipated, since the cobalt rich phase exhibits a stoichiometry between iron cobaltite and pure cobalt spinel, which is antiferromagnetic at 5 K. The iron rich phase on the other hand has a composition similar to cobalt ferrite and hence can be easily aligned in a 10 T magnetic field.

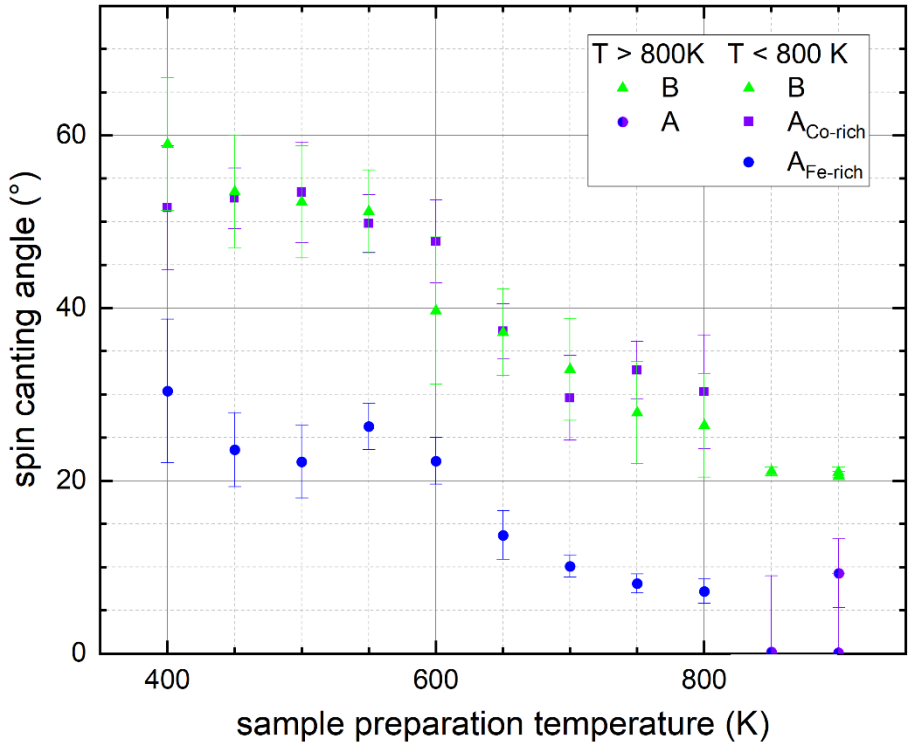

Figure 5.6.12: Intensity ratio A_{23} from Mössbauer spectroscopy of the calcination series.

Magnetometry

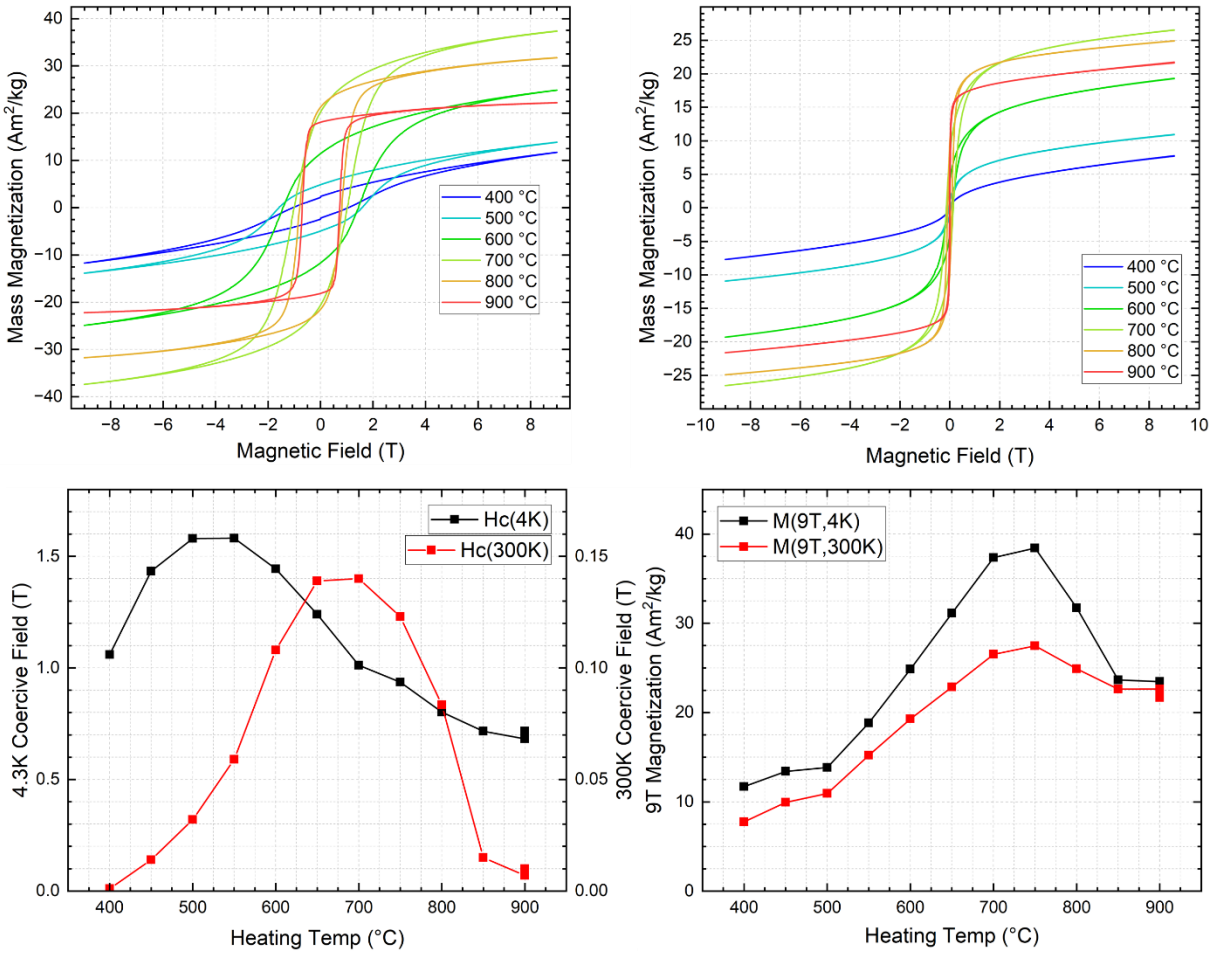

Figure 5.6.13: M(H) 4.3 K and a maximum field of 9 T. b) M(H) at 300 K and a maximum field of 9 T. c) Coercive fields at 4.3K and 300 K. d) High field (9 T) magnetization at 4.3 K and 300 K.

Figure 5.6.13a and b show M(H) curves recorded up to a maximum field of 9 T at 4.3 K and 300 K, respectively, presenting the effect of different calcination temperatures on the magnetic properties. While low calcination temperatures result in an M(H) behavior similar to incompletely compensated antiferromagnet, higher calcination temperatures result in ferrimagnetic behavior, with a rather rectangular shape for maximum calcination temperatures T_{calc} of 900 °C. At 300 K, for low calcination temperatures, we no longer observe open hysteresis loops, which could point to superparamagnetic behavior as discussed below in more detail.

Coercive fields and high field (9 T) magnetization values were extracted from the measurements shown in a) and b), and are depicted in Figure 5.6.13c and d, respectively. One has to keep in mind that the majority of the samples shown here are composed of two distinct phases, with the data chiefly representing the Fe-rich phase of higher coercivity. Considering

determined lattice constants (as shown in Figure 5.3.4 in the main text) and the limited speed of phase separation at low T_{calc}, it is reasonable to assume that the trend in $H_C(T_{calc})$ is directly correlated to the composition of the Fe-rich phase (the higher H_C, the more pronounced the phase separation). At 300 K, H_C is strongly reduced for maximum heat treatment, as here, the single phase $FeCo_2O_4$ exhibits a Curie temperature T_C of ca. 400 K. For lower values of T_{calc}, the ordering temperature of the Fe-rich phase is expected to be considerably higher, resulting in a lower reduction in H_C. Decreasing T_{calc} even further leads to monotonous decrease in H_C, reaching close to zero coercive fields for T_{calc} = 400 °C. Presumably, this can be explained by the continuous decrease in size of the Co- and Fe-rich domains with decreasing T_{calc}. As the T_C of the Co-rich phase is expected to already be exceeded at 300 K, the system could be considered as small ferrimagnetic regions in a paramagnetic matrix, whereby the distinct reduction in H_C could be assigned to superparamagnetic relaxation.

9 T magnetization values, used to approximate saturation magnetization behavior, display a marked increase up to ca. 40 Am^2/kg for T_{calc} of 750 °C, when going from single-phase to phase separated materials. Based on estimations of the stoichiometries of both phases, it can be concluded that the Co-rich phase may have a negligible contribution to magnetization, being close to the point of compensation, where A- and B-sublattice magnetization cancel each other out. The relatively high maximum magnetization in this case would stem almost exclusively from the more cobalt-ferrite-like Fe-rich phase.[156b] For T_{calc} < 700 °C, M(9 T) continuously decreases, which can be explained by increasing magnetic frustration, as illustrated via in-field Mössbauer spectroscopy, whereby M(9 T) here becomes an increasingly poor approximation of the saturation magnetization.

6. Summary and Outlook

This thesis focuses on composition- and mesostructure- activity relationships of cobalt-based spinel oxides in liquid phase oxidation catalysis. Chapter 3 and 4 deal with the development of suitable synthesis methods for both layered double hydroxide and spinel catalysts, their characterization, and their catalytic testing. Chapter 5 puts a spotlight on the intense characterization of a Co_2FeO_4 spinel, which was synthesized by one of the methods developed beforehand and exhibits surprising structural and magnetic properties.

In chapter 3[109] a systematic substitution series of cobalt-based spinels was synthesized via the crystalline precursor decomposition approach. While the main idea of this approach was developed by Friedel et al,[11] the synthesis method was expanded and adjusted towards other compositions. The as-prepared hydroxides and layered double hydroxides were phase pure and exhibited a platelet-like morphology. In the precursor structure cobalt was systematically and isomorphically substituted by the bivalent and trivalent redox inactive Mg^{2+} and Al^{3+}, as well as by trivalent iron (Fe^{3+}) as a redox active cation. After thermal treatment a systematic substitution series, including Co_3O_4, $MgCo_2O_4$, Co_2FeO_4, Co_2AlO_4, and $CoFe_2O_4$ was obtained. Due to the topotactic transformation along the (001) plane of the precursor structure to the (111) plane of the spinel structure during thermal treatment, the platelet like morphology was obtained and all samples exhibited a predominant 111 surface termination. This sample series is well suited for the investigation of composition-reactivity relationships, as different surface terminations, which might exhibit different catalytic reactivity to a certain reaction, can be neglected. To study mesostructure-reactivity relationships, in this case different morphology and as a consequence different dominant surface termination, isotropic Co_3O_4 and $CoFe_2O_4$ were synthesized via the crystalline precursor decomposition approach and direct precipitation with subsequent thermal treatment, respectively.

All catalysts were tested for their performance in chemical water oxidation by using ceric ammonium nitrate (CAN test), electrochemical oxygen evolution reaction (OER) and H_2O_2 decomposition.

For all those reactions Co_3O_4 showed the highest activity. With decreasing amount of Co^{3+} the activity decreases within the anisotropic substitution series for all water oxidation reactions, underlining the important role of Co^{3+}. Next to Co^{3+}, redox active cations in general enhance the catalytic activity. When considering the same amount of Co^{3+}, the presence of other redox active cations such as iron is beneficial compared to incorporated redox inactive cations.

For H_2O_2 decomposition, Co^{2+} plays a major role. This is shown by the higher relative activity of the only Co^{2+} containing $CoFe_2O_4$, which exhibited the lowest catalytic activity in the two water oxidation reactions CAN test and OER.
Investigation of mesostructure-reactivity relationships by comparing the activity of the predominantly 111 terminated Co_3O_4 and $CoFe_2O_4$ with their isotropic counterparts showed an impact of mesostructure depending on the composition. When no Co^{3+} is present, the surface termination does not influence the activity in a systematic way. However, Co^{3+} plays a dominant role during catalysis when integrated in the 111 surface of Co_3O_4, enhancing the catalytic activity.

In the next step, chapter 4[184] takes a more detailed look on how to tune mesostructure and with that further investigating mesostructure-reactivity relationships. The preceding chapter dealt with the impact of composition and surface facets on oxygen evolving reactions. Now, a closer look was taken at the impact of synthesis conditions, here precipitation pH, during the crystalline precursor decomposition approach. Two series of LDHs with a cobalt to iron ratio of 2 to 1 and their corresponding Co_2FeO_4 spinels were synthesized. One series was prepared using the conventional crystalline precursor decomposition approach in aqueous solution. The precipitation pH was varied in 0.5 steps from pH 7.5 to 9.5, resulting in five crystalline and platelet-like LDHs, which showed no distinct differences in composition, crystallinity, surface area, or pore size distribution. After thermal transformation to the corresponding spinels, also no significant differences between the five samples were observed. The second series on the other hand was prepared by using the microemulsion-assisted co-precipitation approach. Here, microemulsions are used to confine the reaction space within micelles, while all other synthesis parameters were the same as for the first series. The limited reaction space let to highly nano scaled and more isotropic particles, which showed a systematic increase in pore size with increasing precipitation pH. Even after calcination, the resulting spinels retained their nano scaled morphology and the distinct trend in pore size distribution.
This controlled tuning of the pore size through using the microemulsion-assisted co-precipitation approach made the sample series suited candidates for the investigation of confinement effects during OER. While the two LDH and spinel series exhibit the same respective composition, they vary distinctly in mesostructure and for the MACP series the impact of the pore size can be evaluated.
Conventional and MACP LDHs showed a low overpotential and satisfying stability. For the spinels this was only the case for the MACP series, the conventionally prepared spinels showed a strong decrease in activity compared to their LDH precursors.

The conventionally prepared LDHs did not show any trend of overpotential with mesostructure or precipitation pH. However, the MACP LDHs and spinels show a relation between overpotential and pore size. The three MACP LDHs synthesized at pH values larger than 8.5 exhibit pore size distribution maxima larger than 7.8 nm, while all other samples have pore sizes below. Simultaneously, the samples with the largest pore sizes show the highest overpotentials, while all other samples cluster in the range of lower overpotential. The clustering of overpotentials is explained by looking at the pre-conditioning of the catalysts. Even though the series show distinct differences in the beginning of the cycling, their CV shapes align with increasing number of scans. This points towards similar surface properties after pre-conditioning and therefore similar activity. Furthermore, the most active MACP spinels show the highest amount of reversible transformation during cycling, which proposes the highest number of active species within these catalysts. The observed increase in overpotential for MACP samples synthesized at pH values larger than 8.5 was explained with the help of EIS. For these least active samples an increased charge transfer resistance and Tafel slope was observed, which indicates a change in the rate determining step. The R3 resistance, which is assumed to be connected to the oxygen release step, is increased for all samples with an initial pore size distribution maximum larger than 7.8 nm. It is assumed that in pores smaller than this, no oxygen bubble formation is possible, because the critical bubble formation radius cannot be met, as has been observed for hydrogen bubble formation during HER.[147] In larger pores, bubble formation is possible and the oxygen bubbles block the pores and therefore reduce the activity of the catalysts.

Chapter 5 takes a closer look into the structure of the conventional synthesized Co_2FeO_4, which was also investigated in chapter 3 and chapter 4. In these chapters, phase purity was favorable, to be able to connect activity to a certain phase.

An LDH precursor prepared by the aqueous crystalline precursor decomposition approach was calcined in the range of 400 °C to 900 °C in 50 °C steps. The cobalt to iron ratio of 2:1 lies within the spinel miscibility gap of the cobalt iron oxide system. Therefore, due to calcination at different temperatures, a different degree of phase segregation was achieved for the sample series.

Next to the above described platelet morphology, the sample calcined at 400 °C consists of porous single-crystalline-like nano flakes, which exhibit spatial compositional fluctuations of cobalt and iron rich domains on a scale around 5 nm. Also, XRD, PDF and HR-TEM revealed a decreased lattice parameter for the iron rich phase. This deviation was explained by DFT+*U* results, which assigned a higher compressibility to the iron rich phase. Therefore, the

multitude of interfaces between iron rich and cobalt rich domains resulted in an unusually decreased lattice parameter. At elevated calcination temperatures this metastable state is not stabilized anymore and the lattice parameter of the two phases show the expected values. Most surprisingly, the 400 °C sample showed an exchange bias effect, which was explained by the strong coupling of the adjacent AFM cobalt rich and FiM iron rich regions within the platelets. Usually, this effect is mostly observed in core shell particles or otherwise designed interfaces, not in this kind of self-assembled powders, showing the versatility of the crystalline precursor decomposition approach and a possibility for using phase separation as a feasible tool for the engineering of magnetic properties.

In summary, investigation of composition-reactivity relationships revealed and underlined the importance of Co^{3+} and redox pairs in 111 surfaces for water oxidation reactions. Limiting reaction space enables the control of pore size distribution in LDHs and corresponding spinels, showing an advantage of small pore sizes during OER. An additional highly detailed characterization revealed surprising properties of a Co_2FeO_4 spinel, going beyond the targeted catalytic application, namely an exchange bias effect.

For the future, such systematic investigations of composition- and mesostructure- reactivity relationships should be continued and transferred to other mesostructural features, compositions and beyond. Also, a closer look should be taken to the real structure of the working catalyst and mechanistic details of catalytic reactions through *operando* and *in situ* studies. With the help of theory, favorable compositions and mechanistical pathways can be identified. The investigation of magnetic properties and their connection to catalytic activity should also be focused on, as for example certain spin states have been found to enable easier electron transfer.[185] In addition, automated data analysis and machine learning will be able to contribute to finding especially structure-reactivity relationships, which are otherwise sometimes tedious to detect.

Concluding, this work showed the importance of controlled synthesis conditions for the investigation of composition- and structure- reactivity relationships. The presented robust syntheses and thorough characterization helped to unravel these relationships through providing reproducible catalysts with tunable properties to the consortium of CRC/TRR 247, in which this work was embedded. By revealing important parameters and trends for activity, more active and stable catalysts can be designed, helping to pave the way towards a net zero carbon emission economy.

7. Bibliography

[1] I. Fechete, Y. Wang, J. C. Védrine, *Catal. Today* **2012**, *189*, 2-27.

[2] a) I. Azevedo, C. Bataille, J. Bistline, L. Clarke, S. Davis, *Energy Clim. Change* **2021**, *2*, 100049; b) Z. W. Seh, J. Kibsgaard, C. F. Dickens, I. Chorkendorff, J. K. Nørskov, T. F. Jaramillo, *Science* **2017**, *355*, eaad4998.

[3] a) J. C. Védrine, I. Fechete, *C. R. Chim.* **2016**, *19*, 1203-1225; b) S. Najafishirtari, K. Friedel Ortega, M. Douthwaite, S. Pattisson, G. J. Hutchings, C. J. Bondue, K. Tschulik, D. Waffel, B. Peng, M. Deitermann, *Chem. - Eur. J.* **2021**, *27*, 16809-16833.

[4] a) B. R. Yeo, G. J. Pudge, K. G. Bugler, A. V. Rushby, S. Kondrat, J. Bartley, S. Golunski, S. H. Taylor, E. Gibson, P. P. Wells, *Surf. Sci.* **2016**, *648*, 163-169; b) Y. Lei, F. Mehmood, S. Lee, J. Greeley, B. Lee, S. Seifert, R. E. Winans, J. W. Elam, R. J. Meyer, P. C. Redfern, *Science* **2010**, *328*, 224-228; c) Q. Hua, T. Cao, X. K. Gu, J. Lu, Z. Jiang, X. Pan, L. Luo, W. X. Li, W. Huang, *Angew. Chem.* **2014**, *126*, 4956-4961.

[5] a) S. T. Oyama, ACS Publications, **1996**; b) R. Schlögl, *Top. Catal.* **2016**, *59*, 1461-1476; cR. Schlögl, *Angew. Chem., Int. Ed.* **2015**, *54*, 3465-3520.

[6] a) I. Tyablikov, L. Rodionova, P. Sobolev, I. Ivanova, *Pet. Chem.* **2016**, *56*, 267-274; b) V. Russo, R. Tesser, E. Santacesaria, M. Di Serio, *Ind. Eng. Chem. Res.* **2013**, *52*, 1168-1178.

[7] D. Chen, C. Chen, Z. M. Baiyee, Z. Shao, F. Ciucci, *Chem. Rev.* **2015**, *115*, 9869-9921.

[8] a) G. Ertl, *Angew. Chem., Int. Ed.* **2008**, *47*, 3524-3535; b) A. M. Doyle, S. K. Shaikhutdinov, S. D. Jackson, H. J. Freund, *Angew. Chem., Int. Ed.* **2003**, *42*, 5240-5243.

[9] a) S. W. Chee, T. Lunkenbein, R. Schlögl, B. R. Cuenya, *J. Phys.: Condens. Matter* **2021**, *33*, 153001; b) L. Negahdar, C. M. Parlett, M. A. Isaacs, A. M. Beale, K. Wilson, A. F. Lee, *Catal. Sci. Technol.* **2020**, *10*, 5362-5385.

[10] Q. Zhao, Z. Yan, C. Chen, J. Chen, *Chem. Rev.* **2017**, *117*, 10121-10211.

[11] K. F. Ortega, S. Anke, S. Salamon, F. Ozcan, J. Heese, C. Andronescu, J. Landers, H. Wende, W. Schuhmann, M. Muhler, T. Lunkenbein, M. Behrens, *Chem-Eur J* **2017**, *23*, 12443-12449.

[12] R. Allmann, H. Jepsen, *Neues Jahrbuch für Mineralogie Monatshefte* **1969**, *1969*, 544À551.

[13] M. Catti, G. Ferraris, S. Hull, A. Pavese, *Phys. Chem. Miner.* **1995**, *22*, 200-206.

[14] M. Behrens, I. Kasatkin, S. Kuhl, G. Weinberg, *Chem Mater* **2010**, *22*, 386-397.

[15] A. I. Khan, D. O'Hare, *J Mater Chem* **2002**, *12*, 3191-3198.

[16] Z. P. Xu, J. Zhang, M. O. Adebajo, H. Zhang, C. H. Zhou, *Appl Clay Sci* **2011**, *53*, 139-150.

[17] V. Rives, *Layered double hydroxides: present and future*, Nova Publishers, **2001**.

[18] a) M. Vucelic, W. Jones, G. Moggridge, *Clays Clay Miner.* **1997**, *45*, 803-813; b) X. Duan, D. G. Evans, *Layered double hydroxides, Vol. 119*, Springer Science & Business Media, **2006**.

[19] G. Fan, F. Li, D. G. Evans, X. Duan, *Chem. Soc. Rev.* **2014**, *43*, 7040-7066.

[20] K.-H. Goh, T.-T. Lim, Z. Dong, *Water Res.* **2008**, *42*, 1343-1368.

[21] a) P. H. Chang, T. J. Lee, Y. P. Chang, S. Y. Chen, *ChemSusChem* **2013**, *6*, 1076-1083; b) A. Hanif, M. Sun, T. Wang, S. Shang, D. C. Tsang, J. Shang, *J. Cleaner Prod.* **2021**, *313*, 127956.

[22] L. Vigna, A. Nigro, A. Verna, I. V. Ferrari, S. L. Marasso, S. Bocchini, M. Fontana, A. Chiodoni, C. F. Pirri, M. Cocuzza, *Acs Omega* **2021**, *6*, 20205-20217.
[23] Z. Yang, F. Wang, C. Zhang, G. Zeng, X. Tan, Z. Yu, Y. Zhong, H. Wang, F. Cui, *RSC Adv.* **2016**, *6*, 79415-79436.
[24] V. A. Shirin, R. Sankar, A. P. Johnson, H. Gangadharappa, K. Pramod, *J. Controlled Release* **2021**, *330*, 398-426.
[25] X. Wang, Q. Chen, Y. Zheng, M. Hong, H. Fu, *React. Funct. Polym.* **2020**, *147*, 104371.
[26] a) R. Wang, Z. Qiu, S. Wan, Y. Wang, Q. Liu, J. Ding, Q. Zhong, *Chem. Eng. J.* **2022**, *427*, 130863; b) F. Dionigi, J. Zhu, Z. Zeng, T. Merzdorf, H. Sarodnik, M. Gliech, L. Pan, W. X. Li, J. Greeley, P. Strasser, *Angew. Chem.* **2021**.
[27] a) A.-E. Stamate, O. D. Pavel, R. Zavoianu, I.-C. Marcu, *Catalysts* **2020**, *10*, 57; b) C. Chen, L. Tao, S. Du, W. Chen, Y. Wang, Y. Zou, S. Wang, *Adv. Funct. Mater.* **2020**, *30*, 1909832; c) M. Duan, M. Qiu, S. Sun, X. Guo, Y. Liu, X. Zheng, F. Cao, Q. Kong, J. Zhang, *Appl Clay Sci* **2022**, *216*, 106360.
[28] F. L. Theiss, G. A. Ayoko, R. L. Frost, *Appl. Surf. Sci.* **2016**, *383*, 200-213.
[29] S. Naseem, B. Gevers, R. Boldt, F. J. W. Labuschagné, A. Leuteritz, *RSC Adv.* **2019**, *9*, 3030-3040.
[30] a) Z. P. Xu, G. Q. Lu, *Chem Mater* **2005**, *17*, 1055-1062; b) F. Kovanda, T. Rojka, P. Bezdička, K. Jirátová, L. Obalová, K. Pacultová, Z. Bastl, T. Grygar, *J. Solid State Chem.* **2009**, *182*, 27-36.
[31] M. a. A. Aramendía, V. Borau, C. Jiménez, J. M. Marinas, J. R. Ruiz, F. J. Urbano, *J. Solid State Chem.* **2002**, *168*, 156-161.
[32] a) T. S. Munonde, H. Zheng, P. N. Nomngongo, *Ultrason. Sonochem.* **2019**, *59*, 104716; b) V. V. Naik, T. Ramesh, S. Vasudevan, *J. Phys. Chem. Lett.* **2011**, *2*, 1193-1198.
[33] a) G. Hu, N. Wang, D. O'Hare, J. Davis, *Chem. Commun.* **2006**, 287-289; b) J. Yu, J. Liu, A. Clearfield, J. E. Sims, M. T. Speiegle, S. L. Suib, L. Sun, *Inorg. Chem.* **2016**, *55*, 12036-12041.
[34] L. Pesic, S. Salipurovic, V. Markovic, D. Vucelic, W. Kagunya, W. Jones, *J Mater Chem* **1992**, *2*, 1069-1073.
[35] a) A. Holleman, E. Wiberg, N. Wiberg, de Gruyter, Berlin, New York, **2007**; b) C. Janiak, H.-J. Meyer, D. Gudat, P. Kurz, in *Riedel Moderne Anorganische Chemie*, de Gruyter, **2018**.
[36] A. Seko, K. Yuge, F. Oba, A. Kuwabara, I. Tanaka, *Phys. Rev. B* **2006**, *73*, 184117.
[37] a) D. Dwibedi, C. Murugesan, M. Leskes, P. Barpanda, *Mater. Res. Bull.* **2018**, *98*, 219-224; b) K. R. Sanchez-Lievanos, J. L. Stair, K. E. Knowles, *Inorg. Chem.* **2021**, *60*, 4291-4305; c) A. Bloesser, H. Kurz, J. Timm, F. Wittkamp, C. Simon, S. Hayama, B. Weber, U.-P. Apfel, R. Marschall, *ACS Appl. Nano Mater.* **2020**, *3*, 11587-11599.
[38] a) D. Santos-Carballal, A. Roldan, R. Grau-Crespo, N. H. de Leeuw, *Phys. Rev. B* **2015**, *91*, 195106; b) M. Harada, M. Kuwa, R. Sato, T. Teranishi, M. Takahashi, S. Maenosono, *ACS Appl. Nano Mater.* **2020**, *3*, 8389-8402; c) Y. Liu, S. Qing, X. Hou, G. Feng, R. Zhang, X. Wang, S. Wang, Z. Gao, H. Xiang, *Journal of Materials and Applications* **2018**, *7*, 82-89; d) M. Siddique, N. Butt, *Phys. B (Amsterdam, Neth.)* **2010**, *405*, 4211-4215.
[39] X. Zhao, L. Mao, Q. Cheng, J. Li, F. Liao, G. Yang, L. Xie, C. Zhao, L. Chen, *Chem. Eng. J.* **2020**, *387*, 124081.
[40] X. W. Lou, D. Deng, J. Y. Lee, J. Feng, L. A. Archer, *Adv. Mater.* **2008**, *20*, 258-262.
[41] M. Amiri, M. Salavati-Niasari, A. Akbari, *Adv. Colloid Interface Sci.* **2019**, *265*, 29-44.
[42] K. K. Kefeni, B. B. Mamba, *Sustainable Mater. Technol.* **2020**, *23*, e00140.

[43] P. Stelmachowski, G. Maniak, J. Kaczmarczyk, F. Zasada, W. Piskorz, A. Kotarba, Z. Sojka, *Appl Catal B-Environ* **2014**, *146*, 105-111.
[44] J. Thomas, N. Thomas, F. Girgsdies, M. Beherns, X. Huang, V. D. Sudheesh, V. Sebastian, *New J Chem* **2017**, *41*, 7356-7363.
[45] X. Wei, D. Chen, *Mater Lett* **2006**, *60*, 823-827.
[46] V. Kumar, C. R. Mariappan, R. Azmi, D. Moock, S. Indris, M. Bruns, H. Ehrenberg, G. V. Prakash, *Acs Omega* **2017**, *2*, 6003-6013.
[47] E. Budiyanto, M. Q. Yu, M. M. Chen, S. DeBeer, O. Rudiger, H. Tuysuz, *Acs Appl Energ Mater* **2020**, *3*, 8583-8594.
[48] C. Y. Wan, Y. Nuli, J. H. Zhuang, Z. Y. Jiang, *Mater Lett* **2002**, *56*, 357-363.
[49] F. Schüth, K. Unger, *Prep. Solid Catal.* **1999**, 60-84.
[50] a) L. Tian, H. Zou, J. Fu, X. Yang, Y. Wang, H. Guo, X. Fu, C. Liang, M. Wu, P. K. Shen, *Adv. Funct. Mater.* **2010**, *20*, 617-623; b) J. Q. Wang, G. D. Du, R. Zeng, B. Niu, Z. X. Chen, Z. P. Guo, S. X. Dou, *Electrochim Acta* **2010**, *55*, 4805-4811.
[51] a) N. Armaroli, V. Balzani, *ChemSusChem* **2011**, *4*, 21-36; b) A. L. Santos, M.-J. Cebola, D. M. Santos, *Energies* **2021**, *14*, 3193.
[52] a) B. Zhang, C. Qiu, S. Wang, H. Gao, K. Yu, Z. Zhang, X. Ling, W. Ou, C. Su, *Sci. Bull.* **2021**, *66*, 562-569; b) C. Smith, A. K. Hill, L. Torrente-Murciano, *Energy Environ. Sci.* **2020**, *13*, 331-344.
[53] a) Y. Yan, B. Y. Xia, B. Zhao, X. Wang, *J. Mater. Chem. A* **2016**, *4*, 17587-17603; b) P. J. McHugh, A. D. Stergiou, M. D. Symes, *Adv Energy Mater* **2020**, *10*, 2002453.
[54] E. M. Stuve, in *Encyclopedia of Applied Electrochemistry* (Eds.: G. Kreysa, K.-i. Ota, R. F. Savinell), Springer New York, New York, NY, **2014**, pp. 1445-1453.
[55] J. Kieninger, *Electrochemical Methods for the Micro-and Nanoscale: Theoretical Essentials, Instrumentation and Methods for Applications in MEMS and Nanotechnology*, Walter de Gruyter GmbH & Co KG, **2022**.
[56] A. Karmakar, K. Karthick, S. S. Sankar, S. Kumaravel, R. Madhu, S. Kundu, *J. Mater. Chem. A* **2021**, *9*, 1314-1352.
[57] a) D. M. Morales, M. Risch, *JPhys Energy* **2021**, *3*, 034013; b) P. Connor, J. Schuch, B. Kaiser, W. Jaegermann, *Zeitschrift für Physikalische Chemie* **2020**, *234*, 979-994; c) C. C. L. McCrory, S. H. Jung, J. C. Peters, T. F. Jaramillo, *J Am Chem Soc* **2013**, *135*, 16977-16987.
[58] a) A. Alobaid, C. Wang, R. A. Adomaitis, *J. Electrochem. Soc.* **2018**, *165*, J3395; b) W. Xiang, N. Yang, X. Li, J. Linnemann, U. Hagemann, O. Ruediger, M. Heidelmann, T. Falk, M. Aramini, S. DeBeer, *Nat. Commun.* **2022**, *13*, 1-14.
[59] a) C. Wei, R. R. Rao, J. Peng, B. Huang, I. E. Stephens, M. Risch, Z. J. Xu, Y. Shao-Horn, *Adv. Mater.* **2019**, *31*, 1806296; b) Y. Lee, J. Suntivich, K. J. May, E. E. Perry, Y. Shao-Horn, *J. Phys. Chem. Lett.* **2012**, *3*, 399-404.
[60] R. Frydendal, E. A. Paoli, B. P. Knudsen, B. Wickman, P. Malacrida, I. E. Stephens, I. Chorkendorff, *ChemElectroChem* **2014**, *1*, 2075-2081.
[61] I. C. Man, H. Y. Su, F. Calle-Vallejo, H. A. Hansen, J. I. Martínez, N. G. Inoglu, J. Kitchin, T. F. Jaramillo, J. K. Nørskov, J. Rossmeisl, *ChemCatChem* **2011**, *3*, 1159-1165.
[62] a) P. Sabatier, *Ber. Dtsch. Chem. Ges.* **1911**, *44*, 1984-2001; b) J. Greeley, T. F. Jaramillo, J. Bonde, I. Chorkendorff, J. K. Nørskov, *Nat. Mater.* **2006**, *5*, 909-913.
[63] H. Ooka, J. Huang, K. S. Exner, *Frontiers in Energy Research* **2021**, *9*, 654460.
[64] a) C. Ranaweera, C. Zhang, S. Bhoyate, P. Kahol, M. Ghimire, S. Mishra, F. Perez, B. K. Gupta, R. K. Gupta, *Mater. Chem. Front.* **2017**, *1*, 1580-1584; b) R. Zhang, Y.-C. Zhang, L. Pan, G.-Q. Shen, N. Mahmood, Y.-H. Ma, Y. Shi, W. Jia, L. Wang, X. Zhang, *ACS Catal.* **2018**, *8*, 3803-3811; c) C. L. I. Flores, M. D. L. Balela, *J. Solid State Electrochem.* **2020**, *24*, 891-904.

[65] Y. Garsany, I. L. Singer, K. E. Swider-Lyons, *J. Electroanal. Chem.* **2011**, *662*, 396-406.
[66] H. A. El-Sayed, A. Weiß, L. F. Olbrich, G. P. Putro, H. A. Gasteiger, *J. Electrochem. Soc.* **2019**, *166*, F458.
[67] a) I. Spanos, S. Neugebauer, R. Guterman, J. Yuan, R. Schlögl, M. Antonietti, *Sustainable Energy Fuels* **2018**, *2*, 1446-1451; b) S. Bhandari, P. V. Narangoda, S. O. Mogensen, M. F. Tesch, A. K. Mechler, *ChemElectroChem* **2022**, *9*, e202200479.
[68] X. Xiao, A. J. Bard, *J Am Chem Soc* **2007**, *129*, 9610-9612.
[69] A. El Arrassi, Z. Liu, M. V. Evers, N. Blanc, G. Bendt, S. Saddeler, D. Tetzlaff, D. Pohl, C. Damm, S. Schulz, *J Am Chem Soc* **2019**, *141*, 9197-9201.
[70] a) N. Ebejer, M. Schnippering, A. W. Colburn, M. A. Edwards, P. R. Unwin, *Anal. Chem.* **2010**, *82*, 9141-9145; b) O. J. Wahab, M. Kang, P. R. Unwin, *Curr. Opin. Electrochem.* **2020**, *22*, 120-128.
[71] J. T. Mefford, A. R. Akbashev, M. Kang, C. L. Bentley, W. E. Gent, H. D. Deng, D. H. Alsem, Y.-S. Yu, N. J. Salmon, D. A. Shapiro, *Nature* **2021**, *593*, 67-73.
[72] F. Dionigi, Z. Zeng, I. Sinev, T. Merzdorf, S. Deshpande, M. B. Lopez, S. Kunze, I. Zegkinoglou, H. Sarodnik, D. Fan, *Nat. Commun.* **2020**, *11*, 1-10.
[73] A. Bergmann, T. E. Jones, E. M. Moreno, D. Teschner, P. Chernev, M. Gliech, T. Reier, H. Dau, P. Strasser, *Nat. Catal.* **2018**, *1*, 711-719.
[74] a) T. Wiegmann, I. Pacheco, F. Reikowski, J. Stettner, C. Qiu, M. Bouvier, M. Bertram, F. Faisal, O. Brummel, J. r. Libuda, *ACS Catal.* **2022**, *12*, 3256-3268; b) F. Reikowski, F. Maroun, I. Pacheco, T. Wiegmann, P. Allongue, J. Stettner, O. M. Magnussen, *ACS Catal.* **2019**, *9*, 3811-3821.
[75] a) T. Falk, E. Budiyanto, M. Dreyer, C. Pflieger, D. Waffel, J. Büker, C. Weidenthaler, K. F. Ortega, M. Behrens, H. Tüysüz, *ChemCatChem* **2021**; b) G. Zhao, S. A. Bonke, S. Schmidt, Z. Wang, B. Hu, T. Falk, Y. Hu, T. Rath, W. Xia, B. Peng, *ACS Sustainable Chem. Eng.* **2021**, *9*, 5422-5429; c) P. M. Arnal, M. Comotti, F. Schüth, *Angew. Chem., Int. Ed.* **2006**, *45*, 8224-8227; d) S. H. Joo, J. Y. Park, C.-K. Tsung, Y. Yamada, P. Yang, G. A. Somorjai, *Nat. Mater.* **2009**, *8*, 126-131.
[76] K. Amakawa, Y. V. Kolen'ko, R. Schlögl, A. Trunschke, *ChemCatChem* **2014**, *6*, 3338-3341.
[77] O. Vozniuk, T. Tabanelli, N. Tanchoux, J. M. M. Millet, S. Albonetti, F. Di Renzo, F. Cavani, *Catalysts* **2018**, *8*.
[78] M. M. Thackeray, *Adv Energy Mater* **2021**, *11*.
[79] K. Malaie, M. R. Ganjali, *J Energy Storage* **2021**, *33*.
[80] X. M. Liu, X. Y. Cui, K. Dastafkan, H. F. Wang, C. Tang, C. Zhao, A. B. Chen, C. X. He, M. H. Han, Q. Zhang, *J Energy Chem* **2021**, *53*, 290-302.
[81] A. Kostuch, J. Gryboś, P. Indyka, L. Osmieri, S. Specchia, Z. Sojka, K. Kruczała, *Catal. Sci. Technol.* **2018**, *8*, 642-655.
[82] A. Kostuch, J. Gryboś, S. Wierzbicki, Z. Sojka, K. Kruczała, *Materials* **2021**, *14*, 820.
[83] X. H. Wei, D. H. Chen, W. J. Tang, *Mater Chem Phys* **2007**, *103*, 54-58.
[84] a) J. Zhang, H. M. Su, J. Z. Zhou, G. R. Qian, Z. P. Xu, Y. F. Xi, Y. F. Xu, F. L. Theiss, R. Frost, *J Colloid Interf Sci* **2013**, *411*, 240-246; b) N. P. Funnell, Q. Wang, L. Connor, M. G. Tucker, D. O'Hare, A. L. Goodwin, *Nanoscale* **2014**, *6*, 8032-8036.
[85] a) J. Heese-Gartlein, D. M. Morales, A. Rabe, T. Bredow, W. Schuhmann, M. Behrens, *Chem-Eur J* **2020**, *26*, 12256-12267; b) C. E. Frey, P. Kurz, *Chem-Eur J* **2015**, *21*, 14958-14968.
[86] C. C. L. McCrory, S. Jung, I. M. Ferrer, S. M. Chatman, J. C. Peters, T. F. Jaramillo, *J Am Chem Soc* **2015**, *137*, 4347-4357.
[87] A. J. Schrader, G. De Dominicis, G. L. Schieber, P. G. Loutzenhiser, *Sol Energy* **2017**, *150*, 584-595.

[88] T. M. C. Dinh, A. Barnabe, M. A. Bui, C. Josse, T. Hungria, C. Bonningue, L. Presmanes, P. Tailhades, *Crystengcomm* **2018**, *20*, 6146-6155.
[89] G. Will, N. Masciocchi, W. Parrish, M. Hart, *J Appl Crystallogr* **1987**, *20*, 394-401.
[90] S. Yagi, Y. Ichikawa, I. Yamada, T. Doi, T. Ichitsubo, E. Matsubara, *Jpn J Appl Phys* **2013**, *52*.
[91] T. A. S. Ferreira, J. C. Waerenborgh, M. H. R. M. Mendonca, M. R. Nunes, F. M. Costa, *Solid State Sci* **2003**, *5*, 383-392.
[92] S. Kurajica, J. Popovic, E. Tkalcec, B. Grzeta, V. Mandic, *Mater Chem Phys* **2012**, *135*, 587-593.
[93] a) M. Ferrer, A. Gouveia, L. Gracia, E. Longo, J. Andres, *Modell. Simul. Mater. Sci. Eng.* **2016**, *24*, 025007; b) F. Zasada, W. Piskorz, P. Stelmachowski, A. Kotarba, J.-F. Paul, T. Płociński, K. J. Kurzydłowski, Z. Sojka, *J. Phys. Chem. C* **2011**, *115*, 6423-6432.
[94] a) L. Gong, X. Y. E. Chng, Y. Du, S. Xi, B. S. Yeo, *ACS Catal.* **2018**, *8*, 807-814; b) G. h. Moon, M. Yu, C. K. Chan, H. Tüysüz, *Angew. Chem., Int. Ed.* **2019**, *58*, 3491-3495; c) L. Trotochaud, S. L. Young, J. K. Ranney, S. W. Boettcher, *J Am Chem Soc* **2014**, *136*, 6744-6753.
[95] a) C. G. Morales-Guio, L. Liardet, X. Hu, *J Am Chem Soc* **2016**, *138*, 8946-8957; b) K. Chakrapani, G. Bendt, H. Hajiyani, T. Lunkenbein, M. T. Greiner, L. Masliuk, S. Salamon, J. Landers, R. Schlögl, H. Wende, *ACS Catal.* **2018**, *8*, 1259-1267; c) X. T. Wang, T. Ouyang, L. Wang, J. H. Zhong, T. Ma, Z. Q. Liu, *Angew. Chem.* **2019**, *131*, 13425-13430.
[96] Z. Chen, C. X. Kronawitter, Y.-W. Yeh, X. Yang, P. Zhao, N. Yao, B. E. Koel, *J. Mater. Chem. A* **2017**, *5*, 842-850.
[97] S. Trasatti, O. Petrii, *Pure Appl. Chem* **1991**, *63*, 711-734.
[98] L. B. Kong, C. Lu, M. C. Liu, Y. C. Luo, L. Kang, X. H. Li, F. C. Walsh, *Electrochim Acta* **2014**, *115*, 22-27.
[99] J. R. Goldstein, *J. Catal.* **1974**, *32*, 452-465.
[100] a) E. Coronado, J. R. Galan-Mascaros, C. Marti-Gastaldo, A. Ribera, E. Palacios, M. Castro, R. Burriel, *Inorg. Chem.* **2008**, *47*, 9103-9110; b) Q. Li, L. Xing, X. Lu, N. Li, M. Xu, *Inorg. Chem. Commun.* **2015**, *52*, 46-49.
[101] J.-M. Génin, S. J. Mills, A. G. Christy, O. Guérin, A. Herbillon, E. Kuzmann, G. Ona-Nguema, C. Ruby, C. Upadhyay, *Mineral. Mag.* **2014**, *78*, 447-465.
[102] G. Sawatzky, F. Van Der Woude, A. Morrish, *Journal of Applied Physics* **1968**, *39*, 1204-1205.
[103] C. Cannas, A. Musinu, G. Piccaluga, D. Fiorani, D. Peddis, H. K. Rasmussen, S. Mørup, *The Journal of chemical physics* **2006**, *125*, 164714.
[104] M. J. McKelvy, R. Sharma, A. V. Chizmeshya, R. Carpenter, K. Streib, *Chem Mater* **2001**, *13*, 921-926.
[105] J. O. Abe, A. Popoola, E. Ajenifuja, O. Popoola, *Int. J. Hydrogen Energy* **2019**, *44*, 15072-15086.
[106] N.-T. Suen, S.-F. Hung, Q. Quan, N. Zhang, Y.-J. Xu, H. M. Chen, *Chem. Soc. Rev.* **2017**, *46*, 337-365.
[107] Y. Jiao, Y. Zheng, M. Jaroniec, S. Z. Qiao, *Chem. Soc. Rev.* **2015**, *44*, 2060-2086.
[108] a) L. Wu, L. Yu, X. Xiao, F. Zhang, S. Song, S. Chen, Z. Ren, *Research* **2020**, *2020*; b) S. Saddeler, G. Bendt, S. Salamon, F. T. Haase, J. Landers, J. Timoshenko, C. Rettenmaier, H. S. Jeon, A. Bergmann, H. Wende, *J. Mater. Chem. A* **2021**; c) J. Xie, S. Cao, L. Gao, F. Lei, P. Hao, B. Tang, *Chem. Commun.* **2019**, *55*, 9841-9844; d) A. Indra, P. W. Menezes, N. R. Sahraie, A. Bergmann, C. Das, M. Tallarida, D. Schmeißer, P. Strasser, M. Driess, *J Am Chem Soc* **2014**, *136*, 17530-17536.

[109] A. Rabe, J. Büker, S. Salamon, A. Koul, U. Hagemann, J. Landers, K. Friedel Ortega, B. Peng, M. Muhler, H. Wende, *Chem. - Eur. J.* **2021**, *27*, 17038-17048.
[110] a) T. Maiyalagan, K. R. Chemelewski, A. Manthiram, *ACS Catal.* **2014**, *4*, 421-425; b) S. Saddeler, U. Hagemann, S. Schulz, *Inorg. Chem.* **2020**, *59*, 10013-10024; c) Y. Li, M. Lu, Y. Wu, Q. Ji, H. Xu, J. Gao, G. Qian, Q. Zhang, *J. Mater. Chem. A* **2020**, *8*, 18215-18219.
[111] a) R. V. Maligal-Ganesh, C. Xiao, T. W. Goh, L.-L. Wang, J. Gustafson, Y. Pei, Z. Qi, D. D. Johnson, S. Zhang, F. Tao, *ACS Catal.* **2016**, *6*, 1754-1763; b) X. Fei, P. Wang, D. Zhang, H. Wang, Z. Wu, *ChemCatChem* **2021**, *13*, 2313-2336; c) T. Wang, L. Gao, J. Hou, S. J. Herou, J. T. Griffiths, W. Li, J. Dong, S. Gao, M.-M. Titirici, R. V. Kumar, *Nat. Commun.* **2019**, *10*, 1-9.
[112] M. Jaugstetter, N. Blanc, M. Kratz, K. Tschulik, *Chem. Soc. Rev.* **2022**.
[113] A. Vazhayil, L. Vazhayal, J. Thomas, N. Thomas, *Applied Surface Science Advances* **2021**, *6*, 100184.
[114] a) J. Xiao, A. M. Oliveira, L. Wang, Y. Zhao, T. Wang, J. Wang, B. P. Setzler, Y. Yan, *ACS Catal.* **2020**, *11*, 264-270; b) S. Dresp, F. Dionigi, S. Loos, J. Ferreira de Araujo, C. Spöri, M. Gliech, H. Dau, P. Strasser, *Adv Energy Mater* **2018**, *8*, 1800338.
[115] a) F. Yang, K. Sliozberg, I. Sinev, H. Antoni, A. Bähr, K. Ollegott, W. Xia, J. Masa, W. Grünert, B. R. Cuenya, *ChemSusChem* **2017**, *10*, 156-165; b) M. S. Burke, M. G. Kast, L. Trotochaud, A. M. Smith, S. W. Boettcher, *J Am Chem Soc* **2015**, *137*, 3638-3648.
[116] J. Zhang, Y. F. Xu, G. Qian, Z. P. Xu, C. Chen, Q. Liu, *J. Phys. Chem. C* **2010**, *114*, 10768-10774.
[117] R. Atkin, G. G. Warr, *J. Phys. Chem. B* **2007**, *111*, 9309-9316.
[118] M. Soleimani Zohr Shiri, W. Henderson, M. R. Mucalo, *Materials* **2019**, *12*, 1896.
[119] G. D. Rees, R. Evans-Gowing, S. J. Hammond, B. H. Robinson, *Langmuir* **1999**, *15*, 1993-2002.
[120] S.-J. Cho, S. M. Kauzlarich, J. Olamit, K. Liu, F. Grandjean, L. Rebbouh, G. J. Long, *Journal of Applied Physics* **2004**, *95*, 6804-6806.
[121] J. O. Stoffer, T. Bone, *J. Polym. Sci., Polym. Chem. Ed.* **1980**, *18*, 2641-2648.
[122] M. Cao, X. He, J. Chen, C. Hu, *Cryst. Growth Des.* **2007**, *7*, 170-174.
[123] D. Chen, L. Gao, *J Colloid Interf Sci* **2004**, *279*, 137-142.
[124] a) L. Fagiolari, M. Bini, F. Costantino, G. Gatto, A. J. Kropf, F. Marmottini, M. Nocchetti, E. C. Wegener, F. Zaccaria, M. Delferro, *ACS Appl. Mater. Interfaces* **2020**, *12*, 32736-32745; b) J. He, B. Li, D. G. Evans, X. Duan, *Colloids Surf., A* **2004**, *251*, 191-196.
[125] C. Kumar, D. Balasubramanian, *J Colloid Interf Sci* **1979**, *69*, 271-279.
[126] Y. Li, C.-W. Park, *Langmuir* **1999**, *15*, 952-956.
[127] W. A. Sławiński, A. O. Sjåstad, H. Fjellvåg, *Inorg. Chem.* **2016**, *55*, 12881-12889.
[128] W. Yang, Y. Kim, P. K. Liu, M. Sahimi, T. T. Tsotsis, *Chem. Eng. Sci.* **2002**, *57*, 2945-2953.
[129] F. B. D. Saiah, B.-L. Su, N. Bettahar, *J. Hazard. Mater.* **2009**, *165*, 206-217.
[130] W. Klee, G. Engel, *J. Inorg. Nucl. Chem.* **1970**, *32*, 1837-1843.
[131] H. Hatami, A. Fotovat, A. Halajnia, *Appl Clay Sci* **2018**, *152*, 333-341.
[132] M. Thommes, K. Kaneko, A. V. Neimark, J. P. Olivier, F. Rodriguez-Reinoso, J. Rouquerol, K. S. Sing, *Pure Appl. Chem.* **2015**, *87*, 1051-1069.
[133] H. Fathi, J. P. Kelly, V. R. Vasquez, O. A. Graeve, *Langmuir* **2012**, *28*, 9267-9274.
[134] E. Uzunova, D. Klissurski, I. Mitov, P. Stefanov, *Chem Mater* **1993**, *5*, 576-582.
[135] M. Banach, A. Makara, *J. Chem. Eng. Data* **2011**, *56*, 3095-3099.
[136] K. Mitsuda, H. Kimura, T. Murahashi, *J. Mater. Sci.* **1989**, *24*, 413-419.

[137] F. T. Haase, A. Rabe, F.-P. Schmidt, A. Herzog, H. S. Jeon, W. Frandsen, P. V. Narangoda, I. Spanos, K. Friedel Ortega, J. Timoshenko, T. Lunkenbein, M. Behrens, A. Bergmann, R. Schlögl, B. Roldan Cuenya, *J Am Chem Soc* **2022**, *144*, 12007-12019.
[138] a) F. S. Fedorov, J. Linnemann, K. Tschulik, L. Giebeler, M. Uhlemann, A. Gebert, *Electrochim Acta* **2013**, *90*, 166-170; b) J. Linnemann, L. Taudien, M. Klose, L. Giebeler, *J. Mater. Chem. A* **2017**, *5*, 18420-18428.
[139] R. Boggio, A. Carugati, S. Trasatti, *J. Appl. Electrochem.* **1987**, *17*, 828-840.
[140] B. E. Conway, T. C. Liu, *Berichte der Bunsengesellschaft für physikalische Chemie* **1987**, *91*, 461-469.
[141] A. Bergmann, E. Martinez-Moreno, D. Teschner, P. Chernev, M. Gliech, J. F. de Araújo, T. Reier, H. Dau, P. Strasser, *Nat. Commun.* **2015**, *6*, 8625.
[142] H. M. A. Amin, H. Baltruschat, *Phys. Chem. Chem. Phys.* **2017**, *19*, 25527-25536.
[143] T. Wiegmann, I. Pacheco, F. Reikowski, J. Stettner, C. Qiu, M. Bouvier, M. Bertram, F. Faisal, O. Brummel, J. Libuda, J. Drnec, P. Allongue, F. Maroun, O. M. Magnussen, *ACS Catal.* **2022**, *12*, 3256-3268.
[144] J. Linnemann, K. Kanokkanchana, K. Tschulik, *ACS Catal.* **2021**, *11*, 5318-5346.
[145] W. Xiang, N. Yang, X. Li, J. Linnemann, U. Hagemann, O. Ruediger, M. Heidelmann, T. Falk, M. Aramini, S. DeBeer, M. Muhler, K. Tschulik, T. Li, *Nat. Commun.* **2022**, *13*, 179.
[146] A. Lasia, *Electrochemical Impedance Spectroscopy and its Applications*, Springer New York, NY, **2014**.
[147] S. R. German, M. A. Edwards, H. Ren, H. S. White, *J Am Chem Soc* **2018**, *140*, 4047-4053.
[148] a) A. El Arrassi, Z. Liu, M. V. Evers, N. Blanc, G. Bendt, S. Saddeler, D. Tetzlaff, D. Pohl, C. Damm, S. Schulz, K. Tschulik, *J Am Chem Soc* **2019**, *141*, 9197-9201; b) Z. Liu, M. Corva, H. M. A. Amin, N. Blanc, J. Linnemann, K. Tschulik, *Int. J. Mol. Sci.* **2021**, *22*.
[149] G. Horváth, K. Kawazoe, *J. Chem. Eng. Jpn.* **1983**, *16*, 470-475.
[150] T. H. Wan, M. Saccoccio, C. Chen, F. Ciucci, *Electrochim Acta* **2015**, *184*, 483-499.
[151] K. Chakrapani, F. Özcan, K. F. Ortega, T. Machowski, M. Behrens, *ChemElectroChem* **2018**, *5*, 93-100.
[152] B. Conway, T. Liu, *Berichte der Bunsengesellschaft für physikalische Chemie* **1987**, *91*, 461-469.
[153] a) E. Budiyanto, M. Yu, M. Chen, S. DeBeer, O. Rüdiger, H. Tüysüz, *Acs Appl Energ Mater* **2020**, *3*, 8583-8594; b) S. Y. Srinivasan, K. M. Paknikar, D. Bodas, V. Gajbhiye, *Nanomedicine* **2018**, *13*, 1221-1238; c) Q. Song, Z. J. Zhang, *J Am Chem Soc* **2004**, *126*, 6164-6168; dS. Jauhar, J. Kaur, A. Goyal, S. Singhal, *RSC Adv.* **2016**, *6*, 97694-97719.
[154] a) N. Debnath, T. Kawaguchi, W. Kumasaka, H. Das, K. Shinozaki, N. Sakamoto, H. Suzuki, N. Wakiya, *Journal of Magnetism and Magnetic Materials* **2017**, *432*, 391-395; b) O. Boytsova, O. Makarevich, D. Sharovarov, A. Makarevich, *Inorganic Materials* **2022**, *58*, 673-686.
[155] Y. Hou, Y. Zhao, Z. Liu, H. Yu, X. Zhong, W. Qiu, D. Zeng, L. Wen, *J. Phys. D: Appl. Phys.* **2010**, *43*, 445003.
[156] a) I.-H. Jung, S. A. Decterov, A. D. Pelton, H.-M. Kim, Y.-B. Kang, *Acta Mater.* **2004**, *52*, 507-519; b) M. TAKAHASHI, M. E. FINE, *J. Am. Ceram. Soc.* **1970**, *53*, 633-634.
[157] W. H. Meiklejohn, C. P. Bean, *Physical review* **1956**, *102*, 1413.
[158] K. M. Krishnan, *Fundamentals and applications of magnetic materials*, Oxford University Press, **2016**.

[159] a) V. Skumryev, S. Stoyanov, Y. Zhang, G. Hadjipanayis, D. Givord, J. Nogués, *Nature* **2003**, *423*, 850-853; b) X. He, Y. Wang, N. Wu, A. N. Caruso, E. Vescovo, K. D. Belashchenko, P. A. Dowben, C. Binek, *Nat. Mater.* **2010**, *9*, 579-585.
[160] a) M.-H. Phan, J. Alonso, H. Khurshid, P. Lampen-Kelley, S. Chandra, K. Stojak Repa, Z. Nemati, R. Das, Ó. Iglesias, H. Srikanth, *Nanomaterials* **2016**, *6*, 221; b) G. Salazar-Alvarez, J. Sort, S. Surinach, M. D. Baró, J. Nogués, *J Am Chem Soc* **2007**, *129*, 9102-9108; c) L. W. Martin, Y.-H. Chu, M. B. Holcomb, M. Huijben, P. Yu, S.-J. Han, D. Lee, S. X. Wang, R. Ramesh, *Nano letters* **2008**, *8*, 2050-2055; d) Z.-A. Li, N. Fontaíña-Troitiño, A. Kovács, S. Liébana-Viñas, M. Spasova, R. E. Dunin-Borkowski, M. Müller, D. Doennig, R. Pentcheva, M. Farle, *Sci. Rep.* **2015**, *5*, 1-6.
[161] a) B. Rivas-Murias, M. Testa-Anta, A. S. Skorikov, M. Comesaña-Hermo, S. Bals, V. Salgueiriño, *Nano Letters* **2023**, *23*, 1688-1695; b) S. A. McEnroe, B. Carter-Stiglitz, R. J. Harrison, P. Robinson, K. Fabian, C. McCammon, *Nat. Nanotechnol.* **2007**, *2*, 631-634; cR. Pentcheva, H. S. Nabi, *Phys. Rev. B* **2008**, *77*, 172405.
[162] W.-W. Zhang, M. Chen, *Calphad* **2013**, *41*, 76-88.
[163] E. V. Sturm, H. Cölfen, *Chem. Soc. Rev.* **2016**, *45*, 5821-5833.
[164] J. P. Perdew, A. Ruzsinszky, G. I. Csonka, O. A. Vydrov, G. E. Scuseria, L. A. Constantin, X. Zhou, K. Burke, *arXiv preprint arXiv:0707.2088* **2007**.
[165] S. L. Thomae, N. Prinz, T. Hartmann, M. Teck, S. Correll, M. Zobel, *Rev. Sci. Instrum.* **2019**, *90*, 043905.
[166] X. Yang, P. Juhas, C. L. Farrow, S. J. Billinge, *arXiv preprint arXiv:1402.3163* **2014**.
[167] C. Farrow, P. Juhas, J. Liu, D. Bryndin, E. Božin, J. Bloch, T. Proffen, S. Billinge, *J. Phys.: Condens. Matter* **2007**, *19*, 335219.
[168] A. Buades, B. Coll, J.-M. Morel, in *2005 IEEE computer society conference on computer vision and pattern recognition (CVPR'05), Vol. 2*, Ieee, **2005**, pp. 60-65.
[169] K. Dabov, A. Foi, V. Katkovnik, K. Egiazarian, in *Image Processing: Algorithms and Systems VI, Vol. 6812*, SPIE, **2008**, pp. 62-73.
[170] a) G. Kresse, J. Furthmüller, *Phys. Rev. B* **1996**, *54*, 11169; b) G. Kresse, J. Furthmüller, *Computational materials science* **1996**, *6*, 15-50.
[171] a) J. KresseG, *PhysRevB* **1999**, *59*, 1758G1775; b) P. E. Blöchl, *Phys. Rev. B* **1994**, *50*, 17953.
[172] S. L. Dudarev, G. A. Botton, S. Y. Savrasov, C. Humphreys, A. P. Sutton, *Phys. Rev. B* **1998**, *57*, 1505.
[173] O. Bulavchenko, O. Venediktova, T. Afonasenko, P. Tsyrul'Nikov, A. Saraev, V. Kaichev, S. Tsybulya, *RSC Adv.* **2018**, *8*, 11598-11607.
[174] a) S. Hirai, W. L. Mao, *Appl. Phys. Lett.* **2013**, *102*, 041912; b) P. Smith, C. Spencer, R. Stillwell, *J. Phys. Chem. Solids* **1978**, *39*, 107-111.
[175] L. Chen, Y. Yang, X. Meng, *Appl. Phys. Lett.* **2013**, *102*, 203102.
[176] a) S. Regmi, Z. Li, S. KC, R. Mahat, A. Rastogi, R. Datta, A. Gupta, *Appl. Phys. Lett.* **2022**, *121*, 102401; b) Y. Qu, H. Yang, N. Yang, Y. Fan, H. Zhu, G. Zou, *Mater Lett* **2006**, *60*, 3548-3552; c) L. Shen, M. Althammer, N. Pachauri, B. Loukya, R. Datta, M. Iliev, N. Bao, A. Gupta, *J. Cryst. Growth* **2014**, *390*, 61-66.
[177] F. T. Haase, A. Rabe, F.-P. Schmidt, A. Herzog, H. S. Jeon, W. Frandsen, P. V. Narangoda, I. Spanos, K. Friedel Ortega, J. Timoshenko, *J Am Chem Soc* **2022**, *144*, 12007-12019.
[178] A. Walsh, S.-H. Wei, Y. Yan, M. Al-Jassim, J. A. Turner, M. Woodhouse, B. Parkinson, *Phys. Rev. B* **2007**, *76*, 165119.
[179] Z. Li, E. Fisher, J. Liu, M. Nevitt, *J. Mater. Sci.* **1991**, *26*, 2621-2624.
[180] L. Bai, M. Pravica, Y. Zhao, C. Park, Y. Meng, S. V. Sinogeikin, G. Shen, *J. Phys.: Condens. Matter* **2012**, *24*, 435401.

[181] S. A. McEnroe, B. Carter-Stiglitz, R. J. Harrison, P. Robinson, K. Fabian, C. McCammon, *Nat. Nanotechnol.* **2008**, *3*, 58-58.
[182] T. Daou, J. Grenèche, G. Pourroy, S. Buathong, A. Derory, C. Ulhaq-Bouillet, B. Donnio, D. Guillon, S. Begin-Colin, *Chem Mater* **2008**, *20*, 5869-5875.
[183] K. J. Kim, H. K. Kim, Y. R. Park, G. Y. Ahn, C. S. Kim, J. Y. Park, *Hyperfine interactions* **2006**, *169*, 1363-1369.
[184] A. Rabe, M. Jaugstetter, F. Hiege, N. Cosanne, K. F. Ortega, J. Linnemann, K. Tschulik, M. Behrens, *ChemSusChem* **2023**, *16*, e202202015.
[185] Y. Sun, X. Ren, S. Sun, Z. Liu, S. Xi, Z. J. Xu, *Angew. Chem.* **2021**, *133*, 14657-14665.

8. Appendix

8.1 List of Figures

8.2 List of Tables

8.3 List of Publications

1. Rabe, Anna.; Jaugstetter, Maximilian; Hiege, Felix; Cosanne, Nicolas; Friedel, Klaus; Linnemann, Julia; Tschulik, Kristina; Behrens, Malte, *ChemSusChem* **2023**, 16, 10, e202202015.

2. Haase, Felix Thomas; Rabe, Anna; Schmidt, Franz-Philipp; Herzog, Antonia; Jeon, Hyo Sang, Frandsen, Wiebke; Narangoda, Praveen Vidusha; Spanos, Ioannis; Friedel, Klaus; Timoshenko, Janis; Lunkenbein, Thomas; Behrens, Malte; Bergmann, Arno, Schlögl, Robert, Roldan Cuenya, Beatriz, *J. Am. Chem. Soc.* **2022**, 144, 27, 12007–12019.

3. Brix, Ann Cathrin; Dreyer, Maik; Koul, Adarsh; Krebs, Moritz; Rabe, Anna; Hagemann, Ulrich; Varhade, Swapnil; Andronescu, Corina; Behrens, Malte; Schuhmann, Wolfgang; Morales, Dulce M., *ChemElectroChem* **2022**, 9, 4, e202200092.

4. Dreyer, Maik; Rabe, Anna; Budiyanto, Eko; Ortega, Klaus Friedel; Najafishirtari, Sharif; Tüysüz, Harun; Behrens, Malte, *Catalysts* **2021**, 11, 11, 1312.

5. Dreyer, Maik; Cruz, Daniel; Hagemann, Ulrich; Zeller, Patrick; Heidelmann, Markus; Salamon, Soma; Landers, Joachim; Rabe, Anna; Ortega, Klaus Friedel; Najafishirtari, Sharif; Wende, Heiko; Hartmann, Nils; Knop-Gericke, Axel; Schlögl, Robert; Behrens, Malte, *Chem. Eur. J.* **2021**, 27, 68, 16801-17263.

6. Rabe, Anna; Büker, Julia; Salamon, Soma; Koul, Adarsh; Hagemann, Ulrich; Landers, Joachim; Friedel Ortega, Klaus; Peng, Baoxiang; Muhler, Martin; Wende, Heiko; Schuhmann, Wolfgang; Behrens, Malte, *Chem. Eur. J.* **2021**, 27, 68, 17038-17048.

7. Heese-Gärtlein, Justus; Rabe, Anna; Behrens, Malte, *Z. Anorg.Allg. Chem.* **2021**, 647, 13, 1363– 1372.

8. Füngerlings, Achim; Koul, Adarsh; Dreyer, Maik; Rabe, Anna; Morales, Dulce M.; Schuhmann, Wolfgang; Behrens, Malte; Pentcheva, Rossitza, *Chem. Eur. J.* **2021**, 27, 68, 17145-17158.
9. Dreyer, Maik; Krebs, Moritz; Najafishirtari, Sharif; Rabe, Anna; Friedel Ortega, Klaus Dieter; Behrens, Malte, *Catalysts* **2021**, 11, 5, 550.

10. Heese-Gärtlein, Justus; Morales, Dulce M.; Rabe, Anna; Bredow, Thomas; Schuhmann, Wolfgang; Behrens, Malte, *Chem. Eur. J.* **2020**, 26, 53, 12256-12267.

11. Schneider, Jochen; Wiemann, Malte; Rabe, Anna; Bartsch, Eckhard, *Soft Matter* **2017**, 13, 445-457.

8.4 List of Selected Conference Contributions

Talk "Tuning of Composition, Mesostructure and Activity of Cobalt-based Mixed Spinel Oxides for Oxygen Evolution Reaction" *NAM27*, New York City 2022.

Talk "A Synergistic CoFe Catalyst from Spinel Oxide for Hydrogen Production from Ammonia" *NAM27*, New York City 2022.

Poster "The Roles of Composition and Mesostructure of Cobalt-based Spinel Catalysts in Oxygen Evolution Reactions*" 55. Jahrestreffen Deutscher Katalytiker*, Weimar 2022.

Poster "Synthesis of Iron-Substituted Cobalt Oxides with Controlled Mesostructure and their Application in CO Oxidation" *CataLysis Conference*, Kassel 2022.

Talk "The Roles of Composition and Mesostructure of Cobalt-based Spinel Catalysts in Oxygen Evolution Reactions" *CENIDE conference* (accepted, moved to 2023 due to corona).

Talk "Synthesis of Substituted Cobalt Spinel Catalysts via Thermal Oxidation of Co-precipitated Crystalline Precursors and their Performance Trends in Oxidation Reactions" *54. Jahrestreffen Deutscher Katalytiker,* online 2021.

Poster "Microstructure-reactivity Relationships in the Electrocatalytic Oxygen Evolution Reaction of Cobalt Iron Oxide Catalysts Prepared by Microemulsion-assisted Co-precipitation" *Ertl Symposium,* South Korea/online 2020.

Talk "Microstructure-reactivity Relationships in the Electrocatalytic Oxygen Evolution Reaction of Cobalt Iron Oxide Catalysts Prepared by Microemulsion-assisted Co-precipitation" *ICC,* (accepted, cancelled due to corona), San Diego 2020.

Poster "Impact of Microstructure on the Electrocatalytic Activity in Oxygen Evolution Reaction of Cobalt Iron Oxide Catalysts Prepared by Microemulsion-assisted Co-precipitation", *53. Jahrestreffen Deutscher Katalytiker,* online 2020.

Talk "Synthesis of Cobalt Iron Oxide Catalysts via Co-precipitation of Crystalline Precursors", *CENIDE Conference,* Bergisch Gladbach 2020.

Poster "Impact of Microemulsion-assisted Co-precipitation at Constant pH on the Electrocatalytic Efficiency of Layered Double Hydroxides", *Young Chemists' Symposium*, Essen 2019.

Talk “Impact of Microemulsion-assisted Co-precipitation at Constant pH on the Electrocatalytic Efficiency of Layered Double Hydroxides”, *Young Chemists’ Symposium*, Essen 2019.

Poster “Microemulsion-assisted Co-precipitation of Cobalt Iron LDHs with Enhanced Electrocatalytic Properties” *International Symposium on “Confinement-Controlled Chemistry”*, Bochum 2019.

Talk “Impact of Microemulsion-assisted Co-precipitation at Constant pH on the Electrocatalytic Efficiency of Layered Double Hydroxides”, *EuropaCat,* Aachen 2019.

Poster: “Microemulsion assisted Co-precipitation of Cobalt Iron LDHs with Enhanced Electrocatalytic Properties”, *52. Jahrestreffen Deutscher Katalytiker*, Weimar 2019.

8.5 Curriculum Vitae

Der Lebenslauf ist in der Online-Version aus Gründen des Datenschutzes nicht enthalten.

Der Lebenslauf ist in der Online-Version aus Gründen des Datenschutzes nicht enthalten.

8.6 Declaration of Authorship

Hiermit bestätige ich, die vorliegende Arbeit mit dem Titel

„Tailoring Cobalt-based Spinels for the Investigation of Composition- and Mesostructure-Activity Relationships in Oxidation Catalysis”

Eigenständig verfasst und nur die angegeben Quellen und Hilfsmittel verwendet zu haben. Alle benutzten Quellen sind wörtlich oder sinngemäß als solche kenntlich gemacht. Diese Arbeit wurde in dieser oder ähnlicher Form bisher keinem Prüfungsausschuss oder einer anderen Universität eingereicht.

Essen, den 27. November 2023,

Anna Rabe